

# Staticity, Self-Similarity and Critical Phenomena in a Self-Gravitating Nonlinear $\sigma$ Model

Dissertation  
zur Erlangung des akademischen Grades  
Doktorin der Naturwissenschaften  
an der Formal- und Naturwissenschaftlichen Fakultät  
der Universität Wien

eingereicht von

CHRISTIANE LECHNER

im Oktober 2001

Kunst ist schön,  
macht aber viel Arbeit.

*Karl Valentin*

# ZUSAMMENFASSUNG

Ziel dieser Arbeit ist eine dataillierte Untersuchung spezieller Aspekte der Dynamik einer Klasse nichtlinearer Materiefelder im Rahmen der allgemeinen Relativitätstheorie. Von besonderem Interesse hier sind statische Lösungen (unter Berücksichtigung einer positiven kosmologischen Konstante), selbstähnliche Lösungen sowie die Bildung schwarzer Löcher.

Selbstgravitierende Materiefelder zeigen für Anfangsdaten, die an der Schwelle zum Kollaps liegen, ein Verhalten (sogenannte “kritische Phänomene”), das durch “Scaling”, Selbstähnlichkeit (bzw. Statizität) und Universalität charakterisiert ist. Das hier – in sphärischer Symmetrie – untersuchte  $SU(2)$   $\sigma$  Modell, ist in diesem Zusammenhang von besonderem Interesse, da die dimensionslose Kopplungskonstante in nichttrivialer Weise in die Theorie eingeht. Ziel dieser Arbeit ist, kritische Phänomene, insbesondere den Skalenexponenten und die kritische Lösung, in Abhängigkeit der Kopplung zu untersuchen.

Die Untersuchung erfolgt in zwei Schritten. Zunächst werden selbstähnliche Lösungen (unter Zuhilfenahme der Symmetrie) numerisch konstruiert und deren Stabilität untersucht (Kapitel 4). Wir reproduzieren die Ergebnisse von Bizon et al., die für kleine Kopplungen eine einparametrische Familie von kontinuierlich selbstähnlichen (CSS) Lösungen konstruiert haben. Wir zeigen, daß die erste Anregung dieser Familie eine instabile Mode hat. Weiters konstruieren wir eine diskret selbstähnliche (DSS) Lösung für große Kopplungen, die ebenfalls eine instabile Mode hat. Wir stellen die Hypothese auf, daß die DSS Lösung bei einem bestimmten Wert der Kopplung aus der ersten CSS Anregung in einer homoklinen Loopbifurkation entsteht.

Im zweiten Schritt werden einparametrische Familien von Anfangsdaten numerisch in der Zeit zu entwickelt (Kapitel 5). Nahekritische Anfangsdaten erhält man durch Bisektion. Die kritische Lösung kann an dem (zeitlich) intermediären Verhalten der nahekritischen Evolutionen abgelesen werden. Der Skalenexponent ist durch die Masse der schwarzen Löcher in Abhängigkeit des Parameters der Anfangsdaten bestimmt. Die so erhaltenen Ergebnisse stimmen sehr gut mit den Eigenschaften der oben konstruierten selbstähnlichen Lösungen überein. Für kleine Kopplungen ist die kritische Lösung die erste CSS Anregung. Für große Kopplungen ist es die DSS Lösung. Für mittlere Kopplungen finden wir einen Übergang von CSS zu DSS in der kritischen Lösung. Dieser Übergang ist mit der Hypothese der homoklinen Loopbifurkation konsistent.

Zusätzlich wird in dieser Arbeit über statische Lösungen des Modells (mit positiver kosmologischer Konstante) berichtet (Kapitel 3).

# Abstract

The aim of this work is to study certain aspects of the dynamics of a class of self-gravitating non-linear matter fields. In particular we concentrate on soliton solutions (in the presence of a positive cosmological constant), self-similar solutions and the formation of black holes.

The dynamics of initial data at the threshold of black hole formation are characterized by phenomena (so-called *critical phenomena*) including scaling, self-similarity (resp. staticity) and universality. In this work we concentrate on  $SU(2)$   $\sigma$  models coupled to gravity in spherical symmetry. These models are interesting due to a dimensionless parameter – the coupling – which enters the theory non-trivially. The aim is to investigate how critical phenomena – in particular the critical solution and the scaling exponent – depend on the coupling.

We use two essentially different methods to study the threshold behavior: Making use of the symmetry both discrete (DSS) and continuous (CSS) self-similar solutions are constructed (numerically) by solving boundary value problems (Chapter 4). The stability of these solutions is studied. For small couplings, reproducing results of Bizon et al., we find a discrete one-parameter family of CSS solutions. Of particular interest is the first CSS excitation. For large couplings we construct a DSS solution. Both solutions have one unstable mode. We conjecture, that the DSS solution bifurcates from the CSS solution in a homoclinic loop bifurcation at some value of the coupling constant.

The second method consists of evolving one parameter families of initial data numerically (Chapter 5). By a bisection search the initial data are fine-tuned such that they are close to the threshold. The critical solution then is determined by the intermediate asymptotics of near-critical data. The scaling exponent is determined from the black hole mass as a function of the parameter in the initial data. Our results are in very good agreement with the results on the self-similar solutions we obtained above. For small couplings the critical solution is CSS, for large couplings it is DSS and for intermediate couplings we find a new transition from CSS to DSS in the critical solution, which shows “episodic CSS”. This transition is consistent with the hypothesis of the homoclinic loop bifurcation.

In addition this work also contains results on static solutions of the model in the presence of a positive cosmological constant  $\Lambda$  (Chapter 3).

## Preface

This work originates in a project application to the FWF (Fonds zur Förderung Wissenschaftlicher Forschung), written by Sascha Husa and me under the supervision of Prof. P. C. Aichelburg in 1997. The FWF kindly supported this project (at least in part), which started in March (resp. May) 1998 (Project Nr. P12754-PHY). Michael Pürer joined our group in summer 1998 as a diploma student. In September 1998 Sascha Husa left for Pittsburgh and Jonathan Thornburg took his place in the project.

With the exception of Michael Pürer's work on the massless Klein-Gordon field with a compactified radial coordinate, I try to describe the main results of the project as complete as possible. Naturally, as the project is the joint work of five people with woven contributions, not all of the work presented here was done by myself. Whenever I used the method of someone else in the group (e.g. a code) or present results of runs, that were done by others, I mention this fact at the appropriate place.

I am very grateful to all five members of this group. Apart from everyone's scientific contributions to the project, I thank Prof. P. C. Aichelburg for chairing our numerous discussions, Sascha Husa for the work on the original application, for inviting me to Pittsburgh and for still being interested in collaborating with me, Jonathan Thornburg for his counsel regarding the details of the construction of the DSS solution and for always lending a helping hand in anything concerning computers, Michael Pürer for his computer assistance and the beers we had, and myself for surviving all this.

I think we all are very grateful to Piotr Bizon, who shared his results in advance of publication, for various discussions and his continuous interest in our work. I personally thank him for reading the manuscript of the paper on cosmological solitons and for inviting me to Krakow and introducing me to his family.

For reading and correcting the manuscript of this thesis I thank Prof. P. C. Aichelburg and Sascha Husa, as well as Jonathan Thornburg (who read the sections on the stability of self-similar solutions and the description of the DICE code), Prof. R. Beig for pointing out some mistakes in the first two chapters and Walter Simon and Mark Heinzle for suggestions concerning the introduction.

I am thankful to the gravity group at the institute with its broad range of interests, which gave me the chance to get into contact with a variety of topics through the regular seminars of the group. I am especially thankful to Prof. R. Beig for the seminar on "The Cauchy problem for the Einstein Equations", which gave me the opportunity to study (parts of) the article of the same name in some detail and to present it in some length.

Thanks to all students of the gravity group. Especially to Natascha Riahi and Mark Heinzle, who were forced to listen to the weekly discussions of our project

because of working in the same room. Thanks for housing the coffee machine, for the frequent conversations on all sorts of topics and for the feeling of not being the only fool. To Walter Simon for the impetus to organize various gatherings and barbecues. Thanks also for the room – it was essential to work at some spatial distance from the center of the typhoon! Special thanks to N. N. for the letters at my door. To all of us, who helped organizing the “Gschnas”. It was great fun and I think, we are rather good at this now. Thanks to Herbert Balasin for open ears and to Peter Steier for his advice on how to complete the PhD studies on the bureaucratic side.

[[ ... private part is cut ...]]

# Contents

<b>1</b>	<b>Introduction</b>	<b>9</b>
<b>2</b>	<b>The <math>SU(2)</math> <math>\sigma</math> Model in Spherical Symmetry</b>	<b>14</b>
2.1	The $SU(2)$ $\sigma$ Model . . . . .	14
2.1.1	Non-existence of Asymptotically Flat Soliton Solutions and Static Black Holes for $\Lambda$	
2.2	Spherical Symmetry . . . . .	18
2.2.1	A Regular Center of Spherical Symmetry . . . . .	20
2.2.2	The Mass Function . . . . .	22
2.2.3	The $SU(2)$ $\sigma$ Model in Spherical Symmetry . . . . .	23
2.3	The Einstein Equations and the Field Equation . . . . .	24
2.3.1	Mass Function, Bondi Mass and News Function . . . . .	26
<b>3</b>	<b>Static Solutions of the Self-gravitating <math>\sigma</math> Model in the Presence of a Cosmological <math>\Lambda</math></b>	
3.1	The Static Equations . . . . .	28
3.1.1	Staticity . . . . .	28
3.1.2	The Static Equations . . . . .	29
3.1.3	Exact Solutions . . . . .	30
3.1.4	Horizons and Global Structure . . . . .	31
3.2	Numerical Construction of Static Solutions . . . . .	37
3.2.1	Phenomenology of Static Solutions for $\Lambda > 0$ . . . . .	37
3.2.2	The Limit $\eta \rightarrow \eta_{max}$ . . . . .	39
3.2.3	Stability . . . . .	44
<b>4</b>	<b>Self-similar Solutions of the Self-gravitating <math>\sigma</math> Model</b>	<b>48</b>
4.1	Continuous and Discrete Self-Similarity . . . . .	48
4.1.1	Adapted Coordinates . . . . .	50

4.1.2	Self-Similarity in Spherical Symmetry . . . . .	51
4.1.3	Implications for the matter field . . . . .	58
4.2	Numerical Construction of CSS Solutions . . . . .	60
4.2.1	The “CSS equations” . . . . .	60
4.2.2	Phenomenology of Numerically Constructed Solutions . . .	62
4.2.3	Analytic Continuation beyond the past SSH . . . . .	63
4.3	Stability of CSS Solutions . . . . .	65
4.3.1	Unstable Modes from a Boundary Value Problem . . . . .	70
4.3.2	Gauge Modes . . . . .	71
4.3.3	Unstable Modes from a Matrix Analysis . . . . .	74
4.3.4	Numerical Results of the Stability Analysis . . . . .	76
4.4	Numerical Construction of DSS Solutions . . . . .	80
4.4.1	The DSS Equations . . . . .	81
4.4.2	Regularity at Origin and Past SSH . . . . .	83
4.4.3	Additional Symmetry . . . . .	84
4.4.4	Numerical Construction of DSS solutions via an ODE boundary value problem	84
4.4.5	Numerical Results . . . . .	88
4.4.6	Convergence with the Number of Fourier Coefficients . . .	88
4.4.7	Stability of the DSS Solution . . . . .	91
4.5	The Spectrum of Self-Similar Solutions Relevant for Type II Critical Collapse	95
4.5.1	Comparison of CSS and DSS solutions . . . . .	96
<b>5</b>	<b>Type II Critical Behavior of the Self-gravitating <math>\sigma</math> Model</b>	<b>102</b>
5.1	Introduction to Critical Phenomena . . . . .	103
5.2	Limits of Weak and Strong Coupling . . . . .	109
5.3	Possible End States . . . . .	110
5.4	The first CSS excitation for $0.15 \lesssim \eta < 0.5$ . . . . .	111
5.5	Critical Searches - Setup and Extraction of Results . . . . .	114
5.6	Critical Phenomena for Large Couplings . . . . .	116
5.7	Critical Phenomena for Small Couplings . . . . .	116
5.8	Critical Phenomena for Intermediate Couplings – Transition from CSS to DSS	128
<b>6</b>	<b>Discussion and Outlook</b>	<b>137</b>



<b>A</b>	<b>The Shooting and Matching Method</b>	<b>141</b>
<b>B</b>	<b>Discrete Fourier Transform</b>	<b>143</b>
B.1	Truncated Fourier Series . . . . .	143
B.2	Discrete Fourier Transform . . . . .	145
B.3	Differentiation . . . . .	148
B.4	Pseudo-spectral methods and Aliasing . . . . .	149
<b>C</b>	<b>The “Diamond-Integral-Characteristic-Evolution” Code – DICE</b>	<b>151</b>
C.1	The NSWE Algorithm . . . . .	152
C.2	Treatment of the Origin . . . . .	153
C.3	Integrating the Hypersurface Equations and the Geodesic Equation	154
C.4	Grid Refinements and Adaptive Time Steps . . . . .	155
C.5	Diagnostics, Accuracy and Convergence Tests . . . . .	156
C.6	Measurement of the black hole mass . . . . .	158
<b>D</b>	<b>Conventions</b>	<b>159</b>

# Chapter 1

## Introduction

The theory of general relativity describes gravity in terms of the curvature of the four dimensional Lorentzian manifold representing spacetime. The Einstein equations,  $G_{\mu\nu} = \kappa T_{\mu\nu}$ , relating matter to the curvature of spacetime involve the geometric objects  $T_{\mu\nu}$ , the stress energy tensor of matter, and  $G_{\mu\nu}$ , the Einstein tensor. Behind this simple geometric formulation there hides a coupled system of ten quasi-linear partial differential equations (PDEs), with the components of the metric as dependent variables. In addition, the matter fields themselves are subject to some field equations, which in turn contain the metric and its derivatives. These field equations therefore have to be solved simultaneously with the Einstein equations. Of special physical interest is to formulate and solve the initial value problem. In the “3+1” formulation for example, initial data consist of two symmetric three-tensor fields given on an initial spacelike hypersurface, which are subject to four constraint equations. The remaining six Einstein equations are used to evolve these initial data in time. One question of interest is for example: given smooth initial data, what is the long time behavior of the solution? There are analytic results showing global existence for sufficiently “weak” initial data<sup>1</sup>. On the other hand, singularity theorems<sup>2</sup> predict that sufficiently “strong” initial data develop a singularity in finite time. If the cosmic censorship hypothesis holds, these singularities should be shielded by a horizon such that they are invisible to distant observers. However, according to the complexity of the equations it is clear that i) only a very small number of exact solutions is known and ii) it is very difficult to get an analytic handle on the equations. It is therefore both necessary and extremely fruitful to combine analytic approaches with a numerical treatment of the equations.

An important step to understand the dynamics is to study the possible “end states” for the given matter model. It is reasonable to assume that regular initial data will asymptote to a stationary solution at late times, which could be e.g. a

---

<sup>1</sup>In particular [22]. For a review see [65].

<sup>2</sup>See [61] and [39].

stationary stable black hole, a stable soliton solution (corresponding to a star) or dispersion leading to Minkowski spacetime. Stationarity reduces the equations to an elliptic system. If additional symmetries are imposed, the problem simplifies further. In particular a static soliton or black hole solution, which is spherically symmetric, is obtained by solving a coupled system of (nonlinear) ordinary differential equations (ODEs). Initiated by the work of Bartnik and McKinnon [5], who numerically constructed static soliton solutions to the Einstein Yang-Mills (EYM) system in spherical symmetry, several self-gravitating matter models have been studied with regard to static soliton or black hole solutions<sup>3</sup>. Unfortunately most of the (non-trivial) solutions found are unstable, so they are not relevant for the late time behavior of general initial data. However, a few years later, it turned out that static solutions with a single unstable mode play an important role as intermediate attractors in type I critical collapse, as explained below.

Another fascinating field of research was started by the work of Choptuik [18, 19], who investigated the threshold of black hole formation for the self-gravitating massless Klein-Gordon system in spherical symmetry. Due to the analytic work by Christodoulou<sup>4</sup> it was known that “small” (in a well defined sense) initial data disperse, such that in the long time evolution such data approach Minkowski spacetime, whereas “strong” initial data form a black hole. Choptuik numerically evolved one parameter families of initial data, that interpolated between black hole formation and dispersion. He fine-tuned the parameter such that a “tiny” change in this parameter changed the end state from black hole formation to dispersion or vice versa. Speaking in the language of dynamical systems, the space of initial data (of the model under investigation) is divided into basins of attraction, the attractors in this case being black holes and Minkowski spacetime. From this point of view, Choptuik studied the boundary between two such basins of attraction. The phenomena he found, called *critical phenomena*<sup>5</sup>, can be summarized by the keywords *scaling*, *self-similarity* and *universality*. Scaling relates the black hole mass to the parameter  $p$  in the initial data via the simple power law  $m_{BH} \propto (p - p^*)^\gamma$ , where  $p^*$  is the critical parameter of the family. In particular this means that the black hole masses can be made arbitrarily small by fine-tuning the initial data. Furthermore, all near critical evolutions approach a self-similar solution at intermediate times. Studying several families of initial data in this way Choptuik found that these phenomena, especially the scaling exponent  $\gamma$  and the self-similar solution are *independent* of the family. So critical phenomena are universal within a given model. The numerical resolution of the phenomenon of self-similarity required sophisticated methods. Encouraged by

---

<sup>3</sup>Most of the work was done in spherical symmetry. The Einstein Yang-Mills system was also investigated in axis symmetry. In addition there are investigations concerning slowly rotating, that is stationary solutions to this model, obtained as linear rotational perturbations of the Bartnik McKinnon solutions and the coloured black holes. For details and an extensive list of references see the review article by Volkov and Gal'tsov [74]

<sup>4</sup>For references see e.g. [37].

<sup>5</sup>For details and review articles see Chapter 5.

Choptuik's results several other models were investigated with respect to critical phenomena. Most of the work concentrated on spherical symmetry with the early exception of Abrahams and Evans [1], who considered axially symmetric gravitational waves. All models exhibit the phenomena described above. The scaling exponent  $\gamma$  and the self-similar solution turned out to depend on the model. In particular there are models where the intermediate attractor is continuously self-similar (CSS) and other models, where it is discretely self-similar (DSS). Up to now it is not clear what causes the symmetry to be discrete or continuous. The results by Bizon et al. [10], who studied threshold phenomena of the  $SU(2)$   $\sigma$  model in flat space, indicate that critical phenomena are not tied to the Einstein equations, but are rather a general feature of hyperbolic PDEs. On the other hand, up to now it is not clear whether there are models in flat space which allow for a discretely self-similar solution, or whether DSS is a special feature of the Einstein equations.

It is worth noting that Choptuik's numerical work contributed much to the general understanding of the Einstein equations. In particular it stimulated the (semi-analytic) study of self-similar solutions and their stability properties. It turned out that the self-similar solutions at the threshold of black hole formation have one unstable mode. Furthermore a scaling argument relates the eigenvalue  $\lambda$  of the unstable mode to the scaling exponent  $\gamma$  via  $\gamma = 1/\lambda$ . Taking these results together, one has a good (although not rigorous) understanding of how critical phenomena emerge.

Apart from the phenomena found by Choptuik, some models in addition give rise to another type of critical behavior. There the intermediate attractor is a static (or oscillating) solution with one unstable mode. The black hole masses formed by slightly super-critical data are not arbitrarily small but are a finite fraction of the mass of the static solution. In analogy to statistical physics this kind of critical behavior, where the mass as a function of the parameter  $p$  is discontinuous, was called *type I*, whereas the phenomena found by Choptuik, where the mass is a continuous function of  $p$  are called *type II*.

We remark that the study of type II critical phenomena is entirely based on classical general relativity, ignoring the fact, that for regions with very strong curvature, which necessarily occur in type II critical collapse, the classical theory should be replaced by a quantum theory.

This work is part of a project, which originally aimed at investigating critical phenomena of the self-gravitating  $\sigma$  model in the presence of a cosmological constant. From the results of previous work [2] concerning static solutions of the model on de Sitter background it was reasonable to expect that these solutions would persist when gravity is "turned on". In particular one of the static solutions constructed in [2] has one unstable mode, which would therefore be a candidate for type I critical collapse<sup>6</sup>. It would then have been possible to in-

---

<sup>6</sup>In the coupled situation the "end states" could be de Sitter space and Schwarzschild-de-

investigate the coexistence of type I and type II critical phenomena on one hand, and the dependence of these phenomena on a dimensionless parameter (see below) on the other hand. Therefore we started to investigate existence and stability of static solutions in the presence of a positive cosmological constant  $\Lambda$ . However, because unexpected new phenomena emerged, our attention focused on critical phenomena in the asymptotically flat situation. The work on static solutions with  $\Lambda$  therefore is rather isolated from the rest of this thesis.

The main part of this thesis concentrates on type II critical phenomena of the self-gravitating  $SU(2)$   $\sigma$  model in spherical symmetry (without cosmological constant). We investigate the phenomena both by evolving one parameter families of initial data and doing a bisection search to fine-tune the parameter, and by “directly” constructing (i.e. by imposing the symmetry on the equations and solving the resulting reduced problem) the relevant self-similar solutions and studying their stability properties.

The motivations for choosing the  $SU(2)$   $\sigma$  model as the matter model are, that it is a very *simple* model (in spherical symmetry the field equations reduce to a single nonlinear wave equation) and that the theory contains a *dimensionless parameter*, the coupling constant  $\eta$ . Using dimensional analysis one can expect, that type II critical phenomena and the spectrum of self-similar solutions depend strongly on this parameter. This expectation is supported by previous work on the limits of strong [51] and weak coupling [10] and [53], where the solutions at the threshold are DSS in the limit  $\eta \rightarrow \infty$ , and CSS in the limit of vanishing coupling. This model therefore gives the chance to find out more about the mechanisms that are responsible e.g. for the realization of continuous self-similarity as opposed to discrete self-similarity. In particular the expected transition of the critical solution from CSS to DSS as the coupling is increased is of major interest.

This work is organized as follows: in Chapter 2 the self-gravitating  $SU(2)$   $\sigma$  model is introduced. We give the basic definitions and equations, that are necessary for the work on static solutions, self-similar solutions and critical collapse. The Einstein equations (with and without cosmological constant) and field equations are given with respect to coordinates, that are adapted to spherical symmetry. In particular the time evolution code DICE (see App. C) is based on a characteristic formulation of the initial value problem. The coordinates adjusted to this formulation (Bondi coordinates) are discussed in this chapter.

Chapter 3 deals with static solutions of the model in the presence of a positive cosmological constant  $\Lambda$ . We discuss the static equations, investigate the possible global structures of solutions and describe the numerical results. The limit  $\eta \rightarrow \eta_{max}$ , the maximal value of the coupling constant for which solutions exist, is carried out with care.

Chapter 4 deals with self-similar solutions of the model. We introduce the concept

---

Sitter (Kottler) space.

of self-similarity and its manifestation in Bondi coordinates. The main part of this chapter is dedicated to the numerical construction and linear stability analysis of CSS solutions and a discretely self-similar solution. The equations are given in adapted coordinates, the numerical methods for constructing the solutions are explained, results are discussed and stability of the solutions is investigated. In the last section we summarize which self-similar solutions might be relevant for the dynamics, either as “end states” or as critical solutions. Furthermore we investigate the relation between the DSS solution and the first CSS excitation. We put forward the hypothesis that the DSS solution bifurcates from the CSS solution in a *homoclinic loop bifurcation* at some critical value of the coupling constant  $\eta_C \simeq 0.17$ .

In Chapter 5 we describe our results concerning type II critical phenomena. For very small couplings the stable CSS ground state gives rise to the formation of naked singularities for “intermediately strong” initial data. For these couplings we therefore investigate critical phenomena between dispersion and the formation of naked singularities. For larger couplings the end states are flat space on one hand and black holes on the other hand. As expected, the critical behavior strongly depends on the coupling. For large couplings the critical solution is DSS, whereas for small couplings it is CSS. At intermediate couplings – in the “transition regime” – we find a new behavior, which we call “episodic CSS”. This behavior is consistent with the hypothesis of the homoclinic loop bifurcation, mentioned above.

Appendix A explains the shooting and matching method, which is used for the numerical construction of both static solutions and self-similar solutions.

In Appendix B we explain the method of discrete Fourier transform, which is used for the numerical construction of the DSS solution.

Appendix C describes the DICE code, that evolves the self-gravitating  $SU(2)$   $\sigma$  model in spherical symmetry. This code is used to investigate critical phenomena.

Our conventions concerning curvature quantities and the signature of the metric are those used in [76] (for details see App. D). Throughout this work the speed of light is set to unity,  $c = 1$ . The index notation should be self-explaining.

# Chapter 2

## The $SU(2)$ $\sigma$ Model in Spherical Symmetry

In this chapter we give the basic definitions and equations, that will be used for the work on static solutions as well as on critical collapse. We give the definition of the self-gravitating  $SU(2)$   $\sigma$  model (with and without positive cosmological constant). On spacetime we introduce two coordinate systems, that are adapted to spherical symmetry. For the work on static solutions we choose coordinates such that the hypersurfaces of constant time are spacelike, whereas for the work on critical collapse Bondi-like coordinates are used. Regularity of the metric in these coordinates near the center of spherical symmetry is discussed. Spherical symmetry is also imposed on the matter field via the so called hedgehog ansatz. We write down the Einstein equations and the field equation in these coordinates and give the formulae for the Misner-Sharp mass function as well as the Bondi mass and news function for asymptotically flat configurations.

### 2.1 The $SU(2)$ $\sigma$ Model

The  $SU(2)$   $\sigma$  model was first introduced into physics by Gell-Mann and Lévy [28] in order to describe the meson fields  $\pi_+$ ,  $\pi_-$ ,  $\pi_0$  and  $\sigma$ , subject to the condition  $\pi_+^2 + \pi_-^2 + \pi_0^2 + \sigma^2 = 1$ . Geometrically it is an harmonic map<sup>1</sup> from spacetime  $(M, g)$  to the target manifold  $(SU(2) \simeq \mathbb{S}^3, G)$ , where  $G$  is the standard metric on  $\mathbb{S}^3$ . Harmonic maps are well known in mathematics (see e.g. the review articles by Eells and Lemaire [23, 24]). Some of their applications in physics are described by Misner [55, 56]. In particular Misner points out that harmonic maps are geometrically natural nonlinear theories – as are gravity and Yang-Mills

---

<sup>1</sup>To be more precise, as the base manifold is spacetime with a metric with Lorentzian signature, the map is called a *wave map*.

theory – and could be used to model (the much more involved) nonlinearities in general relativity.

Concerning this work our interest in the  $SU(2)$   $\sigma$  model is mainly based on the fact that the theory contains a dimensionless parameter, while being a very simple generalization of the massless Klein-Gordon field. As will be argued below, both static and critical solutions are likely to depend on this dimensionless parameter. Therefore we are in the position to study (hopefully) a variety of phenomena within a comparatively simple model.

We start by choosing coordinates  $x^\mu$  on spacetime and coordinates  $X^A$  on the target manifold, and denote the map by  $X$ , so

$$\begin{aligned} (\mathbb{M}, g_{\mu\nu}) &\xrightarrow{X^A} (\mathbb{S}^3, G_{AB}) \\ x^\mu &\longrightarrow X^A(x^\mu). \end{aligned} \quad (2.1)$$

The three components  $X^A(x^\mu)$  of the map are scalar fields on spacetime. The harmonic map is defined to be the extremum of the action

$$S_{HM} = -\frac{f_\pi^2}{2} \int \sqrt{-g} \, d^4x \, g^{\mu\nu} \partial_\mu X^A \partial_\nu X^B G_{AB}(X). \quad (2.2)$$

Geometrically the Lagrangian is the pull back of the metric of the target manifold, contracted with the inverse metric on spacetime.  $f_\pi^2$  is the coupling constant of the fields.

Variation of the action with respect to the fields  $X^A$  yields the field equations

$$\square_g X^A + g^{\mu\nu} \tilde{\Gamma}_{BC}^A(X^D) \partial_\mu X^B \partial_\nu X^C = 0, \quad (2.3)$$

where  $\square_g$  is the wave operator on spacetime  $\square_g = g^{\mu\nu} \nabla_\mu \nabla_\nu$ , and  $\tilde{\Gamma}_{BC}^A$  denote the Christoffel symbols of the target manifold. For fixed base space  $(\mathbb{M}, g)$  Eq. (2.3) is a coupled quasi-linear system of wave equations for the  $X^A$ .

The simplest such system would be obtained, if the target manifold were just  $\mathbb{R}$ , for which the field equation for the single field  $X$  would just reduce to the Klein-Gordon equation. On the other hand assuming the base manifold to be one-dimensional and the target manifold being arbitrary, the system (2.3) would describe a geodesic on the target manifold. In this sense harmonic maps are simple geometric generalizations of both the Klein-Gordon field and geodesics.

In order to incorporate gravity, the action (2.2) has to be supplemented by the Einstein-Hilbert action

$$S_{tot} = \int \sqrt{-g} \left( \frac{1}{2\kappa} \mathcal{R} - 2\Lambda \right) + S_{HM}, \quad (2.4)$$

where  $\mathcal{R}$  denotes the Ricci scalar of spacetime,  $\kappa$  contains the gravitational constant  $G$  by  $\kappa = 8\pi G$ . In addition we have introduced a cosmological constant  $\Lambda$ , which we will always consider positive in this work.



Variation of the total action (2.4) with respect to the spacetime metric  $g_{\mu\nu}$  yields the Einstein equations

$$G_{\mu\nu} + g_{\mu\nu}\Lambda = \kappa T_{\mu\nu}, \quad (2.5)$$

where  $T_{\mu\nu}$  is the stress energy tensor of the  $\sigma$  model, obtained from varying the matter part of the action (2.2) with respect to the spacetime metric

$$T_{\mu\nu} = f_\pi^2 \left( \nabla_\mu X^A \nabla_\nu X^B - \frac{1}{2} g_{\mu\nu} (\nabla_\sigma X^A \nabla^\sigma X^B) \right) G_{AB}(X). \quad (2.6)$$

This stress energy tensor satisfies the weak, strong and dominant energy conditions, as defined in [39]. The weak energy condition (WEC) requires  $T_{\mu\nu} w^\mu w^\nu \geq 0$  for all timelike  $w$  corresponding to a positive energy density for all observers. The strong energy condition (SEC) results from the “timelike convergence condition”  $R_{\mu\nu} w^\mu w^\nu \geq 0$  for all timelike  $w$ , which for  $\Lambda = 0$  translates into a condition for the stress energy tensor  $T_{\mu\nu} w^\mu w^\nu \geq (1/2) w_\mu w^\mu T$ . Finally the dominant energy condition (DEC) consists of the weak energy condition plus the requirement that  $T^{\mu\nu} w_\nu$  is non-spacelike for all timelike  $w$ . An equivalent condition is, that the components in any orthonormal basis satisfy  $T^{\hat{0}\hat{0}} \geq |T^{\hat{I}\hat{J}}|$  for all  $\hat{I}, \hat{J}$ .

For the WEC we choose an orthonormal basis  $\{e_I\}_{I=0,1,2,3}$  with the coordinate representation  $e_I = e_I^\mu \partial_\mu$ . We consider the expression  $T_{\mu\nu} e_0^\mu e_0^\nu = T_{\hat{0}\hat{0}}$ , which can be written as

$$T_{\mu\nu} e_0^\mu e_0^\nu = \frac{1}{2} (X_* e_0)^A (X_* e_0)^B G_{AB} + \frac{1}{2} (X_* e_i)^A (X_* e_j)^B \delta^{ij} G_{AB} \geq 0, \quad (2.7)$$

as  $G_{AB}$  is Riemannian and therefore the above expression is a sum of positive (or vanishing) terms. By  $X_* v$  we denoted the push forward of the vector  $v$  from spacetime to the target manifold. As the above relation is valid for any orthonormal basis, the relation  $T_{\mu\nu} w^\mu w^\nu \geq 0$  is satisfied for all timelike  $w$ .

For the SEC again we choose an orthonormal basis as above. Inserting this into the expression  $T_{\mu\nu} e_0^\mu e_0^\nu + (1/2)T$  one finds that

$$T_{\mu\nu} e_0^\mu e_0^\nu + \frac{1}{2} T = 0. \quad (2.8)$$

Again this is valid for all orthonormal bases, and therefore the matter field satisfies the SEC borderline, as the massless Klein-Gordon field does.

Finally to check the DEC we work with the components of  $T_{\mu\nu}$  in an orthonormal base. We have

$$\begin{aligned} T^{\hat{0}\hat{0}} &= T_{\hat{0}\hat{0}} = \frac{1}{2} (X_* e_0)^A (X_* e_0)^B G_{AB} + \frac{1}{2} (X_* e_i)^A (X_* e_j)^B \delta^{ij} G_{AB}, \\ T^{\hat{0}\hat{i}} &= -T_{\hat{0}\hat{i}} = -(X_* e_0)^A (X_* e_i)^B G_{AB} \\ T^{\hat{i}\hat{j}} &= T_{\hat{i}\hat{j}} = (X_* e_i)^A (X_* e_j)^B G_{AB} - \frac{1}{2} \delta_{ij} [-(X_* e_0)^A (X_* e_0)^B + \delta^{kl} (X_* e_k)^A (X_* e_l)^B] G_{AB}. \end{aligned} \quad (2.9)$$

As  $G_{AB}$  is positive definite, we have  $|2G(v, w)| \leq G(v, v) + G(w, w)$ . Therefore  $|T^{\hat{0}\hat{i}}| \leq T^{\hat{0}\hat{0}}$ . One also easily sees, that  $|T^{\hat{i}\hat{j}}| \leq T^{\hat{0}\hat{0}}$  (without summation over  $\hat{i}$ ) and that  $|T^{\hat{i}\hat{j}}| \leq T^{\hat{0}\hat{0}}$  for  $\hat{i} \neq \hat{j}$ . Again the tetrad was chosen arbitrarily, so the relations are valid in any orthonormal base.

Note that the coupling constants  $f_\pi^2$  and  $G$  only enter the equations (2.5) as the product  $\eta := \frac{\kappa f_\pi^2}{2}$ . In units where the speed of light is set to unity  $c = 1$ ,  $G$  has dimension of *length/mass* and  $f_\pi^2$  has dimension of *mass/length*, so their product is dimensionless. Therefore the only scale in the theory is tied to the cosmological constant  $\Lambda$ , which has dimension of  $1/\text{length}^2$ . As  $\Lambda$  merely sets the scale of the theory, its actual numerical value can be eliminated from the equations and only its sign matters.

For fixed  $\Lambda$  on the other hand the presence of the dimensionless product of coupling constants  $\eta := \frac{\kappa f_\pi^2}{2}$  provides a one parameter family of physically different theories.

For  $\Lambda = 0$ , the theory is scale invariant. This implies immediately (as will be explained in Sec. 2.1.1) that for  $\Lambda = 0$  this model does not admit asymptotically flat soliton solutions [6]. On the other hand, as described in Sec. 4.1.3, the scale invariance for  $\Lambda = 0$  is necessary for the existence of self-similar solutions.

### 2.1.1 Non-existence of Asymptotically Flat Soliton Solutions and Static Black Holes for $\Lambda = 0$

Using a scaling argument, it is easy to see that the system (2.3) and (2.5) does not admit static, globally regular, asymptotically flat solutions (so-called *soliton solutions*) apart from the trivial solution, which is Minkowski spacetime with vanishing matter field. Assume there exists a static solution  $(\hat{g}_{\mu\nu}, \hat{X}^A)$  to the system (2.3) and (2.5). We denote the timelike Killing vector by  $\xi = \partial_t$  and choose coordinates  $x^i$  in the hypersurfaces  $\Sigma$  orthogonal to  $\xi$ . For regular solutions  $\Sigma$  is topologically  $\mathbb{R}^3$ . Denoting the induced metric by  $\hat{h}_{ij}$  we can write  $ds^2 = -\hat{N}dt^2 + \hat{h}_{ij}dx^i dx^j$ . Staticity in these coordinates manifests itself in the independence of the metric functions  $\hat{N}$  and  $\hat{h}_{ij}$  and the fields  $\hat{X}^A$  of the time coordinate  $t^2$ .

For static solutions, due to the existence of the Killing vector  $\xi$ , one can define the energy of the field

$$E = - \int_{\Sigma} \sqrt{\hat{h}} d^3x n_\mu \xi^\nu \hat{T}_\nu^\mu = - \int_{\Sigma} \sqrt{\hat{h}} d^3x \hat{N} \hat{T}_0^0. \quad (2.10)$$

Asymptotic flatness guarantees the existence of this integral.  $E$  is a conserved quantity, i. e. independent of the hypersurface  $\Sigma$ , which follows from  $\nabla_\mu(\xi^\nu \hat{T}_\nu^\mu) =$

---

<sup>2</sup>For implications of a spacetime symmetry on the fields  $X^A$  see Sec. 2.2.3

0. Furthermore  $E$  is positive definite as the lapse  $\hat{N}$  is positive, and the energy density  $-\hat{T}_0^0$  is positive as well. Moreover  $\hat{T}_0^0$  vanishes iff  $(X_*e_{\hat{t}}) = 0$  (or equivalently  $X$  is constant), i.e. if the map is trivial.

Since the model for  $\Lambda = 0$  is scale invariant, there exists a one-parameter family of solutions  $\left((\hat{g}_{\mu\nu})_\lambda(x^i) := \hat{g}_{\mu\nu}(\lambda x^i), \hat{X}_\lambda^A(x^i) := \hat{X}^A(\lambda x^i)\right)$ . The corresponding energies  $E_\lambda$  are obtained from  $E$  by  $E_\lambda = \frac{1}{|\lambda|}E$ . As a static solution extremizes the energy (2.10) we must have  $dE_\lambda/d\lambda|_{\lambda=1} = 0$ , so  $E$  has to be zero and therefore the matter field has to vanish,  $\hat{X}^A = \text{const}$ . We are left with a regular, static, asymptotically flat solution to the vacuum Einstein equations, which has to be Minkowski spacetime due to the theorems by Lichnerowicz [50].

It was also shown [43, 42], that this model with  $\Lambda = 0$  neither admits non-trivial static asymptotically flat black hole solutions.

So if one is interested in static solutions of this model, the cosmological constant is essential, or as we shall see in Sec. 3.2.2, the assumption of asymptotic flatness and  $\Sigma$  being  $\mathbb{R}^3$  has to be dropped.

## 2.2 Spherical Symmetry

An isometry is a diffeomorphism  $\Phi$  from  $(M, g)$  to  $(M, g)$ , which maps the metric to itself, i.e.

$$\Phi^*g = g. \quad (2.11)$$

For a one parameter family of such diffeomorphisms  $\Phi_\lambda$ , with  $\Phi_0 = id$  one can define the generator  $\xi = d\Phi_\lambda/d\lambda|_{\lambda=0}$ . Eq. (2.11) then can be formulated in terms of the Lie derivative

$$\mathcal{L}_\xi g = 0, \quad (2.12)$$

or equivalently

$$\xi_{(\mu;\nu)} = 0. \quad (2.13)$$

Such a family of isometries leaves the curvature tensors invariant (this can be seen in taking the analogous steps as in Sec. 4.1), in particular

$$(\mathcal{L}_\xi G)_{\mu\nu} = 0. \quad (2.14)$$

A spacetime is said to be spherically symmetric, if it admits the group  $SO(3)$  as a group of isometries, acting on spacelike two-dimensional surfaces (See e.g. [39]). The group acts transitively but not simply transitively: as the group is three dimensional and the spacelike surfaces are only two-dimensional, it has  $SO(2)$  as an isotropy group. The orbits of the group are surfaces of constant positive curvature.

It can be shown [39] that the metric of a spherically symmetric spacetime can be written as the warped product

$$ds^2 = d\tau^2 + R^2(\tau^i) (d\theta^2 + \sin^2 \theta d\varphi^2), \quad (2.15)$$

where the coordinates  $\theta$  and  $\varphi$  are coordinates on  $\mathbb{S}^2$  – the orbits of  $\text{SO}(3)$  – with the usual range  $0 < \theta < \pi$  and  $0 \leq \varphi < 2\pi$ .  $d\tau^2$  denotes the line element of a two-dimensional Lorentzian manifold (with coordinates  $\tau^i$ ), and  $R(\tau^i)$  is related to the area of the orbits of  $\text{SO}(3)$  by  $A = 4\pi R^2$ .

For this work we use two different choices of coordinates for the Lorentzian two-surfaces: for the work on static solutions (in the presence of a positive cosmological constant), we choose orthogonal coordinates  $(t, \rho)$

$$ds^2 = -A(t, \rho)dt^2 + B(t, \rho)d\rho^2 + R^2(t, \rho)d\Omega^2, \quad (2.16)$$

where  $d\Omega^2 \equiv (d\theta^2 + \sin^2 \theta d\varphi^2)$ . Usually these coordinates are further restricted by choosing the area of the orbits of  $\text{SO}(3)$  as a coordinate. But this is only possible in regions, where  $\nabla_\mu R \neq 0$ . As some of our static solutions will contain hypersurfaces where the gradient  $\nabla_\mu R$  vanishes, we choose a different gauge: we set  $1/B = A =: Q$ , so

$$ds^2 = -Q(t, \rho) dt^2 + \frac{d\rho^2}{Q(t, \rho)} + R^2(t, \rho) d\Omega^2. \quad (2.17)$$

For the investigations on critical collapse, we work with Bondi-like coordinates, i.e. we foliate spacetime by outgoing null cones  $u = \text{const}$ , which emanate from the center of spherical symmetry ( $R = 0$ ) and parameterize these with the area of the two-spheres  $r := \sqrt{A/4\pi}$ , so we get

$$ds^2 = -e^{2\beta(u, r)} du \left( \frac{V}{r}(u, r) du + 2dr \right) + r^2 d\Omega^2. \quad (2.18)$$

The normal vectors to the hypersurfaces  $u = \text{const}$  are null, as  $-\nabla_\mu u = (-1, 0, 0, 0)$  and  $-\nabla^\mu u = (0, -g^{ur}, 0, 0)$ , so  $\nabla_\mu u \nabla^\mu u = 0$ . Furthermore, they generate affinely parametrized geodesics, as

$$\nabla^\sigma u \nabla_\sigma \nabla^\mu u = \nabla^\sigma u \nabla^\mu \nabla_\sigma u = \frac{1}{2} \nabla^\mu (\nabla_\sigma u \nabla^\sigma u) = 0. \quad (2.19)$$

The areal coordinate  $r$  parameterizes these null geodesics, but is not the affine parameter.

Ingoing radial null geodesics are given as the solutions of

$$\frac{dr(u)}{du} = -\frac{V(u, r(u))}{2r(u)}. \quad (2.20)$$

We normalize  $u$  to be proper time at the origin. We require  $\beta(u, r = 0) = 0$ . Regularity at the origin then enforces  $\frac{V}{r}(u, r = 0) = 1$  (see Sec. 2.2.1). The connection between these “Bondi-like” coordinates and Bondi coordinates for which  $\beta_B(u_B, r = \infty) = 0$  is given by a coordinate transformation  $u \rightarrow u_B(u)$ , with

$$e^{2\beta_B(u_B, r)} du_B = e^{2\beta(u, r)} du, \quad (2.21)$$

in particular at infinity we have

$$\frac{du_B}{du} = e^{2H(u)}, \quad \text{with} \quad H(u) := \beta(u, r = \infty). \quad (2.22)$$

Therefore

$$\begin{aligned} \beta_B(u_B, r) &= \beta(u, r) - H(u) \\ \left(\frac{V}{r}\right)_B(u_B, r) &= \left(\frac{V}{r}\right)(u, r) e^{-2H(u)}. \end{aligned} \quad (2.23)$$

For further use we give the square root of the determinant of the metric  $\sqrt{-g} = e^{2\beta} r^2 \sin \theta$  and the inverse metric

$$g^{\mu\nu} = \begin{pmatrix} 0 & -e^{-2\beta} & 0 & 0 \\ -e^{-2\beta} & e^{-2\beta} \frac{V}{r} & 0 & 0 \\ 0 & 0 & \frac{1}{r^2} & 0 \\ 0 & 0 & 0 & \frac{1}{r^2 \sin^2 \theta} \end{pmatrix}. \quad (2.24)$$

## 2.2.1 A Regular Center of Spherical Symmetry

Clearly the coordinates (2.17) and (2.18) break down at a center of spherical symmetry  $R = 0$ ,  $r = 0$  respectively. Apart from the vanishing volume of the two-spheres, which is well known from polar coordinates in flat space, the metric functions  $Q, R$  and  $\beta, \frac{V}{r}$  have to satisfy additional regularity requirements, if one asks for a regular center of spherical symmetry. By definition the metric is regular ( $C^k$ ), if its application to regular ( $C^k$ ) vector fields yields regular ( $C^k$ ) functions on the manifold. The easiest way to examine this is to switch to regular coordinates close to the center.

We start with the coordinates (2.17). First we fix the origin of the coordinate  $\rho$  to be at the center of spherical symmetry,  $R(t, \rho = 0) = 0$ . We choose coordinates  $(t, x, y, z)$ , connected to  $(t, \rho, \theta, \varphi)$  by  $x = \rho \sin \theta \cos \varphi$ ,  $y = \rho \sin \theta \sin \varphi$ ,  $z = \rho \cos \theta$  and  $t = t$ . We assume  $(t, x, y, z)$  to be regular coordinates in the vicinity of  $\rho = 0$ . A function then is regular, if it can be written as a regular function of these coordinates. By specifying the above coordinate transformation we also have implicitly assumed that the coordinate function  $\rho$  has special regularity properties, namely  $\rho$  itself is not regular, but any even power thereof is. First note that  $g(\partial_t, \partial_t) = -Q$ , which is regular if  $Q$  is a regular function of  $(t, x, y, z)$ .

In other words,  $Q$  has to be a regular function of  $t$  and  $\rho^2$ . Second we consider the sum of the spatial components of the metric with respect to the regular coordinates,

$$g(\partial_x, \partial_x) + g(\partial_y, \partial_y) + g(\partial_z, \partial_z) = \frac{1}{Q} + 2\frac{R^2}{\rho^2}. \quad (2.25)$$

This shows, that  $R/\rho$  has to be a regular function of  $t$  and  $\rho^2$ . Having again a look at  $g(\partial_z, \partial_z)$ ,

$$g(\partial_z, \partial_z) = \cos^2 \theta \frac{1}{Q} + \frac{\sin^2 \theta}{\rho^2} R^2, \quad (2.26)$$

we see, that the only possibility for this expression to have a regular limit  $\rho \rightarrow 0$ , is

$$\lim_{\rho \rightarrow 0} \frac{R^2 Q}{\rho^2} = 1, \quad (2.27)$$

so  $Q(t, 0) = 1/R'(t, 0)$ , which we can choose without loss of generality to be 1. Therefore near a regular center of symmetry the metric functions behave as follows

$$\begin{aligned} R(t, \rho) &= \rho + O(\rho^3) \\ Q(t, \rho) &= 1 + O(\rho^2). \end{aligned} \quad (2.28)$$

For the Bondi-like coordinates (2.18) we define in analogy the coordinates  $t = u + r$ ,  $x = r \sin \theta \cos \varphi$ ,  $y = r \sin \theta \sin \varphi$  and  $z = r \cos \theta$ . We have  $g(\partial_t, \partial_t) = -e^{2\beta} \frac{V}{r}$  and

$$g(\partial_x, \partial_x) + g(\partial_y, \partial_y) + g(\partial_z, \partial_z) = 2 - e^{2\beta} \frac{V}{r} + 2e^{2\beta}. \quad (2.29)$$

From this it follows that the metric functions  $\beta$  and  $\frac{V}{r}$  have to be regular functions of  $t$  and  $r^2$ . Looking at  $g(\partial_z, \partial_z)$

$$g(\partial_z, \partial_z) = e^{2\beta} \left(2 - \frac{V}{r}\right) \cos^2 \theta + \sin^2 \theta, \quad (2.30)$$

we see that  $\lim_{r \rightarrow 0} e^{2\beta} \left(\frac{V}{r} - 2\right) = 1$  is a necessary condition for regularity.  $\beta(u, r = 0)$  has already been chosen to be unity, so  $\frac{V}{r}(t, r = 0) = 1$ . It remains to transform these functions of  $t$  and  $r^2$  back to functions of  $u = t - r$  and  $r$ . The first terms in a Taylor series expansion give

$$\begin{aligned} \beta(u, r) &= O(r^2) \\ \frac{V}{r}(u, r) &= 1 + O(r^2). \end{aligned} \quad (2.31)$$

Note however, that  $\beta$  and  $\frac{V}{r}$  if expanded in  $u - u_0$  and  $r$  don't solely contain even powers of  $r$ . The first non-vanishing term with an odd power in  $r$  is e.g. the term  $\dot{\beta}''(u_0, 0)r^3$ .

## 2.2.2 The Mass Function

In spherical symmetry one can define the Misner-Sharp mass function [57]  $m(\tau^i)$ , by

$$1 - \frac{2m}{R} = \nabla_\mu R \nabla^\mu R, \quad (2.32)$$

(for a recent description of the properties of this function see the article by Hayward [41]) which gives

$$m(t, \rho) = \frac{R}{2} \left( 1 + \frac{1}{Q(t, \rho)} \dot{R}^2(t, \rho) - Q(t, \rho) (R'(t, \rho))^2 \right) \quad (2.33)$$

for the coordinates (2.17). Its interpretation for static solutions in the presence of a positive cosmological constant will be described in Sec. 3.1.4.

For the Bondi-like coordinates (2.18) we have

$$m(u, r) = \frac{r}{2} \left( 1 - e^{-2\beta(u, r)} \frac{V}{r}(u, r) \right). \quad (2.34)$$

For an asymptotically flat spacetime, the Bondi mass is obtained by taking the limit  $r \rightarrow \infty$  of  $m(u, r)$  along the null hypersurfaces  $u = \text{const}$ , so

$$m_{\text{Bondi}}(u) = \lim_{r \rightarrow \infty} m(u, r). \quad (2.35)$$

In general, due to radiation (of the matter fields only in spherical symmetry), the Bondi mass will decrease with retarded time  $u$ . We give an explicit formula for the mass loss in Sec. 2.3.1

The formation of an apparent horizon is signalled by the vanishing of the expansion of outgoing null geodesics  $\Theta_+ = 0$ .  $\Theta_+$  can be expressed as the Lie derivative of the area  $A$  of 2-spheres with respect to the tangent to outgoing null geodesics  $l_+^\mu$ , divided by the area:  $\Theta_+ = (\mathcal{L}_{l_+} A)/A$ .

For the Bondi-like coordinates, we have already seen that  $-\nabla^\mu u$  is tangent to the outgoing radial null geodesics ( $u = \text{const}$ ). The area of the 2-spheres is given by  $A = 4\pi r^2$ , so we have

$$\Theta_+ = \frac{-2g^{ur}}{r} = \frac{2e^{-2\beta}}{r}. \quad (2.36)$$

An apparent horizon in these coordinates therefore manifests itself by  $\beta \rightarrow \infty$ . The breakdown of these coordinates at an apparent horizon is due to  $r$  (in connection with  $u$ ) ceasing to be a good coordinate. As stated above the areal coordinate  $r$  parameterizes the null cones  $u = \text{const}$ . This is possible as long as  $\nabla_u r \neq 0$ , which evaluates precisely to  $g^{ur} \neq 0$ , which is then violated at the apparent horizon.

### 2.2.3 The SU(2) $\sigma$ Model in Spherical Symmetry

Imposing a symmetry on spacetime also requires some symmetry properties for the matter. The stress energy tensor  $T_{\mu\nu}$  has to be invariant under the isometry

$$\mathcal{L}_\xi T^{\mu\nu} = 0, \quad (2.37)$$

otherwise the symmetry of spacetime would be incompatible with the Einstein equations.

For the SU(2)  $\sigma$  model we write the stress energy tensor (2.6) as

$$T_{\mu\nu} = (X^*G)_{\mu\nu} - \frac{1}{2}g_{\mu\nu}g^{\sigma\tau}(X^*G)_{\sigma\tau}. \quad (2.38)$$

The Lie derivative of this expression then gives

$$\mathcal{L}_\xi T_{\mu\nu} = \mathcal{L}_\xi(X^*G)_{\mu\nu} - \frac{1}{2}g_{\mu\nu}g^{\sigma\tau}\mathcal{L}_\xi(X^*G)_{\sigma\tau}, \quad (2.39)$$

if  $\xi$  is a Killing vector field.

As the Lie derivative commutes with the pull back

$$\mathcal{L}_\xi(X^*G)_{\mu\nu} = (X^*(\mathcal{L}_{X_*\xi}G))_{\mu\nu}, \quad (2.40)$$

the requirement (2.37) is satisfied if

$$\mathcal{L}_{X_*\xi}G_{AB} = 0. \quad (2.41)$$

This means that either  $X_*\xi \equiv 0$  or the Killing vector field  $\xi$  is mapped to a Killing vector field on the target manifold.

Applying this to spherical symmetry there are essentially two possibilities to make the map spherically symmetric. First, if none of the fields  $X^A$  depends on the angular variables  $\theta$  and  $\varphi$  then the Killing vector fields  $\xi_i$  of spherical symmetry on spacetime would be mapped to the zero vector field at the target manifold. This way one would deal with three fields  $X^A(\tau^i)$ .

The second possibility, which is chosen in this work, uses the symmetry of the target manifold: as the metric  $G_{AB}$  is the metric of constant curvature on  $\mathbb{S}^3$  it also admits SO(3) acting on 2-spheres as a group of isometries. We choose coordinates  $(\phi, \Theta, \Phi)$  such that the line element is given by

$$ds_{\mathbb{S}^3}^2 = d\phi^2 + \sin^2\phi(d\Theta^2 + \sin^2\Theta d\Phi^2). \quad (2.42)$$

Obviously the vector fields

$$\begin{aligned} \Xi_1 &= \sin\Phi\partial_\Theta + \cot\Theta\cos\Phi\partial_\Phi, \\ \Xi_2 &= -\cos\Phi\partial_\Theta + \cot\Theta\sin\Phi\partial_\Phi, \\ \Xi_3 &= -\partial_\Phi \end{aligned} \quad (2.43)$$



are Killing vector fields on the target manifold. We demand now, that the corresponding Killing vector fields on spacetime  $\xi_i$  are mapped to their counterparts on the target manifold, i.e.

$$X_*\xi_i \stackrel{!}{=} \Xi_i. \quad (2.44)$$

This is achieved by the so called *hedgehog ansatz*

$$\phi(x^\mu) = \phi(\tau^i), \quad \Theta(x^\mu) = \theta, \quad \Phi(x^\mu) = \phi. \quad (2.45)$$

This way the field equations (2.3) decouple into a nonlinear wave equation for  $\phi(\tau^i)$  and two equations for  $\Theta$  and  $\Phi$ , which are satisfied identically.

In order to examine regularity of the map at the center of spherical symmetry, we again work with Cartesian coordinates  $X = \phi \sin \Theta \sin \Phi = \phi \sin \theta \cos \varphi = (\phi/r)x$ ,  $Y = \phi \sin \Theta \cos \Phi = \phi \sin \theta \sin \varphi = (\phi/r)y$ ,  $Z = \phi \cos \Theta = \phi \cos \theta = (\phi/r)z$  (for the coordinates (2.17)  $r$  is replaced by  $\rho$ ). The fields  $(X, Y, Z)$  are regular functions on spacetime, iff  $\phi/r$  ( $\phi/\rho$  respectively) is a regular function. Therefore close to the origin we get the expansions

$$\phi(t, \rho) = \rho(1 + O(\rho^2)) \quad (2.46)$$

$$\phi(u, r) = r(1 + O(r^2)). \quad (2.47)$$

for fixed time  $t$  or fixed retarded time  $u$ . Again for fixed  $t$ ,  $\phi$  is a regular function of  $\rho^2$  whereas for fixed  $u$  odd powers of  $r$  appear.

In particular this means that for all times  $t$  ( $u$ ) the origin is mapped to a single point on  $\mathbb{S}^3$ , which is the north pole as defined by (2.42).

## 2.3 The Einstein Equations and the Field Equation

With the hedgehog ansatz (2.45) the field equations (2.3) reduce to the single wave equation

$$\square_g \phi = \frac{\sin(2\phi)}{R^2} \quad \left( \frac{\sin(2\phi)}{r^2} \text{ resp.} \right), \quad (2.48)$$

where  $\square_g \phi$  reads

$$\square_g \phi = \frac{1}{R^2} \left( -\partial_t \left( \frac{R^2}{Q} \partial_t \right) + \partial_\rho (R^2 Q \partial_\rho) \right) \phi \quad (2.49)$$

$$\square_g \phi = e^{-2\beta} \left( \left( \frac{2V}{r^2} + \left( \frac{V}{r} \right)' \right) \partial_r - \frac{2}{r} \partial_u - 2\partial_u \partial_r + \frac{V}{r} \partial_{rr} \right) \phi, \quad (2.50)$$

for the coordinates (2.17), (2.18) respectively.

For the work on static solutions (see Chapter 3) the following combinations of the Einstein equations  $G_\nu^\mu + \Lambda \delta_\nu^\mu = \kappa T_\nu^\mu$  will turn out to be convenient: the combinations  $(^t_t) + (^{\rho}_\rho) - 2(^{\theta}_\theta)$ ,

$$\begin{aligned} \frac{2\dot{Q}(\rho, t)^2}{Q(\rho, t)^3} - \frac{\ddot{Q}(\rho, t)}{Q(\rho, t)^2} + \frac{-2 - \frac{2\dot{R}(\rho, t)^2}{Q(\rho, t)} + 2Q(\rho, t)R'(\rho, t)^2}{R(\rho, t)^2} - Q''(\rho, t) = \\ = 2\eta \left( \frac{-2\sin(\phi(r, t))^2}{R(r, t)^2} - \frac{\dot{\phi}(r, t)^2}{Q(r, t)} + Q(r, t)\phi'(r, t)^2 \right), \end{aligned} \quad (2.51)$$

$(^t_t) - (^{\rho}_\rho)$ ,

$$\frac{2\left(\ddot{R}(\rho, t) + Q(\rho, t)^2 R''(\rho, t)\right)}{Q(\rho, t)R(\rho, t)} = -2\eta \left( \frac{\dot{\phi}(\rho, t)^2}{Q(\rho, t)} + Q(\rho, t)\phi'(\rho, t)^2 \right) \quad (2.52)$$

of the Hamiltonian constraint  $(^t_t)$  and the time evolution equations  $(^{\rho}_\rho)$  and  $(^{\theta}_\theta)$ , the time evolution equation  $(^{\rho}_\rho)$ ,

$$\begin{aligned} \Lambda - R(\rho, t)^{-2} + \frac{\dot{Q}(\rho, t)\dot{R}(\rho, t)}{Q(\rho, t)^2 R(\rho, t)} - \frac{\dot{R}(\rho, t)^2}{Q(\rho, t)R(\rho, t)^2} - \frac{2\ddot{R}(\rho, t)}{Q(\rho, t)R(\rho, t)} + \\ + \frac{Q'(\rho, t)R'(\rho, t)}{R(\rho, t)} + \frac{Q(\rho, t)R'(\rho, t)^2}{R(\rho, t)^2} = \\ = \eta \left( \frac{-2\sin(\phi(\rho, t))^2}{R(\rho, t)^2} + \frac{\dot{\phi}(\rho, t)^2}{Q(\rho, t)} + Q(\rho, t)\phi'(\rho, t)^2 \right) \end{aligned} \quad (2.53)$$

and the momentum constraint  $(^t_\rho)$ ,

$$\frac{-\dot{R}(\rho, t)Q'(\rho, t)}{Q(\rho, t)^2 R(\rho, t)} + \frac{\dot{Q}(\rho, t)R'(\rho, t)}{Q(\rho, t)^2 R(\rho, t)} + \frac{2\dot{R}'(\rho, t)}{Q(\rho, t)R(\rho, t)} = -2\eta \frac{\dot{\phi}(\rho, t)\phi'(\rho, t)}{Q(\rho, t)}, \quad (2.54)$$

where  $' \equiv \partial_\rho$  and  $\dot{\phantom{x}} \equiv \partial_t$ . Of course  $G_\phi^\phi = G_\theta^\theta$  and all other components vanish identically. (See Chapter 3 on the structure of these equations in the static case.)

For the work on critical collapse in the coordinate frame (2.18) the nontrivial Einstein equations split up into the hypersurface equations (the  $\{rr\}$  and  $\{ur\} - (V/2r)\{rr\}$  components of  $G_{\mu\nu} = \kappa T_{\mu\nu}$ )

$$\beta' = \frac{\eta}{2}r(\phi')^2, \quad (2.55)$$

$$V' = e^{2\beta}(1 - 2\eta\sin(\phi)^2), \quad (2.56)$$

and the subsidiary equations  $-E_{uur} \equiv r^2(G_{uu} - \kappa T_{uu}) - r^2(V/r)(G_{ur} - \kappa T_{ur})$  and  $E_{\theta\theta} \equiv G_{\theta\theta} - 8\pi T_{\theta\theta}$ :

$$E_{uur} \equiv 2V\dot{\beta} - \dot{V} + 2\eta r^2 \left[ \dot{\phi}^2 - \frac{V}{r}\phi'\dot{\phi} \right] = 0, \quad (2.57)$$

$$\begin{aligned}
E_{\theta\theta} \equiv & V(r\beta'' - \beta') + r\beta'V' + \frac{1}{2}rV'' - 2r^2\dot{\beta}' \\
& - \eta r^2\phi' \left( -\frac{V}{r}\phi' + 2\dot{\phi} \right) = 0,
\end{aligned} \tag{2.58}$$

where  $' \equiv \partial_r$  and  $\dot{\phantom{x}} \equiv \partial_u$ .

The contracted Bianchi identity  $\nabla_\mu G_\nu^\mu \equiv 0$  together with  $\nabla_\mu T_\nu^\mu = 0$  for solutions of (2.48) show, that the system (2.48), (2.55) and (2.56) is sufficient to evolve the Einstein  $\sigma$  model: The  $\{\theta\theta\}$  component of the Einstein equations,  $E_{\theta\theta} = 0$  is satisfied, if Eqs. (2.48), (2.55), (2.56) and (2.57) are satisfied. This follows from the “ $r$ -component” of the Bianchi identity:  $E_{\theta\theta}$  can be expressed as an algebraic combination of the other components of the Einstein equations and derivatives thereof.

Furthermore the “ $u$ -component” of the Bianchi identity reads  $(r^2 G_{uu})' \equiv (rV G_{ur})' - e^{2\beta} r^2 \partial_u (e^{-2\beta} G_{ur}) + \frac{1}{2} r e^{2\beta} G_{rr} \partial_u (V e^{-2\beta})$ . Assuming, that Eqs. (2.48), (2.55) and (2.56) are satisfied, then  $(r^2 (G_{uu} - \kappa T_{uu}))' = 0$ . Therefore  $r^2 (G_{uu} - \kappa T_{uu}) = f(u)$ . So if  $G_{uu} = \kappa T_{uu}$  at some hypersurface  $r = \text{const}$  then this equation is satisfied everywhere. Now the regularity conditions at the origin ensure that this equation is satisfied at the origin  $r = 0$ , so the  $\{uu\}$  component of the Einstein equations is satisfied everywhere if the field equation (2.48) and the hypersurface equations (2.55) and (2.56) are satisfied.

So the characteristic initial value problem we deal with consists of the system (2.48), (2.55) and (2.56) together with the initial conditions  $\phi(u = 0, r) = \phi(r)$ . The numerical treatment of this characteristic initial value problem is described in Appendix C.

### 2.3.1 Mass Function, Bondi Mass and News Function

We close this section by giving explicit formulae for the mass function  $m(u, r)$  (2.34) and the mass loss at infinity  $\dot{m}_{\text{Bondi}}(u)$  in terms of the matter field.

The mass function  $m(u, r)$  can be rewritten as an integral over outgoing null rays by the trivial identity  $m(u, r) = \int_0^r m'(u, \bar{r}) d\bar{r}$ .  $m'(u, r)$  is given by

$$m'(u, r) = \frac{1}{2} \left( 1 - e^{-2\beta} \frac{V}{r} \right) - \frac{r}{2} e^{-2\beta} \left( -2\beta' \frac{V}{r} + \left( \frac{V}{r} \right)' \right). \tag{2.59}$$

Using the hypersurface equations (2.55) and (2.56) we obtain

$$m'(u, r) = \frac{\eta}{2} r^2 \left( e^{-2\beta} \frac{V}{r} (\phi')^2 + 2 \frac{\sin^2(\phi)}{r^2} \right), \tag{2.60}$$

and therefore

$$m(u, r) = \frac{\eta}{2} \int_0^r \bar{r}^2 d\bar{r} \left( e^{-2\beta} \frac{V}{\bar{r}} (\phi')^2 + 2 \frac{\sin^2(\phi)}{\bar{r}^2} \right). \tag{2.61}$$

This expression together with (2.34) will serve as an accuracy test for the numerical code (see Appendix C).

In order to derive a formula for the mass loss at infinity in terms of the matter field we have to look at the behavior of the metric functions and the field at infinity. The Bondi mass (2.35) is finite if  $\beta = H(u) + a_1(u)/r + O(1/r^2)$  and  $\frac{V}{r} = e^{2H(u)} + b_1(u)/r + O(1/r^2)$ . From (2.61) follows further, that  $\phi(u, r) = \frac{c_1(u)}{r} + O(1/r^2)$ . Using the hypersurface equation (2.55) we find that  $a_1(u) = 0$ , so

$$\beta(u, r) = H(u) + O(1/r^2). \quad (2.62)$$

Inserting these expansions into the formula for the Bondi mass (2.35) we get  $b_1(u) = -2m_{Bondi}e^{2H(u)}$ , so

$$\frac{V}{r}(u, r) = e^{2H(u)} \left( 1 - \frac{2m_{Bondi}}{r} \right) + O(1/r^2). \quad (2.63)$$

The derivative of the mass function  $m(u, r)$  with respect to retarded time  $u$  is given by

$$\dot{m}(u, r) = -\eta r^2 e^{-2\beta} \left( \dot{\phi}^2 - \frac{V}{r} \phi' \dot{\phi} \right), \quad (2.64)$$

where one of the subsidiary Einstein equations (2.57) has been used. This gives for the mass loss at infinity

$$\dot{m}_{Bondi}(u) = -\eta c_1^2(u) e^{-2H(u)}. \quad (2.65)$$

Clearly  $\dot{m}_{Bondi} \leq 0$  corresponding to the energy, that is radiated away to infinity and therefore lost. The expression

$$N(u) := c_1^2(u) e^{-2H(u)} \quad (2.66)$$

is called the *news function*.

# Chapter 3

## Static Solutions of the Self-gravitating $\sigma$ Model in the Presence of a Cosmological Constant

### 3.1 The Static Equations

In this chapter we investigate the question of existence and stability of static solutions to the self-gravitating  $SU(2)$   $\sigma$  model with positive cosmological constant in spherical symmetry. This work is motivated by previous work [2] on static solutions of the model on fixed de Sitter background and by the work of Volkov et al. [75] and Brodbeck et al. [15], who considered the Einstein Yang-Mills system with positive cosmological constant.

The choice of coordinates as well as the introduction of a gauge invariant quantity for the stability analysis follows [75, 15]. In addition we put some emphasis on examining the rôle of the Killing horizon. Our results closely resemble those of [75, 15] with the only difference, that in the limit of maximal coupling (see Sec. 3.2.2) the system is scale invariant. The results on static solutions are summarized in [48].

#### 3.1.1 Staticity

A spacetime  $(M, g)$  is called *stationary*, if it admits a timelike Killing vector field  $\xi$ . If this Killing vector field is in addition hypersurface orthogonal, then the spacetime is called *static*. Hypersurface orthogonality is given if the Frobenius condition

$$\xi_{[\sigma} \nabla_{\mu} \xi_{\nu]} = 0. \quad (3.1)$$

is satisfied.

Consider now a static, spherically symmetric spacetime (see e.g. [76]). If the static Killing vector field  $\xi$  is unique, it has to be invariant under the action of  $\text{SO}(3)$  (As the composition of two isometries is again an isometry, an element of  $\text{SO}(3)$  maps  $\xi$  to a Killing vector field. Furthermore the norm is left invariant, so  $\xi$  is mapped to a timelike Killing vector field. If  $\xi$  is unique, then  $\text{SO}(3)$  has to map  $\xi$  to itself). From this it follows, that  $\xi$  must not have components tangential to the orbits of  $\text{SO}(3)$ , as the only vector field on  $S^2$ , which is left invariant under the action of  $\text{SO}(3)$ , is the zero vector field. Therefore  $\xi$  can be written as  $\xi = \xi^t(t, \rho)\partial_t + \xi^\rho(t, \rho)\partial_\rho$ . We are still free to choose the coordinates  $(t, \rho)$  such that  $\xi = \partial_t$ . With this choice the metric (2.17) in the presence of a hypersurface orthogonal Killing vector field  $\xi = \partial_t$  reads

$$ds^2 = -Q(\rho)dt^2 + \frac{d\rho^2}{Q(\rho)} + R^2(\rho)d\Omega^2. \quad (3.2)$$

Stationarity of spacetime again extends to the field  $\phi$  via the Einstein equations. In order to satisfy (2.37) we set  $\phi = \phi(\rho)$ .

### 3.1.2 The Static Equations

Setting all time derivatives in Eqs. (2.48) and (2.51)–(2.54) to zero, we find that the momentum constraint (2.54) is satisfied identically. The field equation (2.48) and the combinations (2.51) and (2.52) yield the following autonomous system of coupled, nonlinear, second order ODEs

$$(QR^2\phi')' = \sin 2\phi, \quad (3.3)$$

$$(R^2Q')' = -2\Lambda R^2, \quad (3.4)$$

$$R'' = -\eta R\phi'^2. \quad (3.5)$$

Furthermore Eq. (2.53) (multiplied by  $R^2$ ) is a first integral of the above system:

$$2\eta \sin^2 \phi + R^2(\Lambda - \eta Q\phi'^2) + RQ'R' + QR'^2 - 1 = 0. \quad (3.6)$$

From the  $\rho$  component of the contracted Bianchi identities we have  $(\sqrt{Q}R^2G_\rho^\rho)' = R^2(\sqrt{Q})'G_t^t + \sqrt{Q}(R^2)'G_\theta^\theta$ . Assuming Eqs. (3.3)–(3.5) to be satisfied, we have  $QR^2(G_\rho^\rho - \kappa T_\rho^\rho) = \text{const.}$  So if (3.6) is satisfied at some hypersurface  $\rho = \text{const}$  it is satisfied everywhere. Now the conditions (2.28) and (2.46) for a regular center of spherical symmetry yield, that Eq. (3.6) is satisfied at  $\rho = 0$  and therefore it is satisfied everywhere.

As the cosmological constant  $\Lambda$  – if non-zero – sets the length scale of the theory it can be eliminated by switching to the dimensionless variables  $\bar{\rho} = \sqrt{\Lambda}\rho$  and  $\bar{R} = \sqrt{\Lambda}R$ . Or in other words: setting  $\Lambda$  to unity (say) in the above equations

means that all quantities which have dimension of length are measured in units of  $\sqrt{\Lambda}$ .

We are interested in solutions of (3.3)–(3.5) which have a regular center of spherical symmetry  $R = 0$  (at  $\rho = 0$ ) and a Killing horizon  $Q = 0$  at some finite distance from the origin. (See Sec. 3.1.4 for the global structure of such spacetimes). The reason why we look for solutions with a horizon is the following: turning off gravity ( $\eta = 0$ ) Eqs. (3.3) – (3.5) (in combination with the regularity conditions at the origin) describe the de Sitter spacetime (see Sec. 3.1.3), which has a cosmological horizon, and we don't expect the global structure to change when gravity is turned on slightly ( $\eta$  small and positive). Furthermore we can rule out the following possibilities: integrating outward from a regular center

1. the static region “ends” in a singularity,
2. the static region has a second (regular) pole  $R = 0$ <sup>1</sup>,
3. the static region persists up to spatial infinity.

In principle the first case could be produced easily by choosing an arbitrary value  $\phi'(\rho = 0)$  at the regular center (See Sec. 3.2). Nevertheless this case is of no interest here and is therefore discarded. Avoiding this scenario means, that we have to set up a boundary value problem enforcing one of the other cases.

The second case is impossible for  $\Lambda > 0$ : rewriting equation (3.4) as an integral equation (3.19), one sees, that  $Q'$  diverges, whenever  $R$  goes to zero for a second time.

That the last case is impossible, can be seen as follows: assume the static region extends to infinite values of  $\rho$ , i.e.  $Q(\rho) > 0$  for all  $\rho \geq 0$ . Assume further, that  $R'(\rho) > 0$  for all  $\rho \geq 0$  (this second assumption is necessary, as  $R'(\rho)$  is strictly monotonically decreasing (see Eq. (3.20)), so once it gets zero  $R$  decreases until it eventually becomes zero, which in turn would lead to the cases 1 or 2). Then one can show that for  $\rho$  large enough  $Q'$  is bounded from above by  $Q'(\rho) < -const/\rho$ . This means that  $Q$  has to cross zero at some finite value of  $\rho$ , so case 3 is ruled out as well.

We will discuss the implications of Eqs. (3.3) – (3.6) for  $\Lambda = 0$  in Sec. (3.2.2).

### 3.1.3 Exact Solutions

In this section we give some simple exact solutions of Eqs. (3.3)–(3.5), which will be important for the full spectrum of solutions (See Sec. 3.2), as they arise in certain limits.

---

<sup>1</sup>Note that this situation is not ruled out if  $\Lambda = 0$

We start with the solution obtained by setting  $\phi = 0$ . Then  $R''(\rho) = 0$  and therefore (together with the gauge choices  $R(0) = 0, R'(0) = 1$ ) we have  $R(\rho) = \rho$ . Eq. (3.4) then gives  $Q'(\rho) = -2\Lambda\rho/3$  and  $Q(\rho) = 1 - \Lambda\rho^2/3$ . Together we have

$$\phi(\rho) \equiv 0, \quad R(\rho) = \rho, \quad Q(\rho) = 1 - \frac{\Lambda\rho^2}{3}, \quad (3.7)$$

which is the de Sitter spacetime in the static frame.

Another simple solution is obtained by setting  $\phi \equiv \pi/2$ . This violates the regularity condition for the field at the origin. Again we have  $R(\rho) = \rho$ , but  $Q(\rho)$  cannot fulfill the regularity requirement  $Q(0) = 1/R'(0)$  at the origin any more, instead  $Q(\rho) = 1 - 2\eta - \Lambda\rho^2/3$ , so

$$\phi(\rho) \equiv \frac{\pi}{2}, \quad R(\rho) = \rho, \quad Q(\rho) = 1 - 2\eta - \frac{\Lambda\rho^2}{3}. \quad (3.8)$$

This solution behaves like the de Sitter spacetime for large values of  $\rho$ , but has a conical singularity at the origin. In the limit of vanishing coupling  $\eta = 0$ , where spacetime is de Sitter, the solution  $\phi \equiv \pi/2$  has diverging energy density at the origin, but finite total energy (as measured between origin and horizon) maximizing the energy of all regular static solutions that exist on fixed de Sitter background and can be viewed as a “high excitation” limit of this spectrum (see [2]).

For  $\Lambda = 0$  we obtain a solution, which will be of interest in the limit of maximal coupling  $\eta \rightarrow \eta_{max}$  (see Sec. 3.2.2). Eq. (3.4) together with the regularity conditions at the origin give  $Q(\rho) \equiv 1$ . The remaining equations can be solved analytically for  $\eta = 1$  to give the static Einstein universe:

$$\phi(\rho) = \rho, \quad R(\rho) = \sin \rho, \quad Q(\rho) \equiv 1, \quad \eta = 1. \quad (3.9)$$

### 3.1.4 Horizons and Global Structure

Clearly the coordinates (3.2) break down at the horizon  $Q(\rho_H) = 0$ . In order to examine the global structure of spacetime we temporarily switch to outgoing Eddington-Finkelstein coordinates  $(u, r, \theta, \phi)$ , where the retarded time  $u$  is given by

$$u = t - \int \frac{d\rho}{Q(\rho)}. \quad (3.10)$$

The metric (3.2) then reads

$$ds^2 = -Q(\rho)du^2 - 2du d\rho + R(\rho)^2 d\Omega^2. \quad (3.11)$$

Note that the coordinates (3.11) cover only half of the maximally extended spacetime. In order to cover all of spacetime one would have to switch to “Kruskal-like”



double null coordinates, as is done e.g. in [75]. In the following, we will simplify our discussion by only talking about the Killing horizon contained in the portion of spacetime covered here. All statements made can be extended trivially to the complete spacetime and in particular the second component of the horizon by time reflection. We also remark that all solutions have the topology  $S^3 \times R$ .

The static Killing vector field is  $\partial_u = \partial_t$ . The metric (3.11) is regular if  $Q(\rho)$  and  $R(\rho)$  are regular functions, except when  $R = 0$ , which corresponds either to the usual coordinate singularity of spherical symmetry, which has been discussed in Sec. (2.2.1) or to a spacetime singularity, as discussed below.

As described in Sec. 3.1.1 we assume the Killing vector field  $\partial_u$ , to be timelike in some neighborhood of the center  $R = 0$ , i.e.  $g(\partial_u, \partial_u) = -Q(\rho) < 0$ . From the discussion in Sec. 3.1.2 it is clear, that  $Q(\rho)$  has to go to zero at some finite distance from the origin,  $Q(\rho_H) = 0$ . Furthermore  $Q(\rho)$  changes sign there (as  $Q'(\rho) < 0$  the degenerate case of  $Q'(\rho_H) = 0$  is impossible). In regions, where the norm of the Killing vector is positive, i.e.  $Q(\rho) < 0$ , spacetime is dynamic. The slices of constant time  $\rho$  are of topology  $\mathbb{R} \times \mathbb{S}^2$ . They are generated by the Killing vector fields  $\partial_u$  and  $\xi_i$  and are therefore homogeneous. Such regions thus correspond to Kantowski-Sachs models.

The hypersurface  $\rho = \rho_H$  separating the static and dynamic regions, is characterized by  $Q(\rho_H) = 0$ , and is a null hypersurface (as  $\nabla_\mu u \nabla^\mu u = 0$  and  $\nabla^\sigma u \nabla_\sigma \nabla^\mu u = 0$ ). As the Killing vector field  $\partial_u$  is null on and tangent to this hypersurface it is a Killing horizon.

In order to characterize this horizon further, we use the concept of *trapping horizons* introduced by Hayward [40]. In general for asymptotically flat (and asymptotically de Sitter) spacetimes the asymptotic region can be used to classify an event horizon as a black hole horizon (or as a cosmological horizon). Furthermore for the (local) concept of an apparent horizon the asymptotic region is needed to define inward and outward directions.

The concept of a trapping horizon is based solely on the local behavior of null congruences. As in Sec. 2.2.2 the expansions  $\Theta_\pm$  of out- and ingoing null rays emanating from the spheres  $R = \text{const}$  are defined as

$$\Theta_\pm = \frac{1}{R^2} \mathcal{L}_\pm R^2, \quad (3.12)$$

where  $\mathcal{L}_\pm$  denotes the Lie derivative along the null directions

$$l_+ = \partial_\rho \quad \text{and} \quad l_- = 2\partial_u - Q\partial_\rho \quad (3.13)$$

respectively, so

$$\Theta_+ = 2\frac{R'}{R} \quad \text{and} \quad \Theta_- = -2Q\frac{R'}{R}. \quad (3.14)$$

The expansions can be used to define a *trapped surface* in the sense of Penrose [62] as a compact spacelike 2-surface ( $R = \text{const}$ ) for which  $\Theta_- \Theta_+ > 0$ . If one of the

expansions vanishes, the surface is called a *marginal surface*. For a non-trapped surface  $\Theta_-$  and  $\Theta_+$  have opposite signs, which is used to have a local notion of inward and outward: the direction in which the expansion is positive is called *outward*, and in which the expansion is negative is called *inward*.

The closure of a hypersurface, which is foliated by (non-degenerate<sup>2</sup> and non-bifurcating<sup>3</sup>) marginal surfaces is called a *trapping horizon*. At a trapping horizon, the behavior of the non-vanishing expansion can be used to distinguish between *future trapping* and *past trapping* horizons, i.e. supposing  $\Theta_-|_H = 0$  (as is the case in our example) then the horizon is

$$\begin{array}{ll} \text{future trapping} & \text{if } \Theta_+|_H < 0, \\ \text{past trapping} & \text{if } \Theta_+|_H > 0. \end{array} \quad (3.15)$$

The case  $\Theta_+|_H < 0$  means that in the trapped region both outgoing and ingoing future directed null rays converge whereas in the case  $\Theta_+|_H > 0$ , the null rays in the trapped region converge if past directed.

Furthermore the change of the vanishing null expansion  $\Theta_-$  in direction of  $l_+$  leads to a classification of *outer* and *inner* trapping horizons, i.e. the horizon is

$$\begin{array}{ll} \text{outer trapping} & \text{if } \mathcal{L}_+\Theta_-|_H < 0, \\ \text{inner trapping} & \text{if } \mathcal{L}_+\Theta_-|_H > 0. \end{array} \quad (3.16)$$

The meaning of inner and outer are the following: For  $\mathcal{L}_+\Theta_-|_H < 0$  starting from the non-trapped region, where the directions inward and outward are defined as above, one has to move *inward* to approach the horizon, or in other words, the horizon is an outer boundary for the trapped region, whereas for  $\mathcal{L}_+\Theta_-|_H > 0$  the horizon is an inner boundary of the trapped region.

A future outer trapping horizon therefore is suited to describe a black hole horizon, a past outer trapping horizon would describe a white hole horizon. Inner horizons on the other hand describe cosmological horizons, as they occur for example in the de Sitter spacetime.

Our situation is as follows: on the Killing horizon  $Q = 0$ ,  $\Theta_-|_{Q=0} = 0$  while  $\Theta_+|_{Q=0} = 2R'_H/R_H \neq 0$  and  $\mathcal{L}_+\Theta_-|_{Q=0} = -2Q'_H R'_H/R_H \neq 0$  (except when also  $R'_H = 0$ , which we exclude for the moment).

As  $R > 0$  and  $Q' > 0$  for  $\rho > 0$ , the character of the Killing horizon is given by the sign of  $R'_H$ . For  $R'_H > 0$  we have  $\Theta_+|_H > 0$  and  $\mathcal{L}_+\Theta_-|_H < 0$ . The Killing horizon therefore is a past inner trapping horizon, and therefore a cosmological horizon. For  $R'_H < 0$  on the other hand, we have  $\Theta_+|_H < 0$  and  $\mathcal{L}_+\Theta_-|_H > 0$ , which corresponds to a future outer trapping horizon, and therefore to a black hole horizon.

---

<sup>2</sup>for  $\Theta_- = 0 : \mathcal{L}_+\Theta_- \neq 0$

<sup>3</sup>for  $\Theta_- = 0 : \Theta_+ \neq 0$

If  $R' = 0$  anywhere in spacetime, then both expansions vanish. However, this does not mark a trapping horizon, as the product  $\Theta_+ \Theta_-$  does not change sign ( $\Theta_+$  as well as  $\Theta_-$  both cross zero). Instead this means, if it occurs in a non-trapped region, that the meaning of inward and outward directions are interchanged.

Using the expansions  $\Theta_+$  and  $\Theta_-$  (3.14) one can rewrite the quasilocal mass (2.33) as

$$m = \frac{R}{2} \left( 1 + \frac{R^2}{4} \Theta_+ \Theta_- \right). \quad (3.17)$$

so on any marginal two-sphere the quasilocal mass equals  $R/2$ .

Now, which kind of global structure do Eqs. (3.3) – (3.4) allow for? We start by rewriting these equations in the integral forms

$$\phi'(\rho) = \frac{1}{QR^2} \int_0^\rho \sin(2\phi) d\bar{\rho}, \quad (3.18)$$

$$Q'(\rho) = -\frac{2\Lambda}{R^2} \int_0^\rho R^2 d\bar{\rho}, \quad (3.19)$$

$$R'(\rho) = 1 - \eta \int_0^\rho R \phi'^2 d\bar{\rho}. \quad (3.20)$$

We see, that the first derivatives stay finite for any finite value of  $\rho$  as long as the metric functions  $R$  or  $Q$  don't vanish. If we assume the horizon  $Q(\rho_H) = 0$  to be regular (and non-degenerate,  $Q'_H \neq 0$ ), we have to enforce  $\int_0^{\rho_H} \sin 2\phi d\rho = 0$  and therefore

$$\phi'_H = \frac{\sin 2\phi_H}{R_H^2 Q'_H}. \quad (3.21)$$

As  $Q$  is monotonically decreasing with  $\rho$ ,  $\rho_H$  is the only horizon along a  $u = \text{const}$  slice.

Now the areal radius  $R$  of the two-spheres can behave in two essentially different ways: it can increase monotonically for all  $\rho$  or it can have an extremum at some  $\rho_E$ .

In the first case,  $R'(\rho) > 0 \forall \rho > 0$ , the solution exists for all finite  $\rho$ . From Eq. (3.5) we see, that  $0 < R' \leq 1 \forall \rho \geq 0$ . Therefore  $R$  diverges like  $R = O(\rho)$  for large  $\rho$ . From Eq. (3.4) follows, that  $Q' = O(\rho)$  and therefore  $Q = O(\rho^2)$ . Eq. (3.3) shows, that  $\phi$  goes to a constant at infinity. In this case the Killing horizon is a past inner trapping horizon (see Fig. 3.1a)

In the second case  $R'(\rho_E) = 0$ , as  $R''(\rho) \leq 0$  for all  $\rho$  and  $R'(\rho) < 0$  for  $\rho > \rho_E$ ,  $R$  goes to zero at some finite  $\rho_S > \rho_H$  (remember that we excluded the possibility of a second zero of  $R$  in the static region in Sec. 3.1.2). Again time evolution

beyond the horizon exists for all  $\rho < \rho_S$ . However in the limit  $\rho \rightarrow \rho_S$  a spacetime singularity occurs. This can be seen e.g. by investigating the behavior of the Kretschmann invariant

$$\begin{aligned} \mathcal{R}^{\mu\nu\sigma\tau}\mathcal{R}_{\mu\nu\sigma\tau} = & \frac{1}{R^4} \left( 4 + 4R^2 Q'^2 R'^2 + R^4 Q''^2 + \right. \\ & \left. + 8QR' (R^2 Q' R'' - R') + 4Q^2 (R'^4 + 2R^2 R''^2) \right). \end{aligned} \quad (3.22)$$

Since by assumption  $Q(\rho)$ ,  $Q'(\rho)$  and  $R'(\rho)$  are negative in a neighborhood of  $\rho_S$ , all terms are non-negative and clearly not all denominators vanish in the limit  $\rho \rightarrow \rho_S$ . Therefore the Kretschmann invariant blows up like  $1/R^4$  in the limit  $\rho \rightarrow \rho_S$ .

Concerning the character of the Killing horizon, two possibilities arise depending on whether  $R$  attains its maximum in the dynamic or in the static region. If  $\rho_E > \rho_H$  then the Killing horizon again is a past inner trapping horizon (See Fig. 3.1 b). If on the other hand  $\rho_E < \rho_H$ , then the inward and outward direction interchange in the static region and the horizon therefore is a future outer trapping horizon and corresponds thus to a black hole horizon (See Fig. 3.1c).

The three possibilities are summarized in Figs. 3.1a - c. Fig. 3.1a shows the asymptotically de Sitter spacetimes. The areal radius  $R$  is increasing along a  $u = \text{const}$  slice from zero at the origin to infinity at  $\mathcal{I}^+$ . A cosmological horizon separates the static region from an expanding dynamic region.

Fig. 3.1 b shows the situation, where  $R$  develops an extremum in the dynamic region. Beyond the cosmological horizon spacetime initially expands until it reaches its maximal spatial extension at time  $\rho_E$  and then recollapses to a singularity at finite proper time  $\tau_S = \int_{\rho_H}^{\rho_S} d\rho/Q(\rho)$ .

Fig. 3.1 c finally shows a spacetime, where  $R' = 0$  in the static region. At this hypersurface the inward and outward directions interchange. Therefore the collapsing dynamic region is enclosed by the static region. The separating horizon can be interpreted as a black hole horizon.

We close this section by giving an upper bound for  $R(\rho_E)$  for re-collapsing universes (Fig. 3.1b). As already mentioned the dynamic region of our solutions corresponds to Kantowski-Sachs universes. Therefore we can follow the work of Moniz [58] on the cosmic no-hair conjecture of Kantowski-Sachs models. We re-investigate Eq. (3.6). Remember that this equation is  $1/R^2$  times the  $(\rho)$  component of the Einstein equations. As the coordinate  $\rho$  plays the role of a time coordinate in the dynamic region, this equation is the Hamiltonian constraint for the time evolution problem. We rewrite Eq. (3.6) (divided by  $R^2$ ) as

$$R' \left( \frac{|Q'|}{R} + \frac{|Q|R'}{R^2} \right) = \Lambda - \frac{1}{R^2} + \eta \left( |Q|(\phi')^2 + 2 \frac{\sin^2 \phi}{R^2} \right). \quad (3.23)$$

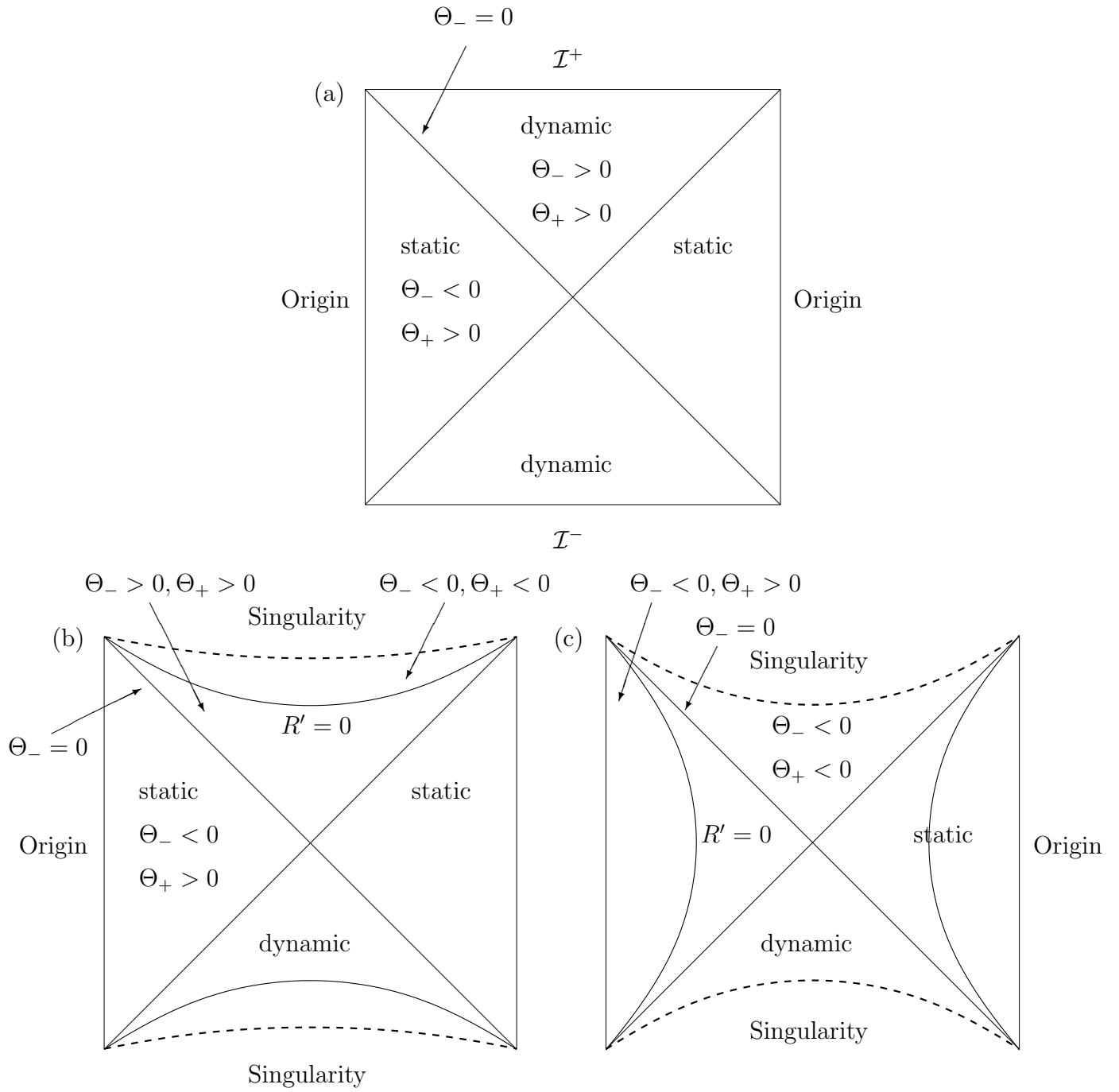


Figure 3.1: Penrose diagrams for the three different global structures of solutions. Any point in the diagram (except where  $R = 0$ ) corresponds to a two-sphere. The description is given in the text.

In terms of geometrical quantities on the spacelike hypersurfaces  $\rho = \text{const}$ , the terms on the left hand side are  $\frac{1}{2}(K^2 - K^{ij}K_{ij})$ ,  $K_{ij}$  being the extrinsic curvature and  $K$  the trace of  $K_{ij}$ . The last term on the right hand side is the energy density  $T_{\mu\nu}n^\mu n^\nu$  and  $1/R^2 = \frac{1}{2}({}^{(3)}\mathcal{R})$  with  ${}^{(3)}\mathcal{R}$  being the three scalar curvature of the slices.

Note that the left hand side can only change sign if  $R'$  changes sign. So if at some instant of time  $\rho_0$  the universe is expanding,  $R'(\rho_0) > 0$ , then the left hand side is positive. Furthermore, as the energy density is positive, we can give a lower bound for the left hand side, namely

$$R' \left( \frac{|Q'|}{R} + \frac{|Q|R'}{R^2} \right) \geq \Lambda - \frac{1}{R^2} \quad (3.24)$$

Suppose now that in addition at  $\rho_0$  the scalar curvature is smaller than  $2\Lambda$ , i.e.  $R(\rho_0) > 1/\sqrt{\Lambda}$ , then the right hand side is positive. As  $R'(\rho_0)$  is positive initially the lower bound on the right hand side increases away from zero, therefore making a change in sign of  $R'$  impossible. We can conclude from this, that if  $R'(\rho_0) > 0$  and  $R(\rho_0) > 1/\sqrt{\Lambda}$  at some time  $\rho_0$ , the universe will expand for ever and approach de Sitter space for late times. On the other hand, a recollapsing universe must have  $R(\rho) < 1/\sqrt{\Lambda}$  for all times  $\rho_H < \rho < \rho_S$ .

## 3.2 Numerical Construction of Static Solutions

The problem of constructing static solutions is given by the boundary value problem Eqs. (3.3)–(3.5) together with the regularity conditions at the origin (2.28) and at the horizon (2.46). In order to determine the global structure of such a solution the data at the horizon (defined by the solution to the above boundary value problem) are used as initial data for the time evolution problem in the dynamic region.

We solve the boundary value problem numerically using a standard shooting and matching method (see Appendix A) provided by routine d02agf of the NAG library [60]. The numerical integration in the dynamic region is performed by routine d02cbf of the NAG library.

In all our numerical calculations we set  $\Lambda = 3$ .

### 3.2.1 Phenomenology of Static Solutions for $\Lambda > 0$

In order to investigate the dependence of the spectrum of solutions on the coupling constant  $\eta$ , we start at  $\eta = 0$  and follow a solution to larger values of  $\eta$ .

For  $\eta = 0$ , the vacuum Einstein equations with positive cosmological constant yield de Sitter spacetime,

$$R(\rho) = \rho, \quad Q(\rho) = 1 - \frac{\Lambda \rho^2}{3}. \quad (3.25)$$

It was already shown in [2], that the remaining boundary value problem for the field on fixed background admits a discrete one-parameter family of regular solutions. In the static region these solution oscillate around  $\pi/2$ . The number of these oscillations  $n$  can be used to parameterize the family. Energy increases with the oscillation number and converges to the energy of the “singular solution”  $\phi \equiv \pi/2$  (see Sec. 3.1.3) from below. Outside the cosmological horizon at  $\rho = \sqrt{3/\Lambda}$  the field goes to a constant at infinity (See Fig. 3.2).

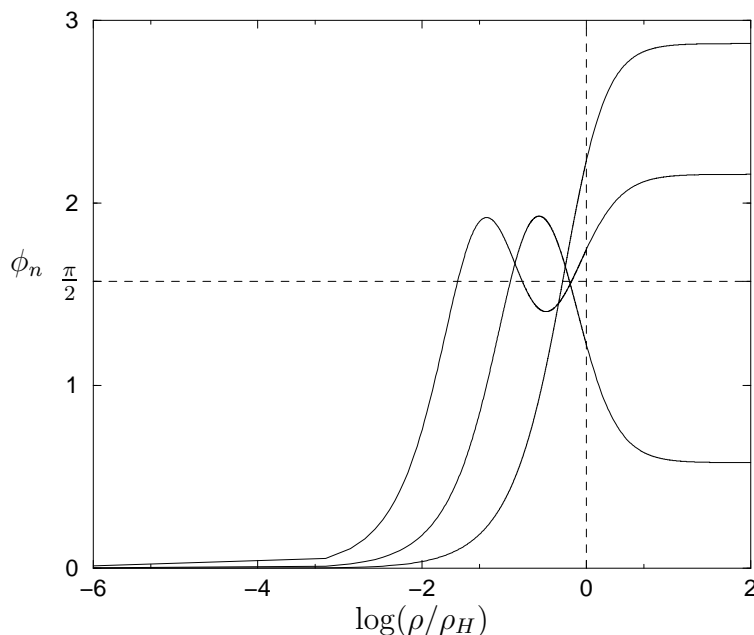


Figure 3.2: The first three excitations  $\phi_n$  on fixed de Sitter background. Within the static region the field oscillates  $n$  times around  $\pi/2$ , outside the horizon, it goes to a constant.

We concentrated on the first three excitations and investigated their behavior as the coupling  $\eta$  was turned on. We find that each member of these excitations exists up to a maximal coupling constant  $\eta_{max}(n)$ . The limit  $\eta \rightarrow \eta_{max}$  needs some care and will be discussed in Sec. 3.2.2. In the following we describe the properties of the solutions for  $0 \leq \eta < \eta_{max}$ .

- For small  $\eta$ ,  $0 \leq \eta < \eta_{crit}(n)$  spacetime is asymptotically de Sitter as sketched in Fig. 3.1a and described in the accompanying text. The field behaves similar as in the uncoupled case.

- For  $\eta = \eta_{crit}(n)$  the areal radius  $R$  does not diverge like  $\rho$  but rather goes to a constant at infinity. For even bigger couplings,  $\eta_{crit}(n) < \eta < \eta_*(n)$  the maximum of  $R$  occurs at earlier and earlier times  $\rho_E$  (see Fig. 3.3) and time evolution ends in a singularity, as described in Fig. 3.1b.
- At  $\eta = \eta_*(n)$  the hypersurface, where  $R$  is extremal merges with the horizon. For bigger  $\eta$ ,  $\eta_*(n) < \eta < \eta_{max}(n)$ ,  $R$  attains its maximum in the static region. The situation is as in Fig. 3.1c.

Figure (3.4) shows the areal radius  $R(\rho)$  for the first excitation for  $\eta$  close to  $\eta_{crit}$ . We have shown in Sec. 3.1.4 that re-collapsing universes must have  $R(\rho) < 1/\sqrt{\Lambda}$  for all  $\rho_H < \rho < \rho_S$ . Fig. 3.4 shows, that  $R(\rho_E)$  for the re-collapsing universe comes close to the upper limit. This suggests that the upper bound for  $R$  is attained in the limit  $\eta \rightarrow \eta_{crit}$  at infinity:  $R(\infty; \eta_{crit}) = 1/\sqrt{\Lambda}$ .

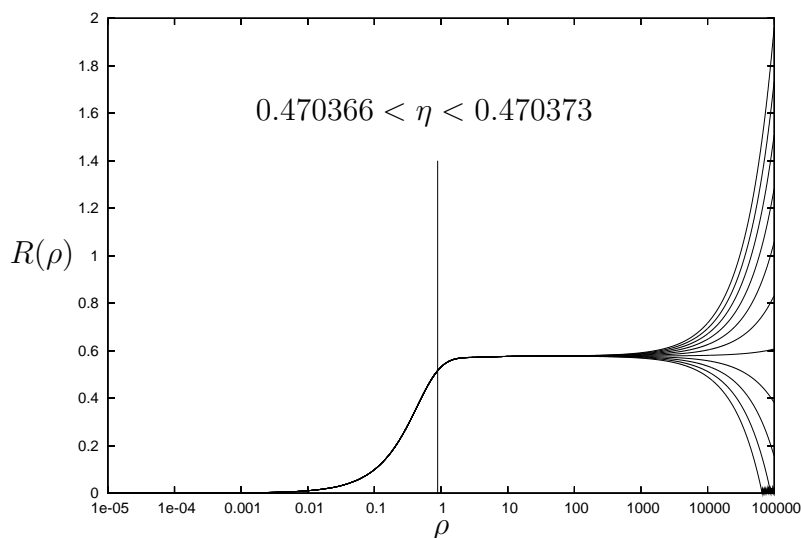


Figure 3.3: The metric function  $R(\rho)$  for the first excitation at couplings  $0.470366 < \eta < 0.470373$ . At  $\eta_{crit}$  the global structure of spacetime changes from asymptotically de Sitter to a spacetime, that ends in a singularity. The vertical line denotes the cosmological horizon at  $\rho = 0.88761$ .

The critical values of the coupling constants,  $\eta_{crit}(n)$ ,  $\eta_*(n)$  and  $\eta_{max}(n)$  depend on the excitation number  $n$ , as can be seen from table 3.1.

### 3.2.2 The Limit $\eta \rightarrow \eta_{max}$

Recall from Sec. 3.1.2 that the cosmological constant  $\Lambda$  sets the length scale in Eqs. (3.3) - (3.5) and that it can be eliminated from these equations, by introducing the dimensionless quantities  $\bar{\rho} = \sqrt{\Lambda}\rho$  and  $\bar{R} = \sqrt{\Lambda}R$ . This corresponds



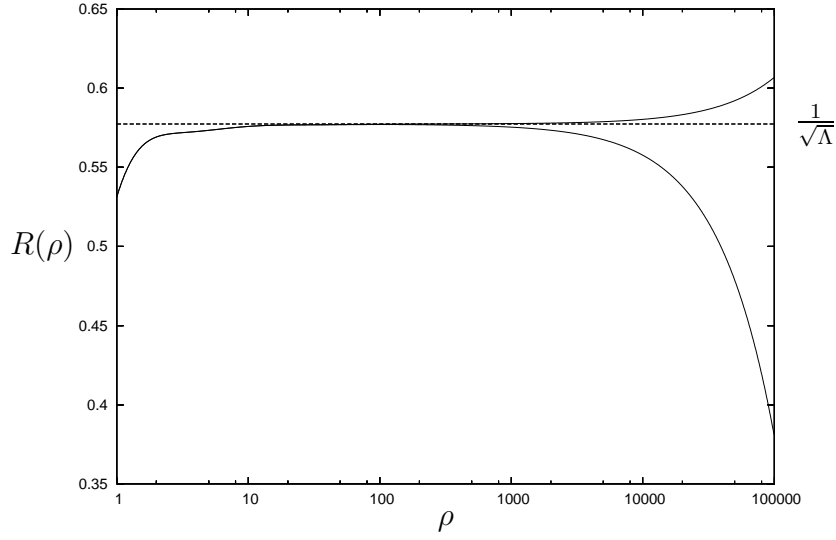


Figure 3.4: The areal radius  $R(\rho)$  for the first excitation in the dynamic region. Plotted are the solutions at  $\eta = 0.4703702$  and  $\eta = 0.470370903$ , close to  $\eta_{crit}(1)$ . The dashed horizontal line denotes  $1/\sqrt{\Lambda}$  ( $\Lambda$  was set to 3 for the numerical calculation). As can be seen, the areal radius of the re-collapsing universe comes close to the upper bound  $1/\sqrt{\Lambda}$ . We argue that therefore and due to the continuous dependence of solutions on the coupling  $\eta$ , the upper bound is attained at infinity for  $\eta = \eta_{crit}$ :  $R(\infty; \eta_{crit}) = 1/\sqrt{\Lambda}$ .

to measuring all quantities that have dimension of length, as e.g. the energy  $E$ , the coordinate distance of the horizon  $\rho_H$  from the origin, the radial geometrical distance of the horizon  $d_H$  from the origin, the areal radius  $R_H$  of the horizon, and  $1/\phi'(0)$ , in units of  $1/\sqrt{\Lambda}$ . We find that all parameters, that have dimension of length go to zero in the limit  $\eta \rightarrow \eta_{max}$  when measured with respect to this length scale. This indicates that  $1/\sqrt{\Lambda}$  is not the appropriate length scale for taking this limit. We therefore switch to the alternative viewpoint with  $\rho_H$  as our length scale, and we fix  $\rho_H = 1$ . In this setup  $\Lambda$  depends on  $\eta$  and the excitation index  $n$  and goes to zero in the limit  $\eta \rightarrow \eta_{max}$ . The parameters  $E$ ,  $d_H$  and  $1/\phi'(0)$  attain finite values when measured in units of  $\rho_H$ , whereas  $R_H/\rho_H$  goes to zero. (See Fig. 3.5) This strongly suggests, that there exists a solution with  $\eta = \eta_{max}$  which obeys Eqs. (3.3)-(3.5) with  $\Lambda = 0$  and has two centers of symmetry. In particular this means that the static region of this solution has no boundary, since any  $t = const$  slice has topology  $\mathbf{S}^3$ .

Furthermore, as can be seen from Fig. 3.6, the dimensionless parameter  $\phi(\rho_H)$  for the first excitation tends to  $\pi$ , and  $R'(\rho_H)$  tends to  $-1$  in the limit  $\eta \rightarrow \eta_{max}$ . As will be shown below,  $\Lambda = 0$  implies  $Q \equiv 1$ . The limiting solution with  $\Lambda = 0$  will therefore satisfy the regularity conditions (2.28) and (2.46) not only at the axis  $\rho = 0$  but also at the second zero of  $R$ , which means that such a solution

n	$\eta_{crit}$	$\eta_*$	$\eta_{max}$
1	0.47037	0.533	1.0
2	0.41981	0.48	0.74255
3	0.41932	0.474	0.64931
4	0.42606	0.4765	0.60260

Table 3.1: The critical values of the coupling constant for the first four excitations. The values of  $\eta_*(n)$  were read off by eye and therefore are not as accurate as the other values. The values of  $\eta_{max}(n)$  are determined as described in Sec. 3.2.2, in particular the value of  $\eta_{max}(1) = 1$  is exact. While  $\eta_{max}(n)$  decreases with the excitation number  $n$  the other critical values do not seem to share this behaviour.

is globally regular with two (regular) centers of spherical symmetry. In fact, for the first excitation this limiting solution is just the static Einstein universe (3.9), which was already given in closed form in Sec. 3.1.3.

These observations allow one to determine the maximal value of the coupling constant  $\eta_{max}(n)$  not as a limiting procedure  $\eta \rightarrow \eta_{max}$ , but rather by solving the boundary value problem Eqs. (3.3) - (3.5) with  $\Lambda = 0$  and with boundary conditions, that correspond to two regular centers of symmetry.

For  $\Lambda = 0$  Eq. (3.4) can be solved immediately to give  $R^2 Q' = const$ . According to the regularity conditions at the axis (2.28) the constant has to vanish, which means that  $Q' \equiv 0$  and therefore  $Q \equiv 1$ . The remaining system of equations is:

$$(R^2 \phi')' = \sin(2\phi) \quad (3.26)$$

$$R'' = -\eta R \phi'^2, \quad (3.27)$$

and

$$2\eta \sin^2 \phi - \eta R^2 \phi'^2 + R'^2 - 1 = 0. \quad (3.28)$$

Note, that this system of ODEs is scale invariant, that is any solution  $R(\rho), \phi(\rho)$  leads via rescaling to the one parameter family of solutions given by  $aR(a\rho), \phi(a\rho)$ . Keeping this in mind, we can fix the scale arbitrarily, e.g. in setting the first derivative of the field  $\phi$  equal to one at the origin:  $\phi'(\rho = 0) = 1$ . Thereby any solution, that is regular at the origin, is determined *entirely* by the value of the coupling constant  $\eta$ . Regularity conditions at the second “pole”  $R(\rho_P) = 0$  are the same as at the origin, except that  $\phi$  either tends to  $\pi$ , if its excitation number is odd, or to 0, if it has even excitation number. This can be inferred from  $\pi/2 < \phi_H < \pi$  for  $n$  odd and  $0 < \phi_H < \pi/2$  for  $n$  even for all  $\eta < \eta_{max}$ , which is true for  $\eta = 0$  and according to (3.21) there cannot be any  $\eta < \eta_{max}$  where a solution with  $n \geq 1$  has  $\phi_H = 0, \pi$  or  $\pi/2$  (apart from the “singular solution”  $\phi \equiv \pi/2$ )<sup>4</sup>. Note that this corresponds to all odd solutions having winding number 1, whereas even solutions are in the topologically trivial sector.

---

<sup>4</sup>If  $\phi_H = 0, \pi$  or  $\pi/2$  then  $\phi'_H = \phi''_H = 0$  and therefore all higher derivatives vanish

These regularity conditions together with the invariance of the equations under reflection at the location of the maximal two-sphere  $R'(\rho_E) = 0$ , causes globally regular solutions  $R(\rho)$  to be symmetric around  $\rho_E$  whereas  $\phi(\rho) - \pi/2$  is either antisymmetric for  $n$  odd or symmetric for  $n$  even. For  $\phi$  symmetric the formal power series expansions of  $R(\rho)$  and  $\phi(\rho)$  around  $\rho = \rho_E$  gives

$$\begin{aligned} R(\rho) &= R(\rho_E) + O((\rho - \rho_E)^4), \\ \phi(\rho) &= \arcsin \sqrt{1/2\eta} + \frac{2\sqrt{1-1/2\eta}}{R(\rho_E)^2\sqrt{2\eta}} \frac{(\rho - \rho_E)^2}{2!} + O((\rho - \rho_E)^4), \end{aligned} \quad (3.29)$$

and for  $\phi - \pi/2$  antisymmetric we get

$$\begin{aligned} R(\rho) &= \frac{2\eta - 1}{\eta\phi'(\rho_E)^2} - (2\eta - 1) \frac{(\rho - \rho_E)^2}{2!} + O((\rho - \rho_E)^4), \\ \phi(\rho) &= \frac{\pi}{2} + \phi'(\rho_E)(\rho - \rho_E) + O((\rho - \rho_E)^3). \end{aligned} \quad (3.30)$$

In order to solve the system (3.26), (3.27) we again use the shooting and matching method on the interval [origin,  $\rho_E$ ] using the above Taylor series expansions to determine the boundary conditions at  $\rho = \rho_E$ . Shooting parameters are now  $\rho_E, \phi'(\rho_E)$  and  $\eta$  for odd solutions and  $\rho_E, R(\rho_E)$  and  $\eta$  for even solutions. The results are displayed in Table 3.2.

$n$	$\eta_{max}$	$\rho_P = d_P$	$E/2\pi f_\pi^2$	$E/2\pi f_\pi^2 d_P$
1	1	$\pi$	$3\pi/2$	$3/2$
2	0.74255	6.74225	11.78039	1.74724
3	0.64931	12.10140	22.43662	1.85405
4	0.60260	19.63717	37.47302	1.90827

Table 3.2: Results for the first three excitations for  $\Lambda = 0$ . Since  $Q \equiv 1$  the coordinate distance  $\rho_P$  of the two regular “poles” equals the radial geometrical distance  $d_P$ . The energy density  $\rho_P$  and energy  $E$  are given in units where  $\phi'(0) = 1$ . The ratio  $E/d_P$  can be compared to the results for solutions with  $\Lambda > 0$  and represents the limit  $\eta \rightarrow \eta_{max}$  for those solutions .

It is clear from (3.29) and (3.30), that regular solutions for  $\Lambda = 0$  can only exist if  $\eta > 1/2$ . Assuming now that our numerical observations concerning the first few excitations extend to higher excitations, we argue as follows: since every “branch” of the “ $\Lambda > 0$  solutions” persists up to a maximal value of  $\eta$ , which can be computed by solving the boundary value problem (3.26),(3.27) together with regularity conditions at the two “poles” – which implies  $\eta > 1/2$  – and since we know, that in the limit  $\eta \rightarrow 0$  there exists an infinite number of excitations [2], we conclude that this whole family of solutions with  $\Lambda > 0$  persists up to some maximal value  $\eta_{max}(n)$ , which is *greater* than  $1/2$ . In other words, for any

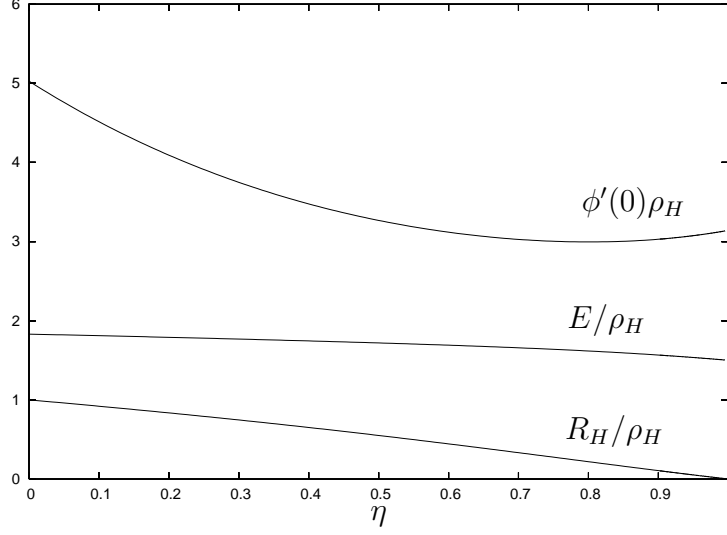


Figure 3.5: Some parameters of the first excitation – measured in units of  $\rho_H$  – as functions of the coupling constant. Except for  $R_H$  the parameters attain finite values in the limit  $\eta \rightarrow \eta_{max}$ , when measured with respect to this unit.

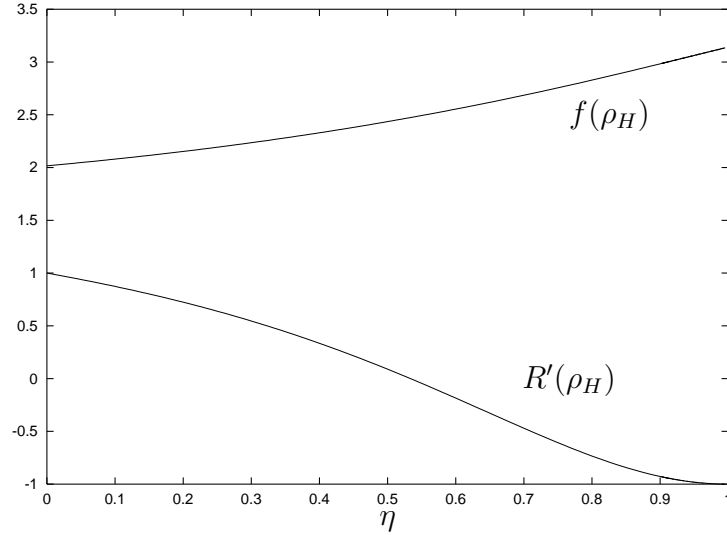


Figure 3.6: The parameters  $\phi(\rho_H)$  and  $R'(\rho_H)$  for the first excitation as functions of  $\eta$ . In the limit  $\eta \rightarrow \eta_{max}$   $\phi(\rho_H)$  tends to  $\pi$  and  $R'(\rho_H)$  goes to  $-1$ , which are necessary conditions for a second regular center of spherical symmetry at  $\rho_H$ .

$\eta < 1/2$  there exists a countably infinite family of solutions with  $\Lambda > 0$ , whereas for  $\eta > 1/2$  our numerical analysis shows, that only a finite number of solutions exists. (See Table 3.2).

### 3.2.3 Stability

In order to analyze the stability properties of the above described static solutions, small perturbations of the metric functions and the field are considered. We set

$$\begin{aligned} Q(t, \rho) &= Q_n(\rho) + \delta Q(t, \rho), \\ R(t, \rho) &= R_n(\rho) + \delta R(t, \rho), \\ \phi(t, \rho) &= \phi_n(\rho) + \delta \phi(t, \rho). \end{aligned} \quad (3.31)$$

$Q_n(\rho)$ ,  $R_n(\rho)$  and  $\phi_n(\rho)$  denote the  $n$ -th static excitation. The perturbations  $\delta Q(t, \rho)$ ,  $\delta R(t, \rho)$  and  $\delta \phi(t, \rho)$  are considered to be small such that the equations can be linearized in these quantities.

Inserting the ansatz (3.31) into Eqs. (2.51) – (2.54), making use of the static equations and linearizing in the perturbations gives a coupled system of linear PDEs for the perturbations. The momentum constraint (2.54) contains only first time derivatives, which enter each term linearly, so this equation can be integrated with respect to time to give

$$\delta Q(t, \rho) = \frac{Q'_n(\rho)\delta R(t, \rho)}{R'_n(\rho)} - \frac{2Q_n(t, \rho)\delta R'(t, \rho)}{R'_n(\rho)} - \frac{2\eta Q_n(\rho)R_n(\rho)\phi'_n(\rho)\delta \phi(t, \rho)}{R'_n(\rho)}. \quad (3.32)$$

The constant of integration, a function  $g(\rho)$  is determined by the Hamiltonian constraint (making use of the other equations) to be

$$g(\rho) = \frac{const}{R_n(\rho)R'_n(\rho)}, \quad (3.33)$$

so for perturbations  $\delta Q(t, \rho)$  regular at the origin, the constant has to vanish and therefore  $g(\rho) \equiv 0$ .

Eqs. (2.52) and (2.48) then give

$$\delta \ddot{R}(t, \rho) = -Q_n^2(\rho) (\delta R''(t, \rho) + \eta \phi_n'^2(\rho) \delta R(t, \rho) + 2\beta R_n(\rho) \phi'_n(\rho) \delta \phi'(t, \rho)) \quad (3.34)$$

and

$$\begin{aligned} & -\frac{R_n^2(\rho)\delta \ddot{\phi}(t, \rho)}{Q_n(\rho)} + (R_n^2(\rho)Q_n^2(\rho)\delta \phi'(t, \rho))' + \\ & + \left( \frac{R_n^2(\rho)\phi'_n(\rho)}{R'_n(\rho)} (Q'_n(\rho)\delta R(t, \rho) - 2Q_n(\rho)\delta R'(t, \rho) - 2\eta Q_n(\rho)R_n(\rho)\phi'_n(\rho)\delta \phi(t, \rho)) \right)' + \\ & + (2R_n(\rho)Q_n(\rho)\phi'_n(\rho)\delta R(t, \rho))' = 2\cos(2\phi_n(\rho))\delta \phi(t, \rho). \end{aligned} \quad (3.35)$$

Now it is important to note, that the form (2.17) still contains a certain gauge freedom. Therefore the perturbations (3.31) may – in addition to physical modes – also represent pure gauge modes. We investigate this, by considering small coordinate transformations

$$t \rightarrow \bar{t} = t + \epsilon \chi^t(t, \rho) \quad (3.36)$$

$$\rho \rightarrow \bar{\rho} = \rho + \epsilon \chi^\rho(t, \rho). \quad (3.37)$$

As described in Sec. 4.3.2 the perturbations (3.31) then transform up to order  $\epsilon$  according to the Lie derivative along  $\chi$  of the “background solution”. In detail we have

$$\begin{aligned} \delta \bar{Q} &= \delta Q - \epsilon(Q'_n \chi^\rho + 2Q_n \chi^t_{,t}) \\ \delta \bar{R} &= \delta R - \epsilon R'_n \chi^\rho \\ \delta \bar{\phi} &= \delta \phi - \epsilon \phi'_n \chi^\rho, \end{aligned} \quad (3.38)$$

where  $\chi$  is subject to the following conditions:

$$\frac{1}{Q_n} \chi^\rho_{,t} = -Q_n \chi^t_{,\rho} \quad (3.39)$$

$$\chi^t_{,t} = -\chi^\rho_{,\rho}. \quad (3.40)$$

Condition (3.39) comes from the fact, that the shift is zero in this gauge and therefore  $\mathcal{L}_\chi(g_n)_{\rho t} = 0$ , and condition (3.40) arises from the fact, that  $\delta g_{tt} = Q_n^2 \delta g_{\rho\rho}$  and therefore  $\mathcal{L}_\chi(g_n)_{tt} = Q_n^2 \mathcal{L}_\chi(g_n)_{\rho\rho}$ . Combining Eqs. (3.39) and (3.40) yields a wave equation for  $\chi^\rho$ :

$$Q_n^2 \chi^\rho_{,\rho\rho} - \chi^\rho_{,tt} = 0. \quad (3.41)$$

Gauge transformations that respect the choice (3.31) therefore are determined by the single function  $\chi^\rho$ , which is subject to Eq. (3.41).

Pure gauge modes are perturbations, that can be removed by a coordinate transformation, i.e. they have to be of the form

$$\begin{aligned} \delta Q &= \epsilon(Q'_n \chi^\rho + 2Q_n \chi^t_{,t}) \\ \delta R &= \epsilon R'_n \chi^\rho \\ \delta \phi &= \epsilon \phi'_n \chi^\rho, \end{aligned} \quad (3.42)$$

with  $\chi^\rho$  and  $\chi^t$  subject to (3.39,3.40). Clearly pure gauge modes satisfy the perturbation equations (3.34)–(3.35).

On the other hand, one can try to combine the perturbations in such a way, that the combination is invariant under a coordinate transformation. One can show, that such a quantity has to be of the form

$$\xi(\rho, t) = a(\rho)(R'_0(\rho) \delta f(\rho, t) - f'_0(\rho) \delta R(\rho, t)), \quad (3.43)$$

where  $a(\rho)$  is an arbitrary function of  $\rho$ , which we choose to be  $1/R_n(\rho)$ . Using the definition for  $\xi$  and Eqs. (3.34), (3.35) we obtain a single pulsation equation for the gauge-invariant quantity  $\xi$ :

$$\begin{aligned}
& - \frac{R_n(\rho)^2 R'_n(\rho)}{Q_n(\rho)} \ddot{\xi}(t, \rho) + Q_n(\rho) R_n(\rho)^2 R'_n(\rho) \xi''(t, \rho) + \left( 2 \eta Q_n(\rho) R_n(\rho)^3 \phi'_n(\rho)^2 + \right. \\
& + R_n(\rho)^2 Q'_n(\rho) R'_n(\rho) + 4 Q_n(\rho) R_n(\rho) R'_n(\rho)^2 \Big) \xi'(t, \rho) + \\
& + \left( \eta R_n(\rho)^3 \phi'_n(\rho)^2 Q'_n(\rho) - 2 \cos(2 \phi_n(\rho)) R'_n(\rho) + \right. \\
& + 2 \eta Q_n(\rho) R_n(\rho)^2 \phi'_n(\rho)^2 R'_n(\rho) + 2 Q_n(\rho) R'_n(\rho)^3 - \\
& \left. - R_n(\rho) (2 \eta \sin(2 \phi_n(\rho)) \phi'_n(\rho) - Q'_n(\rho) R'_n(\rho)^2) \right) \xi(t, \rho) = 0.
\end{aligned} \tag{3.44}$$

As the coefficients do not depend on time, we can work with Fourier modes

$$\xi(t, \rho) = e^{i\sigma t} y(\rho), \tag{3.45}$$

which turns Eq. (3.44) into a linear second order ODE

$$\begin{aligned}
& Q_n(\rho)^2 R_n(\rho)^2 R'_n(\rho) y''(\rho) + \left( 2 \eta Q_n(\rho)^2 R_n(\rho)^3 \phi'_n(\rho)^2 + \right. \\
& + Q_n(\rho) R_n(\rho)^2 Q'_n(\rho) R'_n(\rho) + 4 Q_n(\rho)^2 R_n(\rho) R'_n(\rho)^2 \Big) y'(\rho) + \\
& + \left( -2 \eta Q_n(\rho) R_n(\rho) \sin(2 \phi_n(\rho)) \phi'_n(\rho) + \eta Q_n(\rho) R_n(\rho)^3 \phi'_n(\rho)^2 Q'_n(\rho) - \right. \\
& - 2 \cos(2 \phi_n(\rho)) Q_n(\rho) R'_n(\rho) + 2 \eta Q_n(\rho)^2 R_n(\rho)^2 \phi'_n(\rho)^2 R'_n(\rho) + \\
& \left. + Q_n(\rho) R_n(\rho) Q'_n(\rho) R'_n(\rho)^2 + 2 Q_n(\rho)^2 R'_n(\rho)^3 \right) y(\rho) = -\sigma^2 R_n(\rho)^2 R'_n(\rho) y(\rho).
\end{aligned} \tag{3.46}$$

Again this equation has regular singular points at the origin where  $R(0) = 0$  and at the horizon  $Q(\rho_H) = 0$ . The corresponding regularity conditions for  $y(\rho)$  are

$$y'(0) = 0, \quad y(\rho) \sim (\rho_H - \rho)^\alpha, \quad \text{with} \quad \alpha = -\frac{\sqrt{-\sigma^2}}{Q'_H}, \tag{3.47}$$

for negative  $\sigma^2$ .

If the background solution has  $R'_n > 0$  for all  $\rho < \rho_H$ , then Eq. 3.46 together with the boundary conditions constitutes an eigenvalue problem with eigenvalue  $\sigma^2$  and eigen vector  $y(\rho)$ . As we are interested in unstable modes, we look for negative eigenvalues  $\sigma^2$ .

If on the other hand the background geometry contains a maximal two-sphere  $R'(\rho_E) = 0$  within the static region  $\rho_E < \rho_H$ , then Eq. (3.46) has an additional singular point within the range of integration. The behavior of the two

independent solutions in the vicinity of this singular point is

$$\begin{aligned} y_1(\rho) &= (\rho - \rho_E)^3 \sum_{n=0}^{\infty} a_n (\rho - \rho_E)^n \\ y_2(\rho) &= \sum_{n=0}^{\infty} b_n x^n, \end{aligned} \tag{3.48}$$

so the general solution stays regular near  $\rho = \rho_E$ . Nevertheless, the coefficients of the first and zeroth derivative of  $y(\rho)$  in Eq. (3.46) are singular, which renders the standard numerical shooting and matching methods impossible.

Nevertheless we tried to solve this problem, using a standard relaxation method (routine d02raf of the NAG library [60]) on one hand. On the other hand, we discretized Eq. (3.46) by hand, thereby turning the Sturm Liouville eigen value problem into an algebraic eigen value problem. We only present preliminary results here: for  $\eta = 0$  stability was already analyzed in [2]. It turned out, that the  $n$ -th static excitation has  $n$  unstable modes. Our preliminary investigation of the first three excitations in the coupled case gives, that these solutions keep their unstable modes when gravity is turned on until in the limit of maximal coupling one negative eigenvalue crosses zero. The occurrence of one “indifferent mode” in the limit  $\eta = \eta_{max}$  is due to the fact, that there the equations are scale invariant, i.e. for each coupling  $\eta_{max}(n)$  we have a one parameter family of solutions ( $R_\lambda(\rho) = \lambda R_n(\lambda\rho)$ ,  $\phi_\lambda(\rho) = \phi_n(\lambda)(\rho)$ ). For  $\lambda = 1 + \epsilon$  we can write

$$R_\lambda(\rho) = R_n(\rho) + \epsilon(R_n(\rho) + R'_0(\rho)\rho) \tag{3.49}$$

$$\phi_\lambda(\rho) = \phi_n(\rho) + \epsilon\phi'_n(\rho)\rho, \tag{3.50}$$

which just corresponds to an “indifferent” mode with  $\sigma = 0$ .



# Chapter 4

## Self-similar Solutions of the Self-gravitating $\sigma$ Model

As self-similar solutions usually govern type II critical phenomena (see Chap. 5), it is of great advantage to know about their properties like existence and stability from a “direct construction”. The “direct construction” – in contrast to a construction that uses time evolutions of near critical data (see Chapter 5) – profits from the symmetry, which is imposed on the equations. This way the problem of constructing self-similar solutions reduces to a boundary value problem for ODEs in the case of continuously self-similar solutions (see Sec. 4.2) and to a time-periodic boundary value problem for PDEs in case of discrete self-similar solutions (see Sec. 4.4). CSS solutions of the  $\sigma$  model have already been constructed by Bizon [8] and Bizon and Wasserman [11]. We reproduce their results here. Stability is analyzed via the usual method for CSS solutions (Sec. 4.3.1). In addition J. Thornburg [70] proposed and carried out a method, that is based on discretization of the field and uses the full (nonlinear) field equations (Sec. 4.3.3).

We summarize our results in Table 4.1. In Sec. 4.5.1 finally we compare the CSS (first excitation) and DSS solution in a certain range of couplings, where both solutions exist. Our observations lead us to conjecture, that the DSS solution bifurcates from the first CSS excitation in a homoclinic loop bifurcation at  $\eta \simeq 0.17$ . To our knowledge up to now such a bifurcation has not been observed in the context of self-similar solutions to self-gravitating matter fields.

### 4.1 Continuous and Discrete Self-Similarity

A spacetime  $(M, g)$  is said to be *discretely self-similar (DSS)* if it admits a diffeomorphism  $\Phi_\Delta : M \rightarrow M$ , which leaves the metric invariant up to a constant scale factor, that is

$$(\Phi_\Delta^* g)|_p = e^{2\Delta} g|_p \quad \forall p \in M, \quad (4.1)$$

where  $\Delta$  is a real constant.

A spacetime, that admits a one-parameter family of such diffeomorphisms, parametrized by  $\Delta$  and with  $\Phi_0 = id_M$ , is called *continuously self similar (CSS)*. The generating vector field  $\xi = \frac{d}{d\Delta} \Phi_\Delta|_{\Delta=0}$  is a special case of a conformal Killing vector field. It obeys the conformal Killing equation

$$\begin{aligned}\mathcal{L}_\xi g|_p &= \lim_{\Delta \rightarrow 0} \frac{1}{\Delta} \left( g|_p - ((\Phi_\Delta^{-1})^* g)|_p \right) = \\ &= \lim_{\Delta \rightarrow 0} \frac{1}{\Delta} \left( g|_p - e^{-2\Delta} g|_p \right) = 2 g|_p.\end{aligned}\tag{4.2}$$

with a constant factor in front of the metric at the right hand side. A vector field satisfying (4.2) is called *homothetic*.

At any point  $p \in M$  we can compare the original metric  $g|_p$  and the metric  $\bar{g}$  that results from pulling back  $g|_{\Phi_\Delta(p)}$  to  $p$ ,  $\bar{g}|_p = (\Phi_\Delta^* g)|_p = e^{2\Delta} g|_p$ . As  $g$  and  $\bar{g}$  only differ by a constant rescaling both metrics yield the same covariant derivative,  $\nabla_g = \nabla_{\bar{g}}$ . Therefore the Riemann as well as the Ricci tensors are identical,  $\mathcal{R}_{\mu\tau\nu}^\sigma(\bar{g})|_p = \mathcal{R}_{\mu\tau\nu}^\sigma(g)|_p$  and  $\mathcal{R}_{\mu\nu}(\bar{g})|_p = \mathcal{R}_{\mu\nu}(g)|_p$ . The Ricci scalar scales as the inverse metric,

$$\mathcal{R}(\bar{g})|_p = \bar{g}^{\mu\nu} \mathcal{R}_{\mu\nu}(\bar{g})|_p = e^{-2\Delta} g^{\mu\nu} \mathcal{R}_{\mu\nu}(g)|_p = e^{-2\Delta} \mathcal{R}(g)|_p,\tag{4.3}$$

and therefore the Einstein tensors for both metrics agree:

$$G_{\mu\nu}(\bar{g})|_p = G_{\mu\nu}(g)|_p.\tag{4.4}$$

Now the Riemann, Ricci and Einstein tensor and the scalar curvature (summarized as  $T$ ) behave under the pull-back of a general diffeomorphism  $f : M \rightarrow M$  as

$$(f^* T(g))|_p = T(f^* g)|_p.\tag{4.5}$$

For a DSS spacetime we therefore have

$$\begin{aligned}(\Phi_\Delta^* \mathcal{R})_{\mu\tau\nu}^\sigma|_p &= \mathcal{R}_{\mu\tau\nu}^\sigma|_p, \\ (\Phi_\Delta^* \mathcal{R})_{\mu\nu}|_p &= \mathcal{R}_{\mu\nu}|_p, \\ (\Phi_\Delta^* \mathcal{R})|_p &= e^{-2\Delta} \mathcal{R}|_p, \\ (\Phi_\Delta^* G)_{\mu\nu}|_p &= G_{\mu\nu}|_p.\end{aligned}\tag{4.6}$$

For a CSS spacetime the above considerations directly yield

$$\begin{aligned}\mathcal{L}_\xi \mathcal{R}_{\mu\tau\nu}^\sigma &= \mathcal{L}_\xi \mathcal{R}_{\mu\nu} = 0, \\ \mathcal{L}_\xi \mathcal{R} &= (\mathcal{L}_\xi g^{-1})^{\mu\nu} \mathcal{R}_{\mu\nu} = -2\mathcal{R}, \\ \mathcal{L}_\xi G_{\mu\nu} &= 0.\end{aligned}\tag{4.7}$$

### 4.1.1 Adapted Coordinates

In order to simplify the discussion, we introduce coordinates, that are adapted to the symmetry (see e.g. [35]).

In order to formally construct such a coordinate system for a DSS spacetime, we choose a hypersurface  $\Sigma$ , with  $\Sigma \cap \Phi_\Delta(\Sigma) = \emptyset$ , provide it with coordinates  $(z^i)$ ,  $i = 1, 2, 3$  and label it with  $\tau_0$ . (Up to now this hypersurface can be spacelike, null or timelike). We apply the diffeomorphism to  $\Sigma$ , label  $\Phi_\Delta(\Sigma)$  with  $\tau_0 - \Delta$  and choose the coordinates in this hypersurface such that  $\Phi_\Delta(\tau_0, z^i) = (\tau_0 - \Delta, z^i)$ . Next we choose coordinates  $(\tau, z^i)$  in between these two hypersurfaces, with  $\tau_0 - \Delta \leq \tau \leq \tau_0$  and their restriction to  $\Sigma$  and  $\Phi_\Delta(\Sigma)$  being  $(\tau_0, z^i)$ , respectively  $(\tau_0 - \Delta, z^i)$ . Then we use the diffeomorphism to copy this coordinate patch to the other regions of spacetime. Of course this construction is very far from being unique.

Per construction the diffeomorphism maps a point  $p = (\tau, z^i)$  to the point  $\Phi_\Delta(p) = (\tau - \Delta, z^i)$ . So the Jacobian is the identity,  $\frac{\partial \Phi_\Delta^\mu}{\partial x^\nu} = \delta_\nu^\mu$ .

Using the definition of the pull-back as well as Eq. (4.1) in these coordinates we obtain for  $p = (\tau, z^i)$

$$\begin{aligned} (\Phi_\Delta^* g)_{\mu\nu}|_p &= \frac{\partial \Phi_\Delta^\alpha}{\partial x^\mu} \frac{\partial \Phi_\Delta^\beta}{\partial x^\nu} g_{\alpha\beta}|_{\Phi_\Delta(p)} = g_{\mu\nu}(\tau - \Delta, z^i) = \\ &\stackrel{(4.1)}{=} e^{2\Delta} g_{\mu\nu}(\tau, z^i). \end{aligned} \quad (4.8)$$

As this is valid for any point  $p \in M$  we can conclude that the metric is conformal to a metric  $\tilde{g}$ , which is periodic in the coordinate  $\tau$ , with the conformal factor being an exponential in  $\tau$ ,

$$g_{\mu\nu}(\tau, z^i) = e^{-2\tau} \tilde{g}_{\mu\nu}(\tau, z^i) \quad \text{with} \quad \tilde{g}_{\mu\nu}(\tau + \Delta, z^i) = \tilde{g}_{\mu\nu}(\tau, z^i). \quad (4.9)$$

For a CSS spacetime again we choose a hypersurface  $\Sigma$ , with  $\Sigma \cap \Phi_\Delta(\Sigma) = \emptyset \forall \Delta$ , so the homothetic Killing vector field is transversal to  $\Sigma$ . We choose coordinates  $(z^i)$  on this hypersurface and transport them across spacetime via the one-parameter family of diffeomorphisms. We parameterize the orbits  $\gamma^\mu$  of the homothetic KVF  $\xi$  with  $-\tau$ , so  $\xi = -\partial_\tau$ . The freedom in the construction in this case consists of choosing the hypersurface and applying diffeomorphisms within  $\Sigma$ .

In analogy to (4.8) we have

$$(\mathcal{L}_\xi g)_{\mu\nu} = -\partial_\tau g_{\mu\nu} \stackrel{(4.2)}{=} 2g_{\mu\nu}, \quad (4.10)$$

and therefore

$$g_{\mu\nu}(\tau, z^i) = e^{-2\tau} \tilde{g}_{\mu\nu}(z^i). \quad (4.11)$$

### 4.1.2 Self-Similarity in Spherical Symmetry

The fact that the above introduced adapted coordinates are not unique is no draw back for our purposes. What we are interested in is to find out whether our numerically evolved spacetimes contain self-similar regions. In order to do so, we need to know, what self-similarity looks like in the coordinates our code uses, namely the Bondi-like coordinates in spherical symmetry, defined in Sec. (2.2)).

$$ds^2 = -e^{2\beta(u,r)} du \left( \frac{V}{r}(u,r) du + 2dr \right) + r^2 d\Omega^2. \quad (4.12)$$

Assuming that (4.12) describes a self-similar spacetime, we seek for a coordinate transformation  $(u, r) \rightarrow (\tau(u, r), z(u, r))$ , such that the resulting metric is of the form  $e^{-2\tau} \tilde{g}_{\mu\nu}$ , where  $\tilde{g}_{\mu\nu}$  is periodic in  $\tau$  for a DSS spacetime and independent of  $\tau$  in the case of a CSS spacetime. In the following a “ $\sim$ ” means, that the function is periodic in  $\tau$  with period  $\Delta$ .

The first observation is, that the coordinate transformation does not involve the angles  $\theta$  and  $\varphi$ . So the “ $\mathbb{S}^2$ ”-part of the metric is unchanged. We immediately get

$$r(\tau, z) = e^{-\tau} \tilde{R}(\tau, z) \quad \text{for DSS}, \quad (4.13)$$

$$r(\tau, z) = e^{-\tau} R(z) \quad \text{for CSS}. \quad (4.14)$$

This means that the diffeomorphism maps an  $r = \text{const}$  hypersurface to the hypersurface  $e^\Delta r = \text{const}$ .

In the following we exploit the relations (4.1) and (4.2) with respect to the Bondi coordinates, in order to find the behavior of  $u = \text{const}$  hypersurfaces under the diffeomorphism as well as determining the  $\tau$  dependence of the metric functions  $\beta$  and  $\frac{V}{r}$ .

For the DSS spacetime we write  $\Phi_\Delta(u, r) = (\Phi_\Delta^u(u, r), \Phi_\Delta^r(u, r)) = (\Phi_\Delta^u(u, r), e^\Delta r)$ , the last equality following from (4.13). Therefore  $\partial \Phi_\Delta^r / \partial u = 0$ ,  $\partial \Phi_\Delta^r / \partial r = e^\Delta$ . We first examine the  $rr$  component of (4.1):

$$(\Phi_\Delta^* g)_{rr} = e^{2\Delta} g_{rr} = 0 \quad (4.15)$$

and so

$$\frac{\partial \Phi_\Delta^u}{\partial r} \left( \frac{\partial \Phi_\Delta^u}{\partial r} g_{uu} + 2e^\Delta g_{ur} \right) = 0. \quad (4.16)$$

This formula states, that the null vector  $\nabla^\mu u$ , which is tangent to the outgoing null geodesics generating the  $u = \text{const}$  hypersurfaces, is mapped again to a null vector. If the first factor vanishes,  $\frac{\partial \Phi_\Delta^u}{\partial r} = 0$ , the push forward of  $\nabla^\mu u|_p$  is parallel to  $\nabla^\mu u|_{\Phi_\Delta(p)}$ . If the expression in the parentheses vanishes the push forward would be parallel to the ingoing null geodesic vector  $\nabla^\mu v|_{\Phi_\Delta(p)}$ . Here we are interested in those diffeomorphisms that are connected to the identity map.

Therefore we want the first factor to vanish, so  $\frac{\partial \Phi_\Delta^u}{\partial r} = 0$  and  $\Phi_\Delta^u = \Phi_\Delta^u(u)$ . This shows, that  $u = \text{const}$  hypersurfaces are mapped to  $u = \text{const}$  hypersurfaces.

We invoke now e.g. the  $(u, r)$  component of (4.1) in order to get more information on  $\Phi_\Delta^u(u)$ .

$$\begin{aligned} (\Phi^* \Delta g)_{ur}|_p &= e^{2\Delta} g_{ur}|_p \\ \left( \frac{\partial \Phi_\Delta^u}{\partial u} \right) e^\Delta g_{ur}(\Phi_\Delta(p)) &= e^{2\Delta} g_{ur}(p). \end{aligned} \quad (4.17)$$

Consider now a point  $p$  at the origin, i.e.  $p = (u, r = 0)$ . As the origin is mapped to itself (which follows from (4.13)) the image of the point  $p$  is  $\Phi_\Delta(p) = (\Phi_\Delta^u(u), 0)$ . As described in Sec. (2.2.1) the components of the metric with respect to Bondi-like coordinates are fixed at the origin, due to regularity at the center as well as the choice of retarded time being proper time at the origin. In particular we have  $\beta(u, r = 0) = 0$ . Inserting this into Eq. (4.17) we obtain

$$\left( \frac{\partial \Phi_\Delta^u}{\partial u} \right) = e^\Delta. \quad (4.18)$$

Integrating gives

$$\Phi_\Delta^u(u) = e^\Delta u + \text{const}. \quad (4.19)$$

Reinserting this into (4.17) we get

$$e^{2\beta(\tau-\Delta, z)} = e^{2\beta(\tau, z)}, \quad (4.20)$$

and for the  $(u, u)$  component of (4.1) we have

$$\begin{aligned} (\Phi_\Delta^* g)_{uu}|_p &= e^{2\Delta} g_{uu}|_p \\ \left( \frac{\partial \Phi_\Delta^u}{\partial u} \right)^2 g_{uu}(\Phi_\Delta(p)) &= e^{2\Delta} g_{uu}(p) \\ e^{2\beta(\tau-\Delta, z)} \frac{V}{r}(\tau - \Delta, z) &= e^{2\beta(\tau, z)} \frac{V}{r}(\tau, z). \end{aligned} \quad (4.21)$$

From (4.20) and (4.21) we now see, that both metric functions are periodic functions in  $\tau$

$$\begin{aligned} \beta(u, r) &= \tilde{\beta}(\tau(u, r), z(u, r)), \\ \frac{V}{r}(u, r) &= \frac{\tilde{V}}{r}(\tau(u, r), z(u, r)). \end{aligned} \quad (4.22)$$

Note, that this relation is valid for any set of adapted coordinates constructed as described in Sec. (4.1.1).

For a CSS spacetime we use analogous arguments. We start by writing the homothetic Killing vector as

$$-\partial_\tau|_z \equiv \xi = \xi^u(u, r)\partial_u + \xi^r(u, r)\partial_r. \quad (4.23)$$

Of course we have  $\xi^u = -\partial_\tau u$  and  $\xi^r = -\partial_\tau r$  (both partial derivatives taken at constant  $z^i$ ). (4.14) immediately gives the  $r$  component of  $\xi$ ,

$$\xi^r = -\partial_\tau r(\tau, z)|_z = r(\tau, z). \quad (4.24)$$

As above we examine the  $rr$  component of (4.2),

$$\mathcal{L}_\xi g_{rr} = \xi^\mu g_{rr,\mu} + 2 \xi_{,r}^\mu g_{\mu r} = 2 \xi_{,r}^u g_{ur} = 0. \quad (4.25)$$

So we have  $\xi_{,r}^u = 0$  and  $\xi^u = \xi^u(u)$ . Now the  $uu$  component of the homothetic Killing equation (4.2) reveals

$$\begin{aligned} \mathcal{L}_\xi g_{uu} &= \xi^\mu g_{uu,\mu} + 2 \xi_{,u}^\mu g_{\mu u} = 2 g_{uu} \\ \xi^\mu g_{uu,\mu} + 2 \xi_{,u}^u g_{uu} &= 2 g_{uu}. \end{aligned} \quad (4.26)$$

Again we use the fact that the origin is an orbit of the homothetic Killing vector, so  $\xi|_{r=0} = \partial_u|_{r=0}$ , and  $g_{uu}|_{r=0} = 1$ . So (4.26) gives

$$\xi_{,u}^u = 1 \quad \Rightarrow \quad \xi^u(u) = u + \text{const}. \quad (4.27)$$

Therefore Eq. (4.26) gives

$$\partial_\tau g_{uu} = 0, \quad (4.28)$$

and the  $(ur)$  component of (4.2) yields

$$\begin{aligned} \mathcal{L}_\xi g_{ur} &= \xi^\mu g_{ur,\mu} + \xi_{,u}^\mu g_{\mu r} + \xi_{,r}^\mu g_{u\mu} = 2 g_{ur} \\ \xi^\mu g_{ur,\mu} + 2 g_{ur} &= 2 g_{u,r} \\ \partial_\tau g_{ur} &= 0. \end{aligned} \quad (4.29)$$

So in analogy to (4.22) we have for a CSS spacetime

$$\begin{aligned} \beta(x^\mu) &= \beta(z), \\ \frac{V}{r}(x^\mu) &= \frac{V}{r}(z). \end{aligned} \quad (4.30)$$

We now explicitly write down a set of adapted coordinates for DSS and CSS spacetimes, which will be used later.

As we have seen, the diffeomorphisms map a  $u = \text{const}$  hypersurface to another  $u = \text{const}$ , different from the first. Therefore the  $u = \text{const}$  hypersurfaces are valid candidates for  $\tau = \text{const}$  hypersurfaces, i.e. we may set  $\tau = \tau(u)$ .

For a DSS spacetime the function  $u(\tau)$  has to obey

$$e^\Delta u(\tau) + \text{const} = u(\tau - \Delta). \quad (4.31)$$

The simplest function  $u(\tau)$  satisfying (4.31) is given by

$$u^* - u = e^{-\tau}, \quad (4.32)$$

where we have set  $u^* = \text{const } e^\Delta$ .

For the CSS spacetime we integrate

$$-\frac{du}{d\tau} = \xi^u = u + \text{const}, \quad (4.33)$$

which gives

$$\ln(|u + \text{const}|) = -\tau + c_1, \quad (4.34)$$

$c_1$  – being a simple shift in  $\tau$  – can be chosen arbitrarily, and so we set  $c_1 = 0$ . If we again introduce  $u^* = -\text{const}$ , we have

$$u^* - u = e^{-\tau}, \quad (4.35)$$

the left hand side coming from resolving the absolute value in (4.34) for  $u < u^*$ , which is the region we will be interested in in critical collapse situations.

Finally we parameterize the  $\tau = \text{const}$  hypersurfaces as follows: for a DSS spacetime we set

$$r(\tau, z) = e^{-\tau} \tilde{R}(\tau, z) = e^{-\tau} z \zeta(\tau) \quad \text{with} \quad \zeta(\tau + \Delta) = \zeta(\tau), \quad (4.36)$$

where we require  $\zeta(\tau) > \dot{\zeta}(\tau)$  for all  $\tau$ , such that  $\partial_\tau r(\tau, z) < 0$  for all  $\tau$ . There is still a coordinate freedom contained in  $\zeta(\tau)$ . We keep this in order to describe the null hypersurface, which is mapped to itself via the diffeomorphism (the so called self-similarity horizon) with  $z = \text{const}$ . The resulting condition on  $\zeta(\tau)$  will be given below.

For a CSS spacetime we set

$$r = e^{-\tau} R(z) = e^{-\tau} z. \quad (4.37)$$

Summarizing, we chose the following adapted coordinates for a DSS spacetime

$$\begin{aligned} \tau(u) &= -\ln(u^* - u) & u(\tau) &= u^* - e^{-\tau} \\ &\iff & & \\ z(u, r) &= \frac{r}{(u^* - u)\zeta(\tau)} & r(\tau, z) &= e^{-\tau} z \zeta(\tau), \end{aligned} \quad (4.38)$$

and for a CSS spacetime

$$\begin{aligned} \tau(u) &= -\ln(u^* - u) & u(\tau) &= u^* - e^{-\tau} \\ z(u, r) &= \frac{r}{(u^* - u)} & r(\tau, z) &= e^{-\tau} z. \end{aligned} \quad \Longleftrightarrow \quad (4.39)$$

By construction, the hypersurfaces  $\tau = \text{const}$  are null. For  $u \rightarrow -\infty$  we have  $\tau \rightarrow -\infty$ , whereas for  $u \rightarrow u^*$ ,  $\tau \rightarrow +\infty$ .

The hypersurfaces  $z = \text{const}$ , along which the diffeomorphism acts all meet in the point  $(u = u^*, r = 0)$ . Clearly the adapted coordinates get singular there. Due to the symmetry, which squeezes the geometry into smaller and smaller spacetime regions, this point also has diverging curvature, as can easily be seen as follows: We examine the scalar curvature  $\mathcal{R}$  in adapted coordinates. From (4.6) we have

$$\begin{aligned} (\Phi_\Delta^* \mathcal{R})|_p &= e^{-2\Delta} \mathcal{R}|_p \\ \mathcal{R}(\Phi_\Delta(p)) &= e^{-2\Delta} \mathcal{R}(p) \\ \mathcal{R}(\tau - \Delta, z) &= e^{-2\Delta} \mathcal{R}(\tau, z) \end{aligned} \quad (4.40)$$

and therefore

$$\mathcal{R}(\tau, z) = e^{2\tau} \tilde{\mathcal{R}}(\tau, z) \quad \text{with} \quad \tilde{\mathcal{R}}(\tau - \Delta, z) = \tilde{\mathcal{R}}(\tau, z). \quad (4.41)$$

Note that  $\tilde{\mathcal{R}}$  does in general not agree with the scalar curvature built from the metric  $\tilde{g}$ , introduced in Sec. (4.1.1), although this would have a periodic  $\tau$  dependence as well.

In particular, as  $\tilde{\mathcal{R}}(\tau, z)$  has a periodic  $\tau$  dependence, it is bounded for all  $\tau$  if it is bounded in one “segment” between  $\Sigma$  and  $\Phi_\Delta(\Sigma)$ . So moving along  $z = \text{const}$  we find the scalar curvature blowing up like  $e^{2\tau}$  for  $\tau \rightarrow \infty$ , or  $u \rightarrow u^*$  (unless  $\tilde{\mathcal{R}}$  vanishes identically of course). As the origin is a line of constant  $z$ , this blowup occurs at  $(u = u^*, r = 0)$ . We call the point  $(u^*, 0)$  the *culmination point*, and  $u^*$  the culmination time.

Another point is worth to note. Consider the square of the vector field  $\partial_\tau$ . From (4.38) we have

$$\partial_\tau = (u^* - u)\partial_u + r(-1 + \frac{\dot{\zeta}}{\zeta})\partial_r \quad (4.42)$$

and so

$$\begin{aligned} g(\partial_\tau, \partial_\tau) &= (u^* - u)^2 g_{uu} + 2r(u^* - u)(-1 + \frac{\dot{\zeta}}{\zeta})g_{ur} = \\ &= -e^{-2\tau} e^{2\beta(\tau, z)} \left( \frac{V}{r}(\tau, z) - 2z\zeta(\tau) + 2z\dot{\zeta}(\tau) \right). \end{aligned} \quad (4.43)$$



At the origin ( $z = 0$ ),  $\partial_\tau$  is timelike, which is clear, as the diffeomorphism maps the origin onto itself. Furthermore, as mentioned after (4.36) we assume  $\zeta(\tau) > \dot{\zeta}(\tau)$  for all  $\tau$ .

Moving away from the origin  $z$  grows and goes to infinity for  $u \rightarrow u^*$ . As we assume  $\frac{V}{r}$  to be bounded, the expression in the parentheses in (4.43) will vanish at some value of  $z$ , which depends on  $\tau$ . We can now use the additional gauge freedom, which is contained in  $\zeta(\tau)$  in order to have  $\partial_\tau$  getting null on a hypersurface of constant  $z$ , e.g. at  $z = 1$ . The resulting condition on  $\zeta(\tau)$  reads

$$\left( \frac{V}{r}(\tau, 1) - 2\zeta(\tau) + 2\dot{\zeta}(\tau) \right) = 0. \quad (4.44)$$

So this hypersurface,  $z = 1$ , is a null hypersurface, which is mapped onto itself via the diffeomorphism. It is called the past *self-similarity horizon* (SSH). In fact this self-similarity horizon is just the backwards light cone of the culmination point.

There exists another null hypersurface which is mapped to itself by the diffeomorphism. This is the future light cone of the culmination point, and is called the future SSH. As the culmination point corresponds to a spacetime singularity, the region beyond this future SSH is not determined by the solution given for  $u < u^*$ .

For a CSS spacetime the statements “periodic in  $\tau$ ” have to be replaced by “independent of  $\tau$ ”. Furthermore with our choice of coordinates the location of the past SSH is given by

$$\frac{V}{r}(z_H) = 2z_H. \quad (4.45)$$

Fig. 4.1 shows a schematic diagram of a self-similar spacetime.

Note, that a self-similar spacetime is not asymptotically flat (unless spacetime as a whole is flat). This can be seen by going to infinity on a spacelike hypersurface  $z = \text{const}$  outside the past SSH. As the metric functions are periodic in  $\tau$  (resp. constant) along these hypersurfaces, they do not fulfill the fall-off conditions required by asymptotically flatness.

We close this section by writing down the line element for a DSS (CSS) spacetime with respect to the adapted coordinates (4.38) (respectively (4.39)).

$$ds_{DSS}^2 = e^{-2\tau} \left[ -e^{2\beta(\tau, z)} \left\{ \frac{V}{r}(\tau, z) - 2z\zeta(\tau) + 2z\dot{\zeta}(\tau) \right\} d\tau^2 - e^{2\beta(\tau, z)} 2\zeta(\tau) d\tau dz + z^2 \zeta(\tau)^2 d\Omega^2 \right], \quad (4.46)$$

and

$$ds_{CSS}^2 = e^{-2\tau} \left[ -e^{2\beta(z)} \left\{ \frac{V}{r}(z) - 2z \right\} d\tau^2 - e^{2\beta(z)} 2d\tau dz + z^2 d\Omega^2 \right]. \quad (4.47)$$

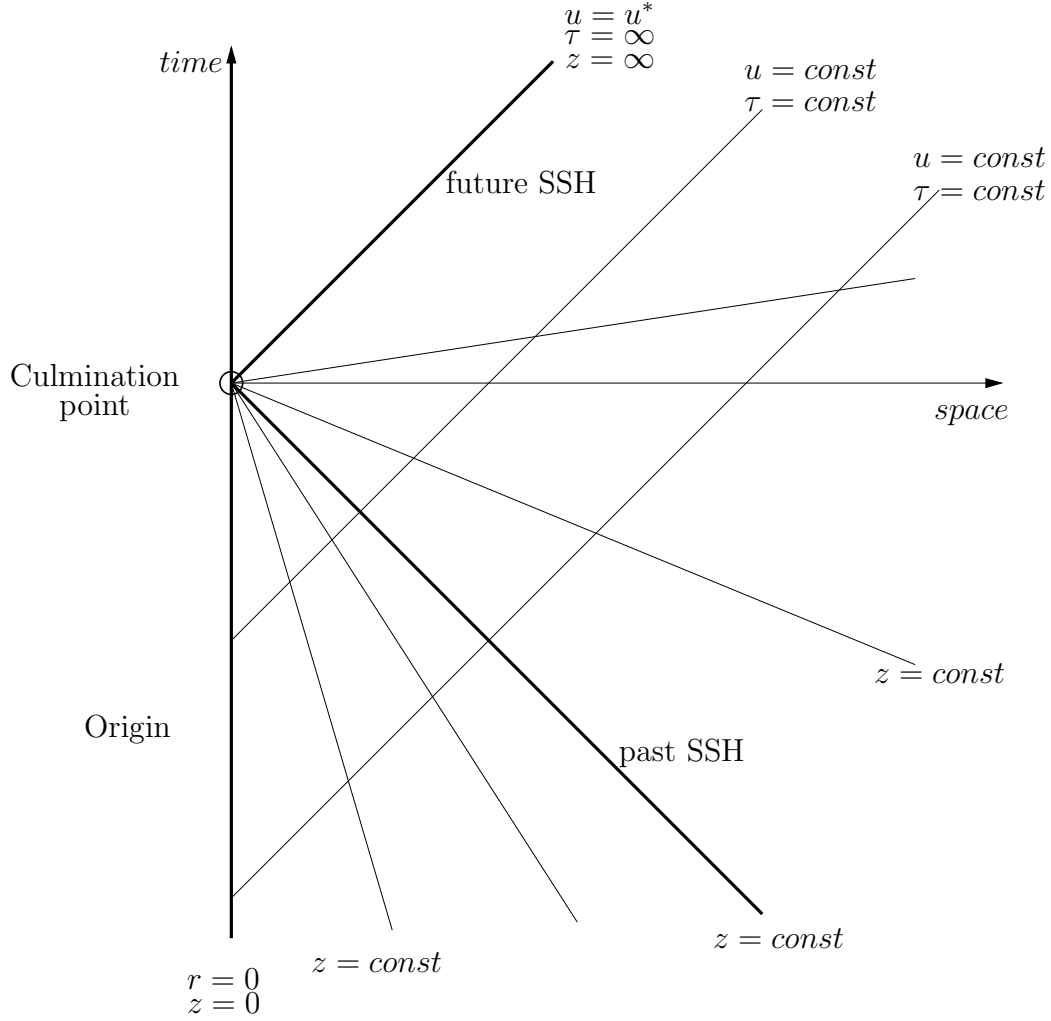


Figure 4.1: A schematic diagram of a self-similar spacetime. The adapted coordinates  $(\tau, z)$  defined in (4.39) cover only the region  $u < u^*$ . In this region the metric functions  $\beta$  and  $\frac{V}{r}$  are constant along  $z = \text{const}$ , thereby shrinking their profile to zero at the culmination point ( $u = u^*, r = 0$ ), where (unless in flat space) a spacetime singularity occurs. The region within the backwards light cone of the culmination point is the one of interest for critical collapse situations.

### 4.1.3 Implications for the matter field

We turn now to the conditions that the symmetries (4.1) and (4.2) imply for the matter field. It is clear that the matter will have to share (at least part of) the symmetry imposed on the stress energy tensor via the Einstein equations, i.e. we have for a DSS spacetime

$$(\Phi_\Delta^* T)_{\mu\nu} = T_{\mu\nu}, \quad (4.48)$$

and for a CSS spacetime

$$\mathcal{L}_\xi T_{\mu\nu} = 0. \quad (4.49)$$

As defined in Sec. 2.1 the stress energy tensor of a harmonic map is

$$T_{\mu\nu}(x) = f_\pi^2 \left( \nabla_\mu X^A(x) \nabla_\nu X^B(x) - \frac{1}{2} g_{\mu\nu}(x) (g^{\sigma\tau}(x) \nabla_\sigma X^A(x) \nabla_\tau X^B(x)) \right) G_{AB}(X(x)). \quad (4.50)$$

The pull-back of this tensor under  $\Phi_\Delta$  is given by

$$\begin{aligned} (\Phi_\Delta^* T)_{\mu\nu}|_p &= \frac{\partial \Phi_\Delta^\alpha}{\partial x^\mu} \frac{\partial \Phi_\Delta^\beta}{\partial x^\nu} \left[ \nabla_\alpha X^A(\Phi_\Delta(p)) \nabla_\beta X^B(\Phi_\Delta(p)) - \right. \\ &\quad \left. - \frac{1}{2} g_{\alpha\beta}(\Phi_\Delta(p)) (g^{\gamma\delta}(\Phi_\Delta(p)) \nabla_\gamma X^A(\Phi_\Delta(p)) \nabla_\delta X^B(\Phi_\Delta(p))) \right] \\ &\quad G_{AB}(X(\Phi_\Delta(p))). \end{aligned} \quad (4.51)$$

As the inverse metric transforms like

$$((\Phi_\Delta)_* g^{-1})^{\gamma\delta}|_{\Phi_\Delta(p)} = e^{2\Delta} g^{\gamma\delta}|_{\Phi_\Delta(p)}, \quad (4.52)$$

we have

$$\begin{aligned} &g^{\gamma\delta}(\Phi_\Delta(p)) \nabla_\gamma X^A(\Phi_\Delta(p)) \nabla_\delta X^B(\Phi_\Delta(p)) = \\ &= e^{-2\Delta} g^{\sigma\tau}(p) \frac{\partial \Phi_\Delta^\gamma}{\partial x^\sigma} \frac{\partial \Phi_\Delta^\delta}{\partial x^\tau} \nabla_\gamma X^A(\Phi_\Delta(p)) \nabla_\delta X^B(\Phi_\Delta(p)). \end{aligned} \quad (4.53)$$

The factor  $e^{-2\Delta}$  cancels with  $e^{2\Delta}$  coming from  $\frac{\partial \Phi_\Delta^\alpha}{\partial x^\mu} \frac{\partial \Phi_\Delta^\beta}{\partial x^\nu} g_{\alpha\beta}(\Phi_\Delta(p))$  in the second term of (4.51). In order to simplify things, we contract (4.51) with  $g^{\mu\nu}(p)$

$$g^{\mu\nu}(p) (\Phi_\Delta^* T)_{\mu\nu}|_p = -2g^{\mu\nu} \frac{\partial \Phi_\Delta^\alpha}{\partial x^\mu} \frac{\partial \Phi_\Delta^\beta}{\partial x^\nu} \nabla_\alpha X^A(\Phi_\Delta(p)) \nabla_\beta X^B(\Phi_\Delta(p)) G_{AB}(X(\Phi_\Delta(p))), \quad (4.54)$$

and switch to adapted coordinates to get

$$\begin{aligned} &g^{\mu\nu}(\tau, z, \omega) \nabla_\mu X^A(\tau - \Delta, z, \omega) \nabla_\nu X^B(\tau - \Delta, z, \omega) G_{AB}(X(\tau - \Delta, z, \omega)) = \\ &= g^{\mu\nu}(\tau, z, \omega) \nabla_\mu X^A(\tau, z, \omega) \nabla_\nu X^B(\tau, z, \omega) G_{AB}(X(\tau, z, \omega)), \end{aligned} \quad (4.55)$$

where we abbreviated the angular coordinates  $\theta$  and  $\varphi$  with  $\omega$ . So the self-gravitating harmonic map, leading to a discretely self-similar spacetime has to be either periodic or “anti-periodic” in the adapted time coordinate  $\tau$ ,

$$X^A(x^\mu) = \tilde{X}^A(\tau, z, \omega) \quad \text{with} \quad \tilde{X}^A(\tau - \Delta, z, \omega) = \pm \tilde{X}^A(\tau, z, \omega), \quad (4.56)$$

and independent of  $\tau$  for a CSS spacetime,

$$X^A(x^\mu) = X^A(z, \omega). \quad (4.57)$$

Concerning the sign in (4.56) we adopt the following convention: if the metric functions are periodic with period  $\tilde{\Delta}$  and the field is “anti-periodic” with respect to this period, then of course it is periodic with respect to twice the period, i.e.  $2\tilde{\Delta}$ . In this case we say that the solution is DSS with period  $\Delta = 2\tilde{\Delta}$ , and has the additional symmetry  $\beta(\tau + \Delta/2, z) = \beta(\tau, z)$  etc. and  $X^A(\tau + \Delta/2, z) = -X^A(\tau, z)$ .

Of course the conditions (4.56) and (4.57) are only necessary conditions for the existence of a regular self-similar spacetime<sup>1</sup>.

Remember, that the self-gravitating nonlinear  $\sigma$  model is a *scale invariant* theory. We stress that this scale invariance is a necessary condition for the existence of self-similar solutions. Consider for example vacuum with a cosmological constant  $\Lambda$ .

$$G_{\mu\nu} + \Lambda g_{\mu\nu} = 0. \quad (4.58)$$

Here the cosmological constant  $\Lambda$  introduces a length scale. Applying the pull-back  $\Phi_\Delta^*$  to Eq. (4.58) we get using Eqs. (4.6) and (4.1)

$$(\Phi_\Delta^*(G + \Lambda g))_{\mu\nu}|_p = G_{\mu\nu} + \Lambda e^{2\Delta} g_{\mu\nu}|_p, \quad (4.59)$$

which does not satisfy (4.58) anymore.

Another example of a model with a length scale would be the self-gravitating nonlinear  $\sigma$  model with an additional potential in the Lagrangian, e.g.  $V(X) = X^A X^B G_{AB}(X)$ . For dimensional reasons this potential has to be multiplied by a constant of dimension  $(1/\text{length})^2$ , which breaks the scale invariance. As this potential term appears in the stress energy tensor multiplied by the metric  $g_{\mu\nu}$ , it would get a factor  $e^{2\Delta}$  under the action of the pull-back  $\Phi_\Delta^*$ , which does not cancel. As this is the only term which transforms that way, again the Einstein equations cannot be satisfied.

Nevertheless a model with a length scale can admit asymptotic self-similarity, i.e. it might display self-similarity at scales which are small compared to the length scale of the theory. This can be seen by writing the equations in adapted coordinates and neglecting the terms which contain a factor  $e^{-\tau}$  or any power thereof.

---

<sup>1</sup>By regular in this context, we mean regular within the backwards light cone of the culmination point

(As  $\tau \rightarrow \infty$  denotes the region close to the culmination point, spatial extensions are already very small). This concerns the terms that are tied to the length scale, therefore the remaining theory again is scale invariant. In this context such terms are called *asymptotically irrelevant*. An example is the Einstein-Yang-Mills system, which admits an asymptotically DSS solution at the (type II) threshold of black hole formation [21]. This solution also has been constructed directly (using the asymptotic symmetry) by Gundlach [34].

## 4.2 Numerical Construction of CSS Solutions

This section deals with the (numerical) construction of CSS solutions of the self-gravitating SU(2)  $\sigma$ -model in spherical symmetry using the hedgehog ansatz introduced in Sec. 2.2.3. This problem has already been studied by Bizon [8] for the simpler case of fixed Minkowski background ( $\eta = 0$ ), and by Bizon and Wasserman for the coupled case [11].

In [8] a discrete one-parameter family of CSS solutions was constructed numerically, the existence was proven analytically and the stability properties of the solutions were given. In [11] this family of solutions was shown to persist up to a coupling constant  $\eta_{max} = 0.5$  by means of the numerical construction. Furthermore, the analytic continuation beyond the past SSH was studied numerically, showing that for each member of the family there exists a critical value of the coupling  $\eta_n^*$  beyond which the analytic continuation contains marginally trapped surfaces.

In order to be able to compare the directly constructed CSS solution to critical solutions obtained by a bisection search of time evolved data, we re-did the (numerical) calculations of [8] and [11], reproducing their results. Furthermore we studied the stability of the solutions for nonzero couplings, which has not been considered in [11].

We will report here on both the numerical construction of the solutions and their analytic continuation beyond the past SSH (in order to make everything self-contained) as well as on their stability properties.

### 4.2.1 The “CSS equations”

We start by combining the symmetry requirement (4.57) with the hedgehog ansatz. For a CSS solution of the self-gravitating nonlinear  $\sigma$  model we have with  $X^A = (\phi, \Theta, \Phi)$

$$\phi(x^\mu) = \phi(z), \quad \Theta(x^\mu) = \theta, \quad \Phi(x^\mu) = \varphi. \quad (4.60)$$

Transforming now Eqs. (2.48), (2.55) and (2.56) to the adapted coordinates defined in (4.39) and dropping all derivatives with respect to  $\tau$ , we get

$$\beta' = \frac{\eta}{2} z (\phi')^2 \quad (4.61)$$

$$\left(\frac{V}{r}\right)' = -\frac{1}{z} \left( -e^{2\beta} + 2\eta e^{2\beta} \sin^2(\phi) + \frac{V}{r} \right) \quad (4.62)$$

and

$$\left( z^2 \left( \frac{V}{r} - 2z \right) \phi' \right)' + 2z^2 \phi' = \sin(2\phi) e^{2\beta} \quad (4.63)$$

or

$$\begin{aligned} \phi'' &= \frac{1}{z^2 \left( -\frac{V}{r} + 2z \right)} \left( -e^{2\beta} \left\{ \sin(2\phi) + z \left( -1 + 2\eta \sin^2(\phi) \right) \phi' \right\} + \right. \\ &\quad \left. + z \left\{ \left( \frac{V}{r} - 4z \right) \phi' \right\} \right), \end{aligned} \quad (4.64)$$

where  $' \equiv \partial_z$ .

The subsidiary Einstein equation “Euur” (2.57) gives in addition

$$\left(\frac{V}{r}\right)' = \eta z \left( 2z - \frac{V}{r} \right) (\phi')^2. \quad (4.65)$$

Eqs. (4.62) and (4.65) can be combined to give an algebraic relation for  $\frac{V}{r}$ :

$$\frac{V}{r} = \frac{-e^{2\beta}(1 - 2\eta \sin^2 \phi) + \eta 2z^3 (\phi')^2}{-1 + \eta z^2 (\phi')^2}. \quad (4.66)$$

As discussed already in Sec. 2.2, regularity at the origin ( $z = 0$ ) as well as the gauge choice for  $u$  requires

$$\phi(0) = 0, \quad \beta(0) = 0, \quad \frac{V}{r}(0) = 1. \quad (4.67)$$

The only free parameter, which determines the solution is

$$\phi'(0) = b. \quad (4.68)$$

According to (4.65)  $\frac{V}{r}$  is decreasing for  $z > 0$  and eventually equals  $2z$  at some  $z_H$ . This marks a singular point of the equations and corresponds physically to the past self-similarity horizon discussed in Sec. 4.1.2.

Eq. (4.65) shows, that at the horizon in addition to  $\frac{V}{r}|_H = 2z_H$ , we have  $\left(\frac{V}{r}\right)'|_H = 0$ . Eq. (4.62) then yields the following relation for  $\beta_H$

$$e^{2\beta_H} = \frac{2z_H}{1 - 2\eta \sin^2(\phi_H)}, \quad (4.69)$$

where  $\beta_H, \phi_H$  denote the fields  $\beta$  and  $\phi$  evaluated at the horizon  $z_H$ .

Furthermore following from Eq. (4.64) regularity at the horizon requires  $\sin 2\phi_H = 0$ , which can be resolved to  $\phi_H = 0 \pmod{\pi}$  or  $\phi_H = \pi/2 \pmod{\pi}$ . The first case is impossible for the following reason: assume  $\phi_H = 0$ , so  $e^{2\beta_H} = 2z_H$  which in turn equals  $\frac{V}{r}|_H$ . So we would have  $e^{2\beta_H} = \frac{V}{r}|_H$ . From Eqs. (4.61) and (4.65) we know that  $\beta' \geq 0$ , whereas  $\frac{V'}{r} \leq 0$  between origin and horizon. As  $e^{2\beta}$  equals  $\frac{V}{r}$  at the origin, the two metric functions cannot attain the same value at the horizon unless they are constant functions, which is the case for vanishing coupling  $\eta = 0$ .

Summarizing we get

$$\phi_H = \frac{\pi}{2}, \quad e^{2\beta_H} = \frac{2z_H}{1-2\eta}. \quad (4.70)$$

One sees immediately, that  $\beta_H$  can only be finite if  $\eta < 0.5$ . CSS solutions, regular at both origin and past SSH, can therefore only exist for small couplings  $\eta \in [0, 0.5)$ .

Note that solutions to (4.61)–(4.63) satisfying (4.67) and (4.70) (if they exist) are analytic in  $z$  and the shooting parameters. (In the vicinity of the singular points  $z = 0$  and  $z_H$  one can use Prop. 1 of [14] to show analyticity, for other  $z$  it follows from the analyticity of the right hand sides of the equations.)

In order to construct regular solutions numerically, we proceed as follows. We consider the boundary value problem, consisting of the coupled system of four first order ODEs Eqs. (4.61), (4.64) and (4.65) subject to the boundary conditions (4.67) and  $\phi_H = \frac{\pi}{2}$ . The relation for  $\beta_H$  can be dropped here, as it results from a subsidiary equation, which is not used for the calculation. (An alternative would be to substitute Eq. (4.65) by the algebraic relation (4.66), thereby reducing the system to three first order ODEs.) The four free shooting parameters at the boundaries are

$$\phi'(0) = b, \quad z_H, \quad \phi'_H, \quad \beta_H. \quad (4.71)$$

For fixed  $\eta$  the problem is solved numerically using the shooting and matching routine d02agf from the NAG Library [60]. We start at  $\eta = 0$  by pinning down one member of the discrete one parameter family of solutions reported by Bizon [8] and follow this solution to higher values of the coupling constant. As we are mainly interested in the ground state and first excited state, we only constructed the first few solutions.

## 4.2.2 Phenomenology of Numerically Constructed Solutions

As in [11] we find that the solutions present on Minkowski background stay regular between origin and past SSH up to a maximal value of the coupling constant  $\eta_{max} = 0.5$ . At this maximal value the metric function  $\beta$  diverges at

the horizon, which can be inferred from (4.70). A more complete picture of this phenomenon can be obtained if one considers the analytic continuation beyond the past SSH, which will be discussed in the next section.

Figure 4.2 shows the shooting parameter  $\phi'(0)$  for the ground state and the first excited state as functions of the coupling. This parameter alone determines the solution. Figure 4.3 shows the value of  $\beta_H$  for the two solutions again as functions of the coupling.

### 4.2.3 Analytic Continuation beyond the past SSH

In order to get a more global picture of the solutions described above, we study the analytic continuation of the solutions beyond the past SSH. We do this by integrating Eqs. (4.61), (4.64) and (4.65) towards larger values of  $z$ , with initial conditions imposed at the horizon  $z_H$ , that are taken from the solutions to the boundary value problem discussed above. Note, that – as the past SSH’s domain of dependence is zero – in general it is not enough to give data there. This procedure only works by the means of analyticity.

As already mentioned above, we have  $(\frac{V}{r})' = 0$  at the horizon. From this it follows, that  $2z - \frac{V}{r} > 0$  for  $z$  close to but larger than  $z_H$ . Therefore  $(\frac{V}{r})' > 0$  for  $z > z_H$  and  $\frac{V}{r}$  is monotonically increasing in the region beyond the horizon. So it might happen, that  $\frac{V}{r}$  eventually equals  $2z$  at some value  $z_S$ , which means that the equations have a second (or counting the origin a third) singular point there.

It was already shown in [11] that this second singular point does not correspond to a second self-similarity horizon (i.e. a null surface that is mapped to itself by the diffeomorphisms), but rather a spacelike hypersurface where  $2m/r \rightarrow 1$ . We will repeat the argument here.

Consider the expression

$$h(z) = \frac{e^{-2\beta}}{2z - \frac{V}{r}}. \quad (4.72)$$

This function is positive for  $z_H < z < z_S$  and diverges, when approaching the past SSH from above:

$$\lim_{z \rightarrow z_H^+} h(z) = +\infty. \quad (4.73)$$

Using Eqs. (4.61) and (4.65) we find for the derivative

$$\begin{aligned} h'(z) &= \frac{e^{-2\beta}}{(2z - \frac{V}{r})^2} \left( -2(2z - \frac{V}{r})\beta' - (2 - (\frac{V}{r})') \right) = \\ &= -\frac{2e^{-2\beta}}{(2z - \frac{V}{r})^2}, \end{aligned} \quad (4.74)$$



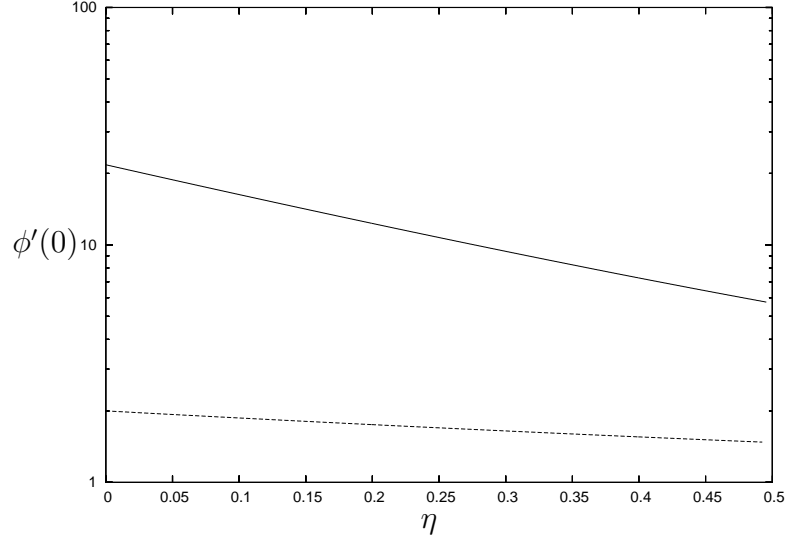


Figure 4.2: The shooting parameter  $\phi'(0)$  for the ground state (dashed line) and the first excitation (solid line) as a function of the coupling constant  $\eta$ .

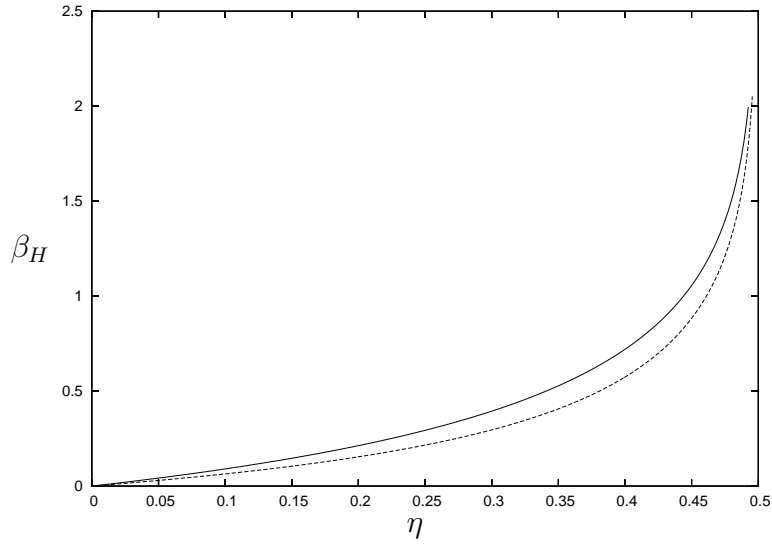


Figure 4.3: The shooting parameter  $\beta_H$  for the ground state (solid line) and the first excitation (dashed line) as a function of the coupling constant  $\eta$ .  $\beta_H$  rises for both solutions as one approaches the maximal coupling  $\eta_{max} = 0.5$  and diverges in the limit, as can be inferred from Eq. 4.70.

which is less than zero in the region we are interested in. From this it follows, that

$$\lim_{z \rightarrow z_S^-} h(z) \text{ exists,} \quad (4.75)$$

and therefore as the denominator vanishes, we have

$$\lim_{z \rightarrow z_S^-} e^{-2\beta(z)} = 0. \quad (4.76)$$

From Eq. (4.66) one finds, that the combination  $(\frac{V}{r} - 2z) e^{-2\beta} (\phi')^2$  stays finite in the limit  $z \rightarrow z_S$ . Making use of this one can show that the scalar curvature, the Kretschmann invariant, the square of the Ricci tensor  $R_{\mu\nu} R^{\mu\nu}$  and the Weyl invariant are bounded when  $z \rightarrow z_S$ . Up to now it is not clear whether  $\phi$  itself has a limit. If so, the above invariants have a limit as well.

As in [11] our numerical integration gives the following results: for each member of the one parameter family, there exists a critical value of the coupling constant  $\eta_n^*$  such that for smaller values of the coupling, the solution extends smoothly up to the future SSH, whereas for stronger couplings the geometry contains marginally trapped surfaces at  $z = z_S > z_H$ . The coordinate location of these marginally trapped surfaces is a decreasing function of the coupling constant and eventually merges with the location of the past SSH in the limit  $\eta \rightarrow \eta_{max}$ . Furthermore the critical value of the coupling increases with the excitation number  $n$ .

### 4.3 Stability of CSS Solutions

In order to answer the question, whether any of the above constructed solutions may play a role as a critical solution in gravitational collapse, it is essential to study the stability properties.

In [8] the stability of the one-parameter family of CSS solutions on Minkowski background was studied. The results reported are, that the  $n$ -th excitation has  $n$  unstable modes, in particular the ground state is stable and the first excitation has one unstable mode. This suggests, that the ground state plays the role of a global attractor in the time evolution of strong enough initial data, and that the first excitation might be a critical solution at the border of two different end states. These predictions were verified in [10]. We will talk about these critical phenomena in more detail in Sec. 5.7.

As the limit  $\eta \rightarrow 0$  is a regular limit concerning the existence of CSS solutions, one expects, that the stability properties of the solutions do not change, when gravity is switched on, at least as long as the coupling constant is small.

We report here on the stability analysis for the coupled case, which we performed in two essentially different ways, and show, that indeed the stability properties of the CSS solutions do not change for small couplings.

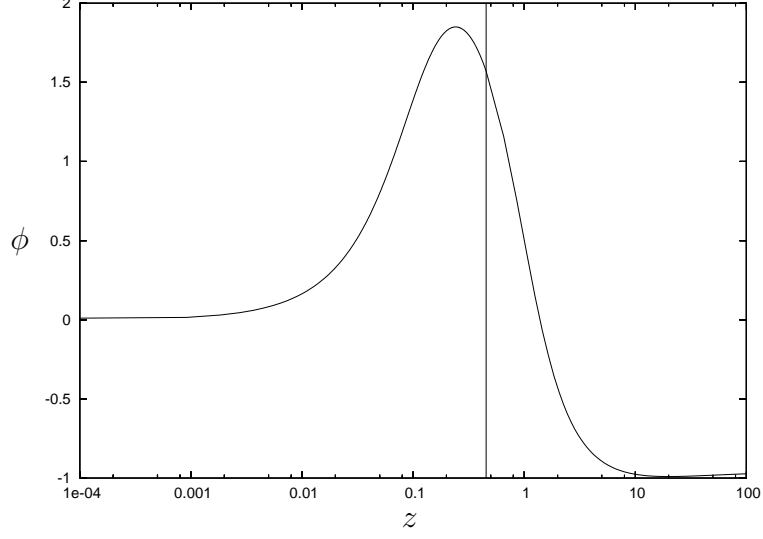


Figure 4.4: The field  $\phi$  of the first excitation for  $\eta = 0.1$ . The vertical line marks the horizon at  $z_H = 0.45457$ .

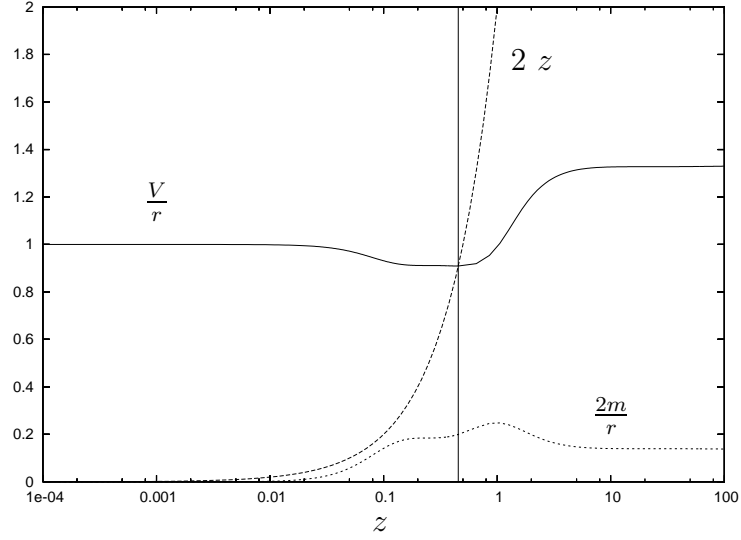


Figure 4.5: The same situation as above. Plotted are the metric function  $\frac{V}{r}$  as well as  $\frac{2m}{r}$  for the first excitation at  $\eta = 0.1$ .  $\frac{V}{r}$  crosses the line  $2z$  at the location of the horizon. As  $\eta$  is well below the critical value  $\eta_1^* \simeq 0.152$ ,  $\frac{V}{r}$  stays well below  $2z$  outside the horizon and  $\frac{2m}{r}$  is far from being unity anywhere.

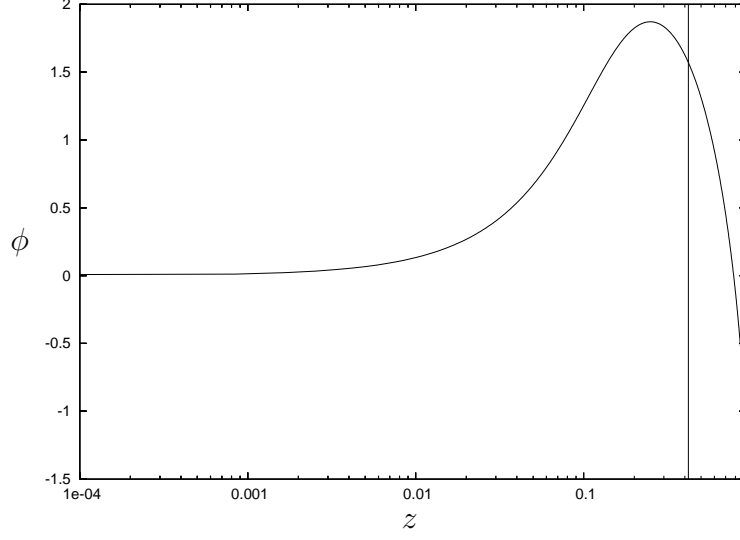


Figure 4.6: The field  $\phi$  of the first excitation for  $\eta = 0.175$ . The vertical line marks the horizon at  $z_H = 0.4198$ . The right boundary of the plot is at the second singular point  $z_S = 0.9292$ .

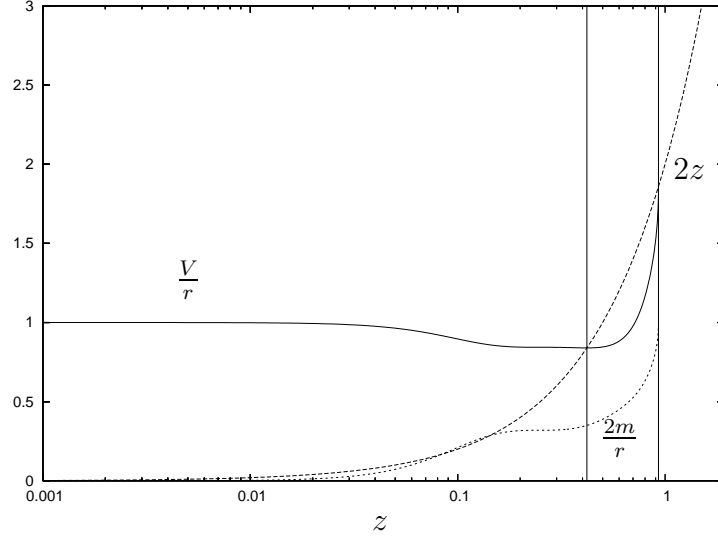


Figure 4.7: The same situation as above. Plotted are the metric function  $\frac{V}{r}$  as well as  $\frac{2m}{r}$  for the first excitation at  $\eta = 0.175$ .  $\frac{V}{r}$  crosses the line  $2z$  at the location of the horizon. As  $\eta$  is above the critical value  $\eta_1^* \simeq 0.152$ ,  $\frac{V}{r}$  equals  $2z$  for a second time at  $z_S = 0.9292$ . At the same time  $\frac{2m}{r}$  tends to 1.

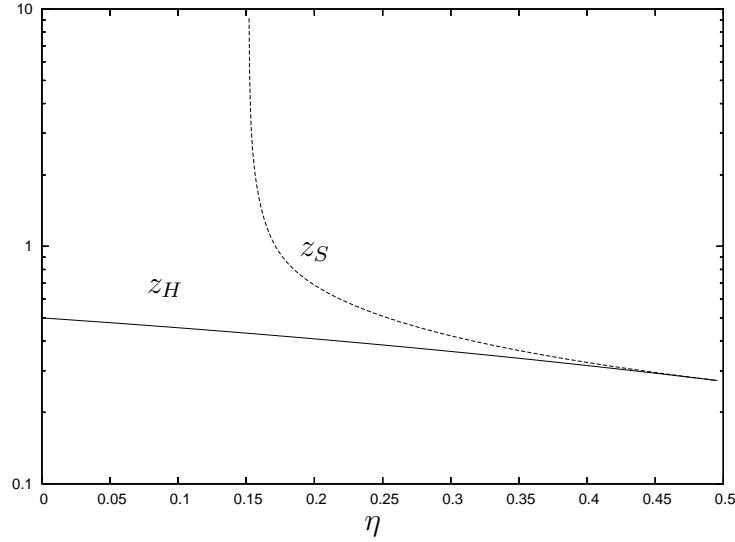


Figure 4.8: The coordinate locations of the past self-similarity horizon  $z_H$  and the second singular point  $z_S$  for the first CSS excitation as functions of the coupling constant  $\eta$ . For  $\eta < \eta_1^* \simeq 0.152$  the analytic extension of the CSS solution is regular up to the future SSH ( $z \rightarrow \infty$ ). For bigger  $\eta$  the solution develops an apparent horizon at the spacelike hypersurface  $z = z_S = \text{const.}$  This hypersurface finally merges with the past SSH in the limit  $\eta \rightarrow 0.5$ . The other excitations behave in a similar way, where  $\eta_n^*$  is an increasing function of the excitation number  $n$ .

The first method is the standard way to determine the stability properties of CSS solutions. The CSS solution is perturbed in a small spherically symmetric, time dependent way. The perturbations then are decomposed into modes with an exponential (and oscillatory) time dependence. Inserting this ansatz into the linearized field equations gives a coupled system of ODEs, with the same singular points as for the background solution. Regularity then requires the perturbations to be solutions to a boundary value problem, or to be more precise to a linear eigenvalue problem, the real part of the eigenvalue, if bigger than zero, being responsible for the exponential growth of the unstable mode. The advantage of this method is that one only deals with ODEs, which can be integrated rather accurately. One main disadvantage is, that if using a shooting and matching method, one needs good initial guesses for the shooting parameters. In other words, one can never be sure, that one obtains *all* of the relevant, i. e. unstable, modes, unless one has further theoretical arguments. Although in all similar situations, where the stability of an “expected-to-be” critical CSS solution was analyzed, the unstable modes were all real, there is no theory guaranteeing this. For the system on fixed Minkowski background it was shown in [8], that the perturbation operator can be brought into a self-adjoint form (using orthogonal

coordinates), therefore the eigenvalues have to be real. Furthermore a theorem for Sturm-Liouville operators could be applied, which determined the number of eigenvalues giving rise to unstable modes.<sup>2</sup> Unfortunately a similar analysis does not exist for the coupled system.

We therefore present an alternative method to compute the unstable modes. This method was proposed and carried out by J. Thornburg [70]. The method uses the full nonlinear field equations. It is based on the observation, that a numerical time evolution maps the discretized field, i.e. the  $N$ -dimensional vector, on the initial slice to a discretized field on a later slice. If the initial configuration is close to a CSS solution and the time step is small enough<sup>3</sup>, then the relation between the deviations from the CSS solution at the initial and final slices is linear, i.e. determined by an  $N \times N$  matrix. The unstable modes can then be extracted from the eigenvalues and eigenvectors of this matrix. The main advantage of this method is, that it should give *all* the unstable modes of the CSS solution that are “seen” by the time evolution code, and therefore, if the number of grid points  $N$  is big enough, all the unstable modes of the continuum problem. A further advantage of this method is, that it uses an already existing evolution code (the DICE code, see App. C). One minor disadvantage of the method is, that the numerical answers are expected to be less accurate than the answers obtained from the ODE boundary value problem. Unfortunately up to now this method suffers from a more serious drawback, namely it fails to converge with respect to resolution. More precisely, increasing the number of grid points, the numerical results move further and further away from the predicted ones (an example is the gauge mode, described below). What is even worse, is that we do not know, why this method does not converge. One possible reason could be that for higher resolutions the method gets increasingly ill-conditioned, that is increasingly sensitive to small numerical errors in the numerical time evolution. Nevertheless, as we get answers for a certain number of grid points ( $N = 500$ ) which are in good agreement with the results of the other method, we are inclined to believe these results (for this number of grid points) and deduce the stability properties from them.

---

<sup>2</sup>We mention that the continuous spectrum of the operator in [8] would seem to be unstable in adapted coordinates  $(\tau, z)$ . In fact these modes are growing as fast as the gauge mode, which shows, that the growth is due to the shrinking of adapted coordinates and therefore these modes are not considered as unstable. We also mention that members of the continuous spectrum oscillate infinitely many times in the vicinity of the horizon. They therefore cannot be detected by the methods described below.

<sup>3</sup>The time step under consideration has to be small such that unstable modes don’t drive the solution out of the linear regime. The time step may consist of several numerical time steps of the evolution code.

### 4.3.1 Unstable Modes from a Boundary Value Problem

In order to analyze the stability of the CSS solutions, we proceed in the usual way. Consider small time-dependent radial perturbations of the CSS solution

$$\phi(\tau, z) = \phi_n(z) + \delta\phi(\tau, z), \quad (4.77)$$

$$\beta(\tau, z) = \beta_n(z) + \delta\beta(\tau, z), \quad (4.78)$$

$$\frac{V}{r}(\tau, z) = \left(\frac{V}{r}\right)_n(z) + \delta V(\tau, z), \quad (4.79)$$

where  $\phi_n, \beta_n, (\frac{V}{r})_n$  denote the  $n$ -th CSS excitation. (Note that by  $\delta V$  we denote the perturbation of the metric function  $\frac{V}{r}$  not of  $V$  alone). As the perturbations are supposed to be small, we can linearize Eqs. (2.48), (2.55), (2.56) in these perturbations. Together with the requirement that the background solutions  $\phi_n, \beta_n, (\frac{V}{r})_n$  solve the CSS equations (4.61), (4.64) and (4.62) (or alternatively (4.65)), one obtains the following linear system of PDEs:

$$\delta\phi'(\tau, z) = z \eta \phi_n'(z) \delta\phi(\tau, z), \quad (4.80)$$

$$\begin{aligned} \delta V'(\tau, z) = & -\frac{1}{z} \left( 2 e^{2\beta_n(z)} (-1 + 2\eta \sin(\phi_n(z))^2) \delta\beta(\tau, z) + \delta V(\tau, z) + \right. \\ & \left. + 2 e^{2\beta_n(z)} \eta \sin(2\phi_n(z)) \delta\phi(\tau, z) \right), \end{aligned} \quad (4.81)$$

$$\begin{aligned} 0 = & 2 e^{2\beta_n(z)} \left( 2z - \left(\frac{V}{r}\right)_n(z) \right) \delta\beta(\tau, z) \left[ \sin(2\phi_n(z)) + z (-1 + 2\eta \sin(\phi_n(z))^2) \phi_n'(z) \right] + \\ & + \delta V(\tau, z) \left[ 2z^2 \phi_n'(z) + e^{2\beta_n(z)} (\sin(2\phi_n(z)) + z (-1 + 2\eta \sin(\phi_n(z))^2) \phi_n'(z)) \right] + \\ & + \left( 2z - \left(\frac{V}{r}\right)_n(z) \right) \left( 2 e^{2\beta_n(z)} \delta\phi(\tau, z) [\cos(2\phi_n(z)) + z \eta \sin(2\phi_n(z)) \phi_n'(z)] + \right. \\ & + z \left\{ \left[ 4z + e^{2\beta_n(z)} (-1 + 2\eta \sin(\phi_n(z))^2) - \left(\frac{V}{r}\right)_n(z) \right] \delta\phi'(\tau, z) + \right. \\ & + z \left( 2z - \left(\frac{V}{r}\right)_n(z) \right) \delta\phi''(\tau, z) + 2\delta\dot{\phi}(\tau, z) \left. \right\} \left. \right) + \\ & + \left[ 2z^2 \left( 2z - \left(\frac{V}{r}\right)_n(z) \right) \right] \delta\dot{\phi}'(\tau, z). \end{aligned} \quad (4.82)$$

We now decompose the general perturbations (4.77) into modes of the form

$$\begin{aligned} \delta\phi(\tau, z) &= e^{\lambda\tau} y(z), \\ \delta\beta(\tau, z) &= e^{\lambda\tau} g(z), \\ \delta V(\tau, z) &= e^{\lambda\tau} h(z). \end{aligned} \quad (4.83)$$

Inserting this ansatz into Eqs. (4.80), (4.82) yields a coupled system of ODEs for the perturbations  $y(z), g(z)$  and  $h(z)$ . This system again suffers from two singular points, the origin  $z = 0$  and the past SSH  $z = z_H$ .

Regularity at the origin restricts the perturbations to

$$y(0) = 0, \quad g(0) = 0, \quad h(0) = 1, \quad (4.84)$$

whereas the first spatial derivative of the field  $y'(0)$  is unconstrained.

At the horizon the requirement of regularity relates  $y'_H$  to the boundary values of the other fields

$$\begin{aligned} y'_H &= \frac{1}{\lambda 2z_H(-1+2\eta)} \left( (-4 + (2-4\eta)\lambda)y_H + 4z_H(\phi'_n)_H(-1+2\eta)g_H - \right. \\ &\quad \left. - (\phi'_n)_H(1+2\eta + z_H^2\eta(1-2\eta)(\phi'_n)_H^2)h_H \right). \end{aligned} \quad (4.85)$$

Eqs. (4.80), (4.82) together with the boundary conditions (4.84), (4.85) constitute an eigenvalue problem, with eigenvalue  $\lambda$  and eigenfunctions  $(y, y', g, h)$ . As already mentioned the eigenvalues and eigenfunctions may be complex. Nevertheless, as the coefficients in Eqs. (4.80), (4.82) are all real the eigenvalues and eigenvectors, if complex, come in complex conjugate pairs.

The resulting problem again is a boundary value problem, consisting of eight linear first order ODEs (Eqs. (4.80), (4.82)) separated into real and imaginary part) and the eight boundary conditions (real and imaginary parts of Eqs. (4.84) and (4.85)). The parameters that have to be matched are

$$\lambda, \quad y_H, \quad g_H, \quad h_H, \quad (4.86)$$

(again real and imaginary parts thereof). As the problem is linear and homogeneous the solutions are only fixed up to an overall scale. We fix that, by setting  $y'(0) = 1$ .

This boundary value problem again was solved numerically, using the shooting and matching routine d02agf of the NAG-library ([60]). The background solution was computed first and interpolated when necessary in order to provide the coefficients in Eqs. (4.80), (4.82).

### 4.3.2 Gauge Modes

Before reporting on the numerical results, we determine the gauge modes, that result from a certain arbitrariness in relating the adapted coordinates  $(\tau, z)$  to Bondi coordinates  $(u, r)$ . Recalling from Sec. 4.1.2 (Eq. (4.39)) we have

$$\begin{aligned} \tau(u) = -\ln(u^* - u) & \quad u(\tau) = u^* - e^{-\tau} \\ & \quad \Longleftrightarrow \\ z(u, r) = \frac{r}{(u^* - u)} & \quad r(\tau, z) = e^{-\tau} z. \end{aligned} \quad (4.87)$$



A shift in the culmination time  $u^* \rightarrow \bar{u}^* = u^* + \epsilon$  (corresponding to a shift of the origin of  $u$ ) yields another pair of adapted coordinates  $(\bar{\tau}, \bar{z})$ , defined as above with respect to  $\bar{u}^*$ . The relation between these two sets of adapted coordinates is given by

$$\begin{aligned}\bar{\tau} &= \tau - \ln(1 + \epsilon e^\tau), \\ \bar{z} &= \frac{z}{1 + \epsilon e^\tau}.\end{aligned}\tag{4.88}$$

For small  $\epsilon$  we linearize to get

$$\begin{aligned}\bar{\tau} &= \tau - \epsilon e^\tau = \tau + \epsilon \chi^\tau(\tau, z) \\ \bar{z} &= z - \epsilon z e^\tau = z + \epsilon \chi^z(\tau, z),\end{aligned}\tag{4.89}$$

where we have introduced the generating vector field  $\chi^\mu(\tau, z)$ . In the following we will treat the vector field  $\chi^\mu$  as general and show in the end, that the form (4.89) is indeed the only possible one.<sup>4</sup>

Such a small coordinate transformation introduces a (small) change in the perturbations according to

$$\begin{aligned}\delta \bar{g}_{\mu\nu} &= \delta g_{\mu\nu} - \epsilon \mathcal{L}_\chi(g_0)_{\mu\nu}, \\ \delta \bar{\phi} &= \delta \phi - \epsilon \mathcal{L}_\chi \phi_0,\end{aligned}\tag{4.90}$$

where in our case the objects with the subscript 0 denote a CSS solution. Pure gauge modes are characterized by

$$\begin{aligned}\delta g_{\mu\nu} &= \epsilon \mathcal{L}_\chi(g_0)_{\mu\nu}, \\ \delta \phi &= \epsilon \mathcal{L}_\chi \phi_0,\end{aligned}\tag{4.91}$$

i.e. modes of this form can be removed by a small change in the coordinates according to (4.89).

We first note, that the coordinate transformations are not completely arbitrary, but have to ensure that a hypersurface  $\bar{\tau} = \text{const}$  still is a null cone, which is reflected by

$$\mathcal{L}_\chi(g_0)_{zz} = 0,\tag{4.92}$$

or

$$\chi_{,z}^\tau = 0 \quad \Rightarrow \quad \chi^\tau = \chi^\tau(\tau).\tag{4.93}$$

The second observation is, that via 4.77 we fixed the “ $\mathbb{S}^2$  - part” of the metric to be  $e^{-2\tau} z^2$ , which gives

$$\mathcal{L}_\chi(g_0)_{\theta\theta} = 0,\tag{4.94}$$

---

<sup>4</sup>In particular the following arguments rule out a coordinate transformation, that resets the origin of  $\tau$ ,  $\tau \rightarrow \tau + c$ : such a coordinate transformation violates (4.98) and therefore does not correspond to a regular perturbation of the CSS solution within our choice of coordinates (especially the choice of  $u$  being proper time at the origin).

or

$$\begin{aligned}\chi^\tau(g_0)_{\theta\theta,\tau} + \chi^z(g_0)_{\theta\theta,z} &= 0, \\ \chi^z &= z\chi^\tau.\end{aligned}\tag{4.95}$$

For the remaining components of (4.91) we get

$$\begin{aligned}\mathcal{L}_\chi(g_0)_{\tau\tau} &= -e^{-2\tau} \left[ 2(-\chi^\tau + \chi_{,\tau}^\tau) e^{2\beta_0} \left( \left( \frac{V}{r} \right)_0 - 2z \right) + \chi^z (e^{2\beta_0} \left( \left( \frac{V}{r} \right)_0 - 2z \right))' + \right. \\ &\quad \left. + 2\chi_{,\tau}^z e^{2\beta_0} \right] = \\ &= -e^{-2\tau} \left[ 2(-\chi^\tau + \chi_{,\tau}^\tau) e^{2\beta_0} \left( \left( \frac{V}{r} \right)_0 - 2z \right) + z\chi^\tau (e^{2\beta_0} \left( \left( \frac{V}{r} \right)_0 - 2z \right))' + \right. \\ &\quad \left. + 2z\chi_{,\tau}^\tau e^{2\beta_0} \right] \\ \mathcal{L}_\chi(g_0)_{\tau z} &= -e^{-2\tau} \left[ (-2\chi^\tau + \chi_{,\tau}^\tau + \chi_{,z}^z) e^{2\beta_0} + 2\chi^z \beta_0' e^{2\beta_0} \right] = \\ &= -e^{-2\tau} \left[ (-\chi^\tau + \chi_{,\tau}^\tau) e^{2\beta_0} + 2z\chi^\tau \beta_0' e^{2\beta_0} \right] \\ \mathcal{L}_\chi \phi_0 &= \chi^z \phi_0'(z) = z\chi^\tau \phi_0'(z).\end{aligned}\tag{4.96}$$

On the other hand the perturbations of the metric functions  $\beta$  and  $\frac{V}{r}$  are related to the perturbations of the components of the metric with respect to  $(\tau, z)$  coordinates via

$$\begin{aligned}\delta g_{\tau\tau} &= -e^{-2\tau} e^{2\beta_0} \left[ 2 \left( \left( \frac{V}{r} \right)_0 - 2z \right) \delta\beta + \delta V \right], \\ \delta g_{\tau z} &= -2e^{-2\tau} e^{2\beta_0} \delta\beta.\end{aligned}\tag{4.97}$$

The regularity requirements at the origin discussed in the last section, namely  $\delta\beta(\tau, 0) = \delta V(\tau, 0) = 0$ , give  $\delta g_{\tau\tau}(\tau, 0) = \delta g_{\tau z}(\tau, 0) = 0$ . Comparing this to (4.96) gives the further restriction on the generating vector field  $\chi^\mu$

$$\chi_{,\tau}^\tau = \chi^\tau,\tag{4.98}$$

and therefore

$$\chi^\tau = e^\tau, \quad \chi^z = ze^\tau,\tag{4.99}$$

which is exactly the coordinate transformation introduced above (4.89).

Finally we combine (4.96), (4.97) with (4.99). In a stability analysis, as described above, we therefore expect to find the gauge mode

$$\begin{aligned}\delta\phi &= \epsilon e^\tau z \phi_n' \\ \delta\beta &= \epsilon e^\tau z \beta_n' \\ \delta V &= \epsilon e^\tau z \left( \frac{V}{r} \right)_n'.\end{aligned}\tag{4.100}$$

### 4.3.3 Unstable Modes from a Matrix Analysis

The following method was proposed and carried out by J. Thornburg [70]. It uses the full (nonlinear) time evolution equations. As already mentioned, the method has the advantage, to give *all* the unstable modes, in contrast to the shooting and matching method described above, where only those unstable modes can be found, which lie close to the “initial guess”.

Consider Eqs. (2.48), (2.55) and (2.56). As described in Sec. 2.3 it is sufficient to prescribe the matter field  $\phi$  at the initial null cone  $u = u_0$  (or  $\tau = \tau_0$ ). The metric functions on the initial slice then are determined by  $\phi$  via the hypersurface equations (2.55) and (2.56). Eq. (2.48) is then used to evolve the configuration (together with Eqs. (2.55) and (2.56) in order to update the metric functions). Altogether the time evolution maps the field  $\phi(\tau_0, z)$  at the initial slice to a field configuration  $\phi(\tau_0 + \Delta\tau, z)$  at a later slice:

$$\phi(\tau_0 + \Delta\tau, z) = F(\phi(\tau_0, z)), \quad (4.101)$$

where  $F$  is the nonlinear operator representing time evolution. Of course the operator  $F$  depends on the time step  $\Delta\tau$ . Clearly, if the initial data correspond to the CSS solution,  $F$  acts as the identity operator,

$$F(\phi_{CSS}(\tau_0, z)) = \phi_{CSS}(\tau, z). \quad (4.102)$$

In an actual numerical time evolution in (1+1) dimensions any smooth function of  $z$  is represented by it's values at the grid points, i.e. the function  $\phi(\tau_0, z)$  is replaced by the N-dimensional vector  $(\phi_i^0)_{i=1,N}$ , where  $\phi_i^0 = \phi(\tau_0, z^i)$ , and  $N$  is the number of grid points. The numerical time evolution then maps this vector to the corresponding vector at the next time step:

$$\phi_i^1 = F_i(\phi_j^0). \quad (4.103)$$

Consider now a small generic perturbation of the CSS solution,  $\phi_{CSS}(\tau_0, z) + \delta\phi(\tau_0, z)$ . If the time step  $\Delta\tau$  is small enough, this configuration is mapped to another small perturbation of the CSS solution at time  $\tau_0 + \Delta\tau$ . Translating this to the language of a finite grid we have

$$\phi_i^1 = (\phi_{CSS})_i^1 + (\delta\phi)_i^1 = F_i((\phi_{CSS})_j^0 + (\delta\phi)_j^0). \quad (4.104)$$

For a small perturbation this can be linearized to give

$$(\phi_{CSS})_i^1 + (\delta\phi)_i^1 = F_i((\phi_{CSS})_j^0) + \left. \frac{\partial F_i}{\partial \phi_j^0} \right|_{(\phi_{CSS}^0)} (\delta\phi)_j^0 = (\phi_{CSS})_i^0 + \left. \frac{\partial F_i}{\partial \phi_j^0} \right|_{(\phi_{CSS}^0)} (\delta\phi)_j^0. \quad (4.105)$$

So for the perturbation the following linear relation holds

$$(\delta\phi)_i^1 = \left. \frac{\partial F_i}{\partial \phi_j^0} \right|_{(\phi_{CSS}^0)} (\delta\phi)_j^0. \quad (4.106)$$

The Jacobian on the right hand side is a  $N \times N$  matrix, which depends on the size of the time step  $\Delta\tau$ . Therefore it has  $N$  eigenvalues  $\{\tilde{\lambda}_i\}_{i=1,N}$ , which are functions of the time step  $\Delta\tau$ . If the Jacobian is diagonalizable we can switch to a basis such that

$$(\delta\phi)_i^1 = \tilde{\lambda}_i (\delta\phi)_i^0, \quad \text{with} \quad \tilde{\lambda}_i = \tilde{\lambda}_i(\Delta\tau). \quad (4.107)$$

For the quotient of differences we get

$$\frac{\delta\phi_i(\tau_0 + \Delta\tau) - \delta\phi_i(\tau_0)}{\Delta\tau} = \frac{\tilde{\lambda}_i - 1}{\Delta\tau} \delta\phi_i(\tau_0). \quad (4.108)$$

In order that the limit  $\Delta\tau \rightarrow 0$  exists, the denominator on the right hand side has to be proportional to  $\Delta\tau$ . We set

$$\tilde{\lambda}_i - 1 = \lambda_i \Delta\tau, \quad (4.109)$$

$\lambda_i$  being constants.

In the limit  $\Delta\tau \rightarrow 0$  we have

$$\delta\dot{\phi}_i(\tau) = \lambda_i \delta\phi_i(\tau) \quad (4.110)$$

and therefore

$$\delta\phi_i(\tau) = e^{\lambda_i(\tau-\tau_0)} \delta\phi_i(\tau_0). \quad (4.111)$$

This is valid with respect to the eigenbasis of the Jacobian. Transforming back to the original basis we have

$$(\delta\phi_k)_i(\tau) = e^{\lambda_k(\tau-\tau_0)} (\delta\phi_k)_i(\tau_0), \quad (4.112)$$

where  $\delta\phi_k$  denotes the  $k$ -th eigenvector of the Jacobian. The perturbation (4.112) now is of the same form as the modes in Eq. (4.83), with the eigenvalues  $\lambda$  being related to the eigenvalues of the time evolution Jacobian via Eq. (4.109).

The Jacobian was computed using the DICE code (described in Appendix C). As this code uses grid points, that are freely falling along ingoing null geodesics, the evolved field  $\phi$  had to be interpolated to give the appropriate values at constant  $z$ . Technically the Jacobian is computed, by first evolving the CSS solution for one time step, and then perturbing each grid point separately, according to the  $N$  perturbations  $(\delta\phi_k)_i^0 = \epsilon \delta_{ik}$ ,  $k = 1, N$ , with  $\epsilon$  small. Each of these perturbations is evolved again for one time step, so in the end the  $N \times N$  numbers  $F_i(\phi_k)$  are known. The Jacobian results from this by a forward differencing. In order to

compute the eigenvalues and eigenvectors of the matrix a linear algebra package (EISPACK [67]) is used.

Finally we want to point out, that although this method only yields  $N$  modes of the perturbation operator, according to the  $N$  grid points involved, we expect to find *all* the relevant unstable modes. The reason for this is, that we expect the unstable modes to vary on scales that are large compared to the grid spacing.

### 4.3.4 Numerical Results of the Stability Analysis

Before we present our results here, we want to stress two points: First we are interested in the stability of the CSS ground state and the first CSS excitation, because we want to get information on the possible roles they might play in the context of critical phenomena. With respect to this, only the stability for small couplings ( $\eta \lesssim \eta_*(0) \sim 0.69$  for the ground state and  $\eta \lesssim 0.2$  for the first excitation) is of interest.

Second we trust the results of the boundary value problem Sec. 4.3.1. On the other hand, as already mentioned, the numerical scheme of the matrix analysis Sec. 4.3.3 does not show convergence with resolution, and results should be taken with some care. Nevertheless, as we will show below, for  $N = 500$  grid points (and  $\eta$  not too large), the results for the gauge modes and the unstable mode for the first excitation are in very good agreement with the theoretical predictions and the results of the boundary value problem. Therefore – for these couplings – we are inclined to trust the results of the matrix analysis, in particular the number of unstable modes.

Given these caveats, we numerically find that the ground state is stable, whereas the first excitation has one unstable mode (both results for  $\eta$  not too large (See Figs. 4.11 and 4.12)).

Fig. 4.9 compares the gauge modes – obtained via the boundary value problem of Sec. 4.3.1 – of the ground state and first excitation at a coupling  $\eta = 0.1$  to the theoretical predictions  $y_{gauge} = z\phi'_n$ . Note that in this figure and in the following ones the overall scale is chosen arbitrarily.

Fig. 4.10 compares the eigenfunctions of the gauge mode and the unstable mode – obtained via the matrix method of Sec. 4.3.3 – of the first CSS excitation for  $\eta = 0.1$  to the results of the boundary value problem. The agreement is very good.

Figs. 4.11 and 4.12 show the real parts of the first few eigenvalues of the ground-state and first excitation. The agreement of the results of the matrix method and the boundary value problem is good for the groundstate at low couplings and very good for the first excitation.

Finally, note that the inverse eigenvalue of the unstable mode of the first CSS excitation  $1/\lambda_1$  as a function of coupling  $\eta$  is very well approximated by a straight

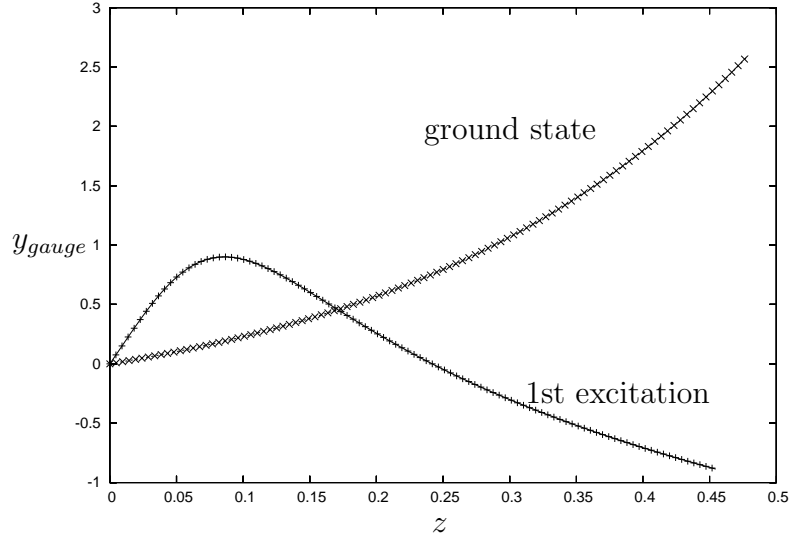


Figure 4.9: The gauge modes for the ground state and the first excitation at a coupling  $\eta = 0.1$ . Plotted are the predicted functions,  $y_{gauge} = z\phi'_n$ , (solid lines), and the corresponding results of the shooting and matching method (“x”, “+”).

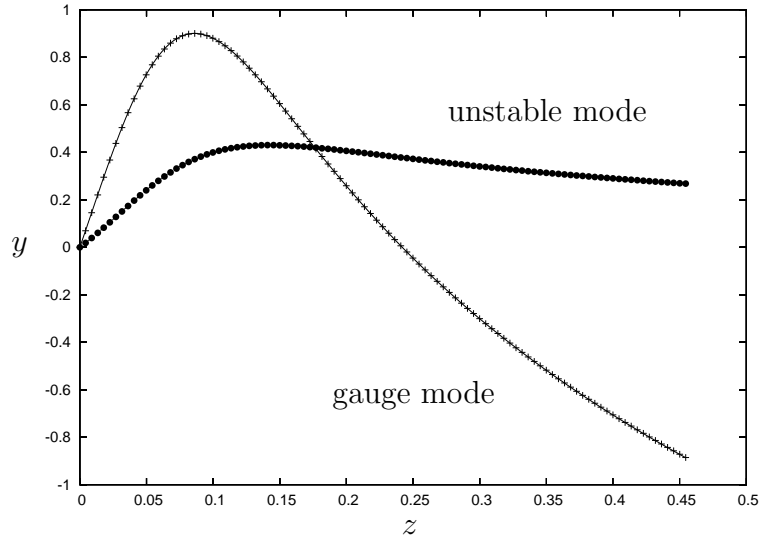


Figure 4.10: The eigenfunctions of the unstable mode ( $\lambda = \lambda_1 = 5.58463$ ) and the gauge mode ( $\lambda = 1$ ) for the first CSS excitation at a coupling  $\eta = 0.1$ . Plotted are the result of a 500 points matrix analysis (dots, only every 5th point is plotted). These are compared to the results from the boundary value problem (lines): the gauge mode is compared to the predicted eigenfunction  $y_{gauge}(z) = z\phi'_1(z)$  and the unstable mode is compared to the result  $y(z)$  of the boundary value problem described in Sec. 4.3.1.

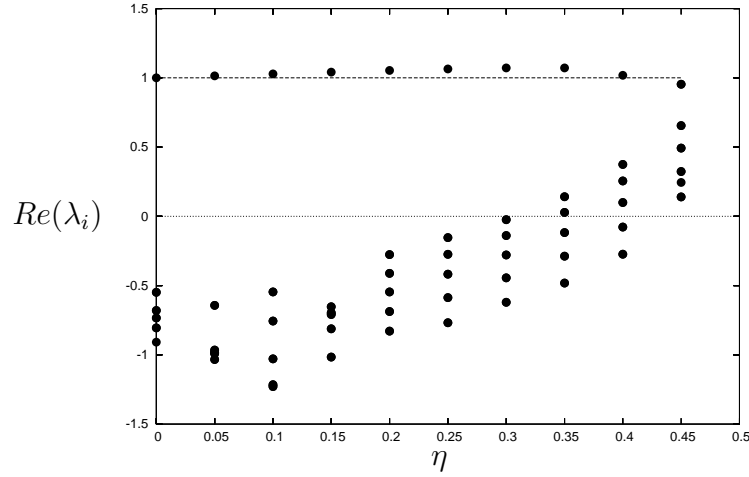


Figure 4.11: Dots represent the real parts of the first few eigenvalues of perturbations of the groundstate as obtained by a matrix analysis with  $N = 500$ . The line  $\lambda = 1$  represents the predicted eigenvalue of the gauge mode. For small  $\eta$  the matrix analysis gives no unstable mode. For bigger  $\eta$  (e.g. at  $\eta = 0.4$ ) the additional positive eigenvalues could not be confirmed by the shooting and matching method.

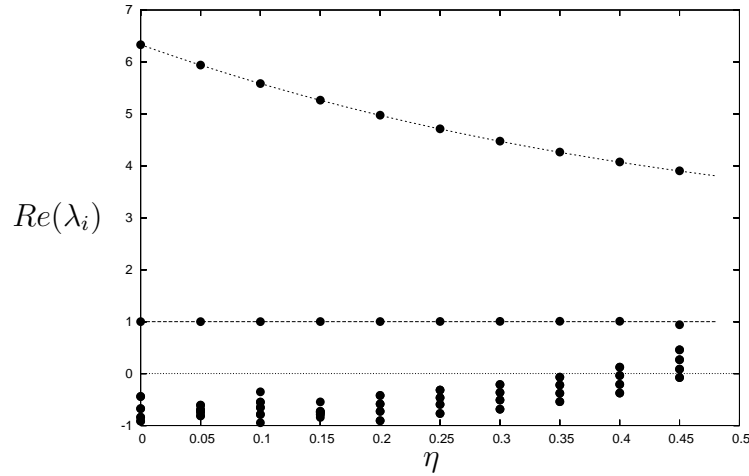


Figure 4.12: The same situation as in Fig. 4.11 for the first CSS excitation. The dashed line starting at  $\eta = 0$  with 6.33 represents the eigenvalue of the unstable mode obtained from the boundary value problem. The agreement of results of the two methods is very good. The matrix analysis gives one unstable mode for  $\eta \leq 0.35$ . The additional positive eigenvalues for larger  $\eta$  (e.g.  $\eta = 0.4$ ) could not be confirmed by the shooting and matching method.

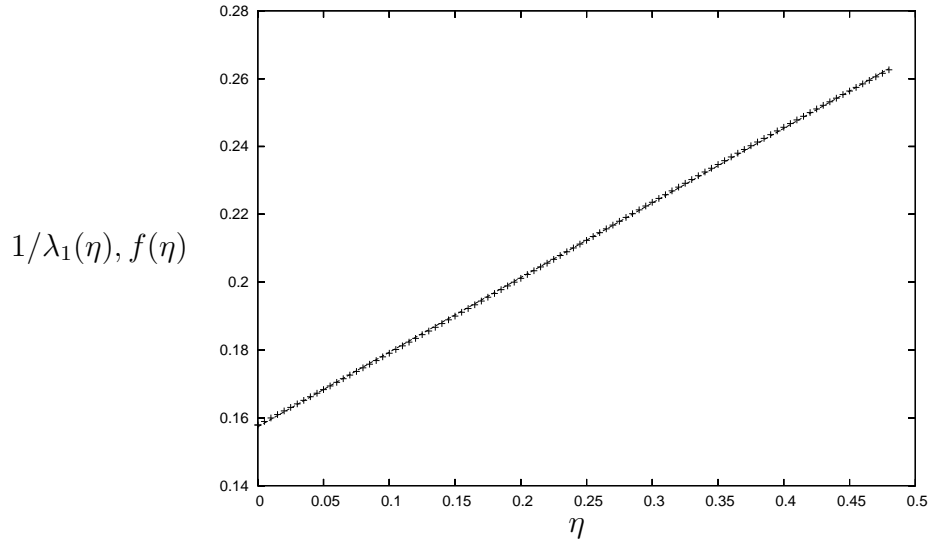


Figure 4.13: Plotted is  $1/\lambda_1$  (dots), where  $\lambda_1$  is the eigenvalue of the unstable mode of the first CSS excitation, obtained by the shooting and matching method of Sec. 4.3.1, as a function of  $\eta$ . This is very well fitted by the straight line  $f(\eta) = 0.21997\eta + 0.15736$  (solid line). See the next figure for the error of this fit.

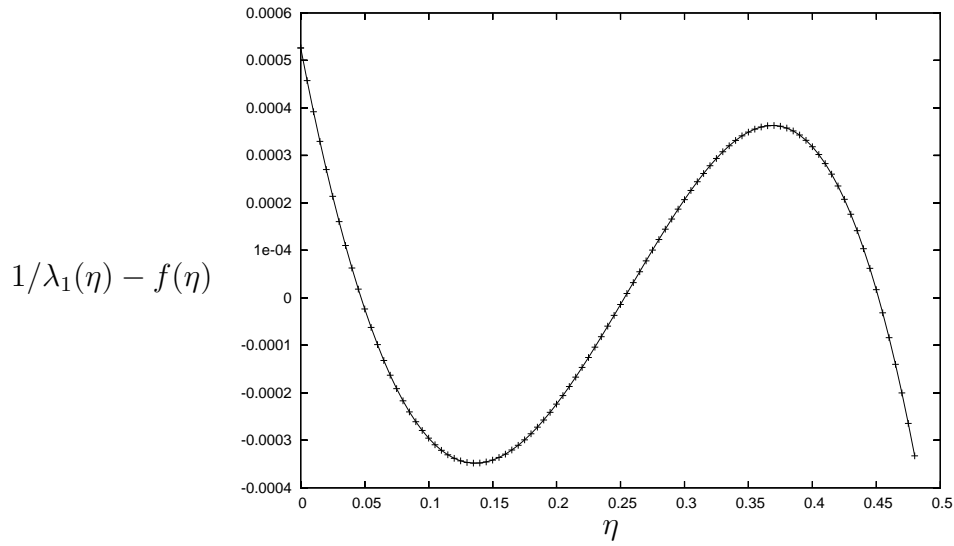


Figure 4.14: The error  $1/\lambda_1(\eta) - f(\eta)$ , where  $f(\eta)$  is the straight line defined in Fig. 4.13.



line (see Figs. 4.13 and 4.14).

## 4.4 Numerical Construction of DSS Solutions

This section deals with the numerical construction of DSS solutions to the self-gravitating nonlinear  $\sigma$  model. Due to the (periodic) time dependence of the metric functions and the field, the numerical construction of DSS solutions is considerably more involved than the corresponding construction of CSS solutions. Concerning self-gravitating matter fields there are essentially two papers (not counting subsequent ones using the same methods) that deal with the problem of constructing time-periodic solutions to a boundary value problem (in space). Seidel and Suen [66] construct solutions to the Einstein-Klein-Gordon system with mass, which are oscillating (periodic in time). Gundlach [35] constructs a DSS solution to the massless Einstein-Klein-Gordon system. Both methods use Fourier series, as suggested by the periodic time dependence, but their “implementations” are different, as will be explained below.

Following Gundlach closely, we present a method, that involves discrete Fourier transform, pseudo spectral methods and the reduction to a boundary value problem for ODEs.

The procedure of construction can be roughly outlined as follows: we are looking for solutions to Eqs. (2.48), (2.55) and (2.56), rewritten in adapted coordinates (4.38), that are regular between origin and past SSH and that are periodic in the adapted time coordinate  $\tau$ . We expand the metric functions as well as the field into Fourier series in time, where the coefficients are functions of the spatial variable  $z$ . Inserting these Fourier series into the equations yields a coupled system of ODEs for the Fourier coefficients. This system has singular points at the origin and the past SSH, so together with the boundary conditions required by regularity we have to solve an ODE boundary value problem for the Fourier coefficients. As the Fourier series consist of infinite many terms and as the problem is nonlinear, one has to truncate the Fourier series at some appropriate maximal frequency. This then yields a boundary value problem for a finite system of ODEs, which again can be solved by the means of a shooting and matching routine.

Seidel, Suen and Gundlach use different methods for explicitly setting up the ODEs. Seidel and Suen truncate the series and plug the truncated series into the equations (see Appendix B). Comparing coefficients yields the desired coupled system of ODEs for the coefficients. The disadvantage of this method is, that these direct expressions quickly get horribly complicated as one allows for more and more coefficients.

Gundlach on the other hand uses so called *pseudo-spectral methods*, that is, he does part of the computations in “real” space and part in Fourier space (see

Appendix B). Basically the variables are the Fourier coefficients, but in order to set up the ODEs, the coefficients are transformed back to real space, there the algebraic manipulations are carried out in order to define the derivatives of the functions, which then in turn are transformed back to Fourier space. This requires a pair of (backward and forward) Fourier transformations at each integration step. Employing a *fast Fourier transform (FFT)* instead of the ordinary discrete Fourier transform (DFT) is essential for reducing computational cost.

#### 4.4.1 The DSS Equations

We start by transforming Eqs. (2.48), (2.55) and (2.56) to the adapted coordinates (4.38) defined in Sec. 4.1.2. This gives

$$\beta' = \frac{\eta}{2} z (\phi')^2 \quad (4.113)$$

$$\left(\frac{V}{r}\right)' = -\frac{1}{z} \left( -e^{2\beta} + 2\eta e^{2\beta} \sin^2(\phi) + \frac{V}{r} \right) \quad (4.114)$$

and

$$\begin{aligned} \phi'' = & \frac{1}{z^2 \left( -\frac{V}{r} + 2z\dot{\zeta} - 2z\dot{\zeta} \right)} \left( -e^{2\beta} \left\{ \sin(2\phi) + z \left( -1 + 2\beta \sin(\phi)^2 \right) \phi' \right\} + \right. \\ & \left. + z \left\{ \left( \frac{V}{r} + 4z\dot{\zeta} - 4\zeta\dot{z} \right) \phi' - 2\zeta \left( \dot{\phi} + z\dot{\phi}' \right) \right\} \right), \end{aligned} \quad (4.115)$$

where  $' \equiv \partial_z$  and  $\dot{\phantom{x}} \equiv \partial_\tau$ . Looking for DSS solutions means that we require  $\beta = \beta(\tau, z)$ ,  $\frac{V}{r} = \frac{V}{r}(\tau, z)$ ,  $\phi = \phi(\tau, z)$ ,  $\zeta = \zeta(\tau)$ , where all the time dependencies being periodic, with some period  $\Delta$ , the determination of which is part of the problem.

Furthermore we fix the coordinate freedom contained in the function  $\zeta$ , by

$$\dot{\zeta}(\tau) - \zeta(\tau) + \frac{1}{2} \frac{V}{r}(\tau, 1) = 0, \quad (4.116)$$

which makes the hypersurface  $z = 1$  null, as explained in Sec. 4.1.2. Assuming that  $\frac{V}{r}(\tau, 1)$  is given, Eq. (4.116) is a first order ODE for  $\zeta(\tau)$ , with periodic boundary conditions.

As we will have to deal with an equation similar to Eq. (4.116) again, we have a short look at the more general equation

$$\dot{f}(\tau) + g(\tau)f(\tau) + h(\tau) = 0, \quad (4.117)$$

where  $g(\tau)$  and  $h(\tau)$  are given functions, periodic in  $\tau$  with period  $\Delta$ , and  $f(\tau)$  is the unknown, which is required to be periodic too with the same period.

The general solution to Eq. (4.117) is given by

$$f(\tau) = e^{-G(\tau)} \left( - \int_{\tau_0}^{\tau} e^{G(\bar{\tau})} h(\bar{\tau}) d\bar{\tau} + c \right), \quad G(\tau) = \int_{\tau_0}^{\tau} g(\bar{\tau}) d\bar{\tau}, \quad (4.118)$$

where the function  $G(\tau)$  as defined above was introduced for abbreviation. The constant  $c$  entering the formula now has to be determined from the required periodicity of  $f(\tau)$ . The behavior of  $G(\tau)$  under a shift of  $\Delta$  is

$$G(\tau + \Delta) = G(\tau_0 + \Delta) + G(\tau), \quad (4.119)$$

so

$$f(\tau + \Delta) = f(\tau) - c e^{-G(\tau)} (1 - e^{-G(\tau_0 + \Delta)}) - e^{-G(\tau)} e^{-G(\tau_0 + \Delta)} \int_{\tau_0}^{\tau_0 + \Delta} e^{G(\bar{\tau})} h(\bar{\tau}) d\bar{\tau}. \quad (4.120)$$

And so, if  $G(\tau_0 + \Delta) \neq 0$ , the constant is determined to be

$$c = \frac{1}{1 - e^{G(\tau_0 + \Delta)}} \int_{\tau_0}^{\tau_0 + \Delta} e^{G(\bar{\tau})} h(\bar{\tau}) d\bar{\tau}, \quad (4.121)$$

and therefore the unique periodic solution to Eq. (4.117) is given by

$$f(\tau) = e^{-G(\tau)} \left( - \int_{\tau_0}^{\tau} e^{G(\bar{\tau})} h(\bar{\tau}) d\bar{\tau} + \frac{1}{1 - e^{G(\tau_0 + \Delta)}} \int_{\tau_0}^{\tau_0 + \Delta} e^{G(\bar{\tau})} h(\bar{\tau}) d\bar{\tau} \right). \quad (4.122)$$

In case  $g(\tau)$  has no zero frequency, i.e.  $G(\tau_0 + \Delta) = 0$ , there is no periodic solution to Eq. (4.117) unless the last integral in (4.120) vanishes as well, in which case there is a one-parameter family of periodic solutions to Eq. (4.117) of the form (4.118).

According to this the solution to Eq. (4.116) can be given in closed form:

$$\zeta(\tau) = \frac{e^{\tau}}{2} \left( - \int_{\tau_0}^{\tau} e^{-\bar{\tau}} \frac{V}{r}(\bar{\tau}, 1) d\bar{\tau} + \frac{1}{1 - e^{-\Delta}} \int_{\tau_0}^{\tau_0 + \Delta} e^{-\bar{\tau}} \frac{V}{r}(\bar{\tau}, 1) d\bar{\tau} \right). \quad (4.123)$$

There is an alternative way to compute  $\zeta$ , namely as Eq. (4.116) is linear in all periodic functions, the Fourier coefficients of  $\zeta$  can be computed directly from the Fourier coefficients of  $\frac{V}{r}(\tau, 1)$ . We will give details on this in Sec. 4.4.4.

Finally we rewrite Eqs. (4.113) – (4.115), using the logarithmic coordinate  $y = \ln z$  instead of  $z$ . This is useful for numerical purposes, as the main variations in the solutions occur close to the origin. We have

$$\beta' = \frac{\eta}{2} (\phi')^2 \quad (4.124)$$

$$\left(\frac{V}{r}\right)' = - \left( -e^{2\beta} + 2\eta e^{2\beta} \sin^2(\phi) + \frac{V}{r} \right) \quad (4.125)$$

and

$$\begin{aligned} \phi'' &= \frac{1}{\left(-\frac{V}{r} + 2e^y \dot{\zeta} - 2e^y \dot{\zeta}\right)} \left( -e^{2\beta} \left\{ \sin(2\phi) + (-1 + 2\eta \sin(\phi)^2) \phi' \right\} + \right. \\ &\quad \left. + \left\{ (2e^y \dot{\zeta} - 2\zeta e^y) \phi' - 2\zeta e^y (\dot{\phi} + \dot{\phi}') \right\} \right), \end{aligned} \quad (4.126)$$

where  $'$  now denotes  $\partial_y$  and  $y = \ln(z)$ .

Note that  $\tau$  does not enter Eqs. (4.113) – (4.115), ((4.124)–(4.126) respectively) explicitly. Therefore, given a solution, abbreviated by  $Z(\tau, z)$ , all expressions resulting from this by a constant shift in  $\tau$ ,  $Z(\tau + \text{const}, z)$  are solutions to the system as well.

#### 4.4.2 Regularity at Origin and Past SSH

Regularity at the origin  $z = 0$ ,  $y = -\infty$  is as usual given by

$$\beta(\tau, z = 0) = 0, \quad \frac{V}{r}(\tau, z = 0) = 1, \quad \phi(\tau, z = 0) = 0, \quad (4.127)$$

and  $\phi'(\tau, z = 0)$  is a free (periodic) function of  $\tau$ . Using the logarithmic coordinate  $y = \ln(z)$ , we start our numerical integration at some finite  $y_0$ . Near the origin  $z = 0$  (i.e.  $y \rightarrow -\infty$ ) the functions behave as

$$\begin{aligned} \beta(\tau, y) &= O(e^{2y}) \\ \frac{V}{r}(\tau, y) &= O(e^{2y}) \\ \phi(\tau, y) &= \phi_1(\tau) e^y + O(e^{2y}) \\ \phi'(\tau, y) &= \phi_1(\tau) e^y + O(e^{2y}), \end{aligned} \quad (4.128)$$

where  $\phi_1(\tau) = \partial_z \phi(\tau, z = 0)$ .

At the past SSH  $z = 1$  (i.e.  $y = 0$ ) the denominator in (4.126) vanishes. Regularity therefore enforces the nominator to vanish as well, that is

$$\begin{aligned} 0 &= -e^{2\beta_H} \left\{ \sin(2\phi_H) + (-1 + 2\eta \sin(\phi_H)^2) \phi'_H \right\} + \\ &\quad + \left\{ \left( \left(\frac{V}{r}\right)_H + 4\dot{\zeta} - 4\zeta \right) \phi'_H - 2\zeta (\dot{\phi}_H + \dot{\phi}'_H) \right\}, \end{aligned} \quad (4.129)$$

where the expressions with subscript  $H$  are periodic functions of  $\tau$ . Suppose now, we are given the functions  $\beta_H, (\frac{V}{r})_H$  and  $\phi_H$ , then Eq. (4.129) is an ODE in time  $\tau$  for  $\phi'_H$ . In fact, if we abbreviate

$$g = \frac{1}{2\zeta} \left( \left( \frac{V}{r} \right)_H + e^{2\beta_H} (-1 + 2\eta \sin^2 \phi_H) \right) \quad (4.130)$$

$$h = \frac{1}{2\zeta} e^{2\beta_H} \sin(2\phi_H) + \dot{\phi}_H, \quad (4.131)$$

and use Eq. (4.116) to replace  $\dot{\zeta}$ , then Eq. (4.129) is of the same form as Eq. (4.117), described in the last section, and has the unique periodic solution (4.122).

### 4.4.3 Additional Symmetry

From critical searches (see Chap. 5 for details), we know, that the critical solution for large couplings, which is DSS, not only is periodic with period  $\Delta$ , but has an additional symmetry, namely

$$\begin{aligned} \beta(\tau + \Delta/2, z) &= \beta(\tau, z), \\ \frac{V}{r}(\tau + \Delta/2, z) &= \frac{V}{r}(\tau, z), \\ \zeta(\tau + \Delta/2, z) &= \zeta(\tau, z), \\ \phi(\tau + \Delta/2, z) &= -\phi(\tau, z), \end{aligned} \quad (4.132)$$

which means that the metric functions as well as  $\zeta$  consist only of even frequencies<sup>5</sup>, whereas the field and its derivatives contain only odd frequencies. As we are interested in the direct construction of the DSS solution, which is the critical solution in a certain range of coupling constants, we impose this additional symmetry on the solution by the means of its Fourier coefficients.

### 4.4.4 Numerical Construction of DSS solutions via an ODE boundary value problem

According to the required periodicity in  $\tau$  of the solution we expand the metric functions,  $\zeta$ , and the field into Fourier series. The truncation of these series is performed according to the discrete Fourier transform described in detail in Appendix B. We denote the number of “collocation points” in “ $\tau$  space” by  $N$ , assuming, that it is an integer multiple of 4. So the equally spaced points in  $\tau$  space are given by  $\tau_k = k\Delta/N$ .

In principle these  $N$  points give rise to  $N$  Fourier coefficients, but the additional symmetry introduced in the last section, Sec. 4.4.3 reduces this number by a

---

<sup>5</sup>even multiples of  $1/\Delta$ .

factor of 2. So each function consists of  $M = N/2$  Fourier coefficients, where we assume, that  $M$  is even. The expansions then are given by

$$\begin{aligned}
\beta_N(\tau_k, z) &= \beta_0(z) + \sum_{l=1}^{M/2-1} (\beta \cos)_{2l}(z) \cos\left(\frac{4\pi lk}{N}\right) + \sum_{l=1}^{M/2-1} (\beta \sin)_{2l}(z) \sin\left(\frac{4\pi lk}{N}\right) + \\
&\quad + (\beta \cos)_M(z) \cos(\pi k) \\
\left(\frac{V}{r}\right)_N(\tau_k, z) &= V_0(z) + \sum_{l=1}^{M/2-1} (V \cos)_{2l}(z) \cos\left(\frac{4\pi lk}{N}\right) + \sum_{l=1}^{M/2-1} (V \sin)_{2l}(z) \sin\left(\frac{4\pi lk}{N}\right) + \\
&\quad + (V \cos)_M(z) \cos(\pi k) \\
\zeta_N(\tau_k, z) &= \zeta_0(z) + \sum_{l=1}^{M/2-1} (\zeta \cos)_{2l}(z) \cos\left(\frac{4\pi lk}{N}\right) + \sum_{l=1}^{M/2-1} (\zeta \sin)_{2l}(z) \sin\left(\frac{4\pi lk}{N}\right) + \\
&\quad + (\zeta \cos)_M(z) \cos(\pi k)
\end{aligned} \tag{4.133}$$

and

$$\phi_N(\tau_k, z) = \sum_{l=1}^{M/2} (\phi \cos)_{2l-1}(z) \cos\left(\frac{2\pi(2l-1)k}{N}\right) + \sum_{l=1}^{M/2} (\phi \sin)_{2l-1}(z) \sin\left(\frac{2\pi(2l-1)k}{N}\right), \tag{4.134}$$

and the expansion for  $\phi'$  follows directly from the one of  $\phi$ . The coefficients for a function with only even frequencies are given by e.g.

$$\beta_0 = \frac{1}{N} \sum_{k=0}^{N-1} \beta_N(\tau_k) \tag{4.135}$$

$$(\beta \cos)_{2l} = \frac{2}{N} \sum_{k=0}^{N-1} \beta_N(\tau_k) \cos\left(\frac{4\pi lk}{N}\right) \quad l = 1, \dots, M/2 - 1 \tag{4.136}$$

$$(\beta \sin)_{2l} = \frac{2}{N} \sum_{k=0}^{N-1} \beta_N(\tau_k) \sin\left(\frac{4\pi lk}{N}\right) \quad l = 1, \dots, M/2 - 1 \tag{4.137}$$

$$(\beta \cos)_M = \frac{1}{N} \sum_{k=0}^{N-1} \beta_N(\tau_k) \cos(\pi k), \tag{4.138}$$

and for a function with odd frequencies by

$$(\phi \cos)_{2l-1} = \frac{2}{N} \sum_{k=0}^{N-1} \phi_N(\tau_k) \cos\left(\frac{2\pi(2l-1)k}{N}\right) \quad l = 1, \dots, M/2 \tag{4.139}$$

$$(\phi \sin)_{2l-1} = \frac{2}{N} \sum_{k=0}^{N-1} \phi_N(\tau_k) \sin\left(\frac{2\pi(2l-1)k}{N}\right) \quad l = 1, \dots, M/2. \tag{4.140}$$

Our variables that have to solve the coupled system of ODEs now are the  $4M$  Fourier coefficients of  $\beta, \frac{V}{r}, \phi$  and  $\phi'$ . Note that  $\zeta$  is not part of the system, as it can be computed whenever  $\frac{V}{r}$  is given at the horizon. The boundary conditions consist of boundary conditions for the coefficients of  $\beta, \frac{V}{r}$  and  $\phi$  at the origin, and on the other hand of the conditions on the coefficients of  $\phi'$  at the horizon, so in total we have  $4M$  boundary conditions imposed on our system of  $4M$  first order ODEs.

The free (shooting) parameters consist of the coefficients of  $\beta, \frac{V}{r}$  and  $\phi$  at the horizon, which make a total of  $3M$ . Furthermore the  $M$  coefficients of  $\phi_1(\tau) = \partial_z \phi(\tau, z=0)$  are free parameters. Nevertheless, as noted in Sec. 4.4.1 the equations (4.113)–(4.115) are translation invariant in  $\tau$ . A constant shift in  $\tau$  therefore transforms a given solution again to a solution. On the other hand, a constant shift in  $\tau$  just changes the Fourier coefficients in a well defined way. We can therefore chose one coefficient of  $\phi_1(\tau)$  arbitrarily, so we are left with only  $M - 1$  shooting parameters at the origin. Finally there is the period  $\Delta$ , which is the last free parameter. So in total we have again  $4M$  shooting parameters.

In order to solve the boundary value problem for the ODEs again a shooting and matching method is used (see Appendix A). We describe now in detail, how the system of ODEs is “set up” numerically. The first step consists of providing good initial guesses for the shooting parameters. Given these guesses, Eq. (4.116) is solved for  $\zeta$ . As this equation is linear in the periodic functions, it can be solved directly in Fourier space. Applying the rules for differentiation in Fourier space, as given in Appendix B to  $\zeta$  and comparing coefficients, Eq. (4.116) has the following solution in Fourier space

$$\zeta_0 = \frac{1}{2} V_0|_{y=0} \quad (4.141)$$

$$(\zeta \cos)_{2l} = \frac{1}{2(1 + (4\pi l/\Delta)^2)} \left( (V \cos)_{2l}|_{y=0} + \frac{4\pi l}{\Delta} (V \sin)_{2l}|_{y=0} \right) \quad (4.142)$$

$$(\zeta \sin)_{2l} = \frac{1}{2(1 + (4\pi l/\Delta)^2)} \left( -\frac{4\pi l}{\Delta} (V \cos)_{2l}|_{y=0} + (V \sin)_{2l}|_{y=0} \right) \quad (4.143)$$

$$(\zeta \cos)_{N/2} = \frac{1}{2} (V \cos)_{N/2}|_{y=0}. \quad (4.144)$$

In the next step, the coefficients of  $\phi'_H$  have to be computed from the coefficients of  $\zeta$  and the other variables at the horizon. To do this, the variables are transformed back to real space. There formula (4.122) is used to obtain  $\phi'_H$  as a function of  $\tau$ . Transformation to Fourier space then yields the desired coefficients. Note, that each time such a “backward-forward transformation pair” is used, the number of coefficients is first increased by some factor and after the operations in real space have been performed and the forward transformation has been applied, the number of coefficients is reduced to the original size again. This is a way to reduce aliasing errors, as explained in more detail in App. B.

After these first steps are completed, all the variables, i.e. the Fourier coefficients, are known at the boundaries, the coefficients of  $\zeta$  are determined and the period  $\Delta$  has some definite value. In order to integrate the ODEs, the spatial derivatives of the Fourier coefficients have to be determined. This is achieved again by a transformation to real space. There the right hand sides of Eqs. (4.124) – (4.126) are evaluated, and a transformation back to Fourier space yields the desired derivatives of the coefficients. Again for de-aliasing the number of coefficients is first increased and after all the operations reduced again. These operations have to be carried out at each integration step, which is determined internally by the NAG routine’s integrator. This huge amount of Fourier transformations for a single integration to the matching point, necessitates the use of the fast Fourier transform.

The shooting and matching routine d02agf again was taken from the NAG library ([60]). We mention one technical detail, concerning the magnitude of the variables. As the solution is expected to be smooth, the “higher” Fourier coefficients should decrease exponentially in magnitude. As the NAG routine uses some mixture of absolute and relative error to determine the local error of the solution, it is necessary to rescale the variables to approximate unity.

As the shooting and matching method needs a good initial guess, we use the results of a “dice-critical-search”. (For details on the setup of a critical search and on the following see Chap. 5). As our initial guess we take the critical solution at  $\eta = 100$ , which is clearly a DSS solution. Since these data are given in terms of Bondi coordinates we have to switch to adapted coordinates. We compute  $u^*$  and the initial guess for the echoing period  $\Delta$  from  $\max(2m/r)$ . The past self-similarity horizon theoretically is determined as the backwards light cone of the culmination point. Another way to determine the SSH is to look for the ingoing null geodesic, along which the metric functions  $\beta$  and  $\frac{V}{r}$  as well as the field  $\phi$  are periodic functions of  $\tau$ . This gives us the initial guesses for the shooting parameters at the horizon. From  $\frac{V}{r}$  at the horizon, we compute  $\zeta$  and finally  $\partial_r \phi(\tau, r = 0)$  can be converted into  $\phi_1(\tau)$ , as the relation between Bondi coordinates and adapted coordinates is already fixed.

We start at  $\eta = 100$  with  $N = 16$ , and follow the solution down to smaller values of  $\eta$ . As will be reported in the next section, the echoing period  $\Delta$  increases “sharply” for  $\eta$  below 0.5. This increase of the period will necessitate a larger and larger number of coefficients.

Given a solution obtained with a certain number of Fourier coefficients  $M$ , we can double the number of coefficients with the second half set to zero. This way we obtain a reasonable initial guess for the problem with  $2M$  coefficients.



## 4.4.5 Numerical Results

Applying the method described in the last section, Sec. 4.4.4, we find good numerical evidence, that the system Eqs. (4.124) – (4.126) admits a discretely self similar solution for  $100 > \eta \gtrsim 0.17$ . The smallest value of  $\eta$ , where we constructed a DSS solution, was  $\eta = 0.17262$ . At this coupling constant already a large number of coefficients is necessary. Lowering  $\eta$  further would require at least  $N = 256$ , i.e. 128 Fourier coefficients per dependent variable. With this number of coefficients – in addition for de-aliasing the number of coefficients was increased and decreased by a factor of 8 – a single Newton iteration on an Alpha (ev6 processor) already takes several days.

We find the following behavior: Fig. 4.15 shows that below  $\eta \sim 0.3$  the period  $\Delta(\eta)$  rises sharply with decreasing  $\eta$ . In Sec. 4.5.1 we will give an argument that we expect  $\Delta(\eta)$  to behave like  $-a \ln(\eta - \eta_C) + b$  for  $\eta$  close to a critical coupling constant  $\eta_C$ . Fig. 4.16 shows a fit of  $\Delta(\eta)$  against this function for  $0.1726 \leq \eta \leq 0.195$ . According to this fit the period  $\Delta(\eta)$  would blow up at  $\eta \simeq 0.17$ .

The rise in  $\Delta(\eta)$  also means, that more and more coefficients are needed in order to represent the solution to a given accuracy (see Sec. 4.4.6). Figs. 4.17 and 4.18 illustrate this fact. Fig. 4.17 shows that at a fixed coupling the coefficients decay exponentially with the coefficient number. Nevertheless the slope of the decay decreases with decreasing coupling. Fig. 4.18 shows the coefficients of the field  $\phi$  as functions of the coupling  $\eta$ . With decreasing  $\eta$  the coefficients grow.

## 4.4.6 Convergence with the Number of Fourier Coefficients

As a test for accuracy, we can use the “supplementary” combination of the Einstein equations, Eq. (2.57), which for an exact solution should evaluate to zero. Transformation to self-similar coordinates and multiplication by  $e^{-\tau}\zeta(\tau)$  yields

$$\begin{aligned}
0 = & 2\dot{\beta}\frac{V}{r}\zeta - \frac{\dot{V}}{r}\zeta - (\zeta - \dot{\zeta})\left[e^{2\beta} - \frac{V}{r} - 2\eta e^{2\beta}\sin^2(\phi) + \eta\frac{V}{r}(\phi')^2 - \right. \\
& \left. - 4\eta e^y\zeta\dot{\phi}\phi' - 2\eta e^y(\zeta - \dot{\zeta})(\phi')^2\right] + 2e^y\eta\dot{\phi}^2\zeta^2 - 2\eta\frac{V}{r}\zeta\dot{\phi}\phi',
\end{aligned}
\tag{4.145}$$

where  $' = \partial_y$ .

To compute the right hand side of (4.145), the Fourier coefficients of the numerically computed solution and their derivatives with respect to  $\tau$  are taken, and (4.145) is evaluated in  $\tau$  space. A Fourier transformation yields the coefficients of the expression. Again, in order to diminish aliasing errors, the coefficients

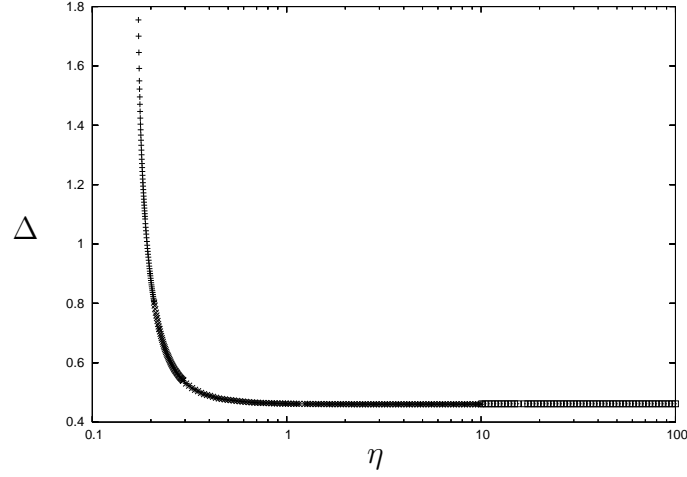


Figure 4.15: The period  $\Delta$  of the DSS solution as a function of the coupling constant  $\eta$ . The number of coefficients used to produce the results of this figure were:  $M = 8$  ( $N = 16$ ) for  $10 < \eta < 100$ ,  $M = 16$  ( $N = 64$ ) for  $0.2933 < \eta < 10$ ,  $M = 32$  ( $N = 64$ ) for  $0.2079 < \eta < 0.2933$  and  $M = 64$  ( $N = 128$ ) for  $0.1726 < \eta < 0.2079$ .

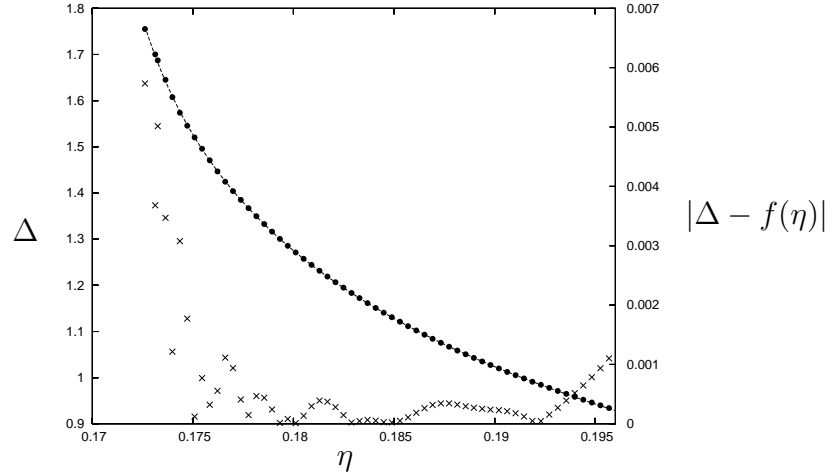


Figure 4.16: “+” represent the period  $\Delta$  of the DSS solution in the region of smallest  $\eta$ , where we constructed the solutions. All the solutions are obtained with 64 coefficients ( $N = 128$ ). In the region  $0.1726 \leq \eta \leq 0.195$  these data were fitted against the function  $f(\eta) = -a \ln(\eta - \eta_C) + b$ . The fit determines the critical coupling to be  $\eta_C \simeq 0.17$ , and the constant  $a = 0.36278$ . The fitted function  $f(\eta)$  is plotted as dashed line. On the right axis the error is plotted. Presumably due to an insufficient number of coefficients the error increases towards the lower end of the interval.

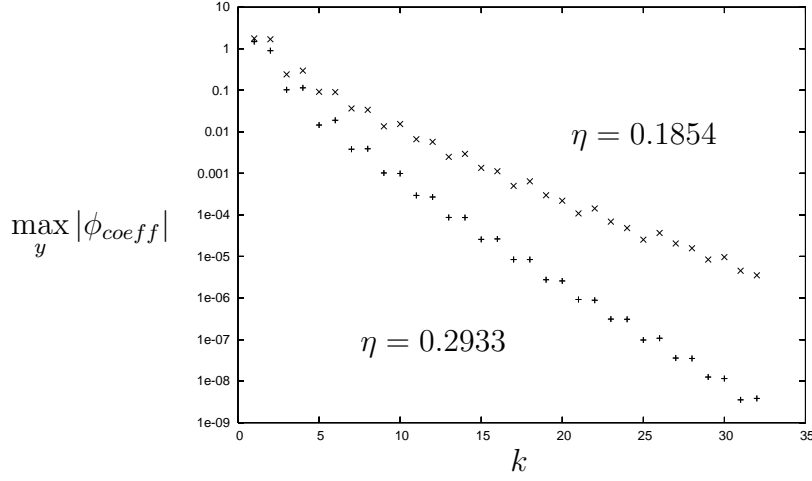


Figure 4.17: This figure illustrates the exponential fall-off of the Fourier coefficients. Plotted is the maximum over  $y = \ln(z)$  of the Fourier coefficients of  $\phi$  versus the coefficient number  $k$  for the two coupling constants  $\eta = 0.2933$  and  $\eta = 0.1854$ . The solutions were computed using  $M = 32$  Fourier coefficients. For both couplings the magnitude of the coefficients decreases exponentially. However, the slope of this decrease is steeper for larger couplings.

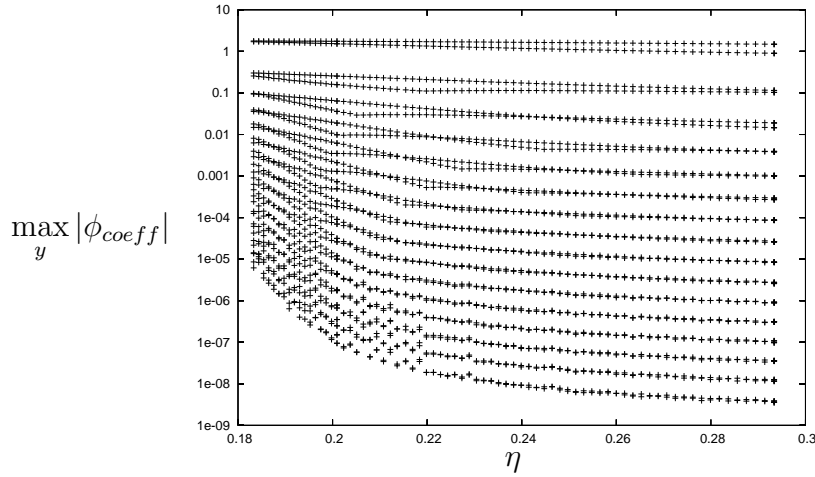


Figure 4.18: The magnitude of the Fourier coefficients as a function of the coupling constant  $\eta$ . All solutions were computed using  $M = 32$  Fourier coefficients. Plotted is again the maximum over the spatial variable  $y = \ln(z)$  of the coefficients of  $\phi$ . See also Fig. 4.25 for a comparison of errors at the lower and upper end of the  $\eta$  interval shown in this figure.

are increased before the first transformation and decreased again after the back transformation.

Figs. 4.19 – 4.24 show this error for the two couplings  $\eta = 0.2933$  and  $\eta = 0.1726$ . At each coupling the solutions computed with a given number of coefficients are compared to those, obtained by using twice this number. One can see, that doubling the number of coefficients shrinks the error by several orders of magnitude. Furthermore at  $\eta = 0.1726$  a larger number of coefficients is needed in order to keep the error at the same magnitude as for higher couplings. Fig. 4.25 shows that keeping the number of Fourier coefficients fixed, the error increases with decreasing  $\eta$ .

#### 4.4.7 Stability of the DSS Solution

The stability of DSS solutions might be analyzed in a similar way as the stability properties of CSS solutions. Denoting the metric functions and the field by  $Z(\tau, z)$  we write the perturbed DSS solution as

$$Z(\tau, z) = \tilde{Z}_{DSS}(\tau, z) + \delta Z(\tau, z), \quad (4.146)$$

where  $\tilde{Z}_{DSS}(\tau, z)$  is the DSS solution which is periodic in  $\tau$ . The equations are then linearized in the perturbations  $\delta Z$ . The main difference to the corresponding problem for CSS solutions is, that the coefficients are not independent of time, but depend on time  $\tau$  in a periodic way. Therefore one sets

$$\delta Z(\tau, z) = e^{\lambda\tau} \delta\tilde{Z}(\tau, z), \quad (4.147)$$

where  $\delta\tilde{Z}(\tau, z)$  is periodic in  $\tau$  with the period  $\Delta$  of the DSS solution. Inserting this ansatz into the linearized equations again yields a time-periodic boundary value problem (the boundary conditions originating from regularity at the origin and the past SSH). This problem can be solved in the same way as above. Due to lack of time we had to postpone these computations.

Instead J. Thornburg adapted the “matrix analysis” (Sec. 4.3.3) to perturbations of DSS solutions. The method works as described in Sec. 4.3.3 with the only difference, that one has to evolve the (slightly perturbed) DSS solution for a whole period (or alternatively due to the additional symmetry for half a period) instead of integrating only for one time step. The reason for this is, that the perturbations depend not only exponentially on time  $\tau$  but also periodically, as can be seen from (4.147). In order to extract the eigenvalues  $\lambda$ , one has to make sure, that the unknown function  $\delta\tilde{Z}$  drops out of the problem, which is the case, when slices are compared, that are half a period apart.

We mention, that again we expect gauge modes to be detected by this method. As for CSS perturbations, there is one gauge mode with  $\lambda = 1$ . But now due to

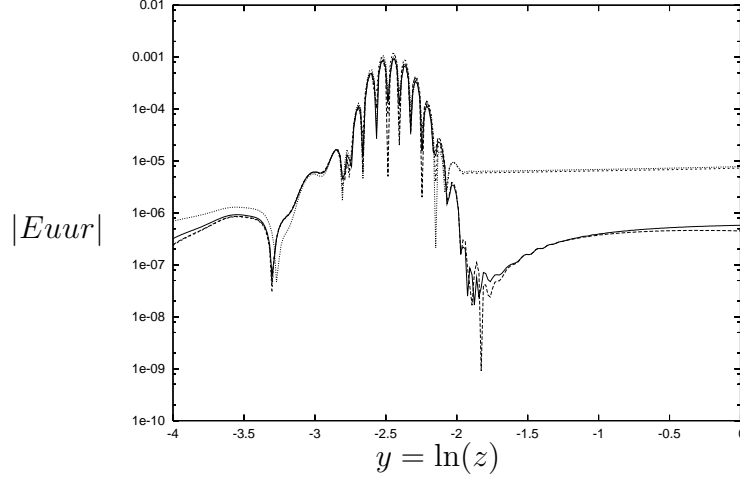


Figure 4.19: The error of the subsidiary Einstein equation (4.145) for  $\eta = 0.29336$ . The solution was obtained with  $N = 32$ . Plotted is the absolute value of the expression (4.145) as a function of the spatial variable  $y$  at the time steps  $\tau_i = i\Delta/N$  for  $i = 0, 4, 8, 12$ , thereby spanning almost half the period. The echoing period was computed to be  $\Delta = 0.5403$ .

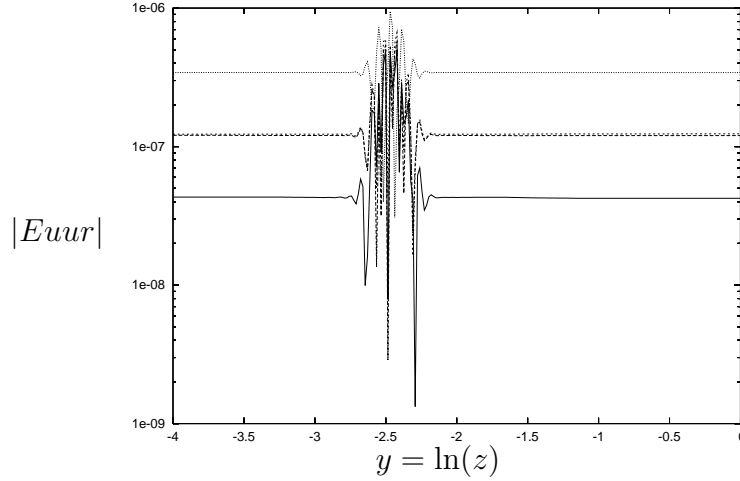


Figure 4.20: The same situation as in Fig. 4.19, where this time the solution was computed using  $N = 64$ . Plotted is the absolute value of the expression (4.145) as a function of the spatial variable  $y$  at the time steps  $\tau_i = i\Delta/N$  for  $i = 0, 8, 16, 24$ , i.e. at (approximately) the same time steps as in Fig. 4.19. The period computed with  $N = 64$  is  $\Delta = 0.5399$ . From these figures it is clear that the error is reduced by several orders of magnitude, when increasing the number of Fourier coefficients.

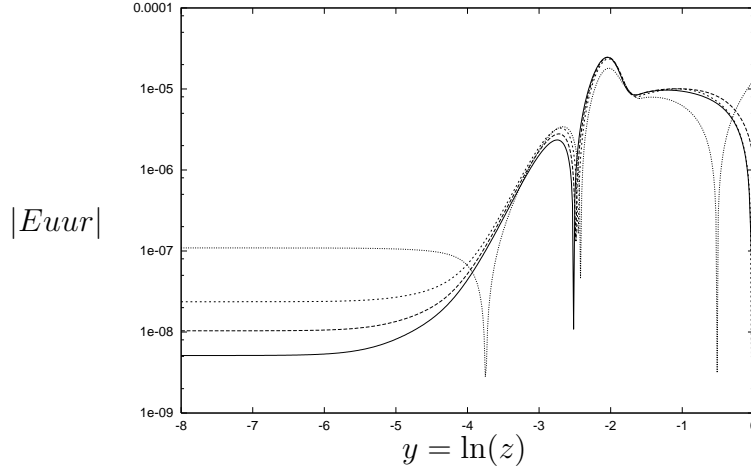


Figure 4.21: The error of the subsidiary Einstein equation (4.145) for  $\eta = 0.1726$ . The solution was obtained with  $N = 128$ . Plotted is the absolute value of expression (4.145) as a function of the spatial variable  $y$  at the time steps  $\tau_i = i\Delta/N$  for  $i = 0, 16, 32, 48$ . The computed value of the period is  $\Delta = 1.7551$ .

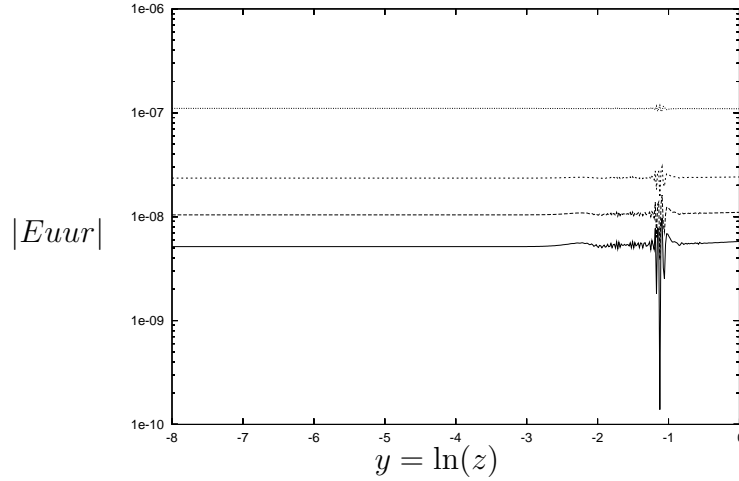


Figure 4.22: The same situation as in Fig. 4.21, where this time the solution was computed using  $N = 256$ . Plotted is the absolute value of expression (4.145) as a function of the spatial variable  $y$  at the time steps  $\tau_i = i\Delta/N$  for  $i = 0, 32, 64, 96$ . With this number of coefficients the period was computed to be  $\Delta = 1.7521$ . Again the error is reduced by several magnitudes, by doubling the number of Fourier coefficients. Note that at this small coupling constant ( $\eta = 0.1726$ ) more Fourier coefficients are needed to obtain a similar accuracy than in Figs. 4.19 and 4.20 for  $\eta = 0.2933$ .

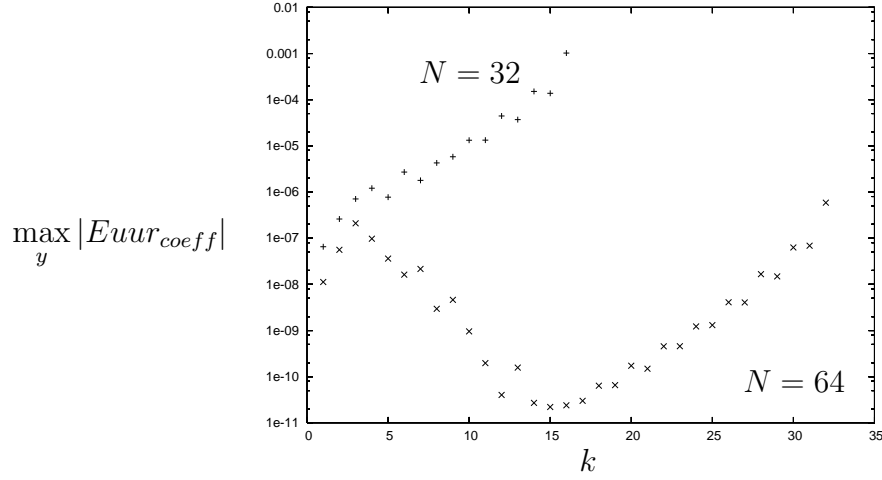


Figure 4.23: For  $\eta = 0.29336$  the Fourier coefficients of the expression (4.145) are compared for solutions obtained with  $N = 32$  (denoted by “+”) and  $N = 64$  (denoted by “x”). Shown is the maximum over the spatial coordinate  $y = \ln(z)$  of the absolute value of the Fourier coefficients plotted against the coefficient number.

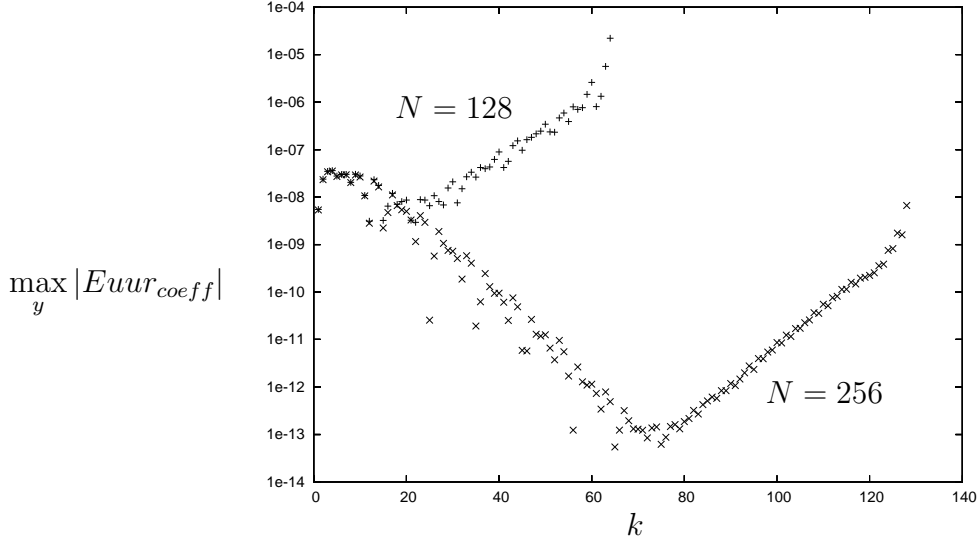


Figure 4.24: For  $\eta = 0.17262$  the Fourier coefficients of the expression (4.145) are compared for solutions obtained with  $N = 128$  (denoted by “+”) and  $N = 256$  (denoted by “x”). Shown is the maximum over the spatial coordinate  $y = \ln(z)$  of the absolute value of the Fourier coefficients plotted against the coefficient number.

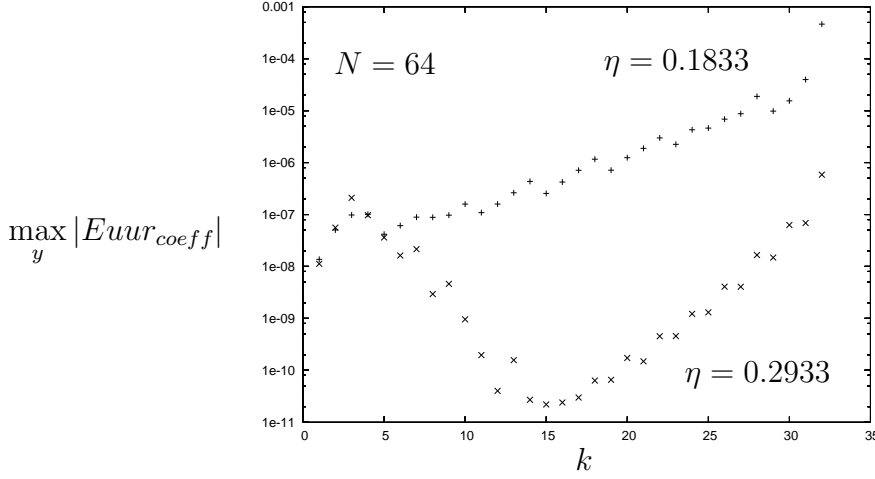


Figure 4.25: A comparison of the error for a fixed number of coefficients ( $M = 32, N = 64$ ) for two different values of the coupling constant  $\eta$ . Plotted is the maximum over  $y$  of the Fourier coefficients of the expression (4.145) against the coefficient number. Compare these errors to Fig. 4.18, where the magnitude of the coefficients of the variable  $\phi$  are shown. As the latter increase relative to the first coefficients, the solution obtained with a fixed number of coefficients gets less accurate.

the translation invariance in  $\tau$  of the DSS equations, an additional mode<sup>6</sup> with  $\lambda = 0$  should show up, with the eigenfunction being of the form

$$\delta \tilde{Z}(\tau, z) = \partial_\tau \tilde{Z}_{DSS}(\tau, z). \quad (4.148)$$

Again the method suffers from non-convergence with grid resolution. But for a certain number of grid points the gauge modes are reproduced rather well.

Using this method Jonathan Thornburg investigated stability of the DSS solution for some values of the coupling constant. He reports [71] that the DSS solution has one unstable mode for  $\eta \geq 0.18$ . For  $\eta = 0.1726$  the numerical results are not reliable.

## 4.5 The Spectrum of Self-Similar Solutions Relevant for Type II Critical Collapse

We summarize the results on existence, properties and stability of self-similar solutions in Table 4.1. As will be explained in Chap. 5 the stability properties of

---

<sup>6</sup>We note that this mode is not a gauge mode, i.e. it cannot be removed by a coordinate transformation (see the footnote in Sec. 4.3.2).



the solutions studied here will be essential for the dynamics of the model. The stable CSS ground state probably is a (singular) end state of time evolution for a certain class of initial data. The first CSS excitation and the DSS solution having one unstable mode are candidates for intermediate attractors for near critical initial data in type II critical collapse. As is clear from Table 4.1 the spectrum of these solutions strongly depends on the coupling. For large  $\eta$  we have constructed the DSS solution, which probably ceases to exist at  $\eta \simeq 0.17$ . The CSS solutions on the other hand only exist for  $0 \leq \eta < 0.5$ . Furthermore the existence of marginally trapped surfaces in the analytic continuations of the CSS solutions will be relevant (see Chap. 5 and the remark in [11]).

### 4.5.1 Comparison of CSS and DSS solutions

The results of our numerical simulations of type II critical collapse for intermediate couplings (described in Sec. 5.8) led us to compare the DSS solution with the first CSS excitation in the range  $0.1726 \leq \eta \lesssim 0.18$ . In this range of couplings both solutions exist. Comparing the profiles of the two solutions one sees, that at  $\eta = 0.1726$  one can find a DSS phase such that the DSS and CSS solution resemble each other strongly in some fraction of the DSS “backwards light cone”<sup>7</sup>. This resemblance is rather good up to the past SSH of the CSS solution (which does not agree with that of the DSS solution). Fig. 4.26 illustrates the situation.

For  $\eta = 0.1805$  on the other hand the agreement (for the “best fitting” DSS phase) is not as good as can be seen from Fig. 4.27.

For the following considerations we have to introduce concepts from the theory of dynamical systems<sup>8</sup>, which will also be useful for understanding critical phenomena (see Sec. 5.1). Consider the (characteristic) initial value problem for the  $\sigma$  model in spherical symmetry. As described in Sec. 2.3, a complete set of initial data is given by the field  $\phi$  at the initial null surface,  $\phi_0(r) = \phi(u_0, r)$ . These data then are evolved by the means of Eqs. (2.48), (2.55) and (2.56). This system can be viewed as an infinite dynamical system in the following way: phase space is the set of all (asymptotically flat) initial data. An initial configuration  $\phi_0(r)$  thus corresponds to one point in the (infinite dimensional) phase space. Time evolution (Eqs. (2.48), (2.55) and (2.56)) of the initial data  $\phi_0(r)$  corresponds to a trajectory (an orbit) in phase space.

In adapted coordinates the CSS solution is independent of time. Time evolution maps these data onto themselves, so this solution is a *fixed point* of the system<sup>9</sup>. An initial configuration that corresponds to the DSS solution, is mapped onto

---

<sup>7</sup>By this sloppy formulation we mean the region on a null slice  $\tau = \text{const}$  ( $u = \text{const}$ ) bounded by the intersection of the past SSH with this slice.

<sup>8</sup>Textbooks for dynamical systems are e.g. [3] and [4]. [69] deals with infinite dimensional dynamical systems

<sup>9</sup>neglecting the fact, that the CSS solution is not asymptotically flat

	$0 \leq \eta \lesssim 0.069$	$0.069 \lesssim \eta \lesssim 0.15$	$0.15 < \eta < 0.17$	$0.17 \lesssim \eta \lesssim 0.4$	$0.4 \lesssim \eta < 0.5$	$0.5 < \eta < \infty$
CSS groundstate	CSS ground state exists					
	regular up to future SSH	analytic extension beyond past SSH contains marginally trapped surfaces				
	stable				??	
CSS 1st excitation	CSS 1st excitation exists					
	regular up to future SSH		analytic extension beyond past SSH contains marginally trapped surfaces			
	one unstable mode				??	
DSS solution				DSS solution exists		
				??	one unstable mode .	

Table 4.1: The spectrum of self-similar solutions relevant for type II critical collapse

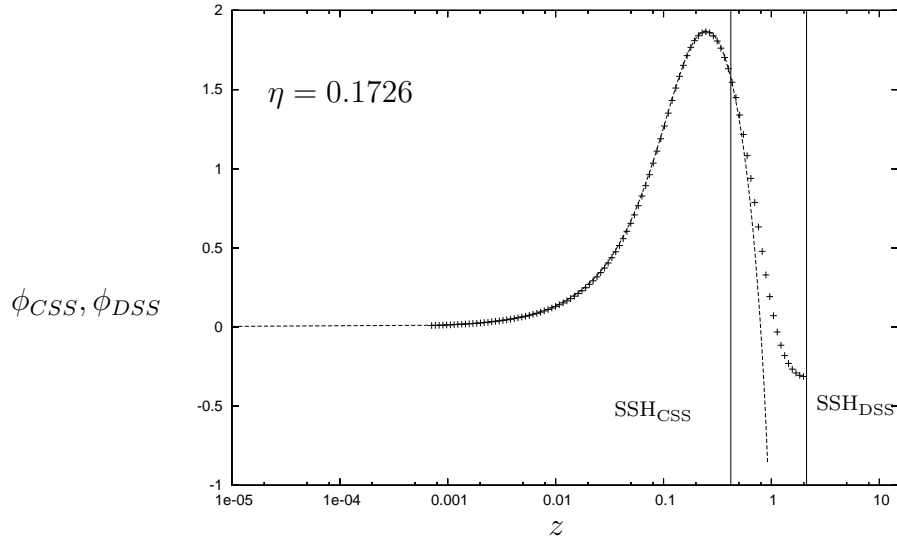


Figure 4.26: Comparison of CSS and DSS solution at the coupling  $\eta = 0.1726$ , the lowest at which we explicitly constructed the DSS solution. Plotted are the CSS solution (dashed line) and the DSS solution (dots) at a special instant of time, where the amplitude of the field  $\phi_{DSS}$  is maximal. The vertical lines denote the intersections of the slice  $\tau = \text{const}$  with the past SSH of the CSS, respectively DSS solution. At this coupling both solutions agree rather well – though not exactly – up to the past SSH of the CSS solution.

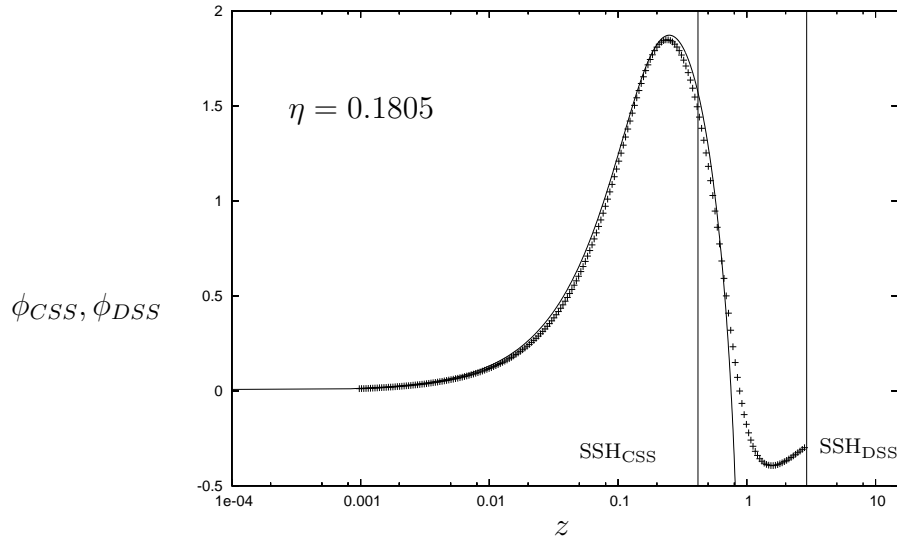


Figure 4.27: The same situation as in Fig. 4.26, for a coupling of  $\eta = 0.1805$ . At this coupling one cannot find an instant of time in the DSS solution, for which the shape of the field resembles that of the CSS solution as closely as for  $\eta = 0.1726$ .

itself after one period  $\Delta$ . The DSS solution therefore can be viewed as a *limit cycle* of the system.

Our dynamical system depends on a parameter, the coupling constant  $\eta$ . Existence and stability properties of fixed points and limit cycles in a dynamical system may depend on such an “external” parameter. In particular the number of fixed points and limit cycles might change at some critical value of the parameter  $\eta_C$ . This “process” is called *bifurcation*. There are so-called local bifurcations, where the appearance of a new fixed point (or limit cycle) is connected to a change in stability of the already existing fixed point. And there are *global* bifurcations, where the fixed point keeps its stability properties (for the possibilities of global bifurcations in two dimensions see e.g. Chap. 8.4 in [68]).

Here we are interested in *homoclinic loop bifurcations*, which are global bifurcations. Fig. 4.28 shows a schematic picture of a homoclinic loop bifurcation (for the simple case of phase space being two dimensional): for  $\eta < \eta_C$  a fixed point with one unstable direction exists. Increasing the parameter towards  $\eta_C$  the stable and unstable manifold bend more and more towards each other until at  $\eta = \eta_C$  they merge and a homoclinic loop develops: one can “leave” the fixed point along the unstable manifold and return to it via the stable manifold. Of course such a “motion” would take infinite time. For  $\eta > \eta_C$  the homoclinic loop separates from the fixed point as a limit cycle. Stable and unstable manifold of the fixed point break apart. During this “process” the fixed point does not change stability. In principle the emerging limit cycle can be either stable or unstable. Approaching the critical value of the parameter from above, it is clear that the period of the limit cycle diverges in the limit  $\eta \rightarrow \eta_C^+$ . For a homoclinic loop bifurcation [68] gives the scaling of the amplitude as  $O(1)$  and of the period of the limit cycle as  $O(\ln(\eta - \eta_C))$ .

Returning to our situation, we concentrate on the “vanishing” of the DSS solution at  $\eta \sim 0.17$ . We summarize some features of this process:

1. CSS and DSS solution “come close” in phase space as one approaches  $\eta \sim 0.17$  from above. They lie “farther apart” for bigger  $\eta$ .
2. The first CSS excitation does not change stability around  $\eta \sim 0.17$ .
3. The DSS period  $\Delta$  rises sharply and seems to diverge at  $\eta \simeq 0.17$ .
4. The amplitude of the DSS oscillations is  $O(1)$ .

This suggests, that the DSS solution “emerges” from the CSS solution at  $\eta \sim 0.17$  in a bifurcation. From 2. one might conclude, that the bifurcation is not a local bifurcation (as would be e.g. a Hopf bifurcation) but rather a global one. 3. and 4. suggest that the bifurcation is a *homoclinic loop bifurcation*<sup>10,11</sup>.

<sup>10</sup>3. and 4. would also fit to an “infinite loop bifurcation”, but we consider this as unlikely.

<sup>11</sup>The DSS solution has the additional symmetry  $\phi_{DSS}(\tau + \Delta/2, z) = -\phi_{DSS}(\tau, z)$ . Therefore,

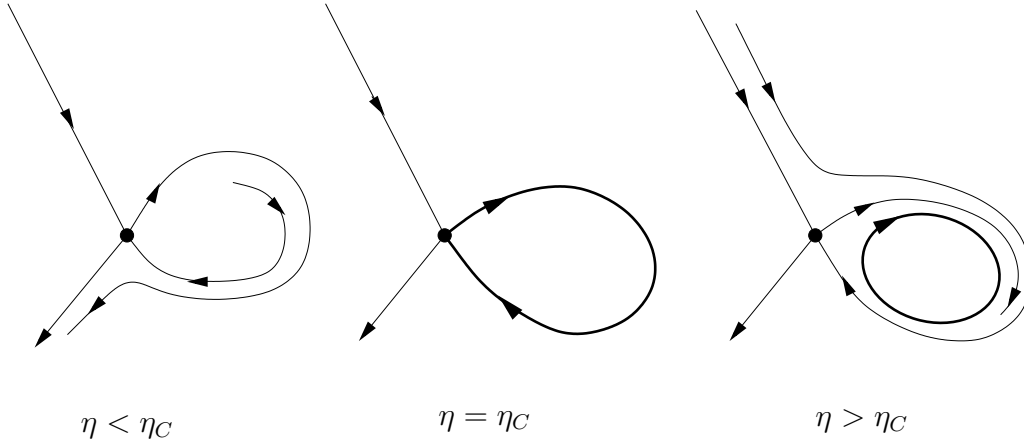


Figure 4.28: Example of an homoclinic loop bifurcation: at  $\eta < \eta_C$  a fixed point with one unstable direction exists. At  $\eta = \eta_C$  the unstable manifold and the stable manifold merge to form a homoclinic loop. For  $\eta > \eta_C$  the homoclinic loop separates from the fixed point as a limit cycle. The fixed point does not change stability throughout.

Assuming, that we really deal with a homoclinic loop bifurcation at  $\eta_C \simeq 0.17$ , we can give the following arguments for the behavior of the period  $\Delta$  of the DSS solution: For  $\eta$  slightly bigger than  $\eta_C$ , where CSS and DSS are already “close”, we separate the period into the time  $T$ , the DSS solution spends in the vicinity of the CSS solution and the remainder  $T_{rem}$ . As the DSS solution has the additional symmetry  $\phi(\tau + \Delta/2, z) = -\phi(\tau, z)$ , the DSS solution comes close to the CSS solution twice (to  $\phi_{CSS}$  and  $-\phi_{CSS}$ ) during one period. Therefore we can write

$$\Delta = 2T + 2T_{rem}. \quad (4.149)$$

If DSS is close to CSS we can expand the DSS solution in terms of the CSS solution and its perturbations:

$$\phi_{DSS}(\tau, z) = \phi_{CSS}(z) + \delta\phi_{unstable}(\tau, z) + \delta\phi_{stable}(\tau, z). \quad (4.150)$$

Note that in this equation the coordinates  $\tau$  and  $z$  are adapted to the symmetry of the CSS solution, in particular the DSS solution is not periodic in the coordinate  $\tau$ . This fact does not matter here, as we are only interested in the local behavior in the vicinity of the CSS solution.

---

if there is a phase at which the DSS solution resembles the CSS solution  $\phi_{CSS}$ , within the same cycle there is another phase (separated by  $\Delta/2$ ) at which it resembles  $-\phi_{CSS}$ . Strictly speaking a *heteroclinic loop* connecting  $\phi_{CSS}$  to  $-\phi_{CSS}$  forms at the bifurcation point. The bifurcation therefore should be called *heteroclinic loop* bifurcation. Nevertheless we prefer to stick to the term homoclinic here, because we think this expresses the essential features.

We define  $\tau_1$  to be the moment of time, where the stable modes have shrunk to order  $\epsilon$  ( $\|\delta\phi_{stable}\| = \epsilon$  in some suitable norm). According to the definition of a homoclinic loop bifurcation, the admixture of the unstable mode in (4.150) depends on  $\eta$  and goes to zero as  $\eta$  tends to  $\eta_C$ . Therefore we can always find a value  $\eta_0$  such that the norm of the unstable mode at this moment of time  $\tau_1$  is less than  $\epsilon$  for all  $\eta_C < \eta < \eta_0$ . We define  $\tau_2 > \tau_1$  to be the moment of time, where the unstable mode has grown to order  $\epsilon$  ( $\|\delta\phi_{unstable}\| = \epsilon$ ). From the stability analysis we know, that the CSS solution has one unstable mode with eigenvalue  $\lambda_1$ , which does not depend strongly on  $\eta$ . Writing  $\delta\phi_{unstable} = A_0 e^{\lambda_1 \tau} y(z)$ , the time  $T$  elapsing between  $\tau_1$  and  $\tau_2$  is given by

$$T = -\frac{1}{\lambda_1} \ln \tilde{A}_0 + \frac{1}{\lambda_1} \ln \frac{\epsilon}{\|y\|}, \quad (4.151)$$

where  $\tilde{A}_0$  denotes the amplitude of the unstable mode at the time  $\tau_1$ .

Now the only expression in (4.151) that depends on the parameter  $\eta$  is the amplitude  $\tilde{A}_0$ . (We neglect the  $\eta$ -dependence of  $\lambda_1$  as  $\lambda_1$  is only slowly varying with  $\eta$ ). By definition it should go to zero for  $\eta \rightarrow \eta_C$ . If we assume further that  $\tilde{A}_0$  is a regular function of  $\eta - \eta_C$ , namely  $\tilde{A}_0(\eta) = a(\eta - \eta_C) + O((\eta - \eta_C)^2)$ , we obtain the following formula

$$T = -\frac{1}{\lambda_1} \ln(\eta - \eta_C) + const. \quad (4.152)$$

We may assume further that for  $\eta$  close to  $\eta_C$ , the remaining part of the period can be approximated by a constant,  $T_{rem} \simeq const.$  Therefore we have

$$\Delta(\eta) = -\frac{2}{\lambda_1} \ln(\eta - \eta_C) + const.^{12} \quad (4.153)$$

Fig. 4.16 shows the period  $\Delta$  fitted against the function  $f(\eta) = -a \ln(\eta - \eta_C) + b$ . As stated there, the fit gives  $\eta_C \simeq 0.17$  and  $a = 0.36278$ . According to Eq. (4.153) this would correspond to an unstable eigenvalue  $\lambda_1 = 5.51298$ . The “true” value of  $\lambda_1$  at  $\eta = 0.17$ , computed with the shooting and matching method as in Sec. 4.3.1, is  $\lambda_1 = 5.14282$ . The relative difference of these quantities is  $\sim 7\%$ . This correspondence of numbers gives a strong support to the hypothesis of the homoclinic loop bifurcation.

---

<sup>12</sup>This argument was pointed out by C. Gundlach [38] to us, however on the basis that a second unstable mode of the CSS solution appears at the bifurcation.

## Chapter 5

# Type II Critical Behavior of the Self-gravitating $\sigma$ Model

This chapter finally deals with type II critical phenomena of the self-gravitating SU(2)  $\sigma$  model in spherical symmetry. This model has already been studied in its limits of strong coupling ( $\eta \rightarrow \infty$ ) by Liebling [51] and weak coupling ( $\eta = 0$ ) independently by Bizon et al. [10] and Liebling et al. [53]. They find type II critical behavior governed by self-similar solutions in conformity with Table 4.1. From these results and our knowledge of self-similar solutions (Chap. 4) we expect critical phenomena to depend strongly on the coupling. In particular we expect the critical solution to change from CSS to DSS in some intermediate regime of couplings around  $\eta \sim 0.17$  (see Sec. 5.8).

As is clear from Chap. 4 (especially Table 4.1), for small couplings we have to consider the possibility of the formation of naked singularities – according to the stable CSS ground state – for a certain class of initial data. This is investigated in Sec. 5.3.

In agreement with Table 4.1 we essentially find three different types of critical behavior: for small couplings the critical solution is CSS (see Sec. 5.7), while for large couplings we have DSS critical behavior (see Sec. 5.6). And for some intermediate range of couplings  $0.15 \lesssim \eta \lesssim 0.18$  we find that the intermediate asymptotics of near critical evolutions show a behavior which we call “episodic CSS”: at intermediate times we see a repeated approach to the first CSS excitation. These “episodes” are part of an approach to the DSS solution at couplings where the latter exists, and still have some resemblance with discrete self-similarity at couplings where we think the DSS solution does not exist anymore (see Sec. 5.8). With increasing coupling the “CSS episodes” get less pronounced, while at the same time the number of episodes (or cycles) increases. To our knowledge this sort of transition from CSS to DSS as the critical solution, which is in very good agreement with our results obtained by a direct construction of the self-similar solutions and the hypothesis of a homoclinic loop bifurcation of Chapter 4, has

not been observed in the context of critical phenomena of self-gravitating systems up to now.

The results for large couplings are summarized in [45]. Part of the phenomena in the transition region is described in [72]. A more complete description is given in [49].

In order to avoid confusion originating from the inconsistent use of the notion “the critical solution” in the literature, we fix our convention as follows: by the *critical solution* we denote the intermediate attractor, which by the means of its “stable manifold” separates two different end states in phase space. Solutions that approach the critical solution in some intermediate regime of time are called *near critical solutions* (evolutions, data etc.). The member of a family of initial data with  $p = p^*$  is called *critical data*. With this nomenclature we have constructed the respective “critical solutions” in Chapter 4 and deal with the evolution of “near critical data” in this chapter. It is the aim of the bisection procedure (see Sec. 5.5) to approximate “critical data” as close as possible, but of course they are not realized numerically.

## 5.1 Introduction to Critical Phenomena

There is a couple of excellent review articles on critical phenomena. An elementary introduction to critical phenomena is given by Choptuik, who pioneered the work on this field, in [20]. Gundlach’s reviews [36, 37] give more details as well as an overview of the models studied and the phenomena found. We also mention the review by Brady and Cai [12]. At the moment the most recent reference lists can be found in the article by Wang [77] and on Choptuik’s home-page [17].

The field of study can be explained as follows: in their long time evolution isolated (asymptotically flat) self-gravitating systems are supposed to evolve to some stationary end state, e.g. to a black hole, a stable star or flat space. According to this small number of distinct kinds of end states, the space of initial data is divided into basins of attraction. The “boundaries” of these basins and their “vicinities” are the scope of studies of critical phenomena.

In the simplest models (e.g. the massless Klein-Gordon field studied by Choptuik in spherical symmetry), where only two different end states are possible, namely black holes and Minkowski space, “small” initial data, i.e. initial data, that do not deviate too much from Minkowski data, will finally disperse to infinity, leaving flat space behind, whereas for “strong” initial data, part of the mass present in the initial slice will be trapped and a black hole will form.

Technically one constructs a one parameter family of initial data, parametrized by  $p$ , such that for large values of  $p$  the data evolve to a black hole, whereas for small values of  $p$  the data disperse. E.g. for the  $SU(2)$   $\sigma$  model in spherical symmetry, and working on null slices, Eqs. (2.48), (2.55) and (2.56) show, that



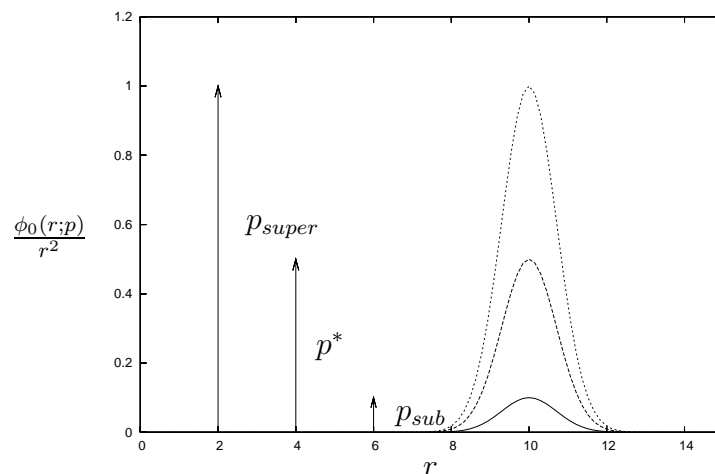


Figure 5.1: A family of Gaussian initial data  $\phi_0(r;p) = pr^2 \exp(-(r - r_0)^2/\sigma^2)$ , where the width  $\sigma$  and the center  $r_0$  are fixed and the amplitude  $p$  parameterizes the family. Depending on the value of  $p$ , the data will finally evolve to a black hole or disperse.

a complete set of initial data is given by the shape of the field  $\phi_0(u = 0, r)$  at the initial null slice. A one parameter family of initial data then can be modeled e.g. by a Gaussian with fixed width and center and the amplitude serving as the parameter. For a family constructed this way, there will be a value of the parameter  $p$ , denoted by  $p^*$ , which separates initial data that disperse (*sub-critical data* with  $p_{sub} < p^*$ ) from those, that form a black hole (*super-critical data* with  $p_{super} > p^*$ ). Phenomena that occur for initial data with  $p \simeq p^*$  are called *critical phenomena* (See Fig. 5.1). One of the original key questions was, whether the black hole mass for slightly super-critical data can be made arbitrarily small (such that the black hole mass as a function of the parameter  $p$  would be continuous) or has a finite value (such that there would be a *mass gap*). The answer is, that depending on the model under investigation, both behaviors can occur. In analogy to statistical physics one distinguishes between two types of critical phenomena, *type I* where the black hole mass shows a mass gap, and *type II*, where the black hole mass is a continuous function of  $p - p^*$ .

In the following we will concentrate on type II critical phenomena and only refer to the other possibility at the end of this section. The first model, for which critical phenomena have been investigated, was the self-gravitating massless Klein-Gordon field. This was done numerically by M. Choptuik [18, 19]. In order to resolve all the features, including self-similarity, he had to develop a sophisticated numerical algorithm, which refines the numerical grid, when variations occur on too small scales to be resolved. Other models have been studied, including e.g. gravitational waves in axial symmetry, perfect fluids, the Einstein-Yang-Mills system etc. For the most recent lists of references see [77] and the bibliography on

Matt Choptuik’s home-page [17].

These investigations showed, that the behavior of near critical evolutions can be characterized by three main features

- Scaling,
- Self-similarity,
- Universality.

Scaling relates the black hole mass of super-critical data, as well as other quantities, that have dimension of length or any power thereof to the parameter  $p$  in the initial data. One finds, that the black hole mass scales as

$$m_{BH} \sim (p - p^*)^\gamma, \quad (5.1)$$

where the exponent  $\gamma$ , called the *critical exponent*, is *independent* of the family of initial data, although it depends in general on the model.

The second general feature of type II critical phenomena is that near critical evolutions spend their intermediate asymptotics in the vicinity of a self-similar solution (which can be either continuous or discrete, depending on the model), before they actually decide whether to disperse or to form a black hole.

The third important point is universality, which means *independence* of the above features of the family of initial data.

An explanation of these phenomena can be given in the language of dynamical systems. Suppose the matter model admits a self-similar solution. For simplicity we concentrate on continuously self-similar solutions  $\phi_{CSS}(z)$ . Suppose further, that the CSS solution has exactly one unstable mode with eigenvalue  $\lambda$  and that an initial configuration, which corresponds to the CSS solution plus a small admixture of the unstable mode leads to either black hole formation or dispersion, depending on the overall sign of the perturbation. In the simplest case the “stable manifold” of this solution divides the phase space into sub and super-critical data. Fig. 5.2 shows a sketch of this scenario using a “phase space picture”.

Then general near critical initial data are attracted by the CSS solution via the stable modes, until they are close to the CSS solution. In this vicinity the solution can be written as a small perturbation of the CSS solution

$$\phi(u, r) = \phi_{CSS}\left(\frac{r}{u^* - u}\right) + C(p)(u^* - u)^{-\lambda}y\left(\frac{r}{u^* - u}\right) + \delta\phi_{stable}(u, r), \quad (5.2)$$

where the eigenvalue  $\lambda$  is real for all known examples and positive. The amplitude of the unstable mode contains information on the initial data, in particular it depends on the parameter  $p$ . For  $p = p^*$  the unstable mode is tuned out completely,

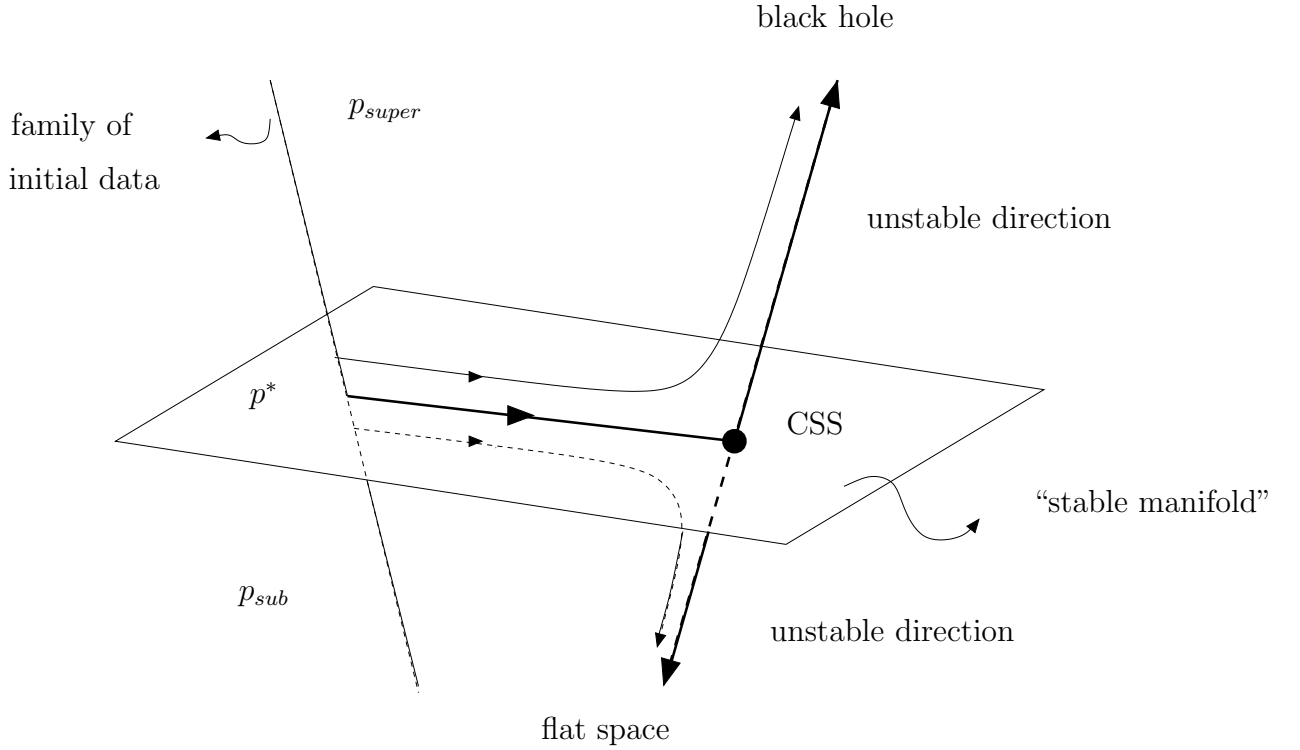


Figure 5.2: A schematic picture of phase space. Every point in this figure corresponds to one configuration  $\phi(r, u = \text{const})$ . In adapted coordinates the CSS solution is a fixed point of the system, it therefore is drawn as a point (large solid circle). The CSS solution has one unstable mode, the “stable manifold” therefore is of co-dimension one. The straight line at the left of the figure represents a one parameter family of initial data, with parameter  $p$ . The value  $p^*$  corresponds to those initial data, that “start out” on the “stable manifold” and are completely attracted to the CSS solution (where they arrive only in the limit  $\tau \rightarrow \infty$ ). For  $p > p^*$  the configuration is initially attracted by the CSS solution via the stable modes until the (initially very small) admixture of the unstable mode takes over and pushes the solution towards black hole formation. For  $p < p^*$  the final state is flat space. Any one parameter family of initial data, cutting the “stable manifold”, will show the same near critical phenomena. Two remarks are in order here: a DSS solution, being periodic in the adapted time  $\tau$ , corresponds to a limit cycle, and should therefore be drawn as a cycle, with near critical data spiraling in and out. Second, this sketch does not claim, that the “stable manifold” is indeed a manifold. It is just a very helpful abstract picture, modeling the essential facts, that have been observed.

and the configuration evolves towards the CSS solution, therefore  $C(p^*) = 0$ . For near critical data, we have  $C(p) = \frac{dC}{dp}(p^*)(p - p^*) + (O((p - p^*)^2))$ .

From (5.2) we can estimate the time for which the solution stays in the vicinity of the CSS solution. Fix  $\tau_1$  to be some instant of time, where near critical solutions are already in the vicinity of the CSS solution, and therefore (5.2) is valid. Let furthermore  $\tau_2 = \tau_1 + T$  be the instant of time when the amplitude of the unstable mode has grown to be  $\epsilon$ , then the time  $T$  spent in the vicinity of the CSS solution is given by

$$\epsilon = \tilde{C}(p)e^{\lambda T}, \quad (5.3)$$

with  $\tilde{C}(p) = C(p)e^{\lambda \tau_1}$ , or

$$T = \frac{1}{\lambda} \ln\left(\frac{\text{const}}{p - p^*}\right). \quad (5.4)$$

So a near critical solution spends longer and longer time in the vicinity of the CSS solution, when  $p$  comes closer and closer to  $p^*$ , until for  $p = p^*$ , the logarithmic time goes to infinity.

In order to explain the scaling of the black hole mass, we “redefine” our family of initial data in the following way: we fix the time  $u_p$ , where the stable modes are already negligible compared to the unstable mode, and the amplitude of the unstable mode has grown to be  $\epsilon$

$$\epsilon = C(p)(u^* - u_p)^{-\lambda}. \quad (5.5)$$

So

$$\epsilon = \frac{dC}{dp}(p^*)(p - p^*)(u^* - u_p)^{-\lambda} \quad (5.6)$$

or resolved for  $u^* - u_p$

$$u^* - u_p = \text{const}(p - p^*)^{1/\lambda} \quad (5.7)$$

where the constant contains  $\epsilon$  and some information on the original family of initial data, but is independent of  $p$ . This way we have constructed a family of initial data  $\phi_0(r; p) = \phi_{CSS}(r/(u^* - u_p)) + \epsilon y(r/(u^* - u_p))$ , which depends on  $r$  only via the ratio  $r/(u^* - u_p)$ . As the field equations are scale invariant, a solution  $\phi(u, r)$  with initial conditions  $\phi_0(r)$  implies the existence of a one parameter family of solutions  $\phi_\sigma(u, r) = \phi(\sigma u, \sigma r)$  with initial conditions  $(\phi_\sigma)_0(r) = \phi_0(\sigma r)$ . From this it follows, that the evolution of our one-parameter family of initial data gives a one-parameter family of solutions of the form

$$\phi_p(u, r) = \phi\left(\frac{u}{u^* - u_p}, \frac{r}{u^* - u_p}\right). \quad (5.8)$$

This is valid for the whole future evolution of the data, even when the linearity assumptions break down.

Assume now, that for super-critical data the solution  $\phi(u, r)$  has an apparent horizon at  $r_H(u)$ . If we fix  $z = r/(u^* - u)$ , then the apparent horizon is located at  $(u_H, r_H = z(u^* - u_H))$  and so the metric function  $\beta(r/(u^* - u), u)$  diverges when  $u \rightarrow u_H$ . Therefore the rescaled solutions  $\beta_p(r/(u^* - u), u) = \beta(r/(u^* - u), u/(u^* - u_p))$  diverge if  $u \rightarrow (u^* - u_p)u_H$ , or  $r \rightarrow (u^* - u_p)r_H$ . The mass of the apparent horizon  $m(z; p) = r_H(z; p)/2$ , measured at constant  $z$ , therefore scales as  $(u^* - u_p)$ .

Remark: the above analysis, of writing near critical data as the CSS solution plus a perturbation is valid only up to some finite radius. Outside this region the near critical solutions – being asymptotically flat – will differ considerably from a small perturbation of the CSS solution. Nevertheless, if the region outside does not influence the black hole mass the latter scales as

$$m_{BH} \sim (u^* - u_p) = \text{const}(p - p^*)^{1/\lambda}. \quad (5.9)$$

So we have derived the scaling law (5.1) with the additional information, that the critical exponent  $\gamma$  is related to the eigenvalue of the unstable mode via

$$\gamma = \frac{1}{\lambda}. \quad (5.10)$$

This relation was derived independently by Koike et al. [47] and Maison [54]. (Evans and Coleman [25] first suggested to look at the linear stability of the CSS solution in order to get an estimate on the critical exponent  $\gamma$ .) Another well defined quantity as pointed out by Garfinkle and Duncan [27], which exhibits scaling, is the maximum of the Ricci scalar at the axis for sub-critical data, the maximum taken over a whole evolution,  $\max_u \mathcal{R}(u, 0)$ . As this quantity has dimension of  $1/\text{length}^2$ , it should scale as

$$\max_u \mathcal{R}(u, 0) \sim (p^* - p)^{-2/\lambda}. \quad (5.11)$$

If a DSS solution is the critical solution, the scaling law undergoes some modification, in that a small wiggle is overlaid. The derivation, as first given independently by Gundlach [35] and Hod and Piran [44], is analogous to the CSS case, a first difference arising in (5.2), where now the DSS solution and its unstable mode have an additional periodic dependence on  $\tau$ . The family of initial data constructed as above, therefore depends periodically on the parameter  $\tau_p$ ,

$$\phi_0(r; p) = \phi_{DSS} \left( \frac{re^{\tau_p}}{\zeta(\tau_p)}, \tau_p \right) + \epsilon y_1 \left( \frac{re^{\tau_p}}{\zeta(\tau_p)}, \tau_p \right). \quad (5.12)$$

Again the equations are scale invariant, therefore the solutions to initial conditions  $\phi_0(r; p)$  behave as

$$\phi_p(r, u) = \phi \left( \frac{re^{\tau_p}}{\zeta(\tau_p)}, \frac{ue^{\tau_p}}{\zeta(\tau_p)}; \tau_p \right). \quad (5.13)$$

Any quantity of dimension length should therefore scale as  $e^{-\tau_p} \zeta(\tau_p) f(\tau_p) = e^{-\tau_p} \tilde{f}(\tau_p)$ , where  $f, \zeta$  and  $\tilde{f}$  are periodic functions of their argument  $\tau_p$ . So we have

$$m_{BH} = c_1(p - p^*)^{1/\lambda} \tilde{f}(-\ln c_1 - \frac{1}{\lambda} \ln(p - p^*)) \quad (5.14)$$

or

$$\ln m_{BH} = \ln c_1 + \frac{1}{\lambda} \ln(p - p^*) + \hat{f}(-\ln c_1 - \frac{1}{\lambda} \ln(p - p^*)), \quad (5.15)$$

where  $\hat{f} = \ln(\tilde{f})$ . Now  $\hat{f}$  is periodic in  $\ln(p - p^*)$  with period  $\Delta/\gamma$ , or since the metric functions have the additional symmetry of consisting only of even frequencies, and therefore have a period of  $\Delta/2$ , the period of  $\hat{f}$  is rather half this value, i.e.  $\frac{\Delta}{2\gamma}$ . Note that there is only one constant  $c_1$ , which depends on the family. The scaling exponent  $\gamma = 1/\lambda$  and the periodic function  $\hat{f}$  are universal.

We close this section with some words on type I critical phenomena, which have been observed in several models, e.g. in the Einstein-Yang-Mills system [21] or the massive minimally coupled scalar field [13]. In this type of transition the intermediate asymptotics is governed by an unstable (the stable manifold being of co-dimension one) static solution or a solution that is oscillating in time. Again the “life-time of the critical solution”, that is the time a near critical solution spends in the vicinity of the intermediate attractor, scales according to (5.4). The major difference to a type II collapse is that the black hole mass for slightly super-critical data is finite, i.e. the black hole mass as a function of the parameter  $p - p^*$  is discontinuous. The magnitude of the mass gap or the fraction of the mass of the intermediate attractor that is radiated away by slightly super-critical data depends on the model.

## 5.2 Limits of Weak and Strong Coupling

The self-gravitating SU(2)  $\sigma$  model has already been investigated with respect to critical phenomena for the two extremes of coupling,  $\eta = 0$  and  $\eta \rightarrow \infty$ .

The case  $\eta = 0$  corresponds to the SU(2)  $\sigma$  model on fixed Minkowski background and was investigated independently by Bizon et al. [10] and Liebling et al. [53]. They looked at the threshold between dispersion and blow up (of the first derivative of  $\phi$  with respect to  $r$ ) at the origin, which is governed by the CSS ground state. They found that the solution at the threshold is the first CSS excitation. A quantity that can be used to examine the scaling, is the maximum (over time) of the energy density at the origin. It was found, that this quantity shows scaling with an exponent  $\gamma = 1/\lambda_{CSS}$ , where  $\lambda_{CSS}$  is the eigenvalue of the unstable mode of the CSS solution for  $\eta = 0$  [7].

The case  $\eta \rightarrow \infty$  on the other hand corresponds to the self-gravitating  $\sigma$  model with three dimensional flat target manifold  $(\mathbb{R}^3, \delta_{AB})$ . This is natural, as the

coupling  $\eta$  corresponds to the inverse of the curvature of the target manifold, the curvature goes to zero, as  $\eta$  tends to infinity. It is also easy to see, by e.g. looking at Eqs. (2.48), (2.55) and (2.56). Defining  $\tilde{\phi} = \sqrt{\eta} \phi$ , rewriting the equations with respect to  $\tilde{\phi}$  and taking the limit  $\eta \rightarrow \infty$  gives the following system of equations

$$\begin{aligned}\beta' &= \frac{1}{2}r^2(\tilde{\phi}')^2, \\ \frac{V'}{r} &= e^{2\beta}(1 - 2\tilde{\phi}^2), \\ \square\tilde{\phi} &= \frac{2\tilde{\phi}}{r^2},\end{aligned}\tag{5.16}$$

which are precisely the equations for the  $\sigma$  model with flat target manifold in the hedgehog ansatz.

This model was investigated by Liebling [51], where in addition he considered a potential. As was explained in Sec. 4.1.3, such a potential is asymptotically irrelevant, the critical behavior of the models with and without this potential should therefore be the same. Liebling found that the critical solution at the threshold of black hole formation is DSS with an echoing period  $\Delta = 0.46$  and a scaling exponent  $\gamma = 0.119$ . Note, that the value of the echoing period nicely fits to the period of the DSS solution at  $\eta = 100$ , described in Sec. 4.4.5.

From these rather different critical phenomena at the limits of very small and very large couplings, one can infer that there will be a transition of the critical solution from CSS to DSS as the coupling is increased.

### 5.3 Possible End States

As is clear from the last section, criticality is only defined with respect to the end states. Usually these two different end states would be black hole formation and dispersion to infinity. If the model allows also for other stable stationary configurations, e.g. for stable static solutions, then these can be considered as possible end states as well.

As was already mentioned in Sec. 2.1.1, the  $SU(2)$   $\sigma$  model does not allow for static asymptotically flat solutions. Therefore it is natural to investigate the transition between black hole formation and dispersion.

On the other hand, as we have seen in Chap. 4, the spectrum of CSS solutions contains a *stable* ground state. Furthermore on fixed Minkowski background this stable ground state governs the “long time behavior” of strong initial data, as was described in [10] and the intermediate asymptotics of near critical data between this singularity formation and dispersion is ruled by the first excitation of this CSS family.

As the ground state and its stability properties persist, when gravity is turned on, it is reasonable to expect, that a naked singularity is a possible “end state” for strong (but not too strong) initial data, at least for couplings less than  $\eta \simeq 0.069$ .

As a first step we tested, whether “semi-strong” (but otherwise arbitrary) data really develop towards the ground state. For  $\eta = 0.01$  and  $\eta = 0.05$  we evolved a Gaussian (5.17) with width  $\sigma = 1.0$  and center  $r_0 = 5.0$  and chose an amplitude  $p = 0.03$ , which is neither too big (such that there is no black hole formation) nor too small (such that the data don’t disperse), but otherwise arbitrary. What we find is, that for such data (chosen rather arbitrarily) the solution evolves towards the CSS ground state (see Figs. 5.3 and 5.5) and stays there, until the lack of resolution near the origin causes the numerical data to break away. (The numerical evolution then does not represent a solution to the Einstein equations anymore). Furthermore we find, that  $\frac{2m}{r}$  stays away from 1 during the evolution. (see Figs 5.4 and 5.6) We can conclude from this, that indeed a naked CSS-singularity is the generic end state of “intermediately strong” initial data.

Due to numerical difficulties, we were not able to determine the value of the coupling constant, from which on black hole formation is the only possible end state for “strong” initial data. Presumably it lies close to  $\eta_0^* \simeq 0.069$ , where the CSS ground state has marginally trapped surfaces. We can only state, that for  $\eta \geq 0.09$  we detect black holes as super-critical end states, which show the expected scaling, and that for  $\eta \geq 0.1$  the black hole masses show second order convergence. (For details see Sec. 5.7).

## 5.4 The first CSS excitation for $0.15 \lesssim \eta < 0.5$

In Section 4.2.3 we demonstrated, that the first CSS excitation, if continued analytically beyond the past SSH, contains marginally trapped surfaces for  $\eta \gtrsim 0.152$ . This fact might prevent this solution to play the role of a critical solution between dispersion and black hole formation for couplings  $0.15 \lesssim \eta < 0.5$ .

In order to investigate this, we matched a certain class of asymptotically flat data<sup>1</sup> to the first CSS solution, the matching point being the past SSH and the matching condition being such that the resulting data were  $C^2$ . J. Thornburg evolved these data (with several values for the parameters) numerically for  $\eta = 0.2$  and found, that they developed an apparent horizon outside the past SSH. It is reasonable to assume, that these data will show the same behavior for couplings  $0.2 < \eta < 0.5$ . For couplings  $0.15 < \eta < 0.2$  the numerical evolution does not

---

<sup>1</sup>These data are given in the following way: at the past SSH the CSS solution is matched to a cubic polynomial such that the resulting data are  $C^2$ . At some distance away from the past SSH the cubic polynomial is matched to a Gaussian, the matching again being  $C^2$ . The two free parameters for these data are the location of the second matching point and the width of the Gaussian, all the other parameters of these data are used to achieve the required smoothness at the matching points.



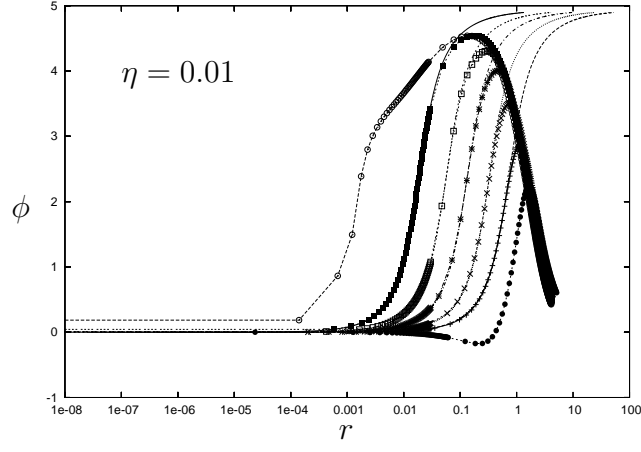


Figure 5.3: Late time behavior of initial data as described in the text for  $\eta = 0.1$ . This figure shows the evolved field  $\phi$  (lines-points) – moving from right to left as time proceeds – for several time steps. The solution clearly comes close to the CSS ground state (lines), and stays there until the grid resolution at the origin becomes too sparse and the evolved data break away from a solution of Einstein equations (this last time step shown in the plot is already “after” the culmination time  $u^*$ ). The culmination time  $u^*$  of the CSS solution was determined by the fit of a single time step to be  $u^* = 11.346$ . For the other time steps the CSS solution was shifted according to  $r = z(u^* - u)$ . The past SSH of the CSS ground state is located where the field equals  $\pi/2 \simeq 1.58$ . This shows that the region, where the evolved data and the CSS ground state agree, extends some way outside the past SSH.

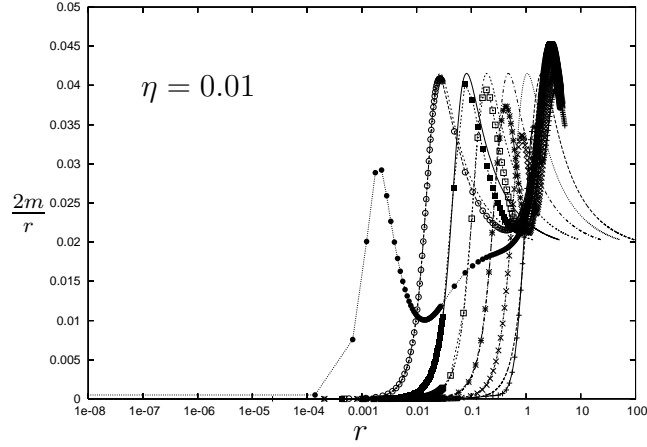


Figure 5.4: The same scenario as in Fig. 5.3, where this time  $\frac{2m}{r}$  is plotted. Note that  $\frac{2m}{r}$  is far from being unity everywhere in the evolved grid. This shows, that the singularity, which is approached via the CSS ground state, is in general not shielded by an apparent horizon,

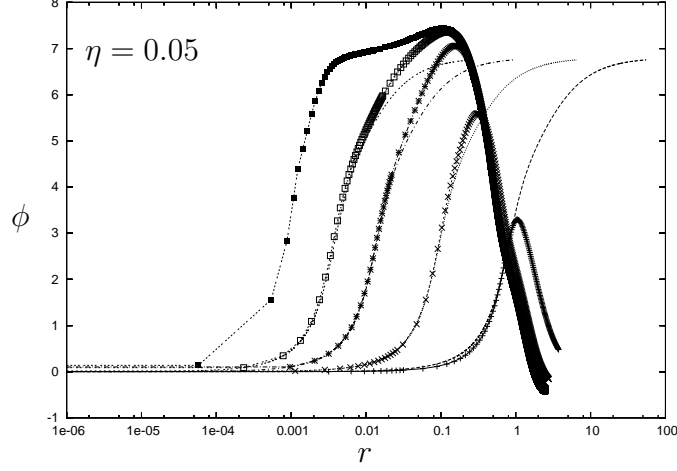


Figure 5.5: For  $\eta = 0.05$  the same initial data as in Figs. 5.3 and 5.4 are evolved. This figure shows the evolved field  $\phi$  (lines-points) for several time steps between  $u = 10.1448$  and  $u = 11.2416$ . Again the solution clearly comes close to the CSS ground state (lines) and breaks away due to insufficient resolution near the origin. (clearly the “latest” time step plotted suffers from insufficient resolution) The culmination time  $u^*$  is determined via the fit to be  $u^* = 11.24085$ .

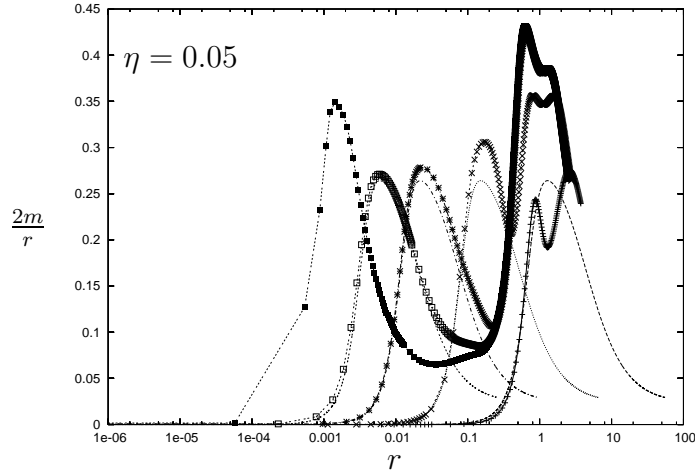


Figure 5.6: Same data as in Fig. 5.5. This time  $\frac{2m}{r}$  is plotted. Note that although growing in time,  $\frac{2m}{r}$  does not come close to one anywhere in the slice before the culmination time is reached. This means that these initial data lead to the formation of a naked singularity.

yield definite results, because at these couplings it is easy to construct data, which do not form an apparent horizon before the evolved data break away from the CSS solution due to numerical errors, which correspond to an excitation of the unstable mode. If one could eliminate (or diminish) these numerical errors, it is likely, that also for these couplings all data of the above described class would form an apparent horizon. At this point we cannot decide this.

If the behavior observed for  $\eta = 0.2$  is generic, it is clear that the CSS solution cannot be found by the means of a critical search between dispersion and black hole formation, because the solution itself (matched to asymptotically flat data) evolves to a black hole – and so would small perturbations independently of the sign of the admixture of the unstable mode. In other words, the CSS solution does not lie at the boundary between dispersion and black hole formation.

Indeed, as stated in Sec. 5.6 the first CSS solution does not show up as a critical solution for  $\eta \geq 0.2$ . In the transition region  $0.15 \lesssim \eta \lesssim 0.18$  as described in Sec. 5.8, the CSS solution appears in the “CSS episodes” of near critical evolutions, but clearly it is not “the critical solution”, i.e. the intermediate attractor, whose unstable mode is tuned out by bisection.

## 5.5 Critical Searches - Setup and Extraction of Results

In order to investigate critical behavior we used several families of initial data, namely a “Gaussian”

$$\phi_0(r) = p r^2 e^{-(r-r_0)^2/\sigma^2}, \quad (5.17)$$

with the center  $r_0$  usually set to be 5.0, the width  $\sigma$  fixed to be either 1.0 or 2.0 and the amplitude  $p$  serving as the parameter. For large couplings also the family

$$\phi_0(r) = -4Ar^2 \left( \frac{r-r_0}{p} \right)^3 e^{-(r-r_0)^4/p^4}, \quad (5.18)$$

generated by keeping the center  $r_0 = 5.0$  and the amplitude  $A$  fixed and varying the width  $p$  as the parameter was used (see [45]).

Furthermore we tried a “double Gaussian”,

$$\phi_0(r) = p r^2 e^{-(r-r_0)^2/\sigma^2} + A r^2 e^{-(r-r_2)^2/\sigma_2^2}, \quad (5.19)$$

with the second Gaussian fixed ( $A = 0.001$ ,  $r_2 = 7.0$ ,  $\sigma_2 = 0.5$ ), width and center of the first Gaussian fixed,  $\sigma = 1.0$ ,  $r_0 = 5.0$  and  $p$  being the parameter.

For a fixed value of the parameter the initial data  $\phi_0$  were evolved using the DICE code (see App. C) until for large couplings either a black hole formed (for the numerical criterion for a black hole see App. C) or the field dispersed (most of

the times measured via  $\max_r 2m/r$  less than some small value, e.g.  $10^{-4}$ , which might of course depend on the coupling; see also remark below). For very small couplings, where we expected naked singularities as super-critical end states, an evolution was defined to be super-critical, whenever the errors grew above some limit<sup>2</sup>.

Starting with some value  $p \in [p_{min}, p_{max}]$ , the interval chosen such that  $p_{min}$  leads to dispersion, while  $p_{max}$  leads to a super-critical end state, the parameter  $p$  was driven towards  $p^*$  by bisection: for  $p_1 > p^*$ , the interval  $[p_{min}, p_1]$  was halved to give the new value of the parameter  $p_2 = (p_{min} + p_1)/2$ , at the same time the interval was reset to  $[p_{min}, p_{max} = p_1]$  and so on. (This description applies if increasing the parameter makes the initial data stronger, as is the case e.g. for  $p$  being the amplitude of a Gaussian. For  $p$  being e.g. the width of a Gaussian the parameter has to be decreased to make the initial data stronger.) Such a bisection search is limited by floating point errors, so a critical search finished, when  $(p_N - p_{N-1})/p_{N-1} < 10^{-14}$ .

Given the result of a critical search, the critical value of the parameter  $p^*$  was approximated by  $p^* = (p_{sub} + p_{super})/2$ , where  $p_{sub}$  was the biggest sub-critical and  $p_{super}$  the smallest super-critical value obtained.

For large couplings, where the critical solution is DSS, the echoing period  $\Delta$  and the culmination time  $u^*$  were determined simultaneously from  $(\max_r \frac{2m}{r})(u)$ . This function of time reflects the periodicity of the DSS solution in logarithmic time  $\tau = -\ln(u^* - u)$  (see Fig. 5.7). A perl script, written by Jonathan Thornburg, extracted  $\Delta/2$  and  $u^*$  using the minima of  $(\max_r \frac{2m}{r})(u)$ , at times  $u_i$ . The times  $\delta u_n$  elapsing between the two adjacent minima at  $u_n$  and  $u_{n+1}$  are given by  $\delta u_n = e^{-(n-1)\Delta/2} \delta u_1$ , a least squares fit of  $\ln(\delta u_n)$  to the straight line  $-(n-1)\Delta + const$  gives the echoing period  $\Delta/2$ . Furthermore for an exact DSS solution these times  $\delta u_n$  sum up in a geometric series to give  $u^* = u_n + \delta u_n/(1 - e^{-\Delta})$  (for any  $n$ ), from which  $u^*$  can be calculated.

In order to examine the scaling of the black hole mass for super-critical data and of the Ricci scalar at the axis for sub-critical data, a whole series of time evolutions was done, starting close to  $p^*$  and increasing (decreasing) the parameter to  $\log(|p - p^*|) \sim -10$ , with steps equally spaced in  $\ln(|p - p^*|)$ . For the details of measuring the black hole mass see App. C. To extract the scaling exponent  $\gamma$  from the black hole masses, a perl script (written by Jonathan Thornburg) least squares fitted  $\ln m_{BH}(x)$  to the straight line  $\gamma x + k$  with  $x = \ln(p - p^*)$ . For an extraction of  $\gamma$  from the scaling of the Ricci scalar usually  $\ln m_{BH}(x)$  was fitted to the straight line by naked eye.

---

<sup>2</sup>Note: it is always a great pleasure to declare the limitations in accuracy of a numerical code a “physical state”.

## 5.6 Critical Phenomena for Large Couplings

For large couplings  $0.2 \leq \eta < 100$ , we find that the critical solution at the threshold of black hole formation is discretely self-similar (See [45]). Figs. 5.7 – 5.11 illustrate this for  $\eta = 100$ . All the runs for these figures were done with the family (5.17) (width  $\sigma = 1.0$ ), with  $r_{outer} = 30.0$  as the initial spatial extension of the grid and with  $N = 2000$  grid points initially.

Fig. 5.7 shows  $\max_r 2m/r$  for  $\eta = 100$ , which if plotted vs.  $-\ln(u^* - u) = \tau$  is a periodic function with period  $\Delta/2$ . (As the metric functions  $\beta$  and  $\frac{V}{r}$  are periodic with period  $\Delta/2$ ,  $\max_r 2m/r$  shows the same periodicity.) Fig. 5.8 shows the Ricci scalar at the origin  $r = 0$ ,  $\mathcal{R}(u, r = 0)$ , which behaves as  $e^{2\tau} \tilde{R}(\tau)$ , where  $\tilde{R}$  denotes a periodic function of its argument. Figs. 5.9 and 5.10 show the scaling of the black hole mass for super-critical initial data and  $\max_u \mathcal{R}(u, r = 0)$  for sub-critical data respectively. Fig. 5.9 also shows the superimposed wiggles in the mass scaling. Finally Figs. 5.11 and 5.12 show that a near critical evolution comes close to the DSS solution at intermediate times for  $\eta = 100$  and  $\eta = 0.2933$  respectively. Compared are the field  $\phi$  as evolved from near critical initial data, and the DSS solution itself, constructed as described in Sec. 4.4.

Table 5.1 (taken from [45]) gives the scaling exponent  $\gamma$ , the echoing period  $\Delta/2$  and the value of the critical parameter for families (5.17) and (5.18) for various values of the coupling constant  $\eta$ . As can be seen from this table, for very large couplings  $\eta = 100$ , the scaling exponent  $\gamma \simeq 0.1185$  and the echoing period  $\Delta \simeq 0.461$  are in very good agreement with the results for  $\eta = \infty$  reported in [51] ( $\gamma = 0.119$ ,  $\Delta = 0.46$ ). When decreasing the coupling, the scaling exponent  $\gamma$  hardly changes (the variation is at most 5%) whereas the echoing period  $\Delta$  starts to increase at lower couplings, which is in good agreement with the results presented in Sec. 4.4.5. Indeed, as can be seen from Fig. 5.13, the echoing period  $\Delta_{crit}$  of near critical evolutions matches the period  $\Delta_{DSS}$  of the “exact” DSS solution, as described in Sec. 4.4.5 for  $\eta \geq 0.2$ .

For  $\eta = 0.18$ , although the DSS solution still exists, the observed DSS periodicity for near critical evolutions is only approximate. This phenomenon will be described in more detail in Sec. 5.8.

## 5.7 Critical Phenomena for Small Couplings

For small couplings we investigated critical phenomena between dispersion and singularity formation ( $0 \leq \eta \lesssim 0.07$ ) and between dispersion and black hole formation ( $0.07 \lesssim \eta \lesssim 0.14$ ). We find that the critical phenomena in this range of couplings is governed by the first CSS excitation described in Sec. 4.2.

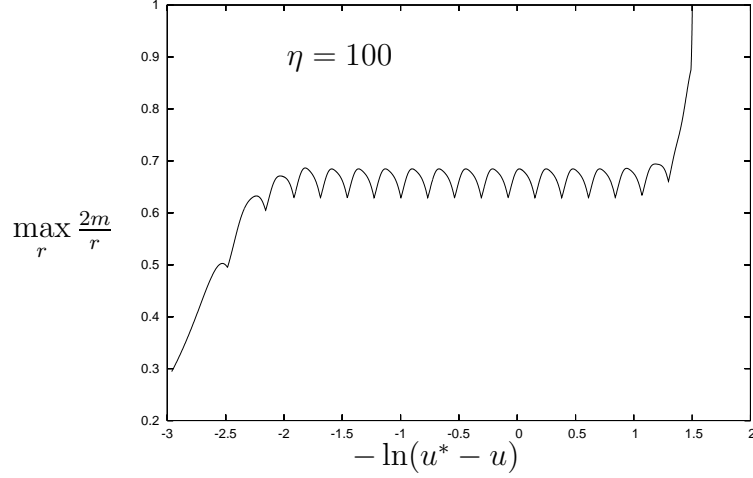


Figure 5.7:  $\max_r \frac{2m}{r}$  as a function of  $\tau = \ln(u^* - u)$ . The echoing period  $\Delta$  was computed to be 0.4599. This is the easiest way to extract the echoing period from a near critical solution.

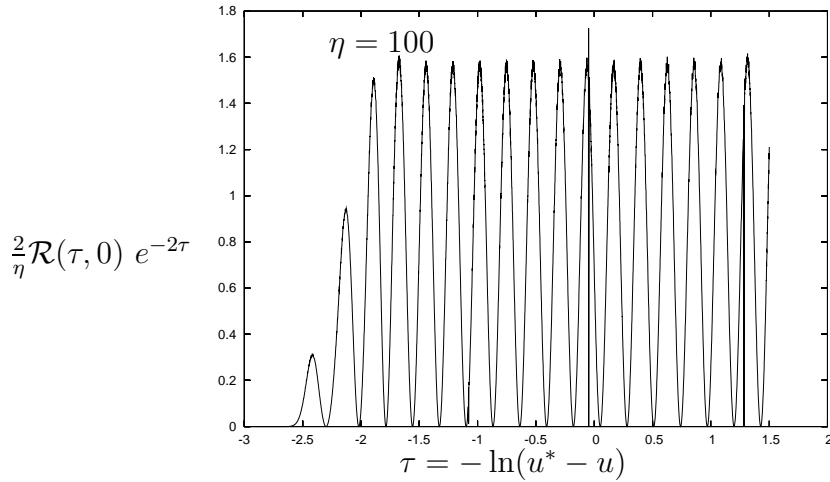


Figure 5.8: The Ricci scalar at the center of spherical symmetry as a function of  $\tau = -\ln(u^* - u)$ . As was discussed in Sec. 4.1.2 the Ricci scalar behaves like  $\mathcal{R}(\tau, z) = e^{-2\tau} \tilde{R}(\tau, z)$ , with  $\tilde{R}$  being periodic in  $\tau$ . (Remark: the vertical lines in the middle of the figure and near the right end are errors, that occur at each grid refinement, but which do not seem to influence the time evolution.)

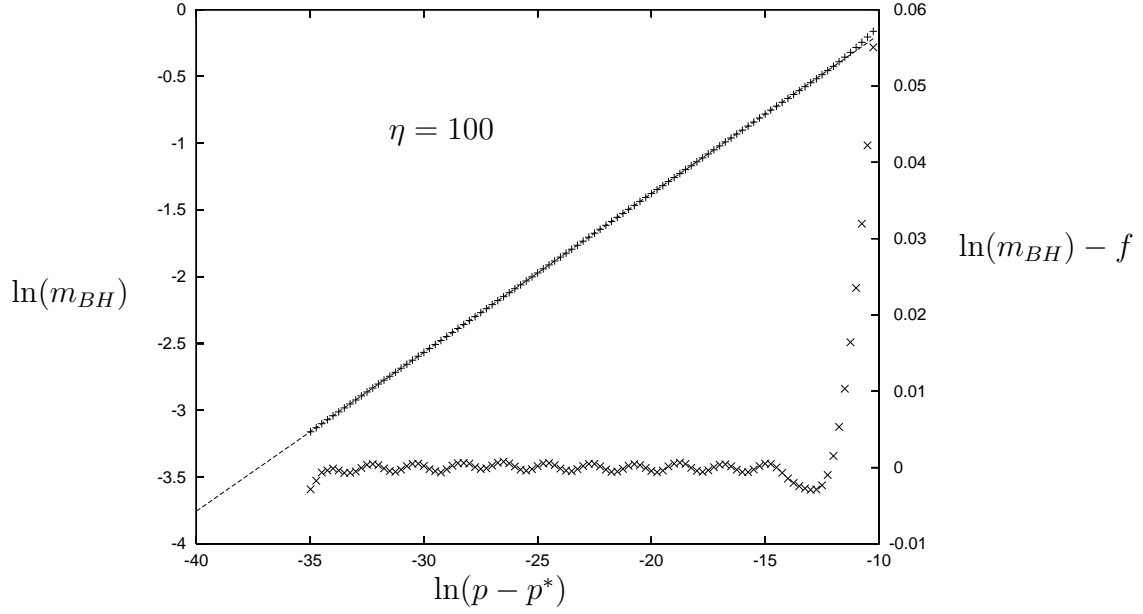


Figure 5.9: The scaling of the black hole mass  $m_{BH}$ . Plotted are the masses obtained from a series of time evolutions (dots) together with the straight line  $f(\ln(p - p^*)) = \gamma \ln(p - p^*) + k$ , where  $\gamma = 0.1189$ , versus the left axis. At the right axis the difference of these functions is plotted. This reveals the “fine structure” of the mass scaling, oscillations with period  $\Delta/2\gamma$ .

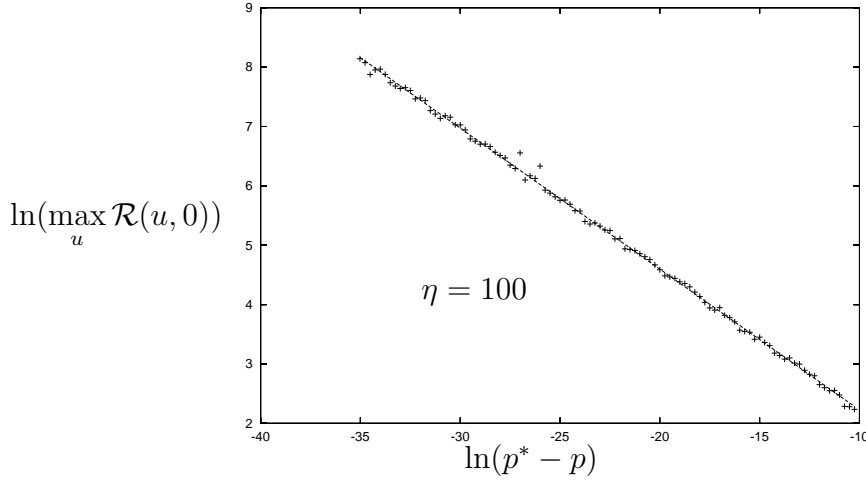


Figure 5.10: The scaling of  $\max_u \mathcal{R}(u, 0)$  for sub critical evolutions as a function of  $\ln(p^* - p)$ . The overlaid straight line has slope  $-2\gamma$ . (Remark: the “escaping” points in the middle of the graph presumably stem from a grid refinement.)

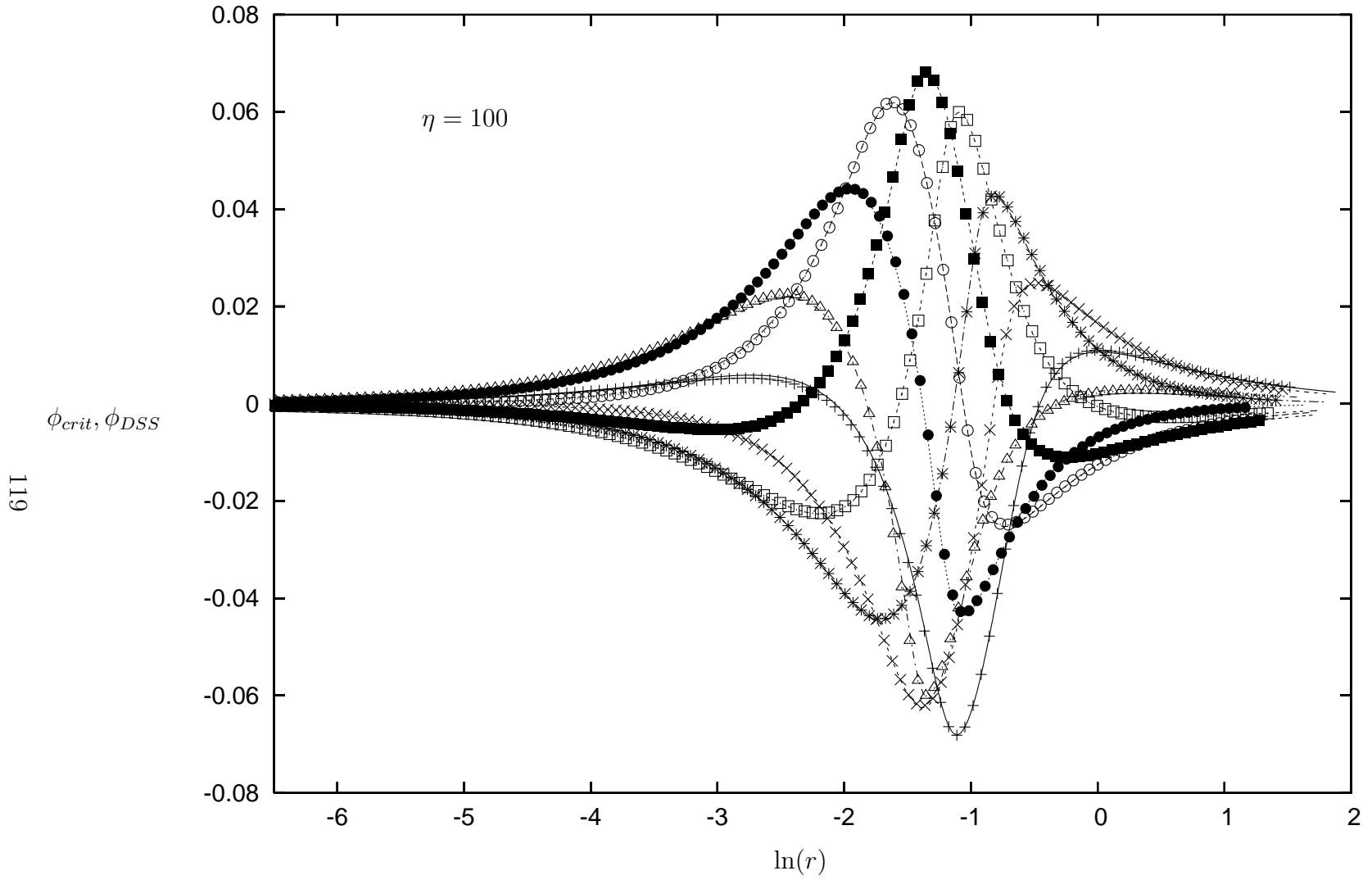


Figure 5.11: Snapshots of the critical solution  $\phi_{crit}$  (solid lines) at  $\eta = 100$  compared to the DSS solution  $\phi_{DSS}$  (dots). The snapshots are taken at times  $\tau_i = i\Delta/N$  for  $N = 16$  and  $i = 0, 2, 4, 6, 8, 10, 12, 14$ , i.e. spanning one period.



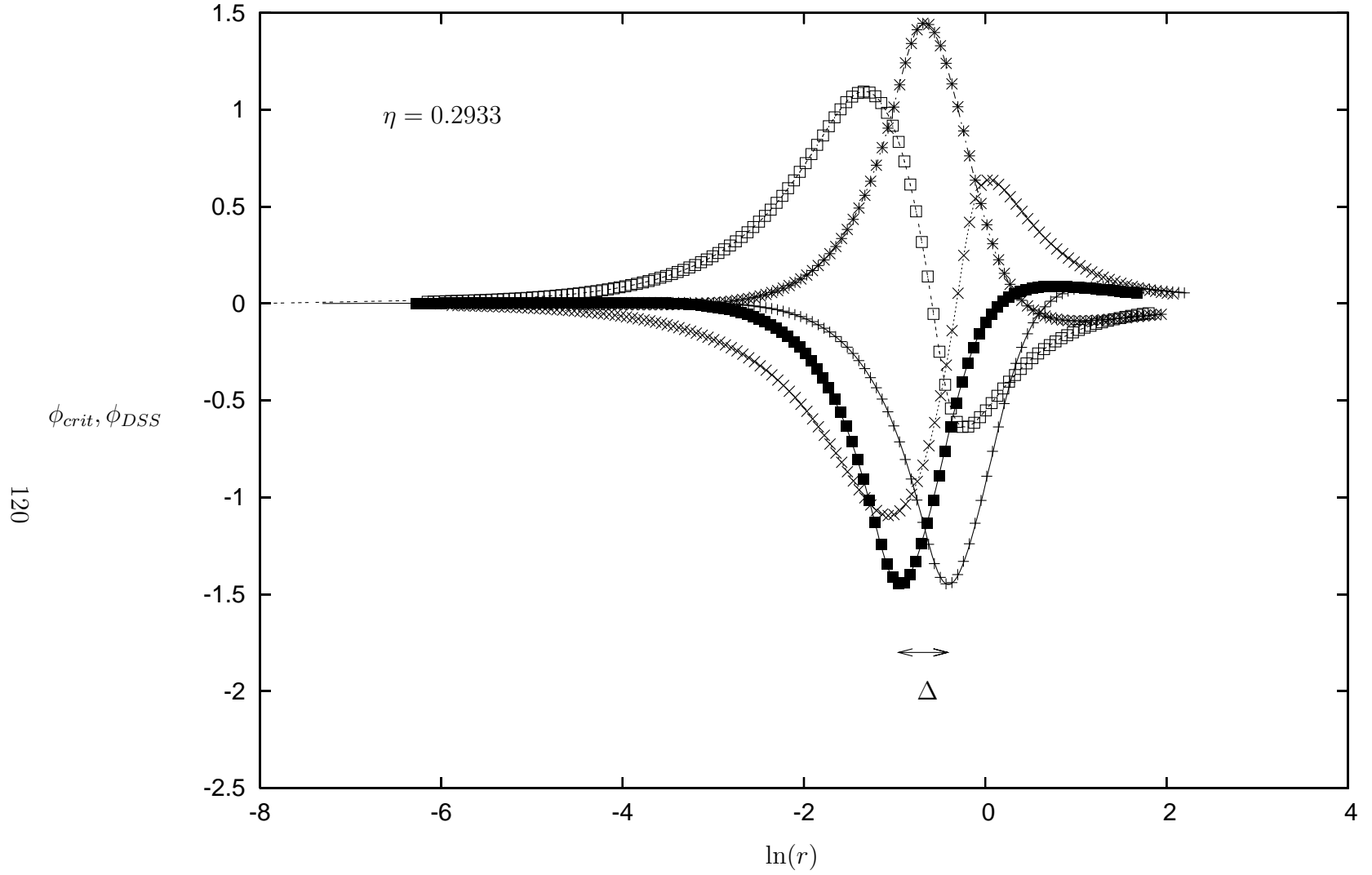


Figure 5.12: Snapshots of the critical solution  $\phi_{crit}$  (solid lines) at  $\eta = 0.2933$  compared to the DSS solution  $\phi_{DSS}$  (dots). Snapshots are taken at times  $\tau_i = i\Delta/N$  for  $N = 64$  and  $i = 0, 16, 32, 48, 64$ . Note that for  $\tau = \Delta$  the critical solution retains its shape at  $\tau = 0$ , but is shifted in  $\ln(r)$  by  $-\Delta = -0.5399$ .

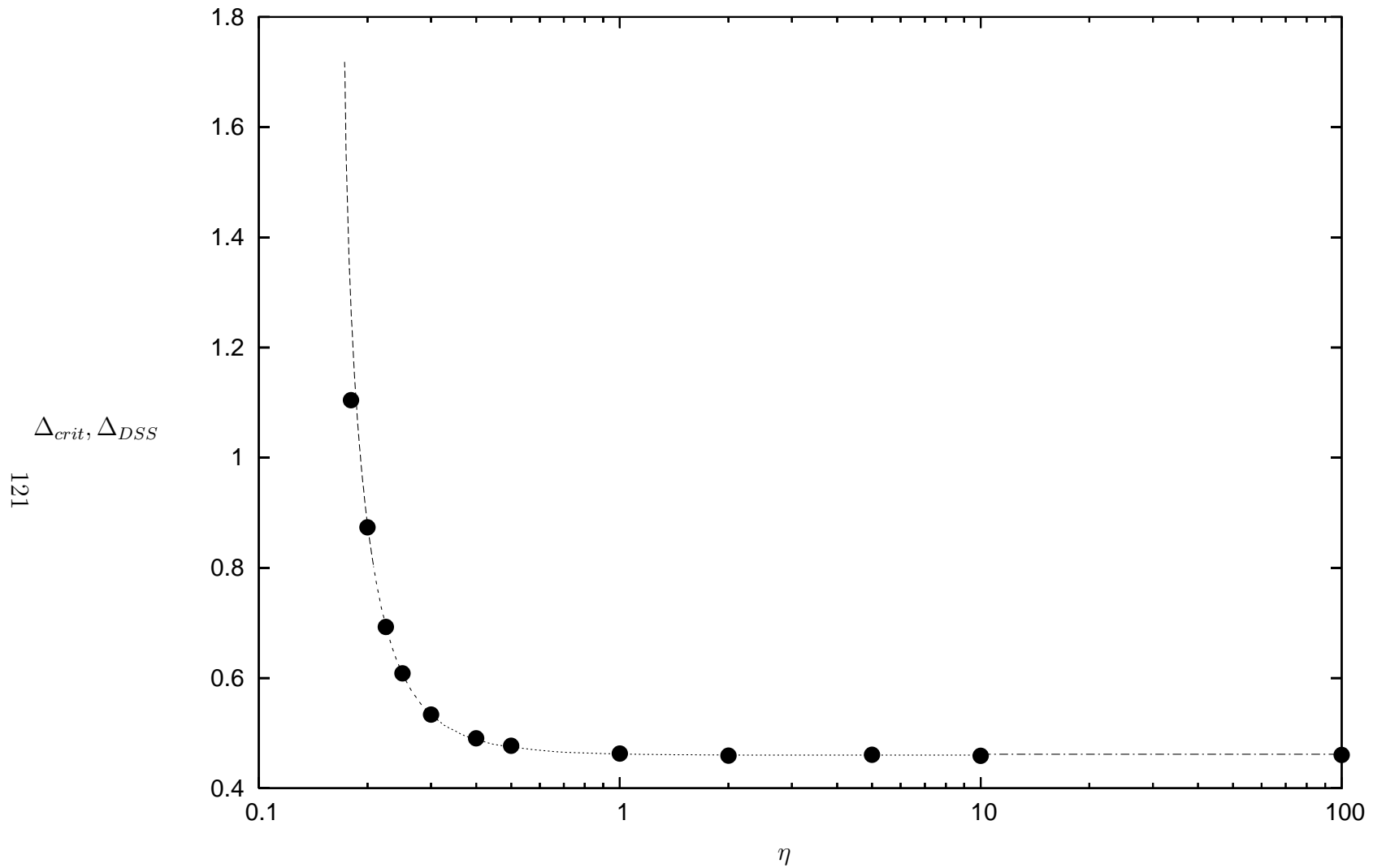


Figure 5.13: The echoing period  $\Delta_{crit}$  (large solid dots) as a function of the coupling constant  $\eta$ , compared to the period  $\Delta_{DSS}$  of the DSS solution (see Fig. 4.15). (The values of  $\Delta_{crit}$  are taken from [45].)

$\eta$	Initial Data Family 5.17			Initial Data Family 5.18			
	Parameter is $A$			Parameter is $\sigma$			
	$A^*$	$\Delta/2$	$\gamma$	$A$	$\sigma^*$	$\Delta/2$	$\gamma$
0.18	0.019 523 015	0.5522	0.1063	0.003	1.083 153 54	0.5478	0.1028
0.2	0.018 942 512	0.4367	0.1091	0.002	0.615 317 49	0.4327	0.1150
0.225	0.018 241 056	0.3464	0.1207	0.002	0.651 519 42	0.3472	0.1169
0.25	0.017 578 042	0.3043	0.1173	0.002	0.688 851 73	0.3046	0.1173
0.3	0.016 392 639	0.2668	0.1152	0.002	0.766 003 44	0.2675	0.1146
0.4	0.014 534 866	0.2452	0.1132	0.002	0.929 746 89	0.2445	0.1139
0.5	0.013 167 548	0.2386	0.1152	0.0015	0.707 335 37	0.2386	0.1130
1	0.009 528 975 1	0.2314	0.1163	0.0015	1.210 138 07	0.2313	0.1155
2	0.006 809 778 3	0.2295	0.1179	0.0010	1.064 744 72	0.2305	0.1167
5	0.004 333 205 6	0.2304	0.1183	0.0005	0.734 344 76	0.2308	0.1178
10	0.003 070 144 2	0.2293	0.1186	0.0005	1.318 800 46	0.2312	0.1182
100	0.000 972 589 54	0.2302	0.1187	0.0001	0.631 472 58	0.2311	0.1182

Table 5.1: This table shows two families of near-critical initial data parameters for various coupling constants  $\eta$ . For the Gaussian-like initial data family 5.17, we use the ‘amplitude’  $A$  as the parameter  $p$  (at a fixed ‘width’  $\sigma = 1$ ), with a numerical grid of 16 000 grid points. For the family 5.18, we use the ‘width’  $\sigma$  as the parameter  $p$  (with different ‘amplitudes’  $A$  for different coupling constants), with 8000 grid points. For each coupling constant and each family, the table also shows the max  $2m/r$  echoing period  $\Delta/2$  of the near-critical evolution, and the mass-scaling-law critical exponent  $\gamma$  determined for the entire critical search. For  $\eta = 0.18$  the DSS symmetry is only approximate (see Sec. 5.8 for details). This table is taken from [45]. All the runs for this table were done by J. Thornburg.

For the couplings where black holes form ( $0.07 \lesssim \eta$ ) the black hole mass scales according to (5.1) with a scaling exponent  $\gamma$  that corresponds to  $1/\lambda_{CSS}$ , the relative error being at most 3 %.

For couplings where the end state is the CSS ground state ( $\eta \lesssim 0.07$ ) the quantity  $\max_u \mathcal{R}(u, 0)$  for sub-critical data exhibits scaling according to (5.11), although only for small values of  $(p - p^*)$ . Furthermore this time the scaling exponent  $\gamma$  differs from the theoretical prediction  $1/\lambda_{CSS}$  by up to 15 %. The reason for this inaccuracy is not clear to us at the moment. One possible reason could be, that for these small couplings  $\ln((p - p^*)/p^*) < 10^{-14}$ , which limits the determination of  $p^*$  due to floating point round off errors, does not allow to reduce the admixture of the unstable mode of the CSS solution in the initial data as much as is the case for large couplings, where we observe a beautiful scaling law (Sec. 5.6). Whether this is indeed the reason could be checked by switching to higher numerical precision. Another possible reason might be, that the code does not work as accurately for small couplings as it does for large couplings. Convergence tests would be a first

check of this.

Figs. 5.14 – 5.20 illustrate the critical phenomena for the couplings  $\eta = 0.11$  and  $\eta = 0.1$ . Figs. 5.14 and 5.16 show the scaling of the black hole mass for super-critical data and of the quantity  $\max_u \mathcal{R}(u, 0)$  for sub-critical data. Both figures show the results for various initial grid resolutions ( $N = 500, 1000, 2000, 4000$ ). As described in [45] the critical value of the parameter  $p^*$  depends on the grid resolution. This was taken into account in Figs. 5.14 – 5.16, i.e. for each resolution  $N$  the corresponding value  $p^*(N)$  was used. In [45] it was shown, that for large values of the coupling the critical value  $p^*(N)$  shows second order convergence with the grid resolution. We note that this is also the case for small (presumably  $\eta \gtrsim 0.07$ ) couplings. For  $\eta = 0.11$  and the initial data family (5.17) with fixed width  $\sigma = 1$  and variable amplitude the respective values are

$$\begin{aligned} p^*(500) &= 0.0214965187393766, & p^*(1000) &= 0.0214974987387296, \\ p^*(2000) &= 0.0214977388532529, & p^*(4000) &= 0.0214977981419972. \end{aligned}$$

The differences are

$$\begin{aligned} \delta p_1 &= p^*(1000) - p^*(500) = 9.79999352997835 \cdot 10^{-07}, \\ \delta p_2 &= p^*(2000) - p^*(1000) = 2.40114523302609 \cdot 10^{-07}, \\ \delta p_3 &= p^*(4000) - p^*(2000) = 5.92887442994738 \cdot 10^{-08}, \end{aligned} \tag{5.20}$$

and the ratios thereof

$$\frac{\delta p_1}{\delta p_2} = 4.08138308136726, \quad \frac{\delta p_2}{\delta p_3} = 4.0499175035613. \tag{5.21}$$

In addition to the convergence of  $p^*(N)$  we demonstrate convergence of the black hole mass. Fig. 5.15 shows the differences of the black hole masses  $m_{BH}(N)$  of Fig. 5.14. The difference between runs with  $N$  and  $2N$  grid points, and the difference between runs with  $2N$  and  $4N$  grid points multiplied by a factor of four are close throughout the shown interval of  $p - p^*$ .

Finally Figs. 5.17 – 5.20 deal with the intermediate asymptotics of near critical data for  $\eta = 0.1$ . Fig. 5.17 shows, that near critical data evolve towards the first CSS excitation, stay there for some time and then deviate again. Fig. 5.18 investigates the deviation of the evolved field  $\phi$  from the CSS solution. According to the theory this deviation should be dominated by the unstable mode of the CSS solution. An additional complication arises from switching to adapted coordinates, in that an error in determining the culmination time  $u^*$  brings the gauge mode (Sec. 4.3.2) into the game. In Fig. 5.18 we have taken this fact into account in the following way: according to the theory the evolved field should behave as  $\phi(\tau, z) = \phi_{CSS}(z) + e^{\lambda\tau} y(z)$ , where we assume that all the stable modes

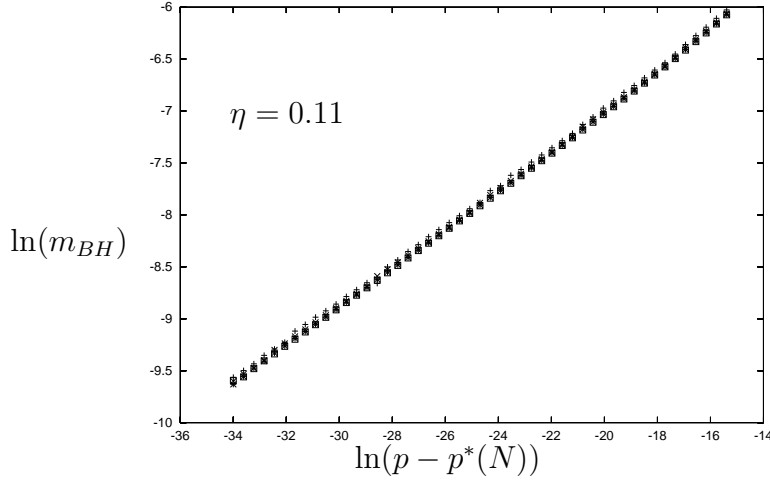


Figure 5.14: The mass scaling for  $\eta = 0.11$  for the family (5.17) (with fixed width  $\sigma = 1$  and variable amplitude). Different symbols denote different grid resolutions: “+” denote  $N = 500$  grid points initially, “x”  $N = 1000$ , “\*”  $N = 2000$  and “□”  $N = 4000$ . The straight line has a slope of  $\gamma \simeq 0.185$ , which is in good agreement with  $1/\lambda_1 = 0.181$ . (The relative error is 2%.)

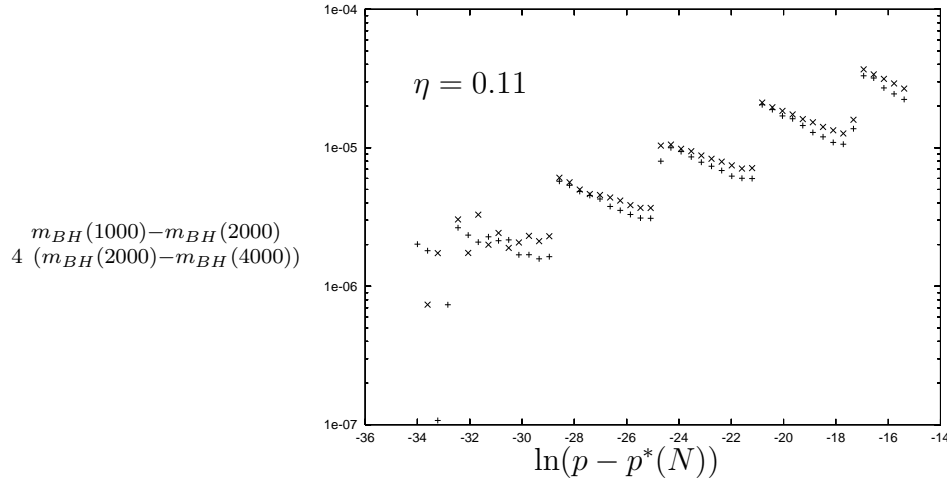


Figure 5.15: The differences of black hole masses of Fig. 5.14 for different initial grid resolutions: “+” denotes the difference  $(m_{BH})_{1000} - (m_{BH})_{2000}$ , “x” denotes four times the difference  $(m_{BH})_{2000} - (m_{BH})_{4000}$ . These quantities almost lie on top of each other, which shows second order convergence of the black hole mass with the grid resolution (see Sec. C.5).

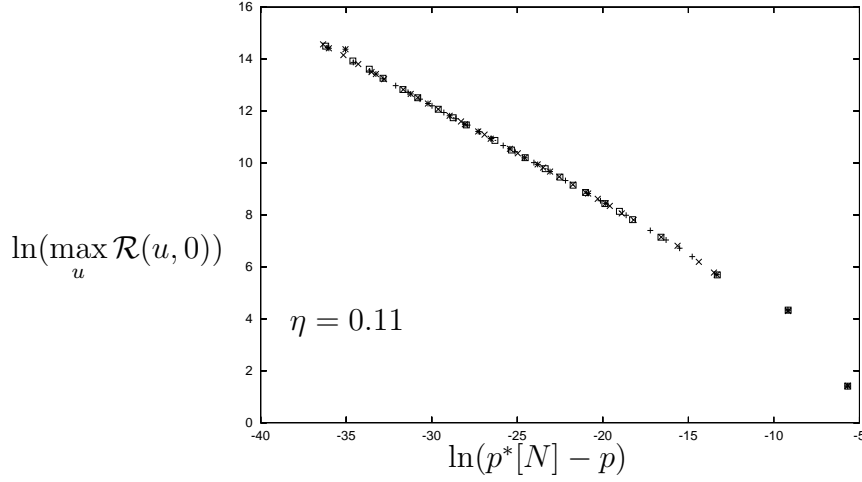


Figure 5.16: The quantity  $\ln(\max_u \mathcal{R}(u, 0))$  for sub-critical data of the same family as in Fig. 5.14 and different grid resolutions: “+” denote  $N = 500$ , “x”  $N = 1000$ , “\*”  $N = 2000$  and “□”  $N = 4000$ . The straight line has a slope of  $-2\gamma$  with  $\gamma \simeq 0.185$ .

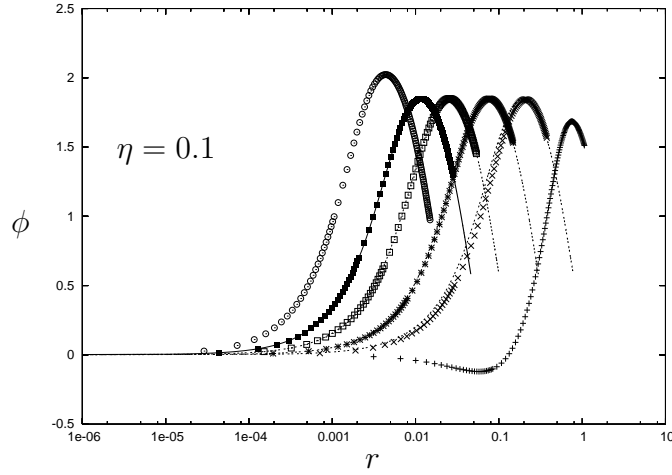


Figure 5.17: The field  $\phi$  of a near critical evolution (dots) at intermediate times between  $u = 12.723$  and  $u = 15.150$  (moving from right to left). The field approaches the CSS solution (solid lines). The culmination time  $u^*$  (determined from the last but second snapshot) is  $u^* = 15.167$ . The past SSH of the CSS solution is located where the CSS solution attains the value  $\pi/2$  for the second time.

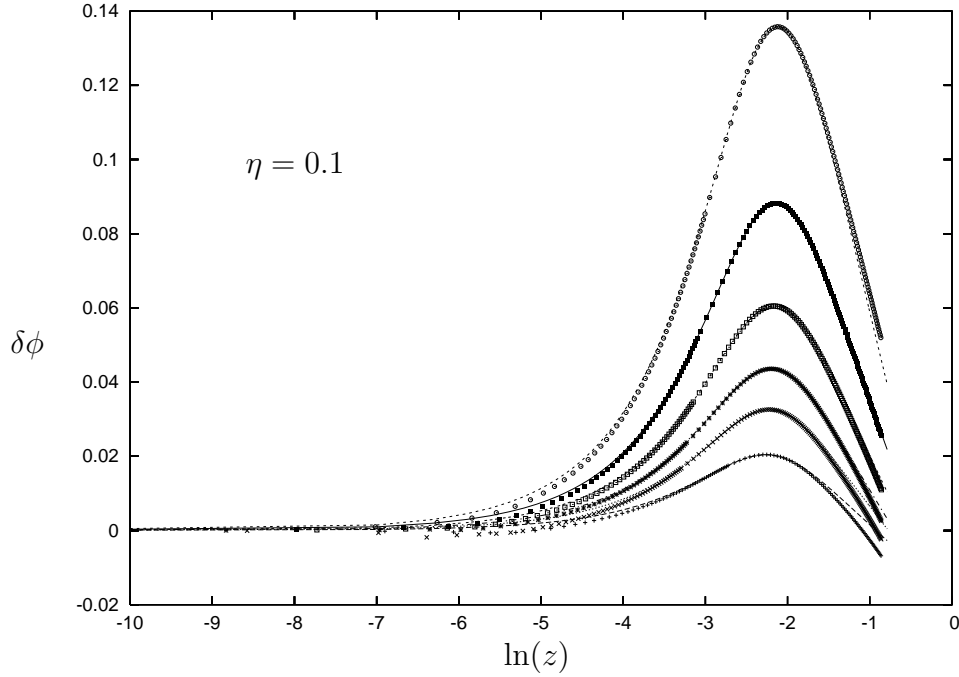


Figure 5.18: The deviation of the critical solution from the CSS solution for several time steps,  $\tau = 3.4169, 3.539, 3.6069, 3.6791, 3.756, 3.838$ . Plotted is the difference between the evolved  $\phi$  and the CSS solution  $\phi_{CSS}$ , i.e.  $\delta\phi(\tau, z) = \phi(\tau, z) - \phi_{CSS}(z)$  (dots). Overlaid is the function  $a(\tau)(y_{unst}(z) + b(\tau)y_{gauge}(z))$  (solid lines), where the parameters  $a(\tau)$  and  $b(\tau)$  were fitted with bare eye such that the maxima of the two functions agreed. The gauge mode has to be taken into account, because of the error in determining  $u^*$ . These parameters should depend on time  $\tau$  as  $a(\tau) = a_0 e^{\lambda\tau}$  and  $b(\tau) = b_0 e^{(1-\lambda)\tau}$ . So from the fit the eigenvalue  $\lambda$  could be determined. From Fig. 5.19 one sees, that the value of  $\lambda$  computed from  $a(\tau)$  is close to the “exact” value of 5.5846. Unfortunately  $b(\tau)$  is not so well behaved (see Fig. 5.20).

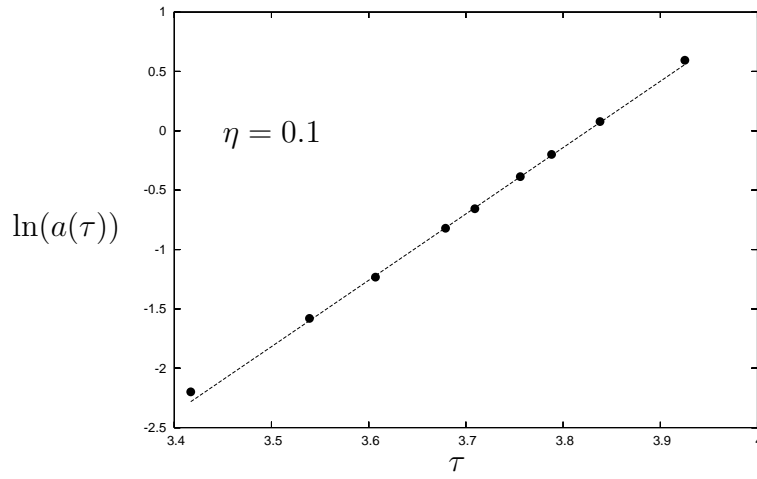


Figure 5.19: The parameter  $a$  of Fig. 5.19 in dependence of  $\tau$  (dots). The solid line has a slope of 5.5846, corresponding to the eigenvalue  $\lambda$  computed from the perturbation analysis.

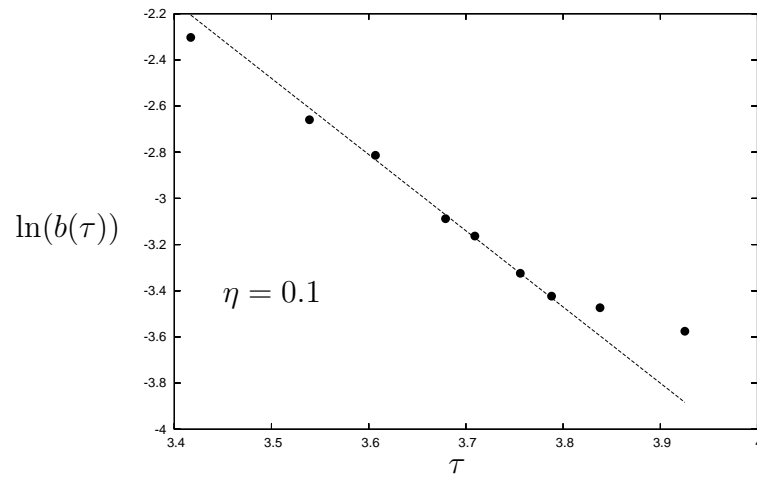


Figure 5.20: The parameter  $b$  of Fig. 5.18 in dependence of  $\tau$  (dots). The solid line has a slope of  $-3.3$ , which would correspond to an eigenvalue  $\lambda = 4.3$ .



already have damped out. In adapted coordinates with slightly different  $u^*$  this would read  $\phi(\tau, z) = \phi_{CSS}(z) + e^{\lambda\tau}y(z) + e^{\tau}y_{gauge}(z)$ . Therefore we try to fit  $\delta\phi(\tau, z) = \phi(\tau, z) - \phi_{CSS}(z)$  to the function  $f(\tau, z) = a(\tau)(y(z) + b(\tau)y_{gauge}(z))$  adjusting  $a$  and  $b$  such that the maxima agree. The fitted parameters then should behave as  $a(\tau) = a_0e^{\lambda\tau}$  and  $b(\tau) = b_0e^{(1-\lambda)\tau}$ . Figs. 5.19 and 5.20 show that  $a(\tau)$  is in good agreement with the above formulae, whereas  $b(\tau)$  is slightly off.

## 5.8 Critical Phenomena for Intermediate Couplings – Transition from CSS to DSS

Finally we describe the region of couplings  $0.14 \lesssim \eta \lesssim 0.18$ , where the transition from CSS to DSS as critical solution takes place. We know from the last sections (Sec. 5.6 and Sec. 5.7) that for  $\eta < 0.14$  the critical solution is the first CSS excitation whereas for  $\eta \geq 0.2$  the critical solution is DSS. Furthermore in Sec. 4.5.1 we proposed the hypothesis, that the DSS solution merges with the CSS solution at  $\eta \simeq 0.17$  in a homoclinic loop bifurcation and does not exist for smaller  $\eta$ . While our numerical results for the stability of the DSS solution at  $\eta = 0.1726$  are not conclusive (Sec. 4.4.7) it is reasonable to assume that the DSS solution does not change stability.

We start by describing the intermediate asymptotics of near critical evolutions. In the whole range of couplings we find a behavior, which we call “episodic CSS”, that is: the near critical solution approaches the CSS solution  $\phi_{CSS}$ , goes away, approaches its negative  $-\phi_{CSS}$ , goes away etc. until after a small number of such episodes it finally parts to form either a black hole or to disperse. The culmination times  $u^*$  associated with each episode increase with the episodes.

In the following we will describe the critical phenomena we find for the two coupling constants  $\eta = 0.1726$ , where we have constructed the DSS solution, and  $\eta = 0.16$ , where we think, that the DSS solution does not exist.

For  $\eta = 0.1726$  the evolution could be compared to the DSS solution. We find that the DSS solution is approached better and better during the time the solution stays in the neighborhood of the “critical hyper-surface”, although not as good as at higher couplings e.g. at  $\eta = 0.2$ . In [49] we will quantitatively give the “distance” of the near critical solution to the DSS solution in some norm<sup>3</sup> for various coupling constants. These investigations show clearly that for  $\eta = 0.2$  the near critical data approach the DSS solution quickly (roughly within one cycle), stay in the vicinity (with a distance in the above norm of  $\sim 10^{-3}$ ) before they deviate. For  $\eta = 0.1726$  on the other hand the approach to the DSS solution

---

<sup>3</sup>The discretized version of  $\int_0^{r_{max}} r^2 dr |\phi(u_0, r) - \phi_{DSS}(u_0, r)|^2 / \int_0^{r_{max}} r^2 dr$ , where the DSS solution is taken at a time, that minimizes this error and is appropriately shifted in  $\ln r$  and  $r_{max}$  is  $\min(r_{outer}(u_0), r_{SSH}(u))$ .

absorbs all the time the solution stays in the neighborhood and the field only comes as close as  $\sim 10^{-2}$ , before it deviates.

A possible reason for this slow approach (as compared to larger couplings) could be that the stable modes of the DSS solution damp out much more slowly at  $\eta = 0.1726$  than at  $\eta = 0.2$ . It would be very interesting to test this behavior further, in using a higher numerical precision (quartic precision). This way the admixture of the unstable mode in the initial data could be reduced, which would prolong the time the solution stays close to the DSS solution. It should then be possible to observe a closer approach to the DSS solution at  $\eta = 0.1726$ .

Combining the approach to the DSS solution with the fact that CSS and DSS lie “close”, it is clear that we observe the above described CSS episodes.

For  $\eta = 0.16$  the CSS episodes are illustrated in Fig. 5.21. We also studied the way the evolved solution deviates from the CSS solution at the last but one episode. Fig. 5.22 shows the deviation  $\delta\phi$  together with the fitted functions  $f(\tau, z) = a(\tau)(y_{unstable}(z) + b(\tau)y_{gauge}(z))$  defined as in Sec. 5.7. Clearly the fits are not as good as for  $\eta = 0.1$  (see Fig. 5.18). Nevertheless the fits (Fig. 5.23 and 5.24) show that the maximum grows exponentially according to the unstable mode of the CSS solution.

The explanation for the episodes in this case is not as straightforward as for  $\eta = 0.1726$ . A possible explanation would be, that although the DSS solution does not exist, there are still orbits in phase space, which “mimic” a DSS critical solution, i.e. orbits, that do not close exactly, but nevertheless act as intermediate attractors.

Taking this, one would expect, that the black hole mass as well as the scalar curvature exhibit scaling, which is similar to a typical “DSS scaling”. Figs. 5.25 and 5.26 show the scaling of the scalar curvature for the families (5.17) and (5.19) at  $\eta = 0.16$ . The logarithm of the scalar curvature as a function of  $\ln(p^* - p)$  shows oscillations, but not enough of them in order to judge, whether these wiggles are superimposed on a straight line, or whether the wiggles are almost periodic. Using a higher numerical precision probably would yield a clearer picture.

Unfortunately, we were not able to produce reliable results concerning the scaling of the black hole mass at  $\eta = 0.16$ . In all the evolutions, we have looked at, we find that there are two peaks in the function  $2m/r$ , which come close to the threshold (0.995) towards the end of the evolution. The inner peak is afflicted with numerical errors, nevertheless it slows down the evolution, such that in some cases the outer peak cannot reach the threshold anymore. The result in some cases is a “broken” mass scaling. Clearly further work has to be invested here, before any conclusions can be drawn.

For  $\eta = 0.1726$ , where we assume the DSS solution to be the critical solution, although not approached as closely as at higher couplings, the scaling should be more conclusive. Fig. 5.27 shows the quantity  $\ln(\max_u \mathcal{R}(u, 0))$  for sub-critical

data of the family (5.17). A straight line with slope  $-2\gamma$  and  $\gamma = 0.1045$  was fitted to these data with naked eye. In order to investigate the fine structure more closely, this straight line was subtracted from the data. The result is shown in Fig. 5.28. The difference  $\ln(\max_u \mathcal{R}(u, 0)) - f$  is almost periodic, the period being roughly  $\Delta/2\gamma$ , where the echoing period  $\Delta$  was taken from the directly constructed DSS solution. The reason for this periodicity not being exact might lie in the fact, that the DSS solution is not approached close enough. Again higher numerical precision could clarify things.

The scaling of the black hole mass at  $\eta = 0.1726$  is shown in Fig. 5.29. The “worms” displayed approximately align along a straight line with slope  $\gamma = 0.0965$ . The wiggles again are only close to periodic, as shown in Fig. 5.30. We don’t know, whether the discontinuities in the mass scaling in Fig. 5.29 stem from a systematic error in the measurement of the black hole mass.

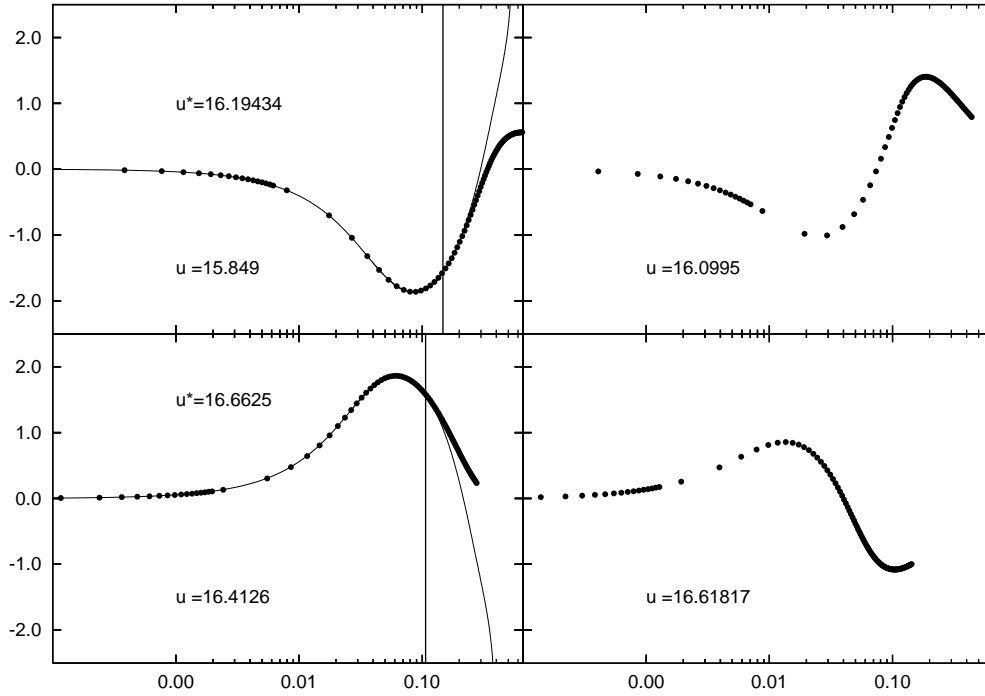


Figure 5.21: For  $\eta = 0.16$  the intermediate asymptotics of near critical data (family (5.17) with fixed width  $\sigma = 1$ ; number of grid points initially  $N = 8049$ ) are shown (dots; not every grid point is plotted). The four plots are snapshots at various times  $u$ , where  $u$  increases from left to right and from top to bottom. On the first and third plot the CSS solution is superimposed (lines), where it has been shifted (in  $\ln r$ ) horizontally such that the first monotonic region agreed best with the evolved data. (The best fit was determined automatically by a fitting script by J. Thornburg). Given the horizontal shift in  $\ln r$ , the corresponding culmination time  $u^*$  is determined, as well as the location of the past SSH, which is denoted by a vertical line in these plots. One clearly sees that the evolved data approach the CSS solution, turn away and then approach its negative. The culmination times associated with each CSS episode increase.

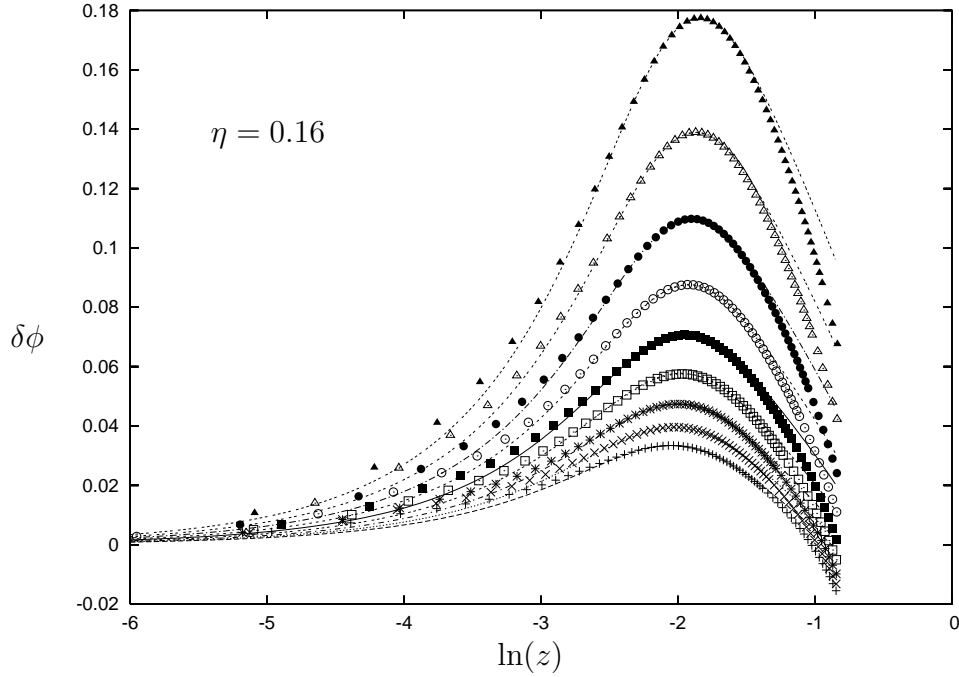


Figure 5.22: The deviation of the critical solution from the CSS solution at the last but one episode. Plotted is  $\delta\phi(\tau, z) = \phi(\tau, z) - \phi_{CSS}(z)$  at several time steps between  $\tau = 0.1576$  and  $\tau = 1.991$  (dots). As in Fig. 5.18 the functions  $a(\tau)(y_{unst} + b(\tau)y_{gauge})$  are overlaid (solid lines) with fitted values of the parameters  $a$  and  $b$ , such that the maxima agree. Again the gauge mode is taken into account in order to correct for the uncertainty in  $u^*$ . Although the agreement of the shapes is not very good, one can infer from Figs. 5.23 and 5.24, that (at least for a short time) the maximum of  $\delta\phi$  grows exponentially with a rate, which is close to the eigenvalue of the unstable mode  $\lambda = 5.202$ .

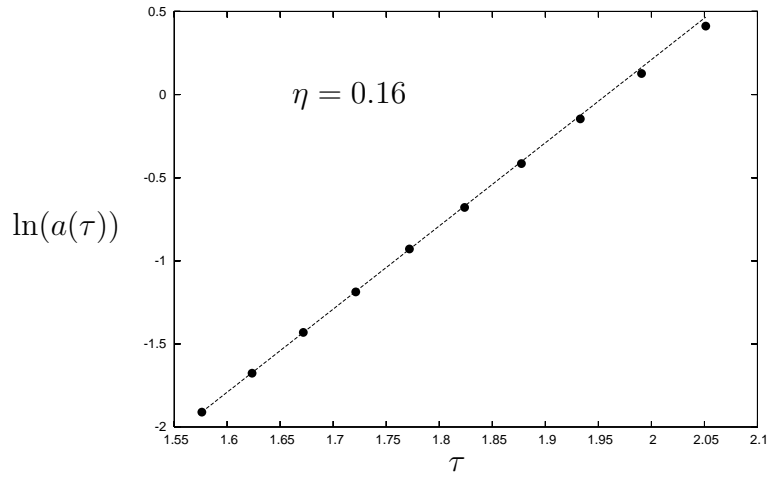


Figure 5.23: The parameter  $a$  of Fig. 5.22 in dependence of  $\tau$  (dots). The solid line has a slope of 5, which is close to the eigenvalue  $\lambda = 5.202$  computed from the perturbation analysis.

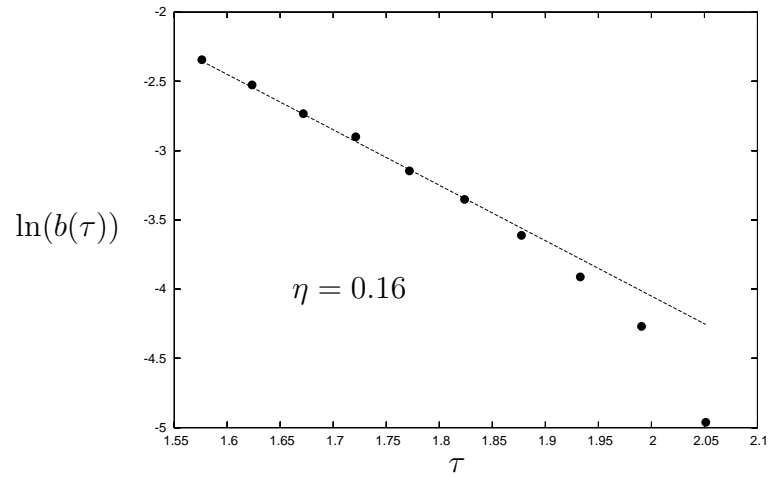


Figure 5.24: The parameter  $b$  of Fig. 5.22 in dependence of  $\tau$  (dots). The solid line has a slope of  $1 - 5 = 4$ , according to  $\ln b(\tau) = (1 - \lambda)\tau + \text{const.}$

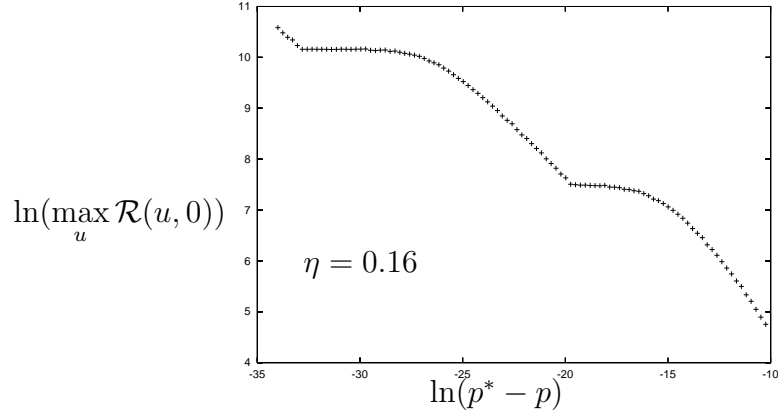


Figure 5.25: Scaling of  $\max_u \mathcal{R}(u, 0)$  for sub-critical data at  $\eta = 0.16$ . The family of initial data was (5.17) with fixed width  $\sigma = 1$ , the number of grid points was  $N = 8049$ .

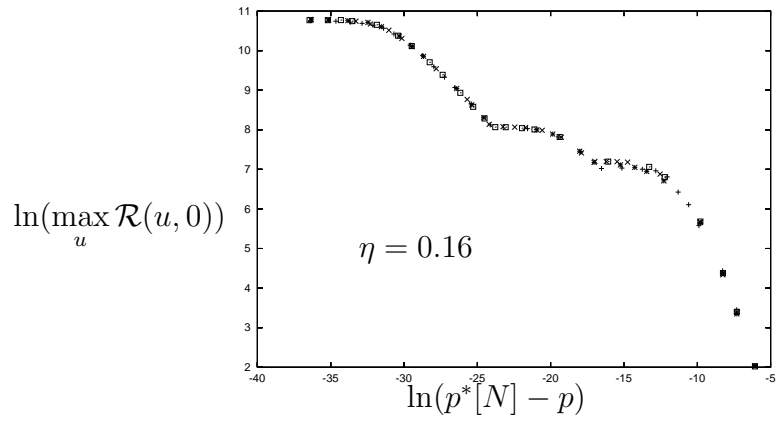


Figure 5.26: The family 5.19 qualitatively yields the same scaling as in Fig. 5.25. The resolutions shown are  $N = 500, 1000, 2000, 4000$ .

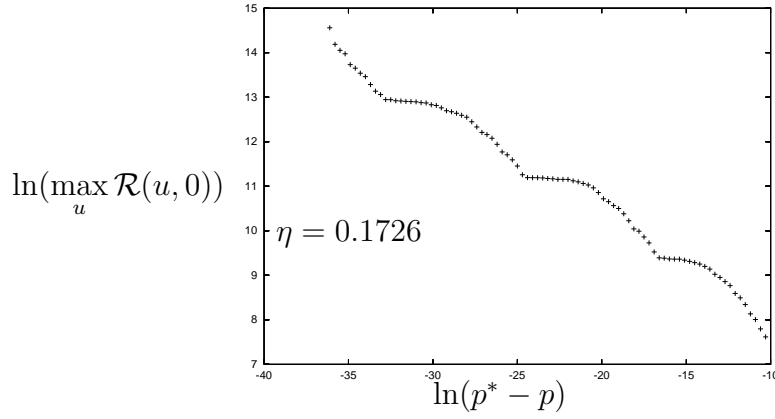


Figure 5.27: Scaling of  $\max_u \mathcal{R}(u, 0)$  for sub-critical data at  $\eta = 0.1726$ . The family of initial data was (5.17) with fixed width  $\sigma = 1$ , the number of grid points was  $N = 2000$ .

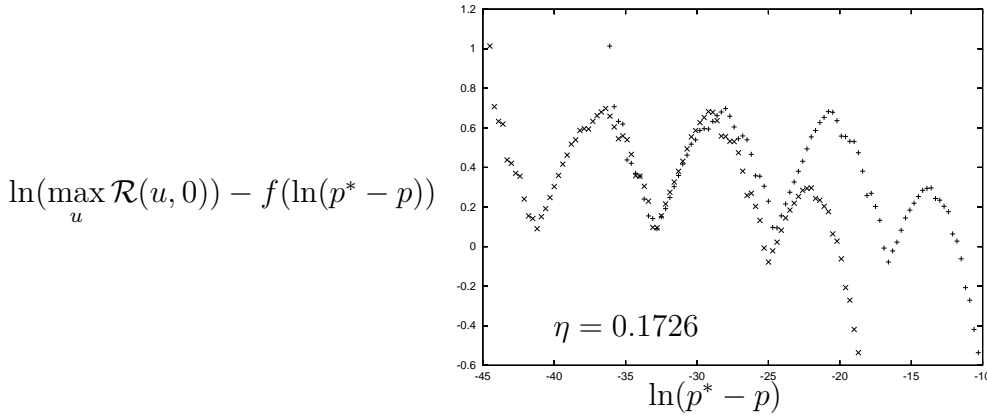


Figure 5.28: The straight line  $f(\ln(p^* - p)) = -2\gamma \ln(p^* - p) + k$  was fitted to  $\ln \max_u \mathcal{R}(u, 0)$  in Fig. 5.27 with naked eye. The fit gave  $\gamma \simeq 0.1045$ . In order to look at the fine structure this function was subtracted from the scalar curvature. The result is shown in this figure (“+”). In order to check for periodicity, the same data were re-plotted (“x”), with a shift in  $\ln(p^* - p)$  of  $\Delta/2\gamma$ . As can be seen, the periodicity is not exact, but close.



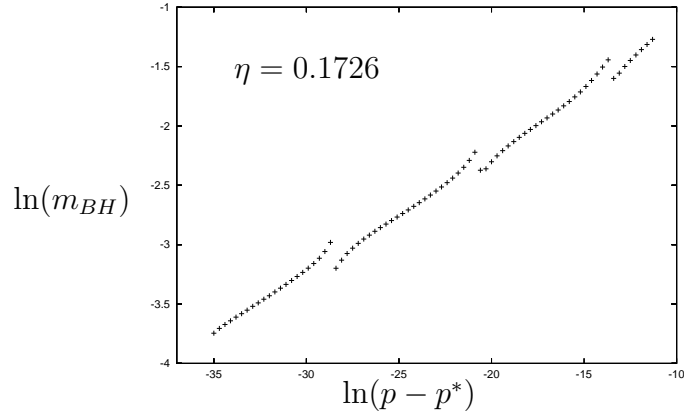


Figure 5.29: Scaling of the black hole mass for super-critical data at  $\eta = 0.1726$  (family (5.17) with fixed width  $\sigma = 1$ , number of grid points was  $N = 2000$ ). Almost all of the runs in this plot stopped because of  $du < 10^{-14}u$ .

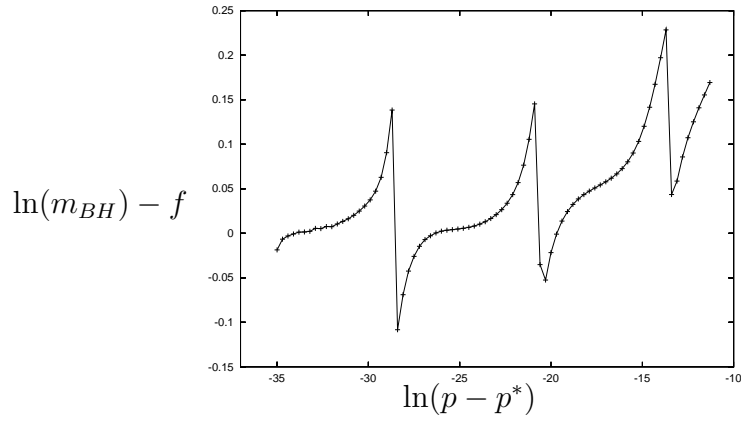


Figure 5.30: The straight line  $f(x) = \gamma x + k$  with  $\gamma = 0.0965$  was subtracted from the data in Fig. 5.29. The result is an almost periodic function of  $\ln(p - p^*)$  with a period roughly equal to  $\Delta/2\gamma$ .

# Chapter 6

## Discussion and Outlook

In this thesis we have reported on our work on the self-gravitating  $SU(2)$   $\sigma$  model in spherical symmetry. We have described our results concerning static solutions in the presence of a positive cosmological constant  $\Lambda$ , on self-similar solutions and on type II critical phenomena.

We have shown numerically that the model (with a positive cosmological constant) admits a discrete one-parameter family of static spherically symmetric regular solutions. These solitonic solutions are characterized by an integer excitation number  $n$ . A given excitation will only exist up to a critical value of the coupling constant  $\eta$ ; the higher  $n$ , the lower the corresponding critical value. Our calculations indicate that the infinite tower of solitons present on a de Sitter background persists at least up to a value of  $\eta = 1/2$ . Thus there exists a  $\eta \geq 1/2$  beyond which the number of excitations is finite and decreases with the strength of the coupling. Qualitatively the  $\sigma$  model under consideration shows striking similarities to the EYM system as studied in detail by Volkov et.al. [75]. The main difference being that the static solutions to the EYM-system depend on the value of the cosmological constant while in our case  $\Lambda$  scales out from the equations and  $\eta$  plays the role of a “bifurcation” parameter. Another difference concerns the globally regular static solutions with compact spatial slices. For the EYM system these appear for definite values of  $\Lambda(n)$  while for the  $\sigma$  model the corresponding solutions exist only in the (singular) limit as  $\Lambda$  goes to zero and definite values of  $\eta$ . Thus in our case there are closed static universes with vanishing cosmological constant, the lowest excitation being the static Einstein cosmos. This is possible because in this case the stress-energy tensor of the  $\sigma$  field is of the form of a perfect fluid with the equation of state  $p = -\mu/3$ . Another interesting aspect is the geometry of a given excitation as a function of the coupling strength: the static region is always surrounded by a Killing horizon separating the static from a dynamical region, which for small couplings becomes asymptotically de Sitter. As the coupling is increased the two-spheres of symmetry beyond the horizon are first past and then become future trapped and

a cosmological singularity develops. Finally, for even stronger couplings, again the region beyond the horizon collapses, but within the static region the in- and outgoing directions (as defined by the sign of the expansion for null geodesics) interchange.

An important question to be answered is whether these solitons are stable under small radially symmetric time dependent perturbations. Here we have presented preliminary results, stating that for  $\Lambda > 0$  all excitations are unstable with their number of unstable modes increasing with  $n$ . This was to be expected at least for small coupling. The lowest excitation thus has a single unstable mode and it is known, from other models, that such a solution can play the role of a critical solution in a full dynamical treatment of spherically symmetric collapse.

As a further step, it would be interesting to study existence and stability of static solutions to this model, that have no regular center of spherical symmetry, but rather a static region, which is bounded by two horizons, in analogy to the Schwarzschild-de-Sitter (Kottler) spacetime. This is currently investigated by N. Müllner [59].

In a further part of this thesis we have numerically reproduced the results of Bizon and Wasserman [11] concerning continuously self-similar solutions to the self-gravitating  $\sigma$ -model in spherical symmetry. We also supplemented this work with a stability analysis. As in [11] we find that a countably infinite spectrum of CSS solutions exists up to a maximal coupling  $\eta = 0.5$ . For vanishing coupling  $\eta = 0$ , the ground state of this family was already given in closed form by Turok and Spergel [73]. The homothetic Killing vector, generating continuous self-similarity, is timelike inside the past self-similarity horizon (the backwards light cone of the culmination point, where in the coupled case a space time singularity occurs). For small couplings all members of the family are regular up to the future self-similarity horizon. For larger couplings – the critical coupling depending on the excitation number – these solutions contain marginally trapped surfaces. A linear stability analysis, carried out with two different (numerical) methods, revealed that the number of unstable modes corresponds to the excitation number of the solution. In particular the ground state is stable and the first excitation has one unstable mode.

The stability properties of the CSS ground state and the first CSS excitation make these solutions relevant for the dynamics of the system. We have shown, that for very small couplings the CSS ground state is the global “end state” for a set of initial data. The singularity at the culmination point in general is not shielded by a horizon, such that the CSS ground state gives rise to the formation of naked singularities. Although the formation of naked singularities is a general end state in this model for small couplings, this behavior cannot be viewed as a violation of the cosmic censorship hypothesis. The blow up (of the energy density) also occurs in flat space, the formation of naked singularities therefore is not due to gravity, but to the matter model itself. On the contrary gravity regularizes these

singularities in the sense, that for bigger couplings the only possible end states for “strong” initial data are black holes.

The first excitation, which lies at the threshold of singularity formation in flat space [10] also is the critical solution between black hole formation and dispersion for small couplings (respectively between the formation of naked singularities and dispersion for very small couplings).

For large couplings on the other hand, the solution at the threshold of black hole formation is discretely self-similar. Both our results of time evolution and critical searches on one hand and the “direct construction” using the (discrete) symmetry and pseudo-spectral methods on the other hand show, that the period  $\Delta$  of the DSS solution rises sharply below  $\eta \simeq 0.3$ . We were able to construct the DSS solution down to a coupling of  $\eta = 0.1726^1$ . At this lowest coupling we compared the DSS solution to the first CSS excitation, and found that there exists a phase of the DSS solutions, where the shapes of both functions agree rather well. At  $\eta = 0.18$  the agreement is not so good. This suggests that the DSS solution bifurcates from the CSS solution at some coupling  $\eta_C$ . Due to the fact, that the CSS solution does not change its stability around  $\eta_C$  we suggest, that the bifurcation is a global bifurcation (in contrast to a local bifurcation), and furthermore that we deal with a homoclinic loop bifurcation. The theory then predicts, that the period  $\Delta$  scales as the logarithm of  $\eta_C - \eta$ . A fit determined  $\eta_C \sim 0.17$ . The results of the stability analysis of the DSS solution are in good agreement with the scaling of the black hole mass and the Ricci scalar: the DSS solution has one unstable mode with an eigenvalue of  $\lambda \sim 9.0$ , which is almost independent of  $\eta$ . At  $\eta = 0.1726$  the numerical results of the stability analysis are not conclusive.

In view of the above described bifurcation scenario, we can expect the critical phenomena in the transition region, where the critical solution changes from CSS to DSS, to be rather complicated. Our results support the following view: at couplings  $\eta \gtrsim 0.17$ , where the DSS solution exists, it is the critical solution. Due to the “closeness” of the DSS and CSS solution, the CSS solution is approached (and left) in several “episodes”. Presumably at couplings close to  $\eta_C$  the stable modes of the DSS solution damp out more slowly than at larger couplings. With the given numerical precision near critical data therefore cannot approach the DSS solution as close as at higher couplings. This results in a periodicity of quantities like  $2m/r$ , which is not exact, as well as in a scaling of the Ricci scalar, which has not an exactly periodic fine structure. Increasing the numerical precision, we could reduce the admixture of the unstable mode in the initial data, thereby prolonging the “life time” of the critical solution. We speculate, that then it would be possible to see an approach to the DSS solution which is as close as at larger couplings.

---

<sup>1</sup>Proceeding further down would need more Fourier coefficients and therefore would increase the computational costs considerably.

At couplings below the bifurcation value of  $\eta_C \sim 0.17$ , we see near critical evolutions approach a configuration which still has some resemblance to discrete self-similarity and which shows CSS episodes. Speaking in terms of dynamical systems it is possible, that the critical solution now has not an exact symmetry, but is an invariant manifold of orbits, that “almost” close. In phase space this invariant manifold lies in the vicinity of the CSS solution. The smaller the coupling, the more pronounced are the CSS episodes, until at a coupling of  $\eta \sim 0.14$  the CSS solution is approached only once and is the critical solution.

To our knowledge this kind of transition from CSS to DSS in the critical solution and the phenomenon of a homoclinic loop bifurcation, has not been observed up to now in the context of type II critical collapse. Liebling and Choptuik for example [52] report on a transition from CSS to DSS in the Brans-Dicke model<sup>2</sup>. But this transition is connected to a change in the stability of the CSS solution.

Further work has to concretize some of the above results mainly with numerical methods. The code would need some improvement for the treatment of the origin, and it has to be tested with respect to convergence for (very) small couplings. Concerning the possible end states for strong initial data at very small couplings it would be interesting to determine the transition (in  $\eta$ ) from naked singularities to black holes more precisely. For small couplings, where the critical solution is CSS, it would be necessary to trace down why the critical exponent deviates by a few percent from the theoretically predicted value. Convergence tests and using a higher numerical precision could give first hints. In order to investigate the phenomena of episodic CSS in more detail, the first step could consist again in using a higher numerical precision.

The “DSS code” could be used to study discretely self-similar or time periodic solutions in other models. In particular it would be interesting to investigate, whether gravity is responsible for the existence of discretely self-similar solutions. As suggested by P. Bizon [9], a first step into this direction would be to study a certain artificial matter model in flat space with a self-interaction which mimics the interaction with gravity.

---

<sup>2</sup>It might be interesting to note, that this Brans-Dicke model in spherical symmetry can be viewed as a  $\sigma$  model with a two-dimensional target manifold of constant negative curvature.

# Appendix A

## The Shooting and Matching Method

As the shooting and matching method is used at several places in this work, we give a short description of it here. A good description of this method can be found e.g. in [63]. Consider the following ODE boundary value problem, given by a coupled system of  $N$  ODEs,

$$\dot{y}^i(t) = F^i(y, t), \quad i = 1, \dots, N. \quad (\text{A.1})$$

and the following  $N$  Dirichlet boundary conditions at the ends of the interval  $[a, b]$ ,

$$\begin{aligned} g_l^j(y(a)) &= 0, & j &= 1, \dots, M, \\ g_r^k(y(b)) &= 0, & k &= 1, \dots, N - M. \end{aligned} \quad (\text{A.2})$$

So  $M$  variables at the left boundary depend on the remaining  $N - M$  variables, which are free parameters  $a_k, k = 1, \dots, N - M$ , and on the right boundary there are  $N - M$  variables, that depend on  $M$  free parameters  $b_j, j = 1, \dots, M$ .

After choosing the values of  $N - M$  variables at the left boundary and  $M$  variables at the right boundary, which we subsume with  $\vec{c} = (a_k, b_j)$ , Eqs. (A.1) can be integrated from both ends of the interval to some matching point  $t_{match} \in (a, b)$ . Of course the values of the solutions  $y(t_{match})$  at the matching point resulting from the integration from left and from right will in general not agree, but there will be a “miss distance”

$$\begin{aligned} f^i(\vec{c}) &= y_{left}^i(t_{match}; a_k) - y_{right}^i(t_{match}; b_j) & i &= 1, \dots, N, k = 1, \dots, N - M, \\ & & j &= 1, \dots, M. \end{aligned} \quad (\text{A.3})$$

If  $F$  is smooth, then  $f$  will depend smoothly on the parameters  $\vec{c}$ . The aim now is to find those values of the parameters for which  $f$  evaluates to zero<sup>1</sup>. This can

---

<sup>1</sup>It might be convenient to replace the solutions  $y^i$  on the right hand side of (A.3) by some function thereof

be achieved via a Newton iteration. For values  $\vec{c}$  close to the initial guess  $\vec{c}_0$ , the miss distance can be expanded as

$$f^i(\vec{c}) = f^i(\vec{c}_0) + \frac{\partial f^i(\vec{c}_0)}{\partial c^j} (c^j - c_0^j) + O((\vec{c} - \vec{c}_0)^2). \quad (\text{A.4})$$

If the initial guess  $\vec{c}_0$  is close to a zero of  $f$  a first approximation to this zero is given by  $\vec{c}$  with

$$0 = f^i(\vec{c}_0) + \frac{\partial f^i(\vec{c}_0)}{\partial c^j} (c^j - c_0^j), \quad (\text{A.5})$$

neglecting the higher order terms. If furthermore the Jacobian  $J^i_j(\vec{c}_0) = \partial f^i / \partial c^j|_{\vec{c}_0}$  is invertible we can solve for  $\vec{c}$ ,

$$c^i = c_0^i - (J^{-1})^i_j(\vec{c}_0) f^j(\vec{c}_0). \quad (\text{A.6})$$

If  $f$  depends linearly on the parameters, then one step is enough, for nonlinear relations several steps have to be applied in order to approach the zero.

Numerically, the Jacobian is computed by first integrating the ODEs (A.1) with the initial guess  $\vec{c}_0$ , and then with the  $N$  perturbed values  $\vec{c}_0 + \delta\vec{c}_k$ ,  $k = 1, \dots, N$  and  $(\delta c_k)^i = \epsilon \delta^i_k$ . The Jacobian can then be obtained by e.g. forward differencing

$$J^i_k(\vec{c}_0) = \frac{f^i(\vec{c}_0 + \delta\vec{c}_k) - f^i(\vec{c}_0)}{\epsilon}. \quad (\text{A.7})$$

# Appendix B

## Discrete Fourier Transform

In suitably chosen coordinates discrete self-similarity manifests itself in a periodic dependence on one of the coordinates. This suggests to work with Fourier expansions. The problem of constructing a DSS solution then reduces to an ODE boundary value problem for the Fourier coefficients. In Sec. B.1 we review the basic properties of Fourier series and truncated Fourier series. In practice we don't work with truncated Fourier series, but with the discrete Fourier transform, which establishes a relation between  $N$  discrete Fourier coefficients and the values of the function at  $N$  “grid points” in real space. The discrete Fourier transform can be viewed as the discrete approximation to the (continuous) Fourier transform. (see Sec. B.2). In Sec. B.3 we define differentiation within this framework. Sec. B.4 explains how algebraic manipulations are executed in “real” space, involving a pair of forward and backward transformations. There has to be taken special care in order to reduce aliasing errors, that result from such a process.

This appendix follows closely [16], which gives a good description of discrete Fourier transform, pseudo-spectral methods and aliasing errors. We only give the basic definitions and cite the main results. For further details and proofs we refer to [16]. Our discussion concerns functions defined on the interval  $[0, 2\pi]$ . For functions, that are defined on the interval  $[0, \Delta]$  any occurrence of the independent variable  $x$  has to be replaced by  $2\pi x/\Delta$ .

### B.1 Truncated Fourier Series

Consider the Hilbert space of (Lebesgue-) square integrable functions  $L^2(0, 2\pi)$  with scalar product

$$(u, v) = \int_0^{2\pi} u(x) \bar{v}(x) \, dx \quad (\text{B.1})$$



and norm

$$||u|| = \int_0^{2\pi} |u(x)|^2 dx. \quad (\text{B.2})$$

The functions  $\phi_k(x) = e^{ikx}$ ,  $k \in \mathbb{Z}$  form an orthogonal system with respect to this scalar product B.1

$$\int_0^{2\pi} \phi_k(x) \bar{\phi}_l(x) dx = 2\pi \delta_{kl}. \quad (\text{B.3})$$

For  $u \in L^2(0, 2\pi)$  the Fourier coefficients of  $u$  are given by

$$\hat{u}_k = \frac{1}{2\pi} \int_0^{2\pi} u(x) e^{-ikx} dx \quad k \in \mathbb{Z}. \quad (\text{B.4})$$

If  $u$  is real then  $\hat{u}_{-k} = \bar{\hat{u}}_k$ .

The (formal) Fourier series of  $u$  is given by

$$Su(x) = \sum_{k=-\infty}^{\infty} \hat{u}_k \phi_k(x). \quad (\text{B.5})$$

The *truncated Fourier series of order  $N$* <sup>1</sup> is the trigonometric polynomial of degree  $N/2$

$$P_N u(x) = \sum_{k=-N/2}^{N/2-1} \hat{u}_k e^{ikx} \quad (\text{B.6})$$

Defining the space of trigonometric polynomials of degree  $N/2$  as

$$S_N = \text{span}\{e^{ikx} \mid -N/2 \leq k \leq N/2 - 1\} \quad (\text{B.7})$$

$P_N u$  is the orthogonal projection of  $u$  upon the space  $S_N$  with respect to the scalar product B.1,

$$(P_N u, v) = (u, v) \quad \text{for all } v \in S_N. \quad (\text{B.8})$$

Equivalently  $P_N u$  is the closest approximation of  $u$  within  $S_N$  with respect to the norm B.2.

For  $u \in L^2(0, 2\pi)$  the Fourier series of  $u$ ,  $Su(x)$  converges to  $u$  in the  $L^2$  norm B.2, that is

$$\int_0^{2\pi} |u(x) - P_N(x)|^2 dx \rightarrow 0 \quad \text{as } N \rightarrow \infty. \quad (\text{B.9})$$

---

<sup>1</sup>The convention to discuss truncated Fourier series in terms of the trigonometric polynomial of degree  $N/2$  rather than  $N$  is not common in the literature but is special to [16]

The Parseval identity states that

$$||u||^2 = 2\pi \sum_{k=-\infty}^{\infty} |\hat{u}_k|^2, \quad (\text{B.10})$$

in particular the series on the right hand side converges. If  $u$  satisfies additional criteria, the convergence B.9 can be improved. E.g. if  $u$  is continuous, periodic ( $u(0^+) = u(2\pi^-)$ ), and of bounded variation on  $[0, 2\pi]$ , then  $Su$  is uniformly convergent, i.e.

$$\max_{x \in [0, 2\pi]} |u(x) - P_N(x)| \rightarrow 0 \quad \text{as } N \rightarrow \infty. \quad (\text{B.11})$$

Concerning the rate of convergence the Parseval identity B.10 gives the following

$$||u - P_N|| = \left( 2\pi \sum_{\substack{k < -N/2 \\ k \geq N/2}} |\hat{u}_k|^2 \right)^{1/2}. \quad (\text{B.12})$$

On the other hand for  $u$  sufficiently smooth and periodic we have

$$\max_{x \in [0, 2\pi]} |u(x) - P_N(x)| \leq \sum_{\substack{k < -N/2 \\ k \geq N/2}} |\hat{u}_k|^2. \quad (\text{B.13})$$

So the rate of convergence of the Fourier series is connected to how fast the Fourier coefficients of  $u$  decay.

We are interested in the following result: if  $u$  is smooth ( $C^\infty$ ) and periodic with all its derivatives on  $[0, 2\pi]$  then the Fourier coefficients  $\hat{u}_k$  decay faster than any negative power of  $k$ . Of course this only applies for  $k$  bigger than some  $k_0$ , the minimal frequency which is needed to represent the essential structure of  $u$ .

Combining this with the formulae for the error (B.12), (B.13) one finds that for  $u$  satisfying the above conditions the error between  $u$  and the truncated Fourier series decays faster than any negative power of  $N$ . This is called *spectral accuracy*, *exponential convergence* or *infinite order accuracy*.

## B.2 Discrete Fourier Transform

For any integer  $N > 0$  consider the “grid points”

$$x_j = \frac{2\pi j}{N} \quad j = 0, \dots, N-1, \quad (\text{B.14})$$

where for our purposes we assume  $N$  to be even. If  $u$  is known at these grid points, then the *discrete Fourier transform* (DFT) of  $u$  is given by

$$\tilde{u}_k = \frac{1}{N} \sum_{j=0}^{N-1} u(x_j) e^{-ikx_j} \quad -N/2 \leq k \leq N/2 - 1. \quad (\text{B.15})$$

As the  $e^{ikx_j}$  satisfy the orthogonality relation

$$\frac{1}{N} \sum_{j=0}^{N-1} e^{ipx_j} = \begin{cases} 1 & \text{if } p = Nm, m \in \mathbb{Z} \\ 0 & \text{otherwise,} \end{cases} \quad (\text{B.16})$$

the *inverse transform* is given by

$$u(x_j) = \sum_{k=-N/2}^{N/2-1} \tilde{u}_k e^{ikx_j} \quad j = 0, \dots, N-1. \quad (\text{B.17})$$

From a computational point of view, the discrete Fourier transform (B.15) involves  $N^2$  multiplications. It is therefore an “ $O(N^2)$ ”-process. Fortunately there exists a less expensive way to compute the  $N$  coefficients  $\tilde{u}_k$ , which is called *Fast Fourier Transform* (FFT). If  $N$  is an integer power of 2, then the computational costs for the discrete Fourier transform using FFT are only of order  $N \log_2 N$ . A good description of the FFT can be found e.g. in [63].

The polynomial

$$I_N u(x) = \sum_{k=-N/2}^{N/2-1} \tilde{u}_k e^{ikx} \quad (\text{B.18})$$

is the  $N/2$  degree *trigonometric interpolant* at the grid points B.14, i.e.  $I_N u(x_j) = u(x_j)$ . This polynomial is also called the *discrete Fourier series* of  $u$ .

The discrete Fourier coefficients  $\tilde{u}_k$  can be regarded as a discrete approximation to the continuous Fourier coefficients  $\hat{u}_k$ , in that using the trapezoidal rule to evaluate the integral B.4 gives  $\tilde{u}_k$ .

The discrete approximation to the inner product B.1 on the space  $S_N$  (B.7) is given by

$$(u, v)_N = \frac{2\pi}{N} \sum_{j=0}^{N-1} u(x_j) \bar{v}(x_j). \quad (\text{B.19})$$

Due to (B.16) it coincides with the inner product B.1 if  $u, v \in S_N$ , i.e.

$$(u, v)_N = (u, v) \quad \text{for all } u, v \in S_N. \quad (\text{B.20})$$

The interpolation operator  $I_N$  can be regarded as an orthogonal projection operator upon the space  $S_N$  with respect to the scalar product (B.19), as

$$(I_N u, v)_N = (u, v)_N \quad \text{for all } v \in S_N \quad (\text{B.21})$$

trivially. Therefore  $I_N u$  is the best approximation to  $u$  within the space  $S_N$  with respect to the norm  $\|u\|_N = \sqrt{(u, u)_N}$ .

The discrete Fourier transform of  $u$  (B.15) can be expressed in terms of the continuous Fourier coefficients of  $u$  (B.4): if  $Su(x_j) = u(x_j)$  one obtains by using the relation (B.16)

$$\tilde{u}_k = \hat{u}_k + \sum_{\substack{m=-\infty \\ m \neq 0}}^{\infty} \hat{u}_{k+Nm}. \quad (\text{B.22})$$

This means that the  $k$ -th mode of the trigonometric interpolant does not only depend on the  $k$ -th mode of  $u$  but also on all the  $(k + Nm)$ -th modes (which cannot be distinguished from the  $k$ -th frequency at the grid points (B.14)). This effect is called *aliasing*.

We can write

$$I_N u = P_N u + R_N u, \quad (\text{B.23})$$

where

$$R_N u(x) = \sum_{k=-\infty}^{\infty} \left( \sum_{\substack{m=-\infty \\ m=0}}^{\infty} \hat{u}_{k+Nm} \right) e^{ikx}. \quad (\text{B.24})$$

$R_N u$  is orthogonal to  $u - P_N u$  with respect to the scalar product (B.1) and therefore we have

$$\|u - I_N u\|^2 = \|u - P_N u\|^2 + \|R_N u\|^2. \quad (\text{B.25})$$

So the error of the discrete Fourier series is always larger than the error of the truncated Fourier series, due to  $R_N u$ , which is called *aliasing error*. Nevertheless it can be shown, that asymptotically the truncation errors and the interpolation errors decay at the same rate.

The sequence of interpolation polynomials shows similar convergence properties as the sequence of truncated Fourier series. E.g. for  $u$  continuous, periodic and of bounded variation on  $[0, 2\pi]$ ,  $I_N u$  converges uniformly to  $u$  on  $[0, 2\pi]$ . Concerning the fall off of the discrete Fourier coefficients we have e.g. for  $u$  being  $C^\infty$  and periodic with all its derivatives: for any fixed  $k \neq 0$  and any positive  $N$  such that  $N/2 > |k|$ , let  $\tilde{u}_k = \tilde{u}_k^{(N)}$  be the  $k$ -th Fourier coefficient of  $I_N u$ . Then Eq. B.22 shows, that  $|\tilde{u}_k^{(N)}|$  decays faster than algebraically in  $k^{-1}$ , uniformly in  $N$ . Using analogous arguments as in Sec. B.1, we therefore get, that the error between a periodic  $C^\infty$  function and its discrete Fourier series decays faster than any negative power of  $N$ .

In this work we use a slightly modified interpolating polynomial. First we define

$$a_0 = \frac{1}{N} \sum_{j=0}^{N-1} u(x_j) \quad (\text{B.26})$$

$$a_l = \frac{2}{N} \sum_{j=0}^{N-1} u(x_j) \cos\left(\frac{2\pi l j}{N}\right) \quad l = 1, \dots, N/2 - 1 \quad (\text{B.27})$$

$$b_l = \frac{2}{N} \sum_{j=0}^{N-1} u(x_j) \sin\left(\frac{2\pi l j}{N}\right) \quad l = 1, \dots, N/2 - 1 \quad (\text{B.28})$$

$$a_{N/2} = \frac{1}{N} \sum_{j=0}^{N-1} u(x_j) \cos(\pi k), \quad (\text{B.29})$$

so

$$\begin{aligned} \tilde{u}_k &= \frac{1}{2}(a_k - ib_k), \quad -N/2 + 1 \leq k \leq N/2 - 1, k \neq 0 \\ \tilde{u}_0 &= a_0, \quad \tilde{u}_{-N/2} = a_{-N/2}. \end{aligned} \quad (\text{B.30})$$

As  $a_{-k} = a_k$  and  $b_{-k} = -b_k$  we can re-write the expression for  $u$  at the grid points (B.17)

$$u(x_j) = a_0 + \sum_{k=1}^{N/2-1} a_k \cos(kx_j) + \sum_{k=1}^{N/2-1} b_k \sin(kx_j) + a_{N/2} \cos\left(\frac{N}{2}x_j\right). \quad (\text{B.31})$$

We now define the interpolating polynomial  $\tilde{I}_N u$  to be

$$\tilde{I}_N u(x) = a_0 + \sum_{k=1}^{N/2-1} a_k \cos(kx) + \sum_{k=1}^{N/2-1} b_k \sin(kx) + a_{N/2} \cos\left(\frac{N}{2}x\right) \quad (\text{B.32})$$

By definition  $\tilde{I}_N u(x)$  agrees with  $I_N u(x)$  at the grid points, but differs from the latter in between (the difference arising solely in the  $N/2$  frequency term).

## B.3 Differentiation

The derivative of  $\tilde{I}_N u(x)$  with respect to  $x$  is given by

$$(\tilde{I}_N u)'(x) = \sum_{k=1}^{N/2-1} a_k (-k) \sin(kx) + \sum_{k=1}^{N/2-1} b_k k \cos(kx) - a_{N/2} \frac{N}{2} \sin\left(\frac{N}{2}x\right) \quad (\text{B.33})$$

As  $\sin(\frac{N}{2}x)$  vanishes at the grid points  $x_j$ , we define the connection between the coefficients of the *collocation derivative* of  $u$  and the coefficients of  $\tilde{I}_N u$  to be

$$\begin{aligned} (ap)_0 &= 0 \\ (ap)_k &= k b_k \quad k = 1, \dots, N/2 - 1 \\ (bp)_k &= -k a_k \quad k = 1, \dots, N/2 - 1 \\ (ap)_{N/2} &= 0, \end{aligned} \quad (\text{B.34})$$

where  $(ap)_k$  and  $(bp)_k$  denote the coefficients of the collocation derivative. Note that interpolation and differentiation do not commute, unless  $u \in \tilde{S}_N$ . One can show that collocation differentiation is spectrally accurate.

## B.4 Pseudo-spectral methods and Aliasing

The way we construct the DSS solutions (see Sec. 4.4) our basic variables are the discrete Fourier coefficients (with respect to  $\tau$ ) of the field  $\phi$ , its derivative  $\phi'$  and the metric functions  $\beta$  and  $\frac{V}{r}$ . In order to set up the ODEs (in the spatial variable  $z$ ) we have to compute the discrete Fourier coefficients of e.g. products of these functions or e.g. the sine of  $\phi$ . This can be done by applying the inverse Fourier transform (B.17) to the coefficients, carrying out the algebraic manipulations and taking the sine in “ $\tau$ -space” and then transforming the result back to Fourier space. The overall computational scheme therefore includes operations carried out in Fourier space as well as operations carried out in “ $\tau$ -space”. Such a method is called *pseudo spectral method*.

This transforming back and forth has to be carried out with care if one wants to keep the aliasing errors as small as possible. To see this consider the smooth and periodic functions  $u(x)$  and  $v(x)$ , with their Taylor series expansions  $u(x) = \sum_{k=-\infty}^{\infty} \hat{u}_k e^{ikx}$  and  $v(x) = \sum_{k=-\infty}^{\infty} \hat{v}_k e^{ikx}$ . We denote their product by  $w(x)$

$$w(x) = u(x)v(x). \quad (\text{B.35})$$

The Fourier coefficients of  $w$ , then are given by

$$\hat{w}_k = \sum_{m+l=k} \hat{u}_m \hat{v}_l \quad -\infty < m, l < \infty. \quad (\text{B.36})$$

Given the discrete Fourier coefficients  $\tilde{u}_k$  and  $\tilde{v}_k$ , and the corresponding inverse transforms  $u_j = \sum_{k=-N/2}^{N/2-1} \tilde{u}_k e^{ikx_j}$  and the analogous expression for  $v_j$ , we define  $w_j$  to be their product in real space,

$$w_j = u_j v_j. \quad (\text{B.37})$$

The discrete Fourier coefficients of  $w_j$  then are given by  $\tilde{w}_k = \frac{1}{N} \sum_{j=0}^{N-1} w_j e^{-ikx_j}$  and therefore

$$\tilde{w}_k = \sum_{m+l=k} \tilde{u}_m \tilde{v}_l + \sum_{m+l=k \pm N} \tilde{u}_m \tilde{v}_l \quad -N/2 \leq m, l, k \leq N/2 - 1. \quad (\text{B.38})$$

We assume for a moment, that the coefficients  $\hat{u}_k, \hat{v}_k$  for  $k < -N/2, k \geq N/2$  are negligible. Then we have  $\tilde{u}_k \simeq \hat{u}_k, \tilde{v}_k \simeq \hat{v}_k$ , i.e. the aliasing errors due to interpolation are negligible, and the sum in (B.36) equals the first sum in (B.38) for  $-N/2 \leq k \leq N/2$ . Then clearly the second sum in (B.38) introduces an error into the product, which again is called aliasing error.

In the following, we describe a method, which reduces this error. The basic idea is to increase the number of Fourier coefficients to  $M$  before transforming to real space, carry out the manipulations in real space with this higher number of grid points, transform back to Fourier space and then throw away the additional modes. If  $M$  is chosen appropriately the second sum in (B.38) does not contribute to the relevant frequencies of  $w$ .

Let  $M > N$ . We define the following  $M$  discrete Fourier coefficients

$$\tilde{U}_k = \begin{cases} \tilde{u}_k & -N/2 < k < N/2 - 1 \\ 0 & -M/2 \leq k < -N/2; N/2 \leq k \leq M/2 \end{cases} \quad (\text{B.39})$$

and the analogous expressions for  $\tilde{V}_k$ . Given these Fourier coefficients, we get the inverse transforms  $U_j = \sum_{k=-M/2}^{M/2-1} \tilde{U}_k e^{ikx_j}$ , where  $j$  now runs from 0 to  $M-1$  and the grid points  $x_j$  are given by  $x_j = 2\pi j/M$  and the analogous expression for  $V_j$ . Let again  $W_j = U_j V_j$  and  $\tilde{W}_k = \frac{1}{M} \sum_{j=0}^{M-1} W_j e^{-ikx_j}$ , then the coefficients  $\tilde{W}_k$  are given according to (B.38)

$$\tilde{W}_k = \sum_{m+l=k} \tilde{U}_m \tilde{V}_l + \sum_{m+l=k \pm M} \tilde{U}_m \tilde{V}_l \quad -M/2 \leq m, l, k \leq M/2 - 1. \quad (\text{B.40})$$

The strategy now is to consider only the coefficients  $\tilde{W}_k$  for  $-N/2 \leq k \leq N/2 - 1$  and throw away the higher frequencies. As  $\tilde{U}_m$  and  $\tilde{V}_l$  are nonzero only for  $-N/2 \leq m, l \leq N/2 - 1$ , the first sum in (B.40) equals the first sum in (B.38) for  $-N/2 \leq k \leq N/2 - 1$ . The aim is now to choose  $M$  such, that the second sum in (B.40) does not contribute to the frequencies of interest. We have  $-N \leq m+l \leq N-2$  and  $M-N/2 \leq k+M \leq M+N/2-1$  and  $-M-N/2 \leq k-M \leq -M+N/2-1$ . So if  $M > 3N/2 - 1$  the second sum in (B.40) does not contribute to  $\tilde{W}_k$  for  $-N/2 \leq k \leq N/2 - 1$ .

For products of higher order  $M$  has to be chosen larger.

# Appendix C

## The “Diamond-Integral-Characteristic-Evolution” Code – DICE

The DICE code evolves the self-gravitating  $SU(2)$   $\sigma$  model in spherical symmetry (optionally with cosmological constant)<sup>1</sup>. Given initial data  $\phi_0(r) = \phi(u_0, r)$  at the initial null slice, Eqs. (2.48), (2.55) and (2.56) are solved numerically, while the “additional” Einstein equations, Eqs. (2.57) and (2.58) merely serve for tests of consistency and accuracy (see Sec. C.5). The diamond integral scheme by Gómez and Winicour [33, 31, 32] is used to integrate the wave equation (2.48) (see Sec. C.1). Grid points freely fall along ingoing null geodesics. The hypersurface equations (2.55) and (2.56) as well as the geodesic equation (2.20) in the latest version are integrated using a second order iterated Runge-Kutta scheme (see Sec. C.3). In the vicinity of the center of spherical symmetry the integration schemes (except for the geodesic equation) are replaced by Taylor series expansions (this follows [26]; see Sec. C.2).

The “kernel” of the DICE code was originally developed by Sascha Husa. Further improvement, development and testing of the code – including improvement of the integration scheme for the ODEs, measurement of the black hole mass, convergence tests, critical search modus etc. – was done by Michael Pürrer and Jonathan Thornburg. M. Pürrer also added the feature to evolve the massless Klein Gordon field with a compactified radial coordinate (see [64]). I helped to develop the physical and analytical foundations of the code, but did not actually participate in writing the code. A description of the DICE code can be found in [45] and in [64].

---

<sup>1</sup>It also optionally evolves the self-gravitating massless Klein-Gordon field in spherical symmetry



## C.1 The NSW E Algorithm

The “central” evolution algorithm uses the NSW E scheme by Gomez and Winicour [33, 31, 32]. It is based on the fact, that the wave operator  $\square_g$  in spherical symmetry can be expressed in terms of the wave operator in 2-dimensions  $\square_h$ , which is defined with respect to the two dimensional metric

$$ds_h^2 = -e^{2\beta} du \left( \frac{V}{r} du + 2dr \right). \quad (\text{C.1})$$

Setting  $\psi := r\phi$ , we can write

$$\square_g \phi = \frac{1}{r} \square_h \psi - \frac{e^{-2\beta}}{r^2} \left( \partial_r \frac{V}{r} \right) \psi. \quad (\text{C.2})$$

Now we use the fact, that any two dimensional metric is conformally flat, i.e. by setting  $d\tilde{u} = \frac{V}{r} du$  we have

$$ds_h^2 = \frac{e^{2\beta}}{\frac{V}{r}} ds_{\tilde{h}}^2 \quad \text{with} \quad ds_{\tilde{h}}^2 = -d\tilde{u} (d\tilde{u} + 2dr). \quad (\text{C.3})$$

The wave operator transforms under this conformal transformation as

$$\square_h \psi = e^{-2\beta} \frac{V}{r} \square_{\tilde{h}} \psi. \quad (\text{C.4})$$

Consider now the parallelogram  $\Sigma$  spanned by the four null lines  $\tilde{u} = \tilde{u}_0, \tilde{u} = \tilde{u}_1, \tilde{v} = \tilde{v}_0, \tilde{v} = \tilde{v}_1$  (see Fig. C.1)<sup>2</sup>. If we integrate Eq. C.4 over  $\Sigma$  we get

$$\int_{\Sigma} d^2x \sqrt{-h} \square_h \psi = \int_{\Sigma} d^2x \sqrt{-\tilde{h}} \square_{\tilde{h}} \psi. \quad (\text{C.5})$$

In double null coordinates  $(\tilde{u}, \tilde{v} = \tilde{u} + 2r)$ ,  $\square_{\tilde{h}}$  reads

$$\square_{\tilde{h}} \psi = -4 \partial_{\tilde{u}} \partial_{\tilde{v}} \psi, \quad (\text{C.6})$$

so (C.5) gives

$$\begin{aligned} \int_{\Sigma} d^2x \sqrt{-h} \square_h \psi &= -2 \int_{\tilde{u}_0}^{\tilde{u}_1} \int_{\tilde{v}_0}^{\tilde{v}_1} d\tilde{u} d\tilde{v} \partial_{\tilde{u}} \partial_{\tilde{v}} \psi = \\ &= 2(-\psi_N + \psi_W + \psi_E - \psi_S). \end{aligned} \quad (\text{C.7})$$

---

<sup>2</sup> $\Sigma$  is chosen such that it is bounded by two null slices, separated by one numerical time step, and the two ingoing null geodesics along which two neighbouring grid points move.

From Eqs. (2.48) and (C.2) we have

$$\square_h \psi = \frac{1}{r} e^{-2\beta} \left( \partial_r \frac{V}{r} \right) \psi + \frac{\sin(2\psi/r)}{r} \quad (\text{C.8})$$

and therefore

$$\begin{aligned} \psi_N &= \psi_W + \psi_E - \psi_S - \frac{1}{2} \int_{\Sigma} d^2x \sqrt{-h} \left( \frac{1}{r} e^{-2\beta} \left( \partial_r \frac{V}{r} \right) \psi + \frac{\sin(2\psi/r)}{r} \right) = \\ &= \psi_W + \psi_E - \psi_S - \frac{1}{2} \iint_{\Sigma} du \, dr \left( \frac{1}{r} \left( \partial_r \frac{V}{r} \right) \psi + \frac{e^{2\beta} \sin(2\psi/r)}{r} \right). \end{aligned} \quad (\text{C.9})$$

The integral on the right hand side can be approximated to second order by

$$\iint_{\Sigma} du \, dr f(u, r) \simeq \frac{1}{2} (f_E + f_W) \Delta u \, \Delta r, \quad (\text{C.10})$$

where  $\Delta u = u^{k+1} - u^k$  and  $\Delta r = \frac{1}{2}(r_E - r_S + r_N - r_W)$ .

Assuming now, that the fields  $\psi, \beta, \frac{V}{r}$  and  $\frac{V'}{r}$  are known at the points  $S, E, W$ , and that furthermore the  $r$  coordinate of  $N$  is known, then the field  $\psi$  at  $N$  can be computed via C.9 and C.10

## C.2 Treatment of the Origin

The values of the field  $\psi$  and the metric functions  $\beta$  and  $\frac{V}{r}$  close to the origin are computed using a Taylor series expansion. Using the fact that  $\psi(u, 0) = \psi'(u, 0) = 0, \partial_u \psi(u, 0) = \partial_u \psi'(u, 0) = 0$ , etc. and the field equation (2.48),  $\psi(u_0 + \Delta u, r)$  is given by

$$\psi(u_0 + \Delta u, r) = \frac{1}{2} \psi''(u_0, 0) r^2 + \frac{1}{6} \psi'''(u_0, 0) r^3 + \frac{1}{6} \psi'''(u_0, 0) r^2 \Delta u + O(\Delta^4). \quad (\text{C.11})$$

Using the hypersurface Eqs. (2.55) and (2.56) together with the Taylor expansion (C.11) the expansions of  $\beta$  and  $\frac{V}{r}$  at the time  $u_0 + \Delta u$  read

$$\begin{aligned} \beta(u_0 + \Delta u, r) &= \eta \left( \frac{1}{16} \psi''(u_0, 0)^2 r^2 + \frac{1}{24} \psi''(u_0, 0) \psi'''(u_0, 0) r^2 du + \right. \\ &\quad \left. + \frac{1}{18} \psi''(u_0, 0) \psi'''(u_0, 0) r^3 \right) + O(\Delta^4) \end{aligned} \quad (\text{C.12})$$

$$\begin{aligned} \frac{V}{r}(u_0 + \Delta u, r) &= 1 - \eta \left( \frac{1}{8} \psi''(u_0, 0)^2 r^2 + \frac{1}{12} \psi''(u_0, 0) \psi'''(u_0, 0) r^2 du + \right. \\ &\quad \left. + \frac{1}{18} \psi''(u_0, 0) \psi'''(u_0, 0) r^3 \right) + O(\Delta^4). \end{aligned} \quad (\text{C.13})$$

At the time step  $u^k$  the coefficients  $\psi''(u^k, 0)$  and  $\psi'''(u^k, 0)$  are extracted from  $\psi$  by fitting the cubic polynomial  $c_1 r^2 + c_2 r^3$  to  $\psi$  at the 5 innermost non origin

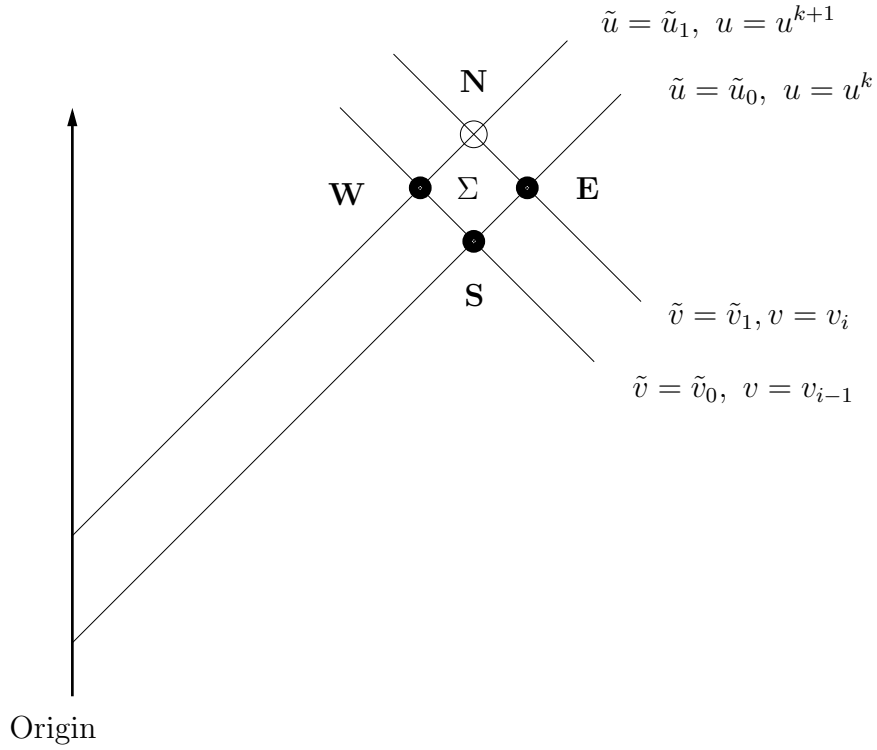


Figure C.1: A schematic diagram illustrating the NSW algorithm. The two dimensional wave operator in flat space  $\square_{\tilde{h}}$  acting on  $\psi = r\phi$  is integrated over the null parallelogram  $\Sigma$ .  $\psi_N$  therefore is given by  $\psi$  at the points S, E, W plus an integral over  $\Sigma$ .

grid points (a further version uses a fit at the time steps  $u^k$  and  $u^{k-1}$  to compute  $\psi''(u^k, 0)$  and  $\psi'''(u^k, 0)$ ).

After integrating the geodesic equation (2.20) the field  $\psi$  at the first three non origin grid points at the time step  $u^{k+1}$  is computed from (C.11). The metric functions  $\beta$  and  $\frac{V}{r}$  at these grid points then are given by (C.12).

### C.3 Integrating the Hypersurface Equations and the Geodesic Equation

As the hypersurface equations (2.55) and (2.56) at any fixed slice  $u = u^k$  are ODEs, they can be integrated using a second order iterated Runge-Kutta scheme [46]. For a general ODE  $\dot{y} = F(y, t)$ , defining

$$y_{pred}^{k+1} = y^k + \Delta t F(y^k, t^k), \quad (\text{C.14})$$

$y^{k+1}$  is given as follows

$$y^{k+1} = y^k + \frac{1}{2}\Delta t \left( F(y^k, t^k) + F(y_{pred}^{k+1}, t^{k+1}) \right). \quad (\text{C.15})$$

At the initial hypersurface, given the initial configuration  $\phi(u=0, r)$ , the metric functions can be computed by integrating the hypersurface equations with the above scheme. At any further slice  $u^k$ , the field  $\psi$  has to be computed at the  $i$ -th grid point, using the NSWE scheme, before the metric functions can be updated at this grid point, using (C.14) and (C.15).

The geodesic equation (2.20), again an ODE, also is integrated with the above method. One difficulty arises due to the fact, that at the time, we integrate the geodesic, the metric function  $\frac{V}{r}$  is not yet known at the next time step. This is solved by taking  $\frac{V}{r}$  and  $\frac{V'}{r}$  at the grid point  $i-1$  at slice  $u^{k+1}$  and doing a linear extrapolation to the  $i$ -th grid point.

## C.4 Grid Refinements and Adaptive Time Steps

In order to be able to “see” type II critical collapse, where the solution at the threshold of black hole formation is self-similar, it is essential for the code to resolve widely varying scales both in space and in time. There are two features that enable the DICE code to manage this resolution: first, the grid points freely fall along the ingoing null geodesics  $v = \text{const}$ . These geodesics tend to focus in regions of strong curvature, as they necessarily occur if the evolved solution stays close to a self-similar solution for some time. This helps to increase the spatial resolution in such regions. Second, as the grid points eventually hit the origin and are dropped from the grid, the number of grid points is doubled each time half of the grid points are lost (this follows [26]) (the values of the grid functions at these additional grid points are obtained by interpolation). This method is most effective, if in addition the outer boundary of the grid is fine tuned to be (slightly outside but) close to the past SSH of the self-similar solution (again this was used by Garfinkle in [26]).

Concerning the time step, the scheme used is not restricted by a Courant-Friedrichs-Lewy (CFL) limit, as the numerical domain of dependence always equals the physical domain of dependence of the grid. Nevertheless, we need an upper bound for the time steps in order to get enough resolution in time. Following Refs. [30, 29] this is achieved by requiring

$$\Delta u \leq \frac{C\Delta r}{\frac{V}{r}}, \quad (\text{C.16})$$

for all grid points. This restricts the time steps such that no grid point is allowed to fall inwards more than  $C/2$  grid spacings within a single time step. (Usually  $C$  is set to 1.5).

Apart from providing enough resolution in time this restriction on the time step also prevents the scheme to run into an apparent horizon  $\Theta_+ = 0$ , where the code would crash due to  $\beta \rightarrow \infty$ . Instead the time evolution slows down before the formation of an apparent horizon due to both  $\Delta r$  going to zero at the apparent horizon (because  $r$  fails to parameterize the outgoing null rays  $u = \text{const}$  there) and an increase in  $\frac{V}{r}$ . This increase in  $\frac{V}{r}$  at a null slice close to an apparent horizon can be explained as follows: first of all according to Eq. 2.55  $\beta$  is non decreasing with  $r$ . So if it gets large somewhere on the slice it stays large for all larger  $r$ . Furthermore at large enough  $r$  the field  $\phi$  and its derivative are small, and therefore the quantity  $2m/r$  is decreasing.  $\frac{V}{r}$  can be written as  $\frac{V}{r} = e^{2\beta}(1 - 2m/r)$ , so  $\frac{V}{r}$  increases monotonically and gets large outside the outermost peak of  $2m/r$ .

## C.5 Diagnostics, Accuracy and Convergence Tests

In order to test the accuracy of the code we use the following quantities. First we compute the mass function 2.34 in two different ways, namely

$$m_{MS} = \frac{r}{2} \left( 1 - \frac{V}{r} e^{-2\beta} \right) \quad (\text{C.17})$$

and

$$m_\rho = \frac{\eta}{2} \int_0^r dr r^2 \left( \frac{V}{r} e^{-2\beta} (\phi')^2 + 2 \frac{\sin^2(\phi)}{r^2} \right). \quad (\text{C.18})$$

For a solution to the Einstein equations, both expressions are identical, for a numerically computed solution nevertheless, they will differ by a small amount due to finite differencing errors. Defining

$$\delta m = \frac{m_{MS} - m_\rho}{m_{total, initial}}, \quad (\text{C.19})$$

where  $m_{total, initial}$  is the mass contained in the grid at the initial slice, we have a measure of accuracy, which should always be  $\ll 1$ .

The other quantities that serve as a check for accuracy are the Einstein equations  $E_{uur}$  (2.57) and  $E_{\theta\theta}$  (2.58), which are not used to compute the solution. Here the question of normalization remains open in part. One possibility would be to define the sum of the absolute values of each term contributing to the expressions  $E_{uur}$  and  $E_{\theta\theta}$ , calling them  $E_{|uur|}$ ,  $E_{|\theta\theta|}$  and use this as the normalization (this is e.g. done in 3+1 numerical relativity). The expressions  $E_{uur}/E_{|uur|}$ ,  $E_{\theta\theta}/E_{|\theta\theta|}$  then should always be  $\ll 1$ . J. Thornburg chose a different normalization, which does not only consist of the sum of the absolute values but taking the maximum over the whole slice of the absolute value of each term, and then taking the sum. Calling this expression  $E_{max|uur|}$  he uses  $E_{uur}/(1 + E_{max|uur|})$  and the analogous

expression for  $E_{\theta\theta}$ . The reason for taking the maxima was, that as we are working on null slices and integrate outwards from the origin, errors occurring at some location in the slice are transported outwards. The additional 1 in the denominator reduces the error norm to the pure expression  $E_{urr}$  near the origin, and was introduced to make this norm better behaved close to the origin. What speaks in favor of this normalization is the fact, that the error norms constructed like this in most of the experienced situations are small, when the solution is well behaved, whereas they get large, when something is wrong.

A number of convergence tests was done by J. Thornburg and M. Pürner to test, whether the accuracy really corresponds to second order. Assuming that the fields are globally second order accurate, i.e. that the quantity  $\Psi_N$ , computed numerically with  $N$  grid points differs from the true continuum solution  $\Psi$  by  $\Psi_N = \Psi + c/N^2$ , where  $c$  is independent of the resolution, and all higher order terms are neglected, then  $\Psi_{2N}$ , computed with twice the resolution differs from  $\Psi$  by  $\Psi_{2N} = \Psi + c/(4N^2)$ . Assume now that  $\Psi = 0$ <sup>3</sup>, as is the case e.g. for the above defined quantities  $\delta m$ ,  $E_{urr}$  and  $E_{\theta\theta}$ . Then

$$\Psi_{2N} = \frac{c}{4N^2} = \frac{1}{4}\Psi_N. \quad (\text{C.21})$$

Three excellent examples of these convergence tests can be found in the appendix of [45], where second order convergence is shown for the quantity  $\delta m$  for near critical solutions, and for the quantity  $p^*$ . Further convergence tests of the DICE code can be found in [64].

An additional test on the code was done by M. Pürner who re-investigated critical collapse of the massless Klein-Gordon field with the DICE code, and found the critical solution to be DSS with the reported [19] values of  $\Delta$  and  $\gamma$ . The fact that the Klein-Gordon DSS solution can be resolved with this code is a good test for resolution, as the echoing period  $\Delta \approx 3.43$  in this case is much bigger than for the  $\sigma$  model for large couplings, and therefore is harder to resolve numerically.

We also mention the fact that the critical solution of the  $\sigma$ -model for large couplings agrees rather well with the directly constructed DSS solutions (see Figs. 5.11 and 5.12). This provides a good test for the DICE code as well as for the “DSS code”.

---

<sup>3</sup>If the value of  $\Psi$  is not known in advance, one has to compare three different solutions, with  $N$ ,  $2N$  and  $4N$  grid points. Second order convergence then is given if

$$\Psi_{4N} - \Psi_{2N} = \frac{c}{16N^2} - \frac{c}{4N^2} = \frac{1}{4}(\Psi_{2N} - \Psi_N). \quad (\text{C.20})$$

## C.6 Measurement of the black hole mass

The formation of a black hole is signalled by the formation of an apparent horizon  $\Theta_+ = 0$  (or  $\beta \rightarrow \infty$  or  $\frac{2m}{r} \rightarrow 1$ ). As explained in the last section, the code slows down and stops before an apparent horizon forms. The code “detects” the black hole whenever  $\frac{2m}{r}$  exceeds some threshold close to 1 anywhere in the grid. This threshold is usually set to be 0.995. At each time step the “momentary” black hole mass is defined as the mass  $m_{MS}$  of the outermost such grid point. At each further time step this “momentary mass” should increase, corresponding to additional matter falling into the black hole. If the numerical grid extends to large enough values of  $r$  initially and if the mass does not change substantially from one time step to the other, we have a good estimate for the “final” black hole mass. After detecting a black hole the code either stops because the number of time steps (after black hole detection) exceeds some limit or because the time steps shrink to  $du/u < 10^{-15}$  (which corresponds to the order of floating point roundoff errors).

For large couplings the runs were made with an initial spatial extension of the grid, which lay substantially outside the backwards light cone of the critical solution. For smaller couplings on the other hand, the outer boundary of the grid had to be fine tuned to be close to the backwards light cone, in order to get enough resolution. In this case clearly the final numerical estimate of the mass does not correspond to the final mass of the black hole, but rather measures the apparent horizon close to the past SSH of the critical solution.

# Appendix D

## Conventions

Conventions concerning curvature quantities and the signature of the metric are the same as in [76]. In particular we have

**Signature:**

$$(- + + +) \tag{D.1}$$

**Riemann tensor:**

$$\mathcal{R}^\sigma_{\rho\mu\nu} = \Gamma^\sigma_{\nu\rho,\mu} - \Gamma^\sigma_{\mu\rho,\nu} + \Gamma^\alpha_{\nu\rho}\Gamma^\sigma_{\alpha\mu} - \Gamma^\alpha_{\mu\rho}\Gamma^\sigma_{\alpha\nu} \tag{D.2}$$

**Ricci tensor:**

$$\mathcal{R}_{\rho\nu} = \mathcal{R}^\sigma_{\rho\sigma\nu} \tag{D.3}$$

**Scalar curvature:**

$$\mathcal{R} = g^{\rho\nu}\mathcal{R}_{\rho\nu} \tag{D.4}$$

**Action:**

$$S = \int d^4x \sqrt{-g} \left\{ \frac{1}{2\kappa} (\mathcal{R} - 2\Lambda) + \mathcal{L}_{\mathcal{M}} \right\} \tag{D.5}$$

**Stress energy tensor:**

$$2 \int d^4x \delta_g (\sqrt{-g} \mathcal{L}_{\mathcal{M}}) = \int d^4x \sqrt{-g} (-T_{\mu\nu}) \delta g^{\mu\nu}, \tag{D.6}$$

where  $\delta g^{\mu\nu} \equiv (\delta g^{-1})^{\mu\nu}$

**Einstein equations:**

$$G_{\mu\nu} + \Lambda g_{\mu\nu} = \kappa T_{\mu\nu} \tag{D.7}$$

Throughout this work the speed of light is set to unity,  $c = 1$ .



# Bibliography

- [1] A. M. Abrahams and C. R. Evans. Critical behavior and scaling in vacuum axisymmetric gravitational collapse. *Physical Review Letters*, 70:2980–2983, 1993.
- [2] Peter C. Aichelburg and Christiane Lechner. Sigma model on de Sitter space. *Physical Review D*, 57(10):6176–6180, May 1998.
- [3] V. I. Arnol'd. *Geometrical Methods in the Theory of Ordinary Differential Equations*. Springer, New York, 1983.
- [4] D. K. Arrowsmith and C. M. Place. *An Introduction to Dynamical Systems*. Cambridge University Press, Cambridge, 1990.
- [5] R. Bartnik and J. McKinnon. Particle-like solutions of the Einstein Yang-Mills equations. *Physical Review Letters*, 61:141–144, 1988.
- [6] Piotr Bizoń. Gravitating solitons and hairy black holes. *Acta Physica Polonica B*, 25:877–898, 1994.
- [7] Piotr Bizoń, 2000. personal communication.
- [8] Piotr Bizoń. Equivariant self-similar wave maps from Minkowski spacetime into 3-sphere. *Communications in Mathematical Physics*, 215(1):45–56, December 2000.
- [9] Piotr Bizoń, 2001. personal communication.
- [10] Piotr Bizoń, Tadeusz Chmaj, and Zbislav Tabor. Dispersion and collapse of wave maps. *Nonlinearity*, 13(4):1411–1423, July 2000.
- [11] Piotr Bizoń and Arthur Wasserman. Self-similar spherically symmetric wave maps coupled to gravity. *Physical Review D*, 62:084031, 2000.
- [12] Patrick R. Brady and Mike J. Cai. Critical phenomena in gravitational collapse. In Tsvi Piran and Remo Ruffini, editors, *Proceedings of the Eighth Marcel Grossmann Meeting*, pages 689–704. World Scientific, Singapore, 1989.

- [13] Patrick R. Brady, Chris M. Chambers, and Sergio M. C. V. Gonçalves. Phases of massive scalar field collapse. *Physical Review D*, 56:6057–6061, 1997.
- [14] Peter Breitenlohner, Peter Forgacs, and Dieter Maison. On static spherically symmetric solutions of the Einstein Yang-Mills equations. *Communications in Mathematical Physics*, 163:141–172, 1994.
- [15] O. Brodbeck, M. Heusler, G. Lavrelashvili, N. Straumann, and M. S. Volkov. Stability analysis of new solutions of the EYM system with cosmological constant. *Physical Review D*, 54:7338, 1996.
- [16] Claudio Canuto, M. Yousuff Hussani, Alfio Quarteroni, and Thomas A. Zang. *Spectral Methods in Fluid Dynamics*. Springer-Verlag, New York and Berlin, 2nd printing edition, 1988.
- [17] Matthew W. Choptuik. homepage, <http://laplace.physics.ubc.ca/People/matt/>.
- [18] Matthew W. Choptuik. “Critical” behavior in massless scalar field collapse. In Ray d’Inverno, editor, *Approaches to Numerical Relativity*, pages 202–222. Cambridge University Press, Cambridge (UK), 1992. Proceedings of the International Workshop on Numerical Relativity, Southampton University (Southampton, England), 16–20 December 1991.
- [19] Matthew W. Choptuik. Universality and scaling in gravitational collapse of a massless scalar field. *Physical Review Letters*, 70:9–12, 1993.
- [20] Matthew W. Choptuik. The (unstable) threshold of black hole formation. In Naresh Dadhich and Jayant Narlikar, editors, *Gravitation and Relativity: At the Turn of the Millennium*, pages 67–85. Inter-University Center for Astronomy and Astrophysics, Post Bag 4, Ganeshkhind, Pune 411 007, India, 1998.
- [21] Matthew W. Choptuik, Tadeusz Chmaj, and Piotr Bizoń. Critical behaviour in gravitational collapse of a Yang-Mills field. *Physical Review Letters*, 77:424–427, 1996.
- [22] D. Christodoulou and S. Klainerman. *The global nonlinear stability of the Minkowski space*. Princeton University Press, Princeton, 1993.
- [23] J. Eells and L. Lemaire. A report on harmonic maps. *Bulletin of the London Mathematical Society*, 10:1–68, 1978.
- [24] J. Eells and L. Lemaire. Another report on harmonic maps. *Bulletin of the London Mathematical Society*, 20(5):385–524, 1988.

- [25] Charles R. Evans and Jason S. Coleman. Observation of critical phenomena and selfsimilarity in the gravitational collapse of radiation fluid. *Physical Review Letters*, 72:1782–1785, 1994.
- [26] David Garfinkle. Choptuik scaling in null coordinates. *Physical Review D*, 51(10):5558–5561, May 15 1995.
- [27] David Garfinkle and G. Comer Duncan. Scaling of curvature in subcritical gravitational collapse. *Physical Review D*, 58(6):064024, August 27 1998. (4 pages).
- [28] M. Gell-Mann and M. Lévy. The axial vector current in beta decay. *Nuovo Cimento*, 16:705–726, 1960.
- [29] Dalia S. Goldwirth, Amos Ori, and Tsvi Piran. Cosmic censorship and numerical relativity. In Charles R. Evans, Lee S. Finn, and David W. Hobill, editors, *Frontiers in Numerical Relativity*, pages 414–435. Cambridge University Press, Cambridge (UK), 1989. Proceedings of the International Workshop on Numerical Relativity, University of Illinois at Urbana-Champaign (Urbana-Champaign, Illinois, USA), 9–13 May 1988.
- [30] Dalia S. Goldwirth and Tsvi Piran. Gravitational collapse of massless scalar field and cosmic censorship. *Physical Review D*, 36(12):3575–3581, December 15 1987.
- [31] Roberto Gómez and Jeffrey Winicour. Asymptotics of gravitational collapse of scalar waves. *Journal of Mathematical Physics*, 33(4):1445–1457, April 1992.
- [32] Roberto Gómez and Jeffrey Winicour. Evolution of scalar fields from characteristic data. *Journal of Computational Physics*, 98:11, 1992.
- [33] Roberto Gómez and Jeffrey Winicour. Numerical asymptotics. In Ray d’Inverno, editor, *Approaches to Numerical Relativity*, pages 143–162. Cambridge University Press, Cambridge (UK), 1992. Proceedings of the International Workshop on Numerical Relativity, Southampton University (Southampton, England), 16–20 December 1991.
- [34] Carsten Gundlach. Echoing and scaling in Einstein Yang-Mills critical collapse. *Physical Review D*, 55:6002–6013, 1997.
- [35] Carsten Gundlach. Understanding critical collapse of a scalar field. *Physical Review D*, 55:695–713, 1997.
- [36] Carsten Gundlach. Critical phenomena in gravitational collapse. *Advances in Theoretical and Mathematical Physics*, 2:1–49, 1998.

- [37] Carsten Gundlach. Critical phenomena in gravitational collapse. *Living Reviews in Relativity*, 2(4), 1999.
- [38] Carsten Gundlach, 2001. personal communication.
- [39] Stephen W. Hawking and George F. R. Ellis. *The Large Scale Structure of Space-Time*. Cambridge University Press, Cambridge (UK), 1973.
- [40] Sean A. Hayward. General laws of black hole dynamics. *Physical Review D*, 49:6467–6474, 1994.
- [41] Sean A. Hayward. Gravitational energy in spherical symmetry. *Physical Review D*, 53(4):1938–1949, February 15 1996.
- [42] Markus Heusler. *Black Hole Uniqueness Theorems*. Cambridge Lecture Notes in Physics 6. Cambridge University Press, Cambridge, 1996.
- [43] Markus Heusler. No-hair theorems and black holes with hair. *Helvetica Physica Acta*, 69:501, 1996.
- [44] Shahar Hod and Tsvi Piran. Fine-structure of Choptuik’s mass-scaling relation. *Physical Review D*, 55:440–442, 1997.
- [45] Sascha Husa, Christiane Lechner, Michael Pürrer, Jonathan Thornburg, and Peter C. Aichelburg. Type II critical collapse of a self-gravitating nonlinear  $\sigma$ -model. *Physical Review D*, 62:104007, 2000.
- [46] James M. Hyman. Numerical methodologies for solving partial differential equations. In J. R. Buchler, editor, *NATO Advanced Research Workshop on the Numerical Modeling of Nonlinear Stellar Pulsations: Problems and Prospects*, pages 215–237. Kluwer, Dordrecht, 1989. Also available as Los Alamos National Laboratories Report LA-UR 89-3136.
- [47] Tatsuhiko Koike, Takashi Hara, and Satoshi Adachi. Critical behaviour in gravitational collapse of radiation fluid – a renormalization group (linear perturbation) analysis. *Physical Review Letters*, 74:5170–5173, 1995.
- [48] Christiane Lechner, Sascha Husa, and Peter C. Aichelburg. SU(2) cosmological solitons. *Physical Review D*, 62:044047, 2000.
- [49] Christiane Lechner, Jonathan Thornburg, Sascha Husa, and Peter C. Aichelburg. A new transition between discrete and continuous self-similarity in critical gravitational collapse, 2001. in preparation.
- [50] A Lichnerowicz. *Théories relativistes de la gravitation et de l’électromagnétisme*. Masson, Paris, 1955.

- [51] Steven L. Liebling. Critical phenomena inside global monopoles. *Physical Review D*, 60(6):061502, September 15 1999. (5 pages).
- [52] Steven L. Liebling and Matthew W. Choptuik. Black hole criticality in the Brans-Dicke model. *Physical Review Letters*, 77(8):1424–1427, August 1996.
- [53] Steven L. Liebling, Eric W. Hirschmann, and James Isenberg. Critical phenomena in nonlinear sigma models. *Journal of Mathematical Physics*, 41(8):5691–5700, August 2000.
- [54] Dieter Maison. Nonuniversality of critical behavior in spherically symmetric gravitational collapse. *Physical Letters B*, 366:82–84, 1996.
- [55] Charles W. Misner. Harmonic maps as models for physical theories. *Physical Review D*, 18:4510–4524, 1978.
- [56] Charles W. Misner. Nonlinear model field theories based on harmonic mappings. In Richard A. Matzner and L. C. Shepley, editors, *Spacetime and Geometry: The Alfred Schild Lectures*, pages 82–101. University of Texas Press, Austin (Texas), 1982.
- [57] Charles W. Misner and David H. Sharp. Relativistic equations for adiabatic, spherically symmetric gravitational collapse. *Physical Review B*, 136(2):571–576, October 26 1964.
- [58] P. Vargas Moniz. Kantowski-Sachs universes and the cosmic no-hair conjecture. *Physical Review D*, 47(10):4315–4321, May 15 1993.
- [59] Nikolaus Müllner. Master’s thesis, Universität Wien, 2001.
- [60] NAG. *Fortran Library Manual – Mark 16*. The Numerical Algorithms Group Ltd., Oxford, 1994.
- [61] Roger Penrose. Gravitational collapse and space-time singularities. *Physical Review Letters*, 14:57, 1965.
- [62] Roger Penrose. Structure of space-time. In Cecile M. DeWitt and John A. Wheeler, editors, *Battelle Rencontres: 1967 Lectures in Mathematics and Physics*, pages 121–241. W. A. Benjamin, Inc., New York, Amsterdam, 1968.
- [63] William H. Press, Brian P. Flannery, Saul A. Teukolsky, and William T. Vetterling. *Numerical Recipes: The Art of Scientific Computing*. Cambridge University Press, Cambridge (UK) and New York, 2nd edition, 1992.
- [64] Michael Pürner. Master’s thesis, Universität Wien, 2001.
- [65] Alan Rendall. Local and global existence theorems for the Einstein equations. *Living Reviews in Relativity*, 3(1), 2000.

- [66] E. Seidel and W. M. Suen. Oscillating soliton stars. *Physical Review Letters*, 66:1659–1662, 1991.
- [67] B. T. Smith, J. M. Boyle, Jack J. Dongarra, B. S. Garbow, Y. Ikebe, V. C. Klema, and Cleve B. Moler. *Matrix Eigensystem Routines – EISPACK Guide*, volume 6 of *Lecture Notes in Computer Science*. Springer-Verlag, Berlin and New York, 2nd edition, 1976.
- [68] Steven H. Strogatz. *Nonlinear Dynamics and Chaos*. Addison-Wesley Studies in Nonlinearity. Addison-Wesley, Redwood City, California, etc., 2nd print edition, 1994.
- [69] Roger Temam. *Infinite-dimensional dynamical systems in mechanics and physics*. Springer, New York, 1988.
- [70] Jonathan Thornburg, 2000. personal communication; unpublished.
- [71] Jonathan Thornburg, 2001. personal communication; unpublished.
- [72] Jonathan Thornburg, Christiane Lechner, Michael Pürner, Peter C. Aichelburg, and Sascha Husa. Episodic selfsimilarity in critical gravitational collapse. Technical Report UWTHPH-2000-53, 2000.
- [73] Neil Turok and David Spergel. Global texture and the microwave background. *Physical Review Letters*, 64:2736, 1990.
- [74] Mikhail S. Volkov and Dimitri V. Gal’tsov. Gravitating non-abelian solitons and black holes with Yang-Mills fields. *Physics Reports*, 319:1–83, 1999.
- [75] M.S. Volkov, N. Straumann, G. Lavrelashvili, M. Heusler, and O. Brodbeck. Cosmological analogues of the Bartnik–McKinnon solutions. *Physical Review D*, 54:7243–7251, 1996.
- [76] Robert M. Wald. *General Relativity*. University of Chicago Press, Chicago, 1984.
- [77] Anzhong Wang. Critical phenomena in gravitational collapse: the studies so far. Technical report, April 2001.